IMFUFA tekst

- I, OM OG MED MATEMATIK OG FYSIK

Mathematical Modeling of Flow Characteristics in the Embryonic Chick Heart

Jesper Heebøll-Christensen

PhD Dissertation

March 2011

nr. 480 - 2011

Roskilde University,
Department of Science, Systems and Models, IMFUFA
P.O. Box 260, DK - 4000 Roskilde
Tel: 4674 2263 Fax: 4674 3020

Mathematical Modeling of Flow Characteristics

in the Embryonic Chick Heart

By: Jesper Heebøll-Christensen

IMFUFA tekst nr. 480/ 2011 – 281 pages – ISSN: 0106-6242

This ph.d. thesis contains the mathematical modeling of fluid dynamical phenomena in the tubular embryonic chick heart at HH-stages 10, 12, 14, and 16. The models are constructed by application of energy bond technique and involve the elasticity of heart walls with elliptic cross-section, Womersley modified inertia,
and resistance due to friction and curvature of the multilayered tubular heart.

Through the modeling, flow conditions in the embryonic heart are characterized. The models suggest that eccentric rather than concentric deformation of the beating heart is optimal for mean flows induced by the Liebau effect. Additionally the elliptic cross-sectional shape of the embryonic heart may be optimally configured for Liebau induced flow near elliptic eccentricity 0.4. It is furthermore suggested that both peristaltic and Liebau induced pumping effects may be present in the embryonic heart, though the models are not conclusive on this point.

In addition the Liebau effect is investigated in a simpler system containing two elastic tubes joined to form a liquid filled ring, with a compression pump at an asymmetric location. Through comparison to other reports the system validates model construction. Furthermore it is concluded that the observed Liebau effect does depend on the impedance of the tubes, the frequency and position of the compression pump, but above all the characterization of the pumping function. Different pumping functions are employed in the modeling but no defining characteristics of their efficiency have been found.

Mathematical Modeling of Flow Characteristics in the Embryonic Chick Heart

Ph.D thesis
in Applied Mathematics
by Jesper Heebøll-Christensen

Roskilde University
Department of Science, Systems and Models
Research division IMFUFA

January 2011

Abstract

This ph.d. thesis contains the mathematical modeling of fluid dynamical phenomena in the tubular embryonic chick heart at HH-stages 10, 12, 14, and 16. The models are constructed by application of energy bond technique and involve the elasticity of heart walls with elliptic cross-section, Womersley modified inertia, and resistance due to friction and curvature of the multilayered tubular heart.

Through the modeling, flow conditions in the embryonic heart are characterized. The models suggest that eccentric rather than concentric deformation of the beating heart is optimal for mean flows induced by the Liebau effect. Additionally the elliptic cross-sectional shape of the embryonic heart may be optimally configured for Liebau induced flow near elliptic eccentricity 0.4. It is furthermore suggested that both peristaltic and Liebau induced pumping effects may be present in the embryonic heart, though the models are not conclusive on this point.

In addition the Liebau effect is investigated in a simpler system containing two elastic tubes joined to form a liquid filled ring, with a compression pump at an asymmetric location. Through comparison to other reports the system validates model construction. Furthermore it is concluded that the observed Liebau effect does depend on the impedance of the tubes, the frequency and position of the compression pump, but above all the characterization of the pumping function. Different pumping functions are employed in the modeling but no defining characteristics of their efficiency have been found.

Dansk resumé

Denne ph.d.-afhandling indeholder den matematiske modellering af fluid dynamiske fænomener af det rørformede embryoniske kyllinge-hjerte ved HH-stadie 10, 12, 14 og 16. Modellerne er konstrueret ved anvendelse af energibåndsteknik og inkluderer elasticiteten af hjertets lag-indelte vægge med et elliptisk tværsnit, en Womersley-modificeret inerti-funktion, samt modstand skabt ved friktion og krumning af det rørformede hjerte.

Gennem modelleringen karakteriseres betingelser for flow i det embryoniske hjerte. Modellerne antyder at excentrisk frem for koncentrisk deformation af det bankende hjerte er optimalt for middelflow induceret ved Liebau-effekten. Tilsvarende findes den optimale elliptiske tværsnit af det embryoniske hjerte potentielt omkring den elliptiske excentricitet 0.4. Det foreslås yderligere, at effekter af både peristaltisk og Liebau-induceret pumpning kan være til stede i det embryoniske hjerte, dog er modellerne ikke konkluderende omkring denne antagelse.

Yderligere er Liebau-effekten undersøgt i et simplere system bestående af to elastiske slanger sammensat i form af en ring fyldt med væske, med en kompressionspumpe placeret i en asymmetrisk position. Gennem sammenligning med andre rapporter validerer dette system modellens konstruktion. Tilmed konkluderes det, at den observerede Liebau-effekt afhænger af impedansen af slangerne samt frekvensen og positionen af kompressionspumpen, men frem for alt afhænger effekten af karakteriseringen af pumpens funktion. Forskellige pumpefunktioner er anvendt i modelleringen men ingen definerende karakteristikker af deres effektivitet i forhold til Liebau-effekten er fundet.

Preface

This is my thesis for the ph.d. study in applied mathematics at Roskilde University, department of Science, Systems and Models, in the research division IMF-UFA.

It is, as I see it, at detailed work in a mathematical discipline that has gone unnoticed by many mathematicians; the discipline involved in the use of energy bond techniques. To some this may seem as an engineering speciality, but be assured that underneath the layer of seemingly physical language and complicated networks lies a thoroughly mathematical discipline involving definitions and theorems and rules for the construction of models, in fact energy bond graphs are just a clever way of illustrating some very complicated mathematical equations.

As such the thesis involves a standard approach of applied mathematics to the problem of modeling the chick embryonic heart: The detailed acquisition and interpretation of the problems in the field of embryological cardiology, the basic definition of conditions and assumptions regarding to the modeled case, the construction of a general model based on the conditions and assumptions, the adjustment of the model to fit the actual case, and the solution of the model and subsequent interpretation of model results in relation to the modeled case. I think, no more justification than this is required.

The purpose of this work is to construct a model for the beating embryonic chick heart. In the end of the thesis a model is setup for this case and simulations of the heart attempted. The result of this attempt is unsuccessful.

The regretful fact is, that following all this work, one of the main goals stands as incomplete, and I have no desire to hide it or complain about it. A detailed modeling procedure and many other simulation results are still worth presenting as well as the whole setup of the embryonic heart.

It has been suggested to me to change the focus of the thesis, such that the modeling of valveless flow phenomena is the focus, and the embryonic chick heart only an application of these phenomena. I have decided not to do so, since I feel it would be dishonest and unwise to change the focus in the 11th hour of the process, especially if only to cover up what may appear as an incomplete work.

The modeling of the embryonic chick heart has been the goal of the modeling procedure all along, and this I feel should be reflected in the thesis as well. As such whole chapters of the thesis are devoted solely to the description of the chick heart, which still takes the center stage in the modeling.

I wish to extend my gratitude to Lars Thrane, Jörg Männer and T. Mesud Yelbuz and all the other guys working at the chicken lab in Hannover for great discussions and for their help in this work. During the project I stayed with them at the Medizinische Hochschule Hannover and participated in the measuring of cardiac activity in the young chicken embryos.

Gratitude should also be extended to my supervisor Johnny Ottesen who has offered assistance with complicated issues in the modeling and helped me greatly in my frustration over problems in the project - mathematically and otherwise.

Last but not least I wish to thank my friend and colleague Jon Josef Papini who has been a good companion and great support for many years. Thanks for scientific discussions, solution ideas to complicated problems and Diplomacy.

Overall the staff at IMFUFA should be thanked for interesting discussions and inputs. This project could not have been completed without those conversations.

Jesper Heebøll-Christensen
IMFUFA/NSM, RUC
New Year's Eve 2010/11

Contents

Chapter 1

Introduction

Embryological genesis and function are important fields in physiological research and have been for many centuries. Seeing the generation of life and the formation of a living being in the foetus is not only interesting from a philosophical or evolutionary point of view; with the necessary knowledge embryologists can save many lives by preventing diseases and malformations before they evolve into problems.

Interestingly the growth of characteristic organs in the early embryonic development are similar for almost all higher vertebrate embryos, such is also the case for the embryonic heart. Therefore it has become common practice among embryologists to study the embryonic heart of the chick; aside from the obvious difference in size the development of the embryonic chick heart parallels that of the human heart almost 1:1 [Taber, 2006a].

The embryonic heart begins its existence as a straight muscle-wrapped tube that starts beating briefly after is creation. While beating the tubular heart curves around itself to form a helical structure, which is the earliest demonstration of left-right asymmetry in the embryo [Männer, 2000]. Subsequently the helical heart tube grows together and eventually transforms into a mature four-chambered heart.

The morphology and pumping mechanisms of the early tubular heart have caught the interests of many researchers, as the heart at this stage of development portrays an entirely different structure than the four-chambered heart of mature animals. The questions are, what causes the heart to have this shape at its early development and what are the mechanisms involved in the tubular heart.

One of the groups working with the tubular heart of the embryo is situated at the Medizinische Hochschule Hannover (the medical university of Hannover, Germany) and is lead by Jörg Männer and T. Mesud Yelbuz. This group have so far made significant contributions to the understanding of the morphology of the tubular heart; how the heart curves to form the helical heart tube in a process referred to as cardiac looping [Männer, 2000, 2004, 2006, 2008]. And in 2008 they

made a remarkable discovery with the OCT imaging technique that the beating heart tube contracts in an eccentric, almost elliptic, contraction pattern, contrary to what was believed [Männer et al., 2008, 2009].

Many years before it was discovered that the tubular heart had a layered structure, and the importance of this structure was proved to be important for peristaltic pumping of the heart by use of concentric contractions [Barry, 1948].

Their discovery increased the interest in fluid propagation and pumping mechanisms of the embryonic heart, which was already discussed intensely since another research group from California Institute of Technology lead by Farouhar, Gharib and Hickerson in 2006 made a discovery of tubular hearts that conflicted with the peristaltic pumping principle that had been assumed so far [Männer et al., 2010].

Their suggestion was that another pumping principle could explain the phenomenon of the tubular heart better than peristalsis: the Liebau effect. Peristaltic pumping can be described as a sliding compression of a tube to push liquid forward, while the Liebau effect is comprised of periodic compressions interacting with the dimensions of the tube to produce a net flow of liquid.

These two principles exists as competing hypotheses for the pumping mechanism of the embryonic heart, and so far it has not been possible to decide which of them correctly describes the flow phenomena of the elliptic layered tubular heart.

1.1 The thesis

This thesis includes the mathematical descriptions of elastic tubes to model the pumping mechanism and fluid propagation of the tubular embryonic heart.

The models are made by application the energy bond technique from the knowledge that pulsating flow and pressure in the elastic tube equals to transport of energy. The construction of the models follows a 'historical' perspective starting with the Windkessel model, expanding to a transmission line and expanding further. Through the thesis the models are continuously expanded to better approximate the tubular heart, ending with the model of a curved layered tube with an elliptic cross-section.

The models are made from basic physical theories and fitted to meet known characteristics of the embryonic heart. The models are setup with material parameters and dimensions of the tubular heart and subsequently applied to simulate the observed compression cycle in a mathematically approximated embryonic heart.

The goal of the modeling and simulation of the embryonic heart is to prove that the embryonic heart can be modeled with the use of first principle physics. Though some additions to the model will be ad hoc approximations to real physical effects

in the heart, it is believed that a successful simulation of the embryonic heart that compares to observed measurements of flow and pressure will be a proof that the heart can be physically described with the model.

Through simulations of the model it is the aim of this thesis to investigate the different hypotheses for the pumping mechanism of the embryonic heart: peristaltic pumping and the Liebau effect. In addition the thesis aims to investigate the difference between a tube with circular cross-section as opposed to an elliptic cross-section, specifically in relation to the mentioned pumping principles.

As a means to investigating the Liebau effect it is specifically investigated if the constructed model is capable of simulating mean flow from a Liebau pump, this is done in relation to an experimental system consisting of two elastic tubes joined together to form a ring and filled with liquid; via the periodic compression at an asymmetric location on the ring a mean flow will be induced from the interaction between compression waves and the impedance of the tube.

The experimental test case is supposed to validate the constructed model of this thesis and its results are specifically compared to two other cases involving a similar Liebau model. Additionally the case is used to investigate different elements and inclusions of the model and thereby to compare different parts of the model in relation to each other.

The discussion following the modeling and simulations in this thesis will focus on the functional behavior of the models rather than the embryological research, it can be summed up by the following three questions:

- *Will the complicated flow and pressure conditions exhibited by the embryonic heart be adequately modeled by the energy bond models constructed in this thesis?*
- *In relation to the possible pumping mechanisms of the embryonic heart are elliptic contractions of the heart tube optimal compared to concentric contractions?*
- *Given the morphology and cross-sectional shape of the tubular heart will a peristaltic or Liebau pumping principle be desirable for the propagation of blood?*

1.1.1 The method in the thesis

The method employed in this thesis and in the modeling and simulation procedure is a rather brute force approach; to find if something is possible often the best and easiest way is simply to do it. With this approach the modeling is carried out continuously through the thesis without hesitation.

Simulations are produced according to setup of the case of the experimental Liebau system and the tubular heart for several stages of embryonic development. Given the comparability of the simulation results to the cases modeled the first of the three questions above is evaluated.

In the event that the simulated cases are successful and it is thus proved that the models can simulate both a peristaltic and a Liebau pumping principle, the third question is answered directly. As it is, there is nothing in the theory stating that both pumping principles can not exist simultaneously, and if it is proved that the models can handle both mechanisms and furthermore can adequately simulate the flow and pressure of the embryonic heart, the third question becomes simply void.

In the modeling and simulation procedure it will be a priori assumed that the model is able to produce peristaltic flow, despite that total occlusion of the tube lumen will be a singularity in the mathematical equations, which is not achievable in the simulations. Peristaltic flow can be produced even if the lumen is not totally closed though perhaps not quite as effective. The question is, if the simulations are able to produce the complicated wave interactions of the Liebau effect, and for that reason the case of the experimental Liebau system is investigated.

In application of the experimental Liebau system the second question is also investigated. Other researchers have already produced results that suggest that elliptical contractions have higher mechanical efficiency than concentric contraction for peristaltic pumping, but it has not been investigated for the Liebau effect. By comparing the results of the Liebau system simulated with concentric and elliptic contraction a suggestive result may be achieved for this question.

1.1.2 The use of the thesis

The models contained in this thesis are constructed from basic elasticity theory and fluid dynamics together with mathematical analysis and theory of differential equations, all fitted into the energy bond formalism. Not many people may understand the energy bond graphs in this thesis, but the equations extracted from them are very real and physically consistent. As such the modeling contained in this thesis has value in itself.

Furthermore the simulations of the experimental Liebau case and the embryonic heart may prove the validity of the model, while simultaneously the results of the simulations may shed light on aspects of the cases modeled. Specifically with regards to the embryonic heart the simulations may improve knowledge of the three questions posed above.

The thesis does not hold the conclusive answer to those three questions. Even though the modeling contained herein may produce simulation results comparative to the embryonic heart there are still room for improvement of the models to

further specialize them in relation to the tubular heart. Regarding the second and third question the modeling may produce suggestive answers to those but to reach conclusive answers many more cases must be studied.

In the thesis the energy bond formalism is treated as a mathematical modeling tool. Though at times reference is made to elements in the energy bond graphs that have specific physical interpretations they should be regarded as abstract mathematical objects that have specific rules and definitions attached to them. The energy bond graphs are never meant as representations of physical networks or electrical circuits, both the energy bond graphs and the language of the energy bond formalism are just convenient tools to handle a complicated modeling discipline.

As such the energy bond technique should be regarded as a specialized mathematical modeling tool, which unfortunately is rarely applied by mathematicians. It will have a central position in the modeling procedure of this thesis and through the process it should become clear that energy bond technique has qualities that are seldom seen in other mathematical disciplines.

1.1.3 Outline of the thesis

This thesis basically includes a long an complicated modeling procedure that starts with the historical introduction to the Windkessel model in section 1.2 below and ends with the layered tube model at the end of chapter 6, and in some instances additions to the models are included in both chapter 7 and 8 as well.

Though the models are built as expansions to each other the thesis is constructed such that it is reasonably possible to skip some steps and read on from chapter 4 or chapter 6, which are designed to follow parallel modeling procedures.

In between the modeling the embryological research is presented and the models will be investigated according to a case involving the Liebau effect. Finally the simulations of the embryonic heart will be setup and simulation results presented and discussed.

Below in section 1.2 is an introduction to the modeling procedure starting with the Windkessel model, progressing to the transmission line and finally introducing the concept for the complicated models of this thesis.

In chapter 2 an introduction to the chick embryo will be presented, involving some of the characteristics of the embryonic heart that will be included in the models and in the simulations of the tubular heart.

In chapter 3 fluid dynamic theory is presented specifically with relation to liquid transport in elastic tubes. The theory presented in this chapter will be employed later in the modeling procedure.

In chapter 4 the first model will be constructed, assuming that the elastic tube has a circular cross-section. The model is constructed in basically two steps; first the fundamental elements concerning flow in elastic tubes are modeled, secondly additional assumptions lead to expansions of the model.

In chapter 5 the cylindric model is tested with respects to a case involving a simple Liebau pump. The simulations of the Liebau pump is compared to two other reports of a similar system. Furthermore the additional elements included to the model in chapter 4 are tested in relation to each other.

In chapter 6 the second and third model are constructed, assuming first that the cross-section of the tube is elliptic and second that the tube has a layered cross-section with an elliptic inner lumen and a circular outer perimeter. The modeling procedure is parallel to that of chapter 4.

In chapter 7 the morphology, materials and pumping function of the embryonic heart is investigated to setup simulations of the heart by the use of the models.

In chapter 8 the results of the simulations are investigated and compared to data of flow and pressure in the embryonic heart. Additionally simulations of a Liebau pump involving an elliptic tube are constructed and investigated.

In chapter 9 the simulation results and models are discussed in relation to the questions asked in the thesis.

The appendixes of the thesis includes the programs used to make the simulations of the Liebau pump and the embryonic heart.

1.2 The Windkessel model

The first attempt to explain or model the pulsatile behavior of the pressure and blood flow in the entire cardiovascular system was done by Reverend Stephen Hales who in his book *Haemastaticks* from 1733 compared the arterial system to that of an elastic reservoir made up of a compressed-air-filled tank. In the German translation of his book this tank was known as a 'Windkessel' [Nichols and O'Rourke, 1998, p. 3].

The Windkessel, which is in fact a common component in present day pipelines and water works, is in relation to modeling typically depicted as an old fire cart where a hose and a piston pump in one end of the cart could be used to take water in from a nearby lake or well into a large reservoir. This reservoir contains water up to a certain level an above that air in a tightly sealed container, when more water is pumped into the reservoir the water level rises and the air will be compressed. The excess air pressure forces a steady flow of water out the fire hose, which is characterized with a very high peripheral resistance. See figure 1.1.

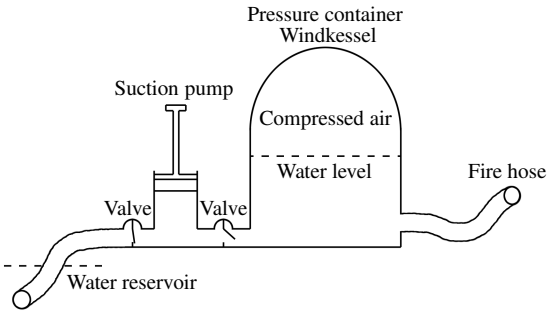

Figure 1.1: The Windkessel model depicted as an old fire cart with a pump, an elastic pressure reservoir, and the peripheral resistance of the fire hose.

As such Hales used the Windkessel analogue to explain how a pulsatile flow from the heart with an elastic reservoir given by the arteries and arterioles could be transformed into a seemingly steady flow in the veins through the peripheral resistance given by capillary tissue.

The Windkessel concept was made known in the late nineteenth and early twentieth century when the German physicist and mathematician Otto Frank consistently used the word for the model by Hales, which he based his research upon. In fact many modern day researchers in the cardiovascular field ascribe the Windkessel model to Frank - not Hales.

Otto Frank was concerned with manometry and measurement of the arterial pressure waves, his goal was an understanding of the arterial properties and arterial function, so that ultimately flow could be predicted from pressure change [Nichols and O'Rourke, 1998, p. 6]. The Windkessel model was the best model for understanding pulsatile blood pressure that Frank knew, and as such he was also painfully aware of its severe limitations.

When modeling the entire arterial system as a single elastic reservoir the notion of pressure wave propagation is completely ignored along with the possibility of wave reflection. In this way Frank sought to explain measured pressure waves with a model that did not posses the explaining power for these phenomena, and his resulting compromise has been criticized by many as contradictory and illogical [Nichols and O'Rourke, 1998, p. 6].

Both Frank and Hales knew that the Windkessel model was not a true picture of the circulatory system, it was the best they had and in some cases it was only a model to visualize the property of the elastic capacity of the arterial system. True criticism should be laid on those that take the Windkessel model too literally.

1.2.1 The modern interpretation

Today the word 'Windkessel' has different meanings in historical and modeling contexts, it is still used in descriptions of the cardiovascular system, for instance by Yoshigi and Keller [1997], but mostly as a first-hand approximation to the concepts of an elastic reservoir and peripheral resistance, which are used to characterize the vascular system and diagnose problems. Researchers refer to the 'Windkessel principle' or the 'Windkessel effect', which is a generalization of the Windkessel model to describe the concept of an elastic reservoir and peripheral resistance.

To see the analogy it is easiest to translate the description of the 'old fire cart'-Windkessel into the language of electrical circuits. Let electrical charge represent the volume of blood, then electrical current is the volume flow, and electrical potential is the driving pressure in the system. With this analogy the Windkessel model is translated into an electrical circuit as seen on figure 1.2.

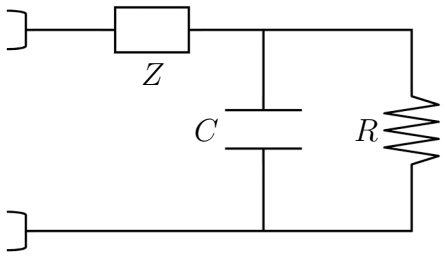

Figure 1.2: The electrically formulated Windkessel model

The capacitor, C, stores charge in the same way the elastic reservoir of the arteries stores blood, the resistance, R, is the peripheral resistance of the capillary tissue, and the component, Z, is used to represent the special impedance on the pulsating blood pressure. In the simpler versions of the model the impedance, Z, is omitted and in other complicated versions of the model more electrical components are included.

Electrical circuits such as this demonstrate the Windkessel principle of an elastic reservoir with an inflow and a resistive outflow. With this kind of analogy it is clear that a multitude of possible electrical networks based on the Windkessel principle can expand the concept of the original Windkessel model. Such models can be made far more advanced, however Hales' original idea of a conduit between a pulsating and a seemingly constant flow is lost in the process.

1.2.2 The transmission line

An example of the expansion of the Windkessel principle through electrical networks comes with the transmission line, which will be of importance for the modeling in chapter 4.

Expansions of the Windkessel principle via the electrical network analogue requires a specific interpretation of the included electrical elements in the model. So to formulate the idea of the transmission line as a plausible model for the cardiovascular system take as starting point the main argument against the Windkessel model that it leaves no possibility for pressure wave propagation in the system.

With the Windkessel principle the capacitor is considered as an elastic container for the volume of blood in the entire arterial system, but a capacitor could equally describe a single arterial section. In this case the capacitance and resistance of the electrically formulated Windkessel model is applied to only a small section of arteries instead of the entire arterial tree.

The capacitance, C, of the model describes the (inverse) compliance of the elastic arterial wall and the resistance, R, models the resistance to flow out of the arterial section. Both of these will depend on the physical properties of the particular section; radius, wall thickness, elasticity, length etc.

Consider the idea that several arterial sections are modeled one after the other: The continuity equation states that whatever flows out of one section must be the inflow to the next, in this way a chain of Windkessel models is achieved.

Additionally the pulsating pressure waves and pulsating volume flow produce accelerating and decelerating velocities in the liquid, and for this, inertial effects of the mass of blood inside the arteries are of great importance. Inertia of mass is conveniently described with an inductance, L, in the electrical analogue, it is placed in serial connection with the resistance since both inertia and flow resistance reacts to the displacement of the same amount of blood.

Conveniently these arguments reformulates the original Windkessel model into a transmission line as seen on figure 1.3, which is a well-known object in standard electro-engineering. The transmission line is terminated in one end with a terminal resistance, R_T, which corresponds to the peripheral resistance in the original Windkessel model, representing the resistance of the capillary tissue.

The current of this model will be the volume current, Q, defined as the volume of liquid flowing past a point between two sections per time [m^3/s], the potential of the model is the hydrodynamic pressure in a section, P, measured in the units of Pascal, [Pa = $kg/m \cdot s^2$]. Resistance is measured as potential difference over current, $\Delta P/Q$, with the units [$kg/s \cdot m^4$]. Capacitance is defined as charge over potential, which is volume change over pressure, $\Delta V/P$, with the units [m^4s^2/kg]. Inductance is defined as the relation between potential difference and the time-derivative of the current, $\Delta P/(dQ/dt)$, with the units [kg/m^4].

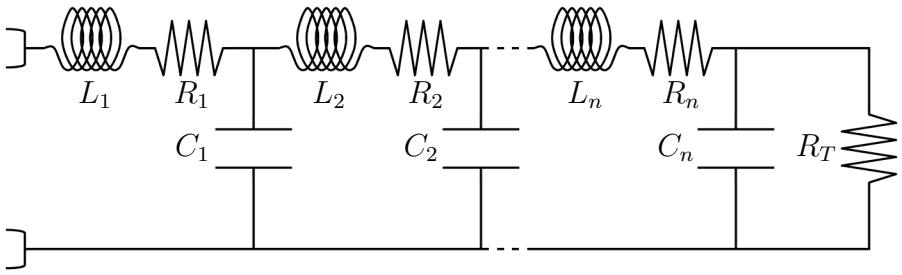

Figure 1.3: The transmission line as an expansion from the Windkessel principle.

To complete this electrical analogue model the functions for resistance, capacitance and inductance must be defined, which will not be attempted here as that requires further interpretation of the physiological phenomena.

1.2.3 The energy bond model

The transmission line is the first step in a generalization of the Windkessel principle, which will make it applicable to model the pulsating flow and pressure in an elastic tube. Through construction of chains of transmission lines it is possible to construct large network models of the cardiovascular system, see for instance [Rideout, 1991].

When defining the resistance, capacitance and inductance of the transmission line it will be clear that the elements of the model are non-linear and interrelated. In an attempt to explicitly describe the non-linear relations a group of physicists lead by Peder Voetmann Christiansen and Niels Boye Olsen from Roskilde University in the 1980ies constructed an expansion to the transmission line. The model they built is reported and validated for blood flow in aorta as a students' project by Nørgaard et al. [1993], and later it is mentioned very briefly in a paper by Larsen et al. [2006].

The model is included in the first part of the modeling in chapter 4, it takes its start in the transmission line, and through the definition of the functions of the electrical elements it is naturally expanded. The model employs the advanced technique of energy bond formalism to expand the electrical network in figure 1.3.

Energy bond technique is a generalization of electrical analogue technique that use the same definitions as in electrical circuits but applies another diagram technique that ensures that the implicit assumptions of electrical circuits are explicitly reflected in the energy bond graphs. The rules and graphs of the energy bond technique are constructed to reflect physical consistency, as such the energy bond technique has more modeling potential than electrical networks.

One advantage of the energy bond technique is the way that models can be constructed in stepwise order, and subsequently tested and expanded. The energy bond technique makes the construction of mathematical models into building blocks that can be added on top of each other, investigated or removed one at a time. This is in contrast to other mathematical methods, for instance differential equations, which are constructed from a set of assumptions that yield a set of equations to be solved; if there is a small change of assumptions a whole new model needs to be derived. If there is a small change of assumptions in an energy bond model, single elements can be removed or changed as desired.

Chapter 2

The Embryonic Heart

The pumping embryonic heart has fascinated scientists for more than two thousand years, visible on top of the yolk as a tiny red spot that seems to pulsate in color. Aristotle who made the first documented observations of the pulsating heart described it as "a speck of blood, in the white of the egg. This point beats and moves as though endowed with life..." [Aristotle., Historia Animalum Book VI 3].

Since the time of Aristotle generations of scientists have stared at the jumping point, fascinated by its frailty and its meaning for development of new life. For instance a quote by William Harvey from his time as a student under Fabricius of Aquapendente in Padua, years before his discovery of the circulatory system, illustrates this fascination and possibly the influence the embryonic heart may have had on the scientific history of medicine:

> "I have seen the first rudiments of the chick as a little cloud in the hen's egg about the fourth or fifth day of incubation, with the shell removed and the egg placed in clear warm water. In the center of the cloud there was a throbbing point of blood, so trifling that it disappeared on contraction and was lost to sight, while on relaxation it appeared again like a red pin-point. Throbbing between existence and non-existence, now visible, now invisible, it was the beginning of life."
>
> - William Harvey circa 1600 [Gibson, 1978].

It was however not until the 1800th century when the motion of the speck of blood was correctly interpreted as the mechanical pumping of the embryonic heart by means of muscular contraction. One of the important researchers in this discovery was Albrecht von Haller who in 1758 made a description of the contraction pattern of the heart that led later scientists to formulate the peristaltic theory of pumping for the embryonic heart [Männer et al., 2010].

Having realized the muscular contractions of the embryonic heart scientists began to discuss the origin of the contractions. Some held the belief that contractions were motivated externally via the nervous system while others believed in a local stimulation. In the end the intrinsic theory seemed to get the upper hand as it was possible to detect a contraction wave going from the venous end of the heart to the atrium and onwards to the ventricle, furthermore the contraction was preceded by distension of the heart wall, which was seen as a local stimulus to contraction. Thus the intrinsic and peristaltic theories appeared to fit together [Männer et al., 2010].

Later still the peristaltic theory ran into problems as it was for instance discovered by Johnstone in 1925 that at the very early stages of the embryonic development only the ventricle shows contractions [Männer et al., 2008]. Scientists instead began to focus on the structure and genesis of the embryonic heart; the existence of cardiac jelly was discovered by Davis in 1924 and later in 1948 Alexander Barry proved its importance for a peristaltic pumping function of the embryonic heart [Barry, 1948].

As such the history of the embryonic chick heart is as much a history of imaging techniques. In the early days of Aristotle and William Harvey the chick embryo was observed with the eye or a magnifying glass at best and described as a tiny speck of blood. With the invention of the microscope by Anton van Leeuwenhoek in the 17th century it was possible to better observe the heart, and shortly thereafter its tubular nature and contraction pattern was recognized. The resolution of microscopy has steadily increased and with the invention of the electron microscope in the 1930ies impressive images could be made of the cell structure of the heart. Movie techniques and modern day optics have further improved the possibilities in envisioning the embryonic heart.

2.1 Hamburger and Hamilton stages

The chick embryo has been a research specimen for embryological research for several hundred years, as it is both simple to obtain chicken eggs and simple to get to the embryo, but in 1951 research in the chick embryo was made even easier. This was the year when Viktor Hamburger and Howard L. Hamilton published their report detailing the embryonic chick development in 46 stages of the 21 days incubation period [Hamburger and Hamilton, 1951].

The work by Hamburger and Hamilton characterizes the embryonic development of the chick from distinguishing diagnostics in the embryo such as the length of the beak, tail, wings or legs, the size and color of the eye, or the number of somites, which are masses of mesoderm that form along the neural tube and eventually will become part of the backbone and adjoining muscles.

By making diagnosis according to the characterizations by Hamburger and Hamilton it is possible to determine and compare the exact development of the chick embryo through the identification of its Hamburger and Hamilton stage (commonly known as HH-stage). The identification of HH-stages has become the primary way of diagnosing development of the chick embryo since Hamburger and Hamilton [1951]. Before their report the development of the embryo was typically characterized according to days and hours of incubation, see for instance [Barry, 1948], but as embryonic development may vary this method was unreliable.

In relation to the overall development of the chick embryo Martinsen [2005] has made a detailed description applying the HH-stages specifically to the embryonic heart (some medical terms are used here and explained later in the text):

HH-stage 6-7 The primary heart tube starts to form.

HH-stage 8-9 First morphological manifestation of the straight heart tube.

HH-stage 10-11 The heart tube is still open ended, onset of the morphological procedure 'cardiac looping', the heart starts to beat.

HH-stage 12-13 The heart tube is a closed system, cardiac looping has completed its dextral looping phase, early formation of endocardial cushions, the beating of the heart is stable, flow is observed.

HH-stage 14-15 Cardiac looping forms the s-shaped heart, onset of the epicardial cell diffusion.

HH-stage 16 Onset of atrial septation, clear atrioventricular and outflow tract cushions.

HH-stage 17-18 Formation of the s-shaped heart complete, epicardial mantle begins to form over the myocardium, onset of trabeculation of the ventricle.

HH-stage 19-20 Formation of a primitive interventricular septum, extensive trabeculation of the ventricle, epicardium covers the inner curvature of the heart.

HH-stage 21-23 Two pairs of endocardial cushions are formed at the outflow tract, valve formation in the atrioventricular cushion begins, epicardial cells penetrate into the myocardium.

HH-stage 24 Cardiac looping completed with the mature s-shaped heart, onset of cardiac septation, loss of original tubular character.

HH-stage 25-46 Cardiac septation transforms the embryonic heart to the mature four-chambered heart.

The description of the embryonic heart development details how the heart grows from the heart tube to the four-chambered heart, many morphological changes happen during this process but only the important ones for this thesis are accounted for here: During HH-stage 15 and onwards epicardium starts to form, this is outer protective layer of the mature heart that will form on top of the myocardial layer and increase its stiffness. The formation of endocardial cushions creates cushions of soft gelatinous material at select positions in the heart tube, and eventually they will grow into the heart valves. The process of cardiac looping is detailed below. The processes of trabeculation and cardiac septation are both processes that will undo the morphology of the tubular heart and transform it to the four-chambered heart, and already from HH-stage 18 the heart tube will start to include a complicated mesh of fibers at its walls.

The embryonic heart starts beating at HH-stage 10 as the first functional organ in the embryo [Männer et al., 2009]. This probably happens in conjunction with the growing of the embryo, which at this stage may have attained a size above the threshold where cell and nutrient transport may no longer be effectively supplied by diffusion. In human cells diffusion lengths range up to about 1 mm [Olufsen, 1998], which fits well with this hypothesis.

From this analysis of the HH-stages of the embryonic heart, it is clear that stages before HH-stage 10 are uninteresting for the modeling, because there is no heart beat, while stages after HH-stages 18 may still be interesting but increasingly harder to model using the models in this thesis due to ventricular trabeculation.

2.2 Cardiac looping

Cardiac morphogenesis has been a research field for more than 300 years, while the knowledge that the embryonic heart actually starts as a simple tube is probably older still. The first record of the fact that the heart tube shows the morphology of a loop was made in 1758 by Albrecht von Haller, while Bradley M. Patten in 1922 introduced the concept that the formation of the heart loop was a distinct process in the development of the heart, effectively coining the term ‘cardiac looping’ [Männer, 2000].

Cardiac looping has seen immense interest from developmental biologists because the looping of the heart tube and concurrent rightward rotation is the earliest left-right asymmetry in the developing vertebrate embryo, and also data from experimental embryology seem to support the idea that abnormal cardiac looping may be responsible for the development of malformed hearts [Männer, 2000].

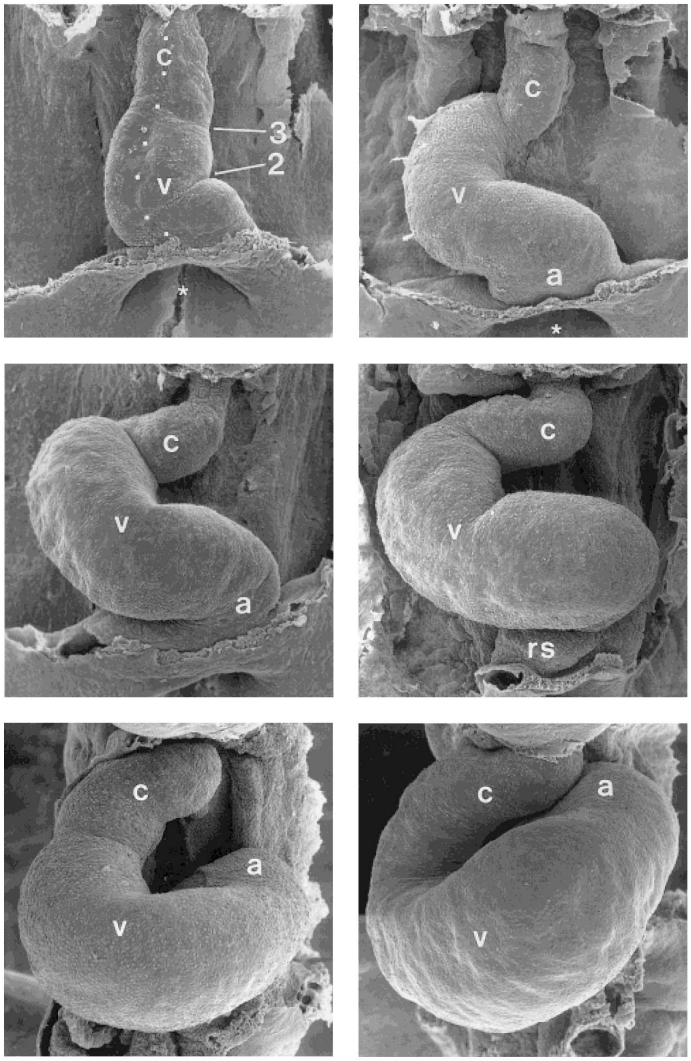

Figure 2.1: Electron microscope images of the looping tubular heart from Männer [2000]. Top left a late HH-stage 10 heart, the lines divide the segments of the primitive right and left ventricle and the outflow tract. Top right a HH-stage 12 heart, clearly looped in the shape of a 'c'. Middle left a HH-stage 13 heart, onset of s-looping. Middle right a HH-stage 14 heart, the 's' shape is barely visible. Bottom left a HH-stage 15 heart, the heart curves in behind itself. Bottom right a HH-stage 16 heart, the 's' shape is now hidden behind the ventricle of the heart. 'c' indicates the conotruncus or outflow tract, 'v' indicates the ventricle, 'a' indicates the atrium and 'rs' indicate the right part of the sinus venosis.

From the formation of the straight heart tube at the very early stages of the embryo, cardiac looping is the process that transforms the heart into a fully developed s-shaped curved heart tube at the onset of cardiac septation and the formation of the four chambered heart, this development is said to go through three phases: dextral looping, formation of the primitive s-loop, and formation of the mature s-loop [Männer, 2004]. A series of electron microscope images from Männer [2000] depicting the looping heart in the stages of interest for the modeling in the thesis is visible on figure 2.1.

At the beginning of cardiac looping around HH-stage 9 the embryonic heart has grown from nothing to a straight and almost symmetric tube (in the so called prelooping phase) oriented along the ventral midline (central) of the embryo. The heart tube consist of the early stages of the future ventricles connected to two venous inlets at its lower end and an arterial outlet at its upper end, which quickly separates into two main arteries destined to become the aorta and pulmonary artery during later stages of development. During the growth of the embryonic heart in the following phases additional 'cardiac segments' (atrioventricular canal, common atrium, systemic venous sinus, outflow tract) are added to the heart tube from its upper and lower end respectively, though the tube remains principally undivided and valveless [Männer, 2008].

Dextral looping is the process that transforms the straight heart tube to a c-shaped curved heart tube. The process starts at HH-stage 9-10 and ends at HH-stage 12. It was previously believed that dextral looping occurred as a result of a spatially confined growth of the heart tube causing the tube to bulge, though it was not possible to explain why the tube would always bulge rightwards. Recent research has however revealed that the looping of the heart is comprised of a lengthwise growth and a consequently ventral bending (towards the front of the embryo) combined with a rightward rotation of the upper part of the tube along the craniocaudal axis (the head-to-toe axis) forcing a counterclockwise rotation of the tube to the right [Männer, 2004].

Following dextral looping the next process transforms the c-shaped curved heart tube into an s-shaped looping heart with the onset at HH-stage 13 until HH-stage 18, with a clear s-shaped loop visible already at HH-stage 14. This process is primarily characterized by the shortening of the distance between the primitive outflow tract at the upper end and the primitive atria at the lower end of the heart tube supposedly combined with a leftward rotation of the lower end of the tube [Männer, 2004].

The final process of maturing the s-shaped loop occurs from HH-stage 19 until HH-stage 24, at which the tubular heart effectively ceases to exist. This process is mainly characterized by an immense growing of the heart and the shift of the outflow tract and the atria to their final positions [Männer, 2000].

All the while these processes transform the straight heart tube into the looping heart, the heart is beating. Starting around early HH-stage 10 the heart beats irregularly and slowly but by the end of stage 10 a clear heart rhythm is present and during later stages the frequency increase [Castenholz and Flórez-Cossio, 1972], blood flow can be detected as early as HH-stage 11 [Castenholz and Flórez-Cossio, 1972] and at stage 12 a peristaltic wavelike contraction pattern can be observed along the length of the heart tube from the atrium to the outflow tract [Taber, 2006a].

Thus it is clear that the interesting stages for the modeling will be HH-stage 10 when the heart starts beating but before the completion of the c-shaped loop, HH-stage 12 with a complete c-shaped heart loop and a complete contraction wave rhythm, HH-stage 14 with an early s-shaped heart loop, and HH-stage 16 with a fully s-shaped heart including all the heart segments of the looping heart, see figure 2.1. These four stages will be the ones in question during the model setup process described in chapter 7.

2.3 Beating of the looping heart

At HH-stage 10 the tubular embryonic heart starts beating. At first the beating is irregular, slow and only periodic in short intervals but late during HH-stage 10 a stable periodic rhythm is formed [Castenholz and Flórez-Cossio, 1972], still the contraction pattern is primitive and only in the subsequent stages will that be improved [Martinsen, 2005].

To achieve propulsion of blood the tubular heart is a layered structure consisting of an inner layer, the endocardium, and an outer layer, the myocardium (before the onset of epicardial formation), and in between the two resides a gelatinous material known as cardiac jelly. The myocardium is a relatively thick layer that contains the contractile muscular fibers of the heart tube known as sacomeres, it has no specific fiber architecture and the muscle fibers are distributed rather randomly Lin and Taber [1994]. The endocardium is a thin one-cell thick layer with composition similar to the myocardium Lin and Taber [1994]. It separates the cardiac jelly and the inner lumen of the heart, and it appears as if the function of the endocardium is to shield the blood inside the heart tube.

The cardiac jelly is an extracellular gelatinous material that contain radially oriented fibers, less at the early HH-stages more at the later stages before trabeculation. It is considerably softer than the other layers but may show existence of anisotropy [Zamir and Taber, 2004]. Following a peristaltic pumping principle Barry [1948] proved the essential function of the cardiac jelly to achieve occlusion of the lumen of the heart tube and hence to propagate liquid in the tube.

In his argument he constructed a cylindric tube and assumed first that it was empty of cardiac jelly. It is a reasonable assumption that the heart tube only achieves about 20 % diametric contraction during systole, and for a tube without cardiac jelly this will not lead to occlusion of the lumen, which is desired for effective peristaltic pumping.

If on the other hand it is assumed that cardiac jelly fills the volume from r_d to R_d, where R_d is the outer sleeve of the heart during diastole, it will have the diastolic volume $V_d = \pi\left(R_d^2 - r_d^2\right)$, and the systolic volume assuming 20 % compression of the tube, $V_s = 0.8\pi\left(R_s^2 - r_s^2\right)$. Under the assumption that cardiac jelly occludes the lumen during systole r_s is set to zero, thus $V_s = 0.8\pi R_s^2$.

For approximation assume that the cardiac jelly is incompressible, such that its volume at diastole equals its systolic volume, $\pi\left(R_d^2 - r_d^2\right) = 0.8\pi R_s^2$. But with the assumption that the heart contracts to 80 % of its diameter during systole $R_s = 0.8R_d \Rightarrow R_s^2 = 0.64R_d^2$, and thus $R_d^2 - r_d^2 = 0.8 \cdot 0.64R_d^2 = 0.512R_d^2$ leading to $r_d = 0.69R_d$. If t describes the thickness of the cardiac jelly, then $r_d = 0.69\left(r_d + t\right)$, which leads to $t = 0.45r_d$. Thus Barry [1948] concluded that the thickness of the concentric layer of cardiac jelly in a cylindric tube needs to be about 45 % of the diastolic radius of the lumen to effectively propel blood with a peristaltic pumping principle. However the calculation includes a small error since Barry multiplied the 80 % compression ratio twice, once as a diametric contraction and once as a contraction of the cross-sectional area; assuming only 80 % diametric contraction leads to the conclusion that the thickness of concentric layer of cardiac jelly should be about 66.7 % of the diastolic lumen radius.

The assumption in Barry's argument is that the heart tube has a concentric contraction pattern, later in the 1980ies it was speculated by Steding and Seidl that the contraction could instead be eccentric and later still using the relatively new imaging technique optical coherence tomography Männer et al. [2008] were able to produce live images of the cross-section of a contracting heart tube, proving that the embryonic heart does in fact contract in an eccentric pattern, which is almost elliptic and can be seen on figure 2.2.

The discovery of the eccentric contracting heart tube does not ruin Barry's argument that the cardiac jelly is important for the propulsion of blood in the embryonic heart, in fact he was right in claiming that the cardiac jelly almost occluded the heart lumen during systole, which is clearly visible on figure 2.2.

At early HH-stages the lumen of the heart tube is described with a low-eccentricity ellipse at diastole, it is almost circular, but during systole the heart contracts such that the elliptic lumen increases its eccentricity until the peak of systole, where the ellipse degenerates with an eccentricity equal to one, the lumen becomes slit-shaped and occluded.

At later HH-stages the diastolic lumen is more bell-shaped than elliptic with the mouth of the bell facing the outer curvature of the looping heart. Additionally it is possible to see spike-formations where the lumen penetrate the cardiac jelly

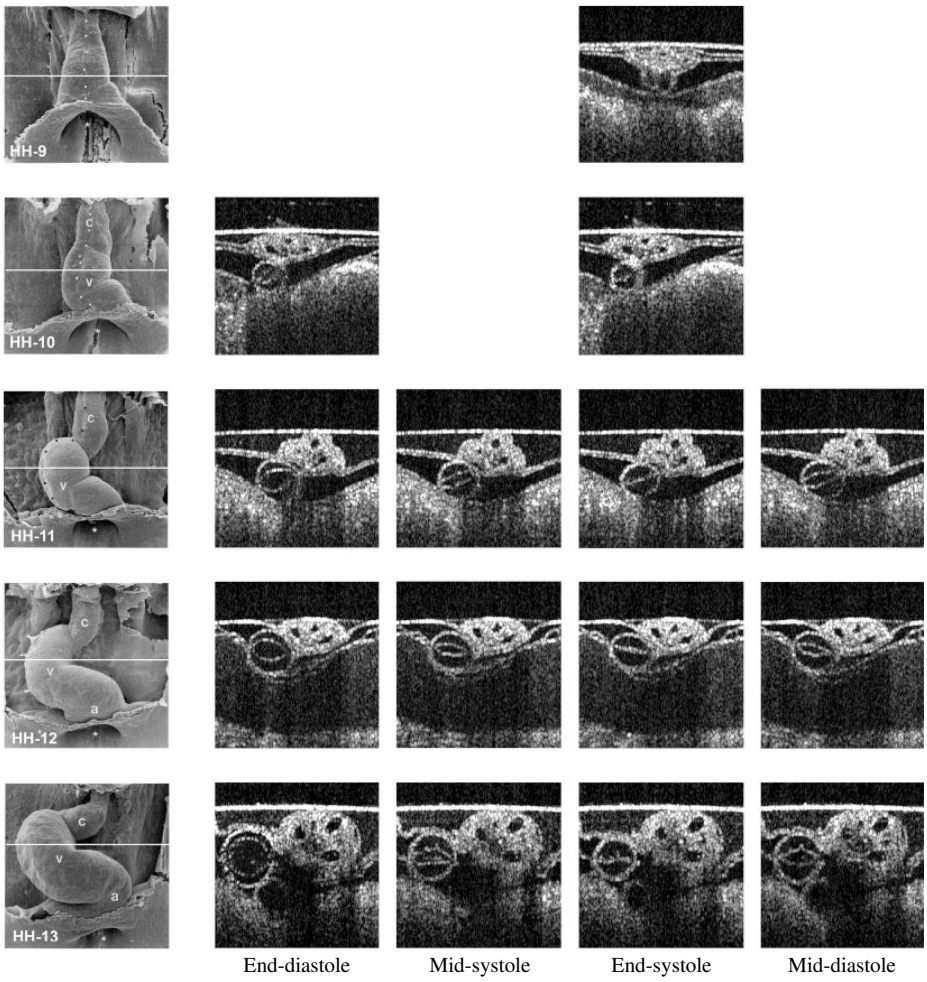

Figure 2.2: OCT images of the layered cross-sections of the beating heart from Männer et al. [2008]. It is clearly seen how the inner endocardial layer contracts almost elliptically while the outer myocardial layer contracts in an almost concentric manner.

and reach out to the myocardium of the heart tube. The lumen is not always completely occluded during systole, yet the contraction pattern is still clearly eccentric [Männer et al., 2009].

Meanwhile the outer sleeve of the heart, the myocardium, contracts in an almost concentric manner, though it is proved by Männer et al. [2009] that the contraction is slightly eccentric from HH-stage 14 to 17 and possibly also earlier. The approximate concentric contraction of the myocardial sleeve seems to confirm the assumption by Barry that the relatively little outer contraction of the heart tube makes the cardiac jelly fill up the entire volume inside the heart tube, essentially through incompressibility.

The construction of the elliptic layer of cardiac jelly in the heart tube comes as a consequence of the generation of the tubular heart, as it grows from two heart-forming fields on either side of the sagittal plane of the embryo (the cross-sectional plane that divides left and right in the body) in a bilateral process during HH-stages 6 and 7, and at HH-stage 8 the two halves get fused together along the major axis of the later elliptic cross-section [Martinsen, 2005]. An interesting question is if there are other reasons that the heart lumen is elliptic apart from its genesis.

One advantage of eccentric contraction seems to be the strain endured by cells in the endocardial inner layer of the heart wall. In hypothetical heart tubes with concentric contraction, like the one suggested by Barry, the endocardial cells undergo severe strains from diastole to end-systole, while heart tubes with the observed eccentric deformation pattern expose the endocardial cells to much lighter dimensional changes. It may be that the observed eccentric contraction is made to minimize stress in the walls of the heart tube [Männer et al., 2008].

Concerning peristaltic transport of fluid it has been proven for technical cases that tubes of elliptic cross-section have a higher mechanical efficiency of peristaltic pumping compared to tubes of circular cross-section, and similar results have been achieved for simple models of the tubular embryonic heart under assumption of peristaltic pumping [Männer et al., 2008]. Thus evidence suggest that the tubular heart is made to optimize blood pumping capabilities.

2.3.1 Optical coherence tomography

Optical Coherence Tomography (OCT) is an echo-based imaging modality that measures the time-of-flight of back-reflected light using low-coherence interferometry. OCT use a near-infrared light source and measures the light scattering and reflection of light relative to light traveling a known reference path inside the OCT apparatus. The system obtains images with a resolution of 10 to 30 μm with depth penetrations of a few millimeters (typically 2-3 mm), deep enough to scan the live pumping heart of the chick embryo [Yelbuz et al., 2002].

The imaging technique of OCT is more or less the same as in the more commonly applied ultrasound technique; a single two-dimensional image scan (known as a B-scan) consists of several thousand one-dimensional scans (A-scans) as the probe beam is laterally scanned across the sample. Alternatively A-scans can be made sequentially at a stationary location to show time-development in the so called M-mode images. Naturally sample speed is essential for this technique; a higher frequency means a higher number of A-scans per second, which can be translated into a better M-mode resolution or a higher number of A-scans per B-scan. A-scan resolution is another important factor in this imaging technique; a typical A-scan beam has a width of 10 to 20 μm in both axial and lateral dimension, which defines the resolution of B-scan images.

OCT was introduced in 1991 and has been thoroughly used in the imaging of semi-transparent tissues (such as the chick embryo) or highly light-scattering tissues (such as the retina of the eye) in its twenty year lifetime. However the techniques used in imaging of chick embryos is no more than ten years old [Yelbuz et al., 2002]. Some of the newest approaches to the technique is the combination with Doppler theory to achieve dimensional as well as dynamical information [Davis et al., 2009] and the combination of images to achieve 3D (or even 4D) images [Liu et al., 2009] as well as a general A-scan resolution and increase in sampling frequency of the OCT equipment.

2.4 Peristaltic pumping vs. the Liebau effect

Following the discovery of muscular contractions of the embryonic heart it was quickly discovered by Albrecht von Haller in 1758 that a wavelike contraction pattern was visible from the venous end of the heart tube towards the arterial end, and that this contraction wave was preceded by a short distension of the wall of the tube given by the compliant reaction to the inflow of blood. These observations made von Haller conclude that the heart contraction reacted to a local pressure stimulus, which fit well together with a peristaltic pumping theory of blood propulsion [Männer et al., 2010].

Peristaltic pumping was already recognized by scientists as the pumping principle of the gut and the ureter, and it was conspicuous to believe the same principle would govern the pumping of blood as well. During the 19th century a long range of scientists succeeded in constructing a convincing description of the embryonic heart as a peristaltic pumping mechanism that responded to intrinsic stimuli to produce a stable propulsion of blood out through the vascular system and even the four-chambered heart was described as peristaltic by Gaskell in 1883 [Männer et al., 2010].

This reveals that in the 18th and 19th century peristaltic pumping was defined in a much broader sense than today. Modern peristaltic pumping can be envisioned as a sliding contraction of the heart tube, or in some cases a sequential contraction, such that the liquid is pushed forward by the contraction wave. From this follows that a peristaltic contraction wave requires a certain length of contractile tube to work.

As such it was contradicting to the peristaltic hypothesis when Johnstone discovered that the HH-stage 10 heart only contracts its ventricle in an almost uniform manner [Männer et al., 2008]. But already the peristaltic pumping theory was in a state of crisis. During the 19th and especially the 20th century peristaltic fluid transport became a more specialized mechanical principle as engineers, physicists and mathematicians achieved interest in this phenomenon, and

at the same time physicians made much more specific definitions of the biological peristalsis of the gut and ureter, so by the beginning of the 20th century the embryonic heart could hardly be described as a peristaltic pump any longer [Männer et al., 2010].

And then in 1954 a new pumping theory was introduced. Gerhart Liebau proposed a pumping principle based on an active pumping action at a single point on the tube creating a pulsating pressure wave that when interacting with the impedance of the heart and vascular system would create a flow. Liebau was mostly interested in the mature heart and he explained his ideas by construction of simple mechanical pumping systems that did not catch the interest of embryologists, but he did in fact speculate about the applicability of his pumping principle as an alternative to the peristaltic pumping in the embryonic heart [Liebau, 1955].

Liebau's theories mostly caught the interest of mathematicians and physicists and for many years after its introduction the so called Liebau effect was mostly considered a phenomenon of relatively simple experimental setups in fluid mechanics. It was speculated that the Liebau effect could have influence on the embryonic heart but it was not until a research group from the California Institute of Technology lead by Farouhar, Gharib and Hickerson in 2006 decided to investigate whether the embryonic zebrafish heart might work as a Liebau pump that Liebau theory was actually considered as a viable alternative to the peristaltic pumping theory [Männer et al., 2010].

The Liebau effect has proven to be a competing theory to the peristaltic pump in relation to the embryonic heart, and it has recently caught interest with many embryologists. It is however not a complete alternative, just like the peristaltic pump the embryonic heart demonstrates behavior that can not be explained with the simple Liebau effect. In a comparison between the two pumping principles Männer et al. [2010] compiles a list of characteristics for the simple technical case of a peristaltic pump:

> Characteristics of the technical peristaltic pump:
>
> The pump is a positive displacement pump that generate flow by pushing the liquid forward.
>
> The pump has non-stationary sites of active compression that moves along the length of a flexible tube.
>
> Movement of active compression sites is seen as a unidirectionally propagating compression wave.
>
> The flow generated is continuous.
>
> No structurally fixed direction of net flow; flow direction depends on the direction of the compression waves.

The generated flow velocity corresponds to the speed of the compression waves.

There is a linear relation between compression wave frequency and flow rate.

It should be noted that these are characteristics of the technical peristaltic pumps used in engineering and industry. In biology there is at least one example of a peristaltic pump that works differently than the technical pump, the gastric emptying of the stomach produce flow velocities far higher than the corresponding compression wave. Furthermore recent computational modeling demonstrate that peristaltic heart tubes can generate pulsatile flow as a consequence of the endocardial cushions at the inflow and outflow regions of the tube [Männer et al., 2010]. Thus it is important to distinguish between technical and biological peristaltic pumps, as the latter is able to demonstrate characteristics not normally described with technical peristalsis.

Correspondingly the list for the characteristics of the Liebau effect by Männer et al. [2010] is compiled for a simple technical Liebau pump involving only a single compression site, despite the fact that a sequence of compressions is likely more appropriate for the embryonic heart [Liebau, 1955]:

Characteristics of the simple Liebau pump:

The pumping tube must have a flexible wall of finite length.

There has to be a mismatch of impedance right and left in relation to the pumping site (preferably at the ends of the flexible tube).

The pump includes only a single stationary site of active compression.

The active compression site must be at an asymmetric position along the tube.

The generated flow is pulsatile.

No structurally fixed direction of net flow; flow direction depends on frequency.

Generation of bidirectional elastic waves traveling along the passive walls of the tube (both upstream and downstream).

The flow velocity can exceed the speed of the traveling elastic waves.

There is a non-linear relationship between compression frequency and flow rate.

Both pumping principles demonstrate valveless pumping action and as such there is no structural dependency (for instance by valves) of the direction or magnitude of the generated flow. For the peristaltic pump the flow follows the direction of the compression waves and is linear dependent on compression wave speed and frequency. For the Liebau pump the flow depends on the frequency of stationary compressions and their position in relation to the distribution of impedance in the tube, the dependency is non-linear and at certain frequencies the flow may change direction.

Generally the embryonic heart demonstrate what appears to be a wave of contractions along its length, which has prompted the peristaltic hypothesis. It has been proved that these contractions can not be generated by passive compliance to a strong singular compression function, and furthermore studies show that when the different cardiac segments are physically isolated they still utilize the same contraction pattern indicating active compression in all segments of the heart [Männer et al., 2010], which all support the peristaltic theory. On the other hand researchers have discovered embryonic hearts in fish and lower vertebrate that only employ a single contraction site, and at the same time it is reported that the contraction wave in higher vertebrate embryos (such as the chick) has a 'kickstart' contraction of the atrium while the rest if the contraction pattern is more steady [Männer et al., 2010], such discoveries seem to support a complicated Liebau mechanism.

It has been argued how the influence of cardiac jelly and the elliptic cross-section optimize the embryonic heart for peristaltic transport, but in fact it can also be hypothesized that cardiac jelly may have a high influence on fluid transport following the Liebau principle via its elastic nature, such that it may amplify the elastic waves responsible for the Liebau effect, regardless that lumen occlusion is not normally observed in standard technical Liebau pumps [Männer et al., 2010].

The two pumping theories have both merits and flaws in relation to the measured characteristics of the heart, but none are strong enough to completely exclude the theory as a possible explanation of the pumping mechanism of the embryonic heart.

2.5 The questions about the embryonic heart

It is made clear how the embryonic heart starts its genesis as a looped multilayered tube and begins beating contractions as soon as it is generated, at first the contractions are simple and irregular but later a clear contraction wave or sequence of contractions is seen traveling the heart tube from the venous end over the atrium and ventricle to the outflow tract.

The tubular heart is generated during HH-stage 9 and 10 as an almost straight tube, but in the subsequent stages the tube curves into a c-shaped tube at HH-stage 12 and an s-shaped tube from HH-stage 14 until HH-stage 24. This happens while the tube is also growing in length by adding new cardiac segments to the embryonic heart, in this way the tubular heart is fully formed at HH-stage 16, all though at later stages the cardiac segments grow further. In the stages following HH-stage 16 the processes of trabeculation and cardiac septation transforms the multilayered looping heart into the mature four-chambered heart. It is not known if the morphology of the looping heart is only a process in forming the mature heart or if the looping has an influence to optimize flow conditions in the heart.

The tube is layered such that between the inner endocardial layer and the outer myocardial layer resides a layer of gelatinous material known as cardiac jelly. The distribution of cardiac jelly in the heart tube is eccentric, forming two cushions on either side of the heart tube such that the inner lumen of the heart tube appears almost elliptic. It has been reasonably established that the cardiac jelly and the elliptic cross-section optimizes conditions for peristaltic pumping, but it is not yet known if it will also have an increased effect on Liebau pumping.

Two hypothetic theories are suggested for the pumping mechanism of the tubular heart: peristaltic pumping or the Liebau effect. Both theories have characteristics that seem to support or conflict with the observations of the embryonic heart, the question has recently been which of these are the correct description of pumping in the heart, but perhaps a more relevant question would be if they are mutually exclusive.

Chapter 3

Flow Theory

The embryonic chicken heart is a special case of bio-mathematical modeling of blood flow, and the first step in the modeling procedure will be to recount some of the established theory on the area. The purpose of this chapter will be to present some of the fundamental concepts and theories, which will be used in the modeling, at the while arguing why the embryonic heart can not be modeled solely from these basic principles.

The concepts and theories herein come from the classic fluid dynamics, which should be subdivided into aerodynamics, concerning compressible fluids, and hydrodynamics, concerning incompressible fluids. Yet many researchers feel the need to express that blood is a special kind of fluid that is bound to demonstrate non-Newtonian behavior and a complex compressibility, therefore they have coined the term 'hemodynamics' for the special study of blood and the cardiovascular system [McDonald, 1968].

The three most important concepts here are the nature of the liquid, the elastic tube walls and the pulsating flow and pressure. This may all be modeled with hydrodynamical theory as a first approximation, which will also be the starting point of this chapter but during the course of the chapter (and especially later chapters) it should be clear that hydrodynamics will not be sufficient, which both warrants the models of chapter 4 and 6 as well as the name 'hemodynamics'.

3.1 Basic properties of fluids

A fluid in physics is a continuous material medium that flows, this is in fact the one thing that distinguishes a fluid from a solid, in more specific terms, a fluid cannot maintain a shear stress for any length of time [Feynman et al., 1964, 40-1]. Fluids are like any other material characterized by their mass density, ρ [kg/m^3], while the special flow property of a fluid is characterized by the measure of the viscosity, η [1 Pa·s = 10 Poise], thicker liquids like honey move less easily than fluids like air or water.

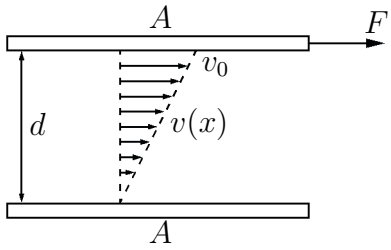

Figure 3.1: The typical model to illustrate viscosity. Imagine two parallel plates of equal area, A, with distance, d, between them. The plates move with speed, v_0, relative to each other. The viscosity can then be found by measuring the force, F, needed to maintain a constant velocity.

The measure of viscosity is usually explained by imagining two parallel plates of equal area, A, separated by a layer of fluid, one plate is held stationary and the other is moved parallel to the first with a slow constant speed, v_0. See figure 3.1. The force, F, required to keep the plate moving will be proportional to the area of the plates and to v_0/d, where d is the distance between the plates. Thus the shear stress, F/A, induced on the liquid is proportional to v_0/d, and the constant of proportionality is called the coefficient of viscosity,

$$\frac{F}{A} = \eta \frac{v_0}{d}. \tag{3.1}$$

Usually the viscosity is a fixed constant at all but the most extreme cases, for blood however it is a little different. The viscosity of blood have two known anomalous properties typically referred to as the 'low shear' and 'high shear' effects; [Nichols and O'Rourke, 1998, p. 18]

Low shear effect: At low shear stress, the apparent viscosity of blood increases markedly. It has been shown with almost certainty that flow may cease in the presence of a very low measurable stress, implying that there is a 'yield stress' under which blood is not a fluid.

High shear effect: In small tubes, the apparent viscosity of blood at high shear stress is smaller than it is in larger tubes. This effect begins to be detectable with tubes of less than 1.0 mm internal diameter (i.e. about 100 times the major diameter of red blood cells).

A fluid in classical physics is either Newtonian or non-Newtonian. A Newtonian fluid obeys a linear relationship between stress and velocity like the one described in equation 3.1, which means a Newtonian fluid has a constant viscosity. Clearly the low shear and high shear effects make blood a non-Newtonian liquid, which in general will make the equations of motion for blood flow unsolvable. It is however commonly assumed that there is a large interval of shear

rates for which blood behaves in all aspects like a Newtonian liquid, in particular it has been demonstrated that for all blood vessels with internal diameter much larger than the diameter of red blood cells blood behaves like a Newtonian liquid [Nichols and O'Rourke, 1998, p. 15].

3.2 Fluid motion

The governing equations for the modeling of any fluid movement are the Navier-Stokes equation together with the equation of continuity,

$$\rho\left(\frac{\partial \mathbf{v}}{\partial t} + (\mathbf{v}\cdot\nabla)\mathbf{v}\right) = \mathbf{f} - \nabla P + \eta\left(\nabla^2\mathbf{v} + \frac{1}{3}\nabla(\nabla\cdot\mathbf{v})\right), \tag{3.2}$$

$$\frac{\partial \rho}{\partial t} + \nabla\cdot(\rho\mathbf{v}) = 0, \tag{3.3}$$

where $\mathbf{v}$ is the velocity field, P is pressure and $\mathbf{f}$ are the external forces applied to the fluid. However, for many cases of fluid motion these equations are impractical, while for other cases they are unsolvable, and so in practice it is common to make a characterization of the flow before model equations are applied.

For instance for many cases for liquid motion it is customary to assume that the liquid is incompressible, ρ is a constant, which simplifies the equations above: the equation of continuity becomes simply $\nabla\cdot\mathbf{v} = 0$, which in turn terminates the last term of the Navier-Stokes equation. Another example is the assumption of Newtonian fluid behavior.

In the case of blood it is debatable if ρ and η can be assumed to be constants: section 3.1 points to the fact that especially η may not be constant under certain circumstances, and it is well-known that both are functions of the blood hematocrit number (the volume percentage of red blood cells in the blood), for the viscosity the low shear and high shear effects are especially dependent on hematocrit levels [Meier, 1987].

For adult human blood the hematocrit is around 48 % for men and 38 % for women and may vary in relation to conditions such as age, health, dehydration, and pregnancy for women. For embryonic blood the hematocrit is much lower, typically not even 20 %. Under these circumstances at least density is considered constant, while the non-Newtonian effects of viscosity may still be seen. Density and viscosity of embryonic blood are discussed further in section 3.5 and 7.3, though in this thesis they are both assumed to be constant.

3.3 Laminar flow vs. turbulent flow

Another important characterization of fluid motion, which has become an important discussion in hemodynamic research, is the determination of the nature of the flow.

General hydrodynamics defines the concepts of laminar and turbulent flow: If there exist an ordering of layers inside the fluid such that each layer, beginning with the outer layer along the boundaries of the liquid, have a uniform velocity the flow is said to be laminar, otherwise it is turbulent.

In ordinary hydrodynamic theory the question of laminar versus turbulent flow can usually be determined by referring to the Reynolds number. This number is basically a comparison of the magnitude of two terms of the Navier-Stokes equation, the advective term of velocity change, $(\mathbf{v} \cdot \nabla)\mathbf{v}$, and the viscous term of velocity change, $\nu\nabla^2\mathbf{v}$, where $\nu = \eta/\rho$ is the kinematic viscosity.

These two terms govern two properties of all kinds of flow, inertia and viscosity. Inertia attempts to continue the motion of a fluid once it is started whereas viscosity acts as a brake. If inertia is dominant the flow is said to be ideal, it is custom to leave out the viscous term from the Navier-Stokes equation in these cases. If viscosity is dominant the flow is usually known as creeping flow and the advective term can be omitted. [Lautrup, 2005, p. 237]

To get a measure of these two terms assume that for a certain region of the fluid the velocity is of a typical size, $|\mathbf{v}| \approx U$, and that it changes by a similar amount over a region of size L. The order of magnitude of the first-order spatial derivative of the velocity will then be $|\nabla\mathbf{v}| \approx U/L$ and the second-order derivative will be of magnitude $|\nabla^2\mathbf{v}| \approx U/L^2$. Consequently the construction of the Reynolds number will be,

$$\mathrm{Re} = \frac{|(\mathbf{v} \cdot \nabla)\mathbf{v}|}{|\nu\nabla^2\mathbf{v}|} \approx \frac{U^2/L}{\nu U/L^2} = \frac{\rho U L}{\eta}. \tag{3.4}$$

For small values of the Reynolds number the flow is laminar and orderly, hence creeping flow ($\mathrm{Re} \ll 1$) is always laminar. For larger values, depending on the flow geometry and other circumstances (for instance if the flow is pulsatile), there will be a critical Reynolds number where turbulence sets in. This critical number is typically in the region of thousands and commonly it is agreed that a flow with Reynolds number below 1000 is laminar whereas above it is uncertain.

For flow in tubes two conventions of the Reynolds number is used: the typical velocity in the tube, U, is given by the mean velocity defined as the liquid flow over the cross-sectional area, $U = Q/\pi r^2$, however the region of change, L, may be given by the inner diameter of the tube or by the inner radius. For typical engineering practice the diameter is used, which will increase the threshold value between laminar and turbulent flow to 2000 [Crane Co., 1982, Granger, 1995],

but following mathematical argumentation the region of possible velocity change should only be the inner radius of the tube, $L = r$, which is also the standard practice in hemodynamic modeling [McDonald, 1952]. The two conventions should never be confused, as that could lead to false assumptions about the nature of the flow. In this thesis the Reynolds number will be defined by use of the inner radius.

Considering flow of blood it has been debated for many years whether the pulsatile flow of blood is laminar or turbulent, especially flow in the larger arteries (of humans and larger animals). It has been observed by McDonald [1952] and others that blood flow in the aorta is mostly laminar but it can at times be turbulent (especially in the peak of the systole), and likewise it is well-known that near bifurcations in the arteries turbulent flow is likely to form.

Many researchers have attempted to calculate typical Reynolds numbers for the flow of blood, it is a difficult process since blood is generally a non-Newtonian liquid with complex density and viscosity, depending on the hematocrit number, and the pulsatile flow makes it hard to determine an average velocity for the computation. The highest Reynolds numbers calculated for blood in the arteries of larger mammals seems to be around 900-1000 while several lower numbers have been calculated all the way down to about 300, this should clearly make the flow laminar yet observations show that turbulent behavior can occur even with Reynolds numbers as low as 550 [McDonald, 1952].

According to McDonald [1952] the observed sort of turbulent onset during the peak of the systole should be possible in all larger mammals, yet later studies show that at least for some larger mammals no turbulence is observed [McDonald, 1955]. Generally it can be debated whether the standard Reynolds number is at all applicable as an indicator of laminar or turbulent pulsatile blood flow or if another effective Reynolds number should be calculated [Hale et al., 1955].

For smaller arteries, capillaries and veins the situation is much more clear, here the vessel dimensions or flow velocity is sufficiently small so that flow is laminar except for the most rare of cases. This applies for the embryonic heart as well, where flow appears to be laminar throughout the cardiovascular system. With viscosity and density as defined in section 7.3, mean velocity, $U \approx 3$ mm/s, and maximum radius, $L \approx 0.25$ mm, a Reynolds number is found, $\mathrm{Re} \approx 0.2$, which lies far below the threshold of turbulent flow.

3.4 Poiseuille flow

Assuming blood is a Newtonian liquid with laminar flow it is logically from hydrodynamic practice to assume that some instances of the blood flow can be described with Poiseuille's equation.

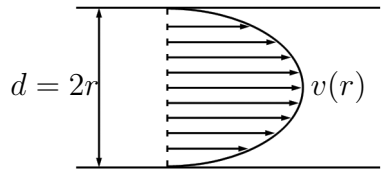

Figure 3.2: The flow profile in a section of tube with pressure driven laminar flow.

There are many ways to derive this equation, here the standard mechanical approach is presented though later other approaches may come into use.

Relate the definition of viscosity from equation 3.1 to a section of tube assumed to be circular with inner radius, R, and length, Δx. Under normal pressure driven flow every layer of liquid inside the tube moves with different velocity, so that the liquid in the center of the tube moves fastest and the liquid near the wall of the tube moves with speeds close to 0. The viscous force retarding the motion of a liquid layer in a distance, r, from the center is proportional to the area of its surface, $2\pi r\Delta x$, and to the velocity gradient across the vessel, dv/dr,

$$F_{viscous} = \eta \cdot 2\pi r\Delta x \cdot \frac{dv}{dr}. \tag{3.5}$$

Note that force and velocity are here both scalar since the flow is everywhere parallel to the wall of the cylindric tube.

The force exerted on the tube section by the pressure is the pressure multiplied by the cross-sectional area, minus the pressure at the distal end,

$$F_{pressure} = \pi r^2(P_1 - P_2), \tag{3.6}$$

where P_1 and P_2 are the pressures at the ends of the tube section.

These two forces are equal and opposite,

$$\pi r^2(P_1 - P_2) = 2\pi r\eta\Delta x\frac{dv}{dr}, \tag{3.7}$$

so the velocity gradient is

$$\frac{dv}{dr} = \frac{r(P_1 - P_2)}{2\eta\Delta x}. \tag{3.8}$$

By integration of the velocity gradient from r to R,

$$v(r) = \int_r^R \frac{r'(P_1 - P_2)}{2\eta\Delta x}dr' = \frac{P_1 - P_2}{4\eta\Delta x}(R^2 - r^2), \tag{3.9}$$

it is seen the the velocity inside the tube section is parabolic with maximum velocity at $r = 0$ and $v(r) = 0$ at $r = R$, see figure 3.2.

To obtain the volume flow, determine the volume of the paraboloid which has this parabola as its profile. That is, integrate the velocity once more over the cross-sectional area of the tube,

$$Q = \int_0^R 2\pi v(r) r dr = \frac{2\pi(P_1 - P_2)}{4\eta\Delta x} \int_0^R r(R^2 - r^2) dr, \tag{3.10}$$

which yields the Poiseuille equation,

$$Q = \frac{\pi R^4 (P_1 - P_2)}{8\eta\Delta x}. \tag{3.11}$$

The Poiseuille equation is a relation between a steady flow of a liquid compared to the viscous drag in a tube of radius R. It is important to note that volume flow is related to the fourth power of the radius so that a two-fold increase in radius causes a 16-fold increase in flow.

The simple derivation of Poiseuille's equation above differs somewhat from the general solution to steady flow in a cylindrical tube in that it considers every layer of liquid as a solid that is only effected by the viscous drag on its surface. The general solution will however yield the same two equations, 6.44 and 3.11, for the flow [Lautrup, 2005, p. 251].

The conditions under which Poiseuille's equation applies to the flow of blood lies implicit in the method of its theoretical derivation, they are however quite severe and definitely deserves a mention;

The liquid is homogeneous, incompressible and Newtonian. Both viscosity and density must be constant in comparison to the size of the blood vessel.

The liquid does not slip at the wall. The assumption that velocity is zero at the wall is held to be universally true for all liquids, yet some researchers have suggested that the anomalous flow properties of blood may be due to special properties of the walls of blood vessels that could cause liquids to slip [Nichols and O'Rourke, 1998, p. 15].

The flow is laminar. This as discussed above is not necessarily true as turbulent flow may occur in larger blood vessels.

The rate of flow is steady. If the velocity of the liquid is accelerated or decelerated the pressure gradient is partly used to alter kinetic energy of the liquid and thus the equations do not hold. As the flow of all large arteries is markedly pulsatile Poiseuille's equation does not apply to those vessels.

The vessel is long compared to the section being studied. Close to the inlet of a vessel the paraboloid velocity profile have not yet been established. The distance required to establish the steady form is known as the inlet length. Every bifurcation of blood vessels should thus be treated as an inlet to a new blood vessel. For liquid flow with low Reynolds numbers the inlet length is very short (only a few tube diameters) and thus it will only have minor effect on the viscous flow [Meier, 1987].

The blood vessel is cylindrical. Most arteries of the systemic circulation are circular in cross-section, but many veins and the pulmonary arteries tend to be elliptical. Many blood vessels taper as they go towards the periphery of the system [Nichols and O'Rourke, 1998, p. 16].

The blood vessel is rigid. For the equation to hold, the diameter of the blood vessel must not vary with the internal pressure, yet blood vessels are elastic. Under these conditions the flow will not be solely a function of the pressure gradient.

With this list of restrictions it seems obvious that Poiseuille's equation does not in itself apply to the pulsatile flow of blood, still if it is considered as only a relation describing viscous friction of liquid inside a cylindrical tube it will be of use.

3.5 The Bernoulli effect

It is reasonably established that blood flow is not Poiseuille flow, mainly because the blood flow is not steady and the walls of the blood vessels are elastic. That is, the blood vessels change their diameter as a function of the pulsatile pressure. The flow of blood may still be laminar but the flow profile is not always parabolic as suggested by Poiseuille's equation. Under these conditions it is customary to apply Bernoulli's equation, which springs from the universal conservation of energy and thus must apply for blood flow.

It is reasonably assumed that blood flow is incompressible under all conditions except the most extreme. This means that under normal flow circumstances a volume of liquid moving along with the flow does not expand or contract but remains constant in time. Written as, the surface integral over a closed volume of the velocity field must remain zero at all times,

$$\oint_S \mathbf{v} \cdot d\mathbf{S} = 0, \tag{3.12}$$

which by use of Gauss' theorem can be changed into the well-known consequence of incompressible flow that the divergence of the velocity field is zero, $\nabla \cdot \mathbf{v} = 0$.

Note that incompressible flow is a condition to the characteristics of the flow not a condition on the liquid itself. Every liquid is in principle compressible and to state incompressibility for the flow is only an approximation that holds for ordinary pressure and velocities below the local speed of sound [Lautrup, 2005, p. 214].

Furthermore it must be reasonable to assume that no place in the heart or arterial system have a higher density of blood than any other, even though the density of blood in capillary tissue or in the veins might be different. The density of blood is spatially independent, then by the equation of continuity,

$$\frac{\partial \rho}{\partial t} + \nabla \cdot (\rho \mathbf{v}) = 0, \tag{3.13}$$

the density is also time-independent.

Assume now for a small section of tube the flow at time, t, is nearly steady, i.e. $\partial \mathbf{v}/\partial t = \mathbf{0}$, so that the flow into the section, Q, equals the flow out of the section. At the mouth of the section the cross-sectional area is A_1, at the end A_2. The flow can then be calculated,

$$Q = A_1 \bar{v}_1 = A_2 \bar{v}_2, \tag{3.14}$$

where $\bar{v}_1$ and $\bar{v}_2$ are average velocities.

The effect of the work done to the liquid at both ends of the section will then be $P_1 A_1 \bar{v}_1$ and $P_2 A_2 \bar{v}_2$.

Likewise the effect of the kinetic energy can be calculated from the mass flux, $\Phi_1 = \rho A_1 \bar{v}_1$ and $\Phi_2 = \rho A_2 \bar{v}_2$, and the square of the velocities, $E_1 = \frac{1}{2}\Phi_1 \bar{v}_1^2$ and $E_2 = \frac{1}{2}\Phi_2 \bar{v}_2^2$.

Finally the effect of the potential energy can be calculated assuming gravity is the only external force on the section, $U_1 = g h_1 \Phi_1$ and $U_2 = g h_2 \Phi_2$, where h_1 and h_2 are the heights above zero at opening and final end of the section.

By conservation laws the flux of energy in both ends of the section must be equal,

$$P_1 A_1 \bar{v}_1 + \frac{1}{2}\rho A_1 \bar{v}_1^3 + g h_1 \rho A_1 \bar{v}_1 = P_2 A_2 \bar{v}_2 + \frac{1}{2}\rho A_2 \bar{v}_2^3 + g h_2 \rho A_2 \bar{v}_2, \tag{3.15}$$

which by the steady flow condition in equation 3.14 becomes,

$$P_1 + \frac{1}{2}\rho \bar{v}_1^2 + g h_1 \rho = P_2 + \frac{1}{2}\rho \bar{v}_2^2 + g h_2 \rho. \tag{3.16}$$

Equation 3.16 is a generalization of the Bernoulli equation. It would be wrong to state the conservation of the energy flux, i.e. $P+\frac{1}{2}\rho\bar{v}^2+gh\rho = [\text{constant}]$, since steady flow is only a local approximation to the pulsatile flow. To make a clearer picture assume that gravitational potential energy has nearly no influence on the flow, i.e. $h_1 \approx h_2$, which gives a local relation between pressure and velocity of the liquid,

$$P_1 = P_2 + \frac{1}{2}\rho\left(\bar{v}_2^2 - \bar{v}_1^2\right). \tag{3.17}$$

It can thus be seen that if the velocity of the blood is increased, $\bar{v}_2 > \bar{v}_1$, the pressure must be correspondingly decreased, $P_2 < P_1$. This sets a local condition on the pressure-flow relationship, which will be used in the modeling procedure in chapter 4 and 6.

3.6 Elasticity of the walls

The elasticity of the vessel walls is one of the main problems for modeling of blood flow, if blood vessels were rigid the flow could be modeled using constant boundary values for some variant of the Navier-Stokes equation. Elastic walls makes the boundaries variable as a function of the pulsatile blood pressure inside the vessel.

The elastic compliance of a section of tube is a relation of the volume increase caused by an increased pressure, a compliance relation for a cylindric tube will be derived here though later in chapter 6 the elastic compliance function will be expanded to a more general level.

Assume a section of cylindric tube has the length Δx and wall thickness h, the section has inner radius R when at rest and the circumference, $c = 2\pi R$. The force needed to extend the circumference by Δc is given by Hooke's law,

$$F_{elastic} = \frac{\Delta c}{c} E\, h\Delta x = \frac{\Delta r}{R} E\, h\Delta x, \tag{3.18}$$

where Δr is the increase of radius given by the stretch in circumference, and where E in equation 3.18 is Young's modulus, which is a material parameter for the linear relation between stress and strain in the same direction.

The increase in pressure inside the liquid is applied directly orthogonal to the arterial wall, yet the force calculated in equation 3.18 is tangential to the surface. To find how a pressure increase, ΔP, causes tangential forces find the force on a small segment of arc of the wall,

$$F_{pressure} = \Delta P \cdot r d\phi \cdot \Delta x. \tag{3.19}$$

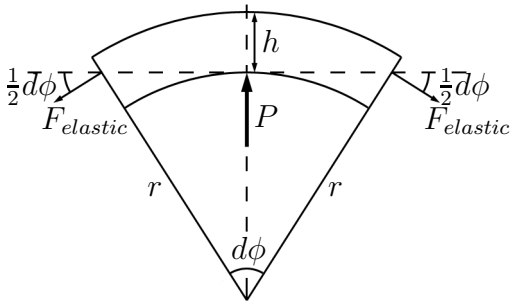

Figure 3.3: The force from the pressure is normal to the tube wall, but it is balanced by the sine-component of the elastic force in the wall.

In the event that the wall has come to rest after the pressure change a new equilibrium is achieved where the force from the pressure is balanced by the normal components of the tangential forces, like shown in figure 3.3,

$$F_{normal} = 2F_{elastic} \sin \frac{1}{2} d\phi, \tag{3.20}$$

since the value of $d\phi$ is infinitesimal, $\sin \frac{1}{2} d\phi$ can be approximated with $\frac{1}{2} d\phi$. Therefore by Newton's third law,

$$\begin{aligned} F_{normal} &= F_{pressure} \\ \frac{\Delta r}{R} E\, h \Delta x d\phi &= \Delta P \Delta x r d\phi \\ \frac{\Delta r}{\Delta P} &= \frac{rR}{Eh}. \end{aligned} \tag{3.21}$$

Assuming that the change in volume derived from a change in radius is given by, $\frac{\Delta V}{\Delta r} = \Delta x 2\pi r$, the volume increase caused by the increase in pressure can be calculated,

$$\frac{\Delta V}{\Delta P} = \frac{\Delta V}{\Delta r} \frac{\Delta r}{\Delta P} = 2\pi \Delta x r \frac{rR}{Eh}. \tag{3.22}$$

Equation 3.22 is non-linear: written in terms of the volume, $\frac{\Delta V}{\Delta P} = \frac{2R}{Eh} V(r)$, it is clear that a volume change is a function of the new volume, which indicates that the modeling of blood vessel compliance may not be done sufficiently with linear stress-strain relations.

3.7 The Moens-Korteweg equation

An interesting relation can be derived from the elasticity of the tube by use of Newton's second law, $F = m \cdot a$.

Over a section of tube with length Δx the difference in tension force from one end to the other is given by the cross-sectional area times the corresponding change in pressure, assuming that area is unchanged with length over the section,

$$-\frac{\Delta F}{\Delta x} = \pi R^2 \frac{\Delta P}{\Delta x}, \tag{3.23}$$

but force is given by mass of the volume, $\rho \Delta x \pi R^2$, times acceleration, $\frac{dv}{dt}$,

$$-\frac{\rho \Delta x \pi R^2}{\Delta x}\frac{dv}{dt} = \pi R^2 \frac{\Delta P}{\Delta x}, \tag{3.24}$$

when taken to the infinitesimal limit of $\Delta x \to dx$,

$$-\frac{dP}{dx} = \rho \frac{dv}{dt}. \tag{3.25}$$

Over the same infinitesimal volume the change in volume flow can be expressed as the time-derivative of volume over the infinitesimal length,

$$-\frac{dQ}{dx} = \frac{d}{dx}\frac{dV}{dt} = \frac{d}{dx}\left(\Delta x 2\pi R \frac{dr}{dt}\right) = 2\pi R \frac{dr}{dt}. \tag{3.26}$$

However the change in flow can also be expressed as the change in cross-sectional area times flow velocity,

$$-\frac{dQ}{dx} = -\frac{d}{dx}\left(Av\right) = -\pi R^2 \frac{dv}{dx}. \tag{3.27}$$

For both of these equations remember that radius is unchanged with length. Set equation 3.26 and 3.27 together,

$$\begin{aligned} 2\pi R \frac{dr}{dt} &= -\pi R^2 \frac{dv}{dx} \\ -\frac{dr}{dt} &= \frac{R}{2}\frac{dv}{dx}. \end{aligned} \tag{3.28}$$

The elastic modulus, E, of the tube wall is given as a relation between the change in stress, $d\sigma = \frac{r}{h} dP$, and strain, $d\epsilon = \frac{dr}{R}$,

$$E = \frac{d\sigma}{d\epsilon} = \frac{R^2}{h}\frac{dP}{dr} = \frac{R^2}{h}\frac{\frac{dP}{dt}}{\frac{dr}{dt}}, \tag{3.29}$$

insert equation 3.28 into equation 3.29,

$$\begin{aligned} E &= -\frac{R^2}{h}\frac{\frac{dP}{dt}}{\frac{R}{2}\frac{dv}{dx}} \\ -\frac{dP}{dt} &= \frac{Eh}{2R}\frac{dv}{dx}. \end{aligned} \tag{3.30}$$

Take the second derivative of both equation 3.25 and equation 3.30,

$$-\frac{d^2P}{dx^2} = \rho\frac{d^2v}{dxdt}, \tag{3.31}$$

and

$$-\frac{d^2P}{dt^2} = \frac{Eh}{2R}\frac{d^2v}{dxdt}, \tag{3.32}$$

and put them together,

$$\frac{d^2P}{dt^2} = \frac{Eh}{2\rho R}\frac{d^2P}{dx^2} \tag{3.33}$$

Recognize that equation 3.33 is the wave equation for a pressure wave that has the wave speed,

$$v_{pw} = \sqrt{\frac{Eh}{2\rho R}}. \tag{3.34}$$

Equation 3.34 is known as the Moens-Korteweg equation and the velocity is known as the pulse wave velocity because it tells how fast the pressure waves travel along the tube. The pulse wave velocity is an important function for physicians as it is one of the few characteristics that can be externally measured, and through the Moens-Korteweg equation it can be used as a measure for arterial stiffness.

It should be noticed however that the Moens-Korteweg only holds under certain circumstances: there should be no or only insignificant change in tube cross-sectional area along the length of the tube, there should only be insignificant change in wall thickness, and the relation $dv(dr^{-1})dx \cdot dt$ should be small to the point of insignificance [Butlin, 2007]. Thus for most cases, specifically arterial pulse wave measurements, the Moens-Korteweg equation should only be considered as an approximation.

3.8 Inertia of the liquid

Finally when pulsating flow and pressure are the defining phenomena of the liquid motion of blood, inertia of the liquid will be a factor in the modeling as well.

The inertia of liquid inside a section of tube with length Δx will simply be a function of the mass of liquid, governed by the density, ρ. However, since inertia is a resistance to acceleration of the liquid it will also be a function of the flow profile, for instance the no-slip condition assumes that liquid near the wall of the tube has constant velocity zero, and thus it is never accelerated.

Assume for a second that the flow has a completely flat flow profile, then the accelerated mass of liquid inside a tube section of length Δx is simply density times volume of the section,

$$M = \rho \Delta x \, \pi R^2. \tag{3.35}$$

If on the other hand the flow is constantly bound to a Poiseuille parabolic flow profile the liquid is not be accelerated equally, close to the wall the acceleration is zero while at the center of the tube the acceleration must peak in order to accelerate the liquid from one parabolic flow profile to another, in fact the acceleration profile itself will have to parabolic, which corresponds to an accelerated mass of inertia given by,

$$M = \rho \Delta x \, 2\pi \int_0^R \frac{R^2 - r^2}{R} dr = \frac{4}{3} \rho \Delta x \, \pi R^2. \tag{3.36}$$

Thus if you want to stop liquid flowing with a Poiseuille parabolic flow profile it will feel as though the liquid is one third heavier than for a flat profile.

As it has already been established the pulsating liquid flow will have neither a flat profile nor a Poiseuille profile, so the inertia of the liquid will be a more complicated function than those suggested here, in section 4.3.3 a theory for modification of the inertia function will be discussed further.

The inertia is defined in relation to acceleration of flow, or more specifically the change in momentum of the flow. The product of accelerated mass, M, times volume flow, Q, is the momentum of flow, p,

$$p = M \cdot Q. \tag{3.37}$$

Notice that momentum of flow is not equal to the momentum of standard kinematics, the units are different, thus the change of the momentum of flow over the length of a section is given by a difference in force times the cross-sectional area,

$$\Delta(A \cdot F) = \frac{dp}{dt} = M \frac{dQ}{dt}, \tag{3.38}$$

which is equal to a difference in pressure times area squared. Let it be assumed that the change in area is insignificant or zero, which is one of the requirements for the Moens-Korteweg equation, thus the square of the area change may be ignored while the pressure difference is found using equation 3.22,

$$\Delta(A^2 \cdot P) = \Delta A^2 P + A^2 \Delta P = \frac{Eh}{2R}\frac{\Delta V}{V}A^2 = M\frac{dQ}{dt}. \tag{3.39}$$

Let the mass be described by the simple accelerated mass from equation 3.35 and rewrite the equation,

$$\frac{V^2}{A^2}\frac{1}{\Delta V}\frac{dQ}{dt} = \frac{Eh}{2\rho R}. \tag{3.40}$$

Volume flow can be written as velocity times cross-sectional area, and letting the change in cross-sectional area approach zero the following relation is obtained,

$$\Delta x^2 \frac{1}{dV}\frac{d}{dt}(Av) = \Delta x \frac{d}{dt}\frac{1}{dV}(Vv) = \Delta x \frac{dv}{dt} = \frac{Eh}{2\rho R}. \tag{3.41}$$

The acceleration of mass is given by an expression that is close to the Moens-Korteweg equation, using integration in time the velocity is found,

$$\frac{dv}{dt} = \frac{Eh}{2\rho R}\frac{1}{\Delta x} \qquad \Rightarrow \qquad v = \frac{Eh}{2\rho R}\int_{t_0} t\frac{1}{\Delta x}dt = \frac{Eh}{2\rho R}\frac{\Delta t}{\Delta x}, \tag{3.42}$$

and letting the length of the section become infinitesimal,

$$\frac{\Delta x}{\Delta t}v = \frac{Eh}{2\rho R} \qquad \Rightarrow \qquad v = \sqrt{\frac{Eh}{2\rho R}}. \tag{3.43}$$

Equation 3.43 is the Moens-Korteweg equation, which demonstrates that under ideal conditions a relation exist between the elastic compliance of the tube and the inertia of liquid, which is responsible for the speed of the pulse wave. This relation will be used further in section 5.3.

The theory and concepts presented in this chapter are some of the fundamentals for liquid flow in tubes and canals, these should be considered as the basis on which the models of the later chapters are based. Although mostly presented in general terms here it should be clear that the concepts presented in this chapter will not alone be sufficient for modeling the flow of blood in the embryonic heart, many special conditions apply to the heart and vessels of the embryo, which is not covered by the simple theory.

Chapter 4

Construction of the Cylindric Tube Model

The model presented in this chapter builds on the fundament of the transmission line model explained in section 1.2.2. In general the model will be an expansion of the transmission line just as the transmission line can be said to be an expansion of the Windkessel model, though another meaning is given to the elements of this model, which should not be traced back to the Windkessel model.

The model presented here is a model for the liquid flow in an elastic tube, it is referred to as the cylindric tube model or circular model as the underlying assumption in the model is that the tube has a circular cross-section, that is, the tube is a hollow cylinder. Eventually the model may also be referred to as the concentric model because it assumes that all deformation of tube volume is a concentric function of radius, contrary to the eccentric models of chapter 6.

The model is based on the use of energy bond technique to explain the relation between flow and pressure and the elastic forces of the tube wall. Before the presentation of the model, a short introduction to this technique is needed.

4.1 Energy bond technique

The energy bond graph technique of just energy bond technique should be viewed as a modeling language or formalism that focus on specific aspects of a physical situation and keeps check on physical consistency at while it allows for a rather simple modular construction of very complicated models. Through this thesis the modeling power and possibilities of the energy bond graph technique should become clear, but in order to introduce the model of this chapter it is first necessary to introduce some basic concepts from the energy bond formalism.

Energy bond graphs are schematic drawings just as electrical networks, but they are not entirely the same. The first and foremost difference between electrical networks and energy bond graphs is that energy bonds trace flow of energy where electric circuits trace current and potential.

Energy bonds include the same elements as electrical networks, i.e. capacitors, resistances, inductors, and also a few more. The elements are viewed through their effect on the energy flow, where in electrical networks they were largely viewed through their effect on current and potential. Mathematically it is equivalent but physically it is a simple change of perspective.

The fundamental idea is that the product of current and potential is the energy flow, so for each energy bond is associated a current-variable, f for flow, and a potential-variable, e for effort. The classical electrical elements of resistance and capacitance and so on work as they always do on these two variables but in energy bond formalism more notice is paid to what this means to the energy in the network. Hence the capacitor is a storage for potential energy, the inductor is a storage for kinetic energy, and the resistance is a leak of energy. A traditional electrical resistance has the current as input and the potential is calculated as current times the resistance, hence it can be viewed as an energy-sink dependent on the kinetic energy. In the same manner it is possible to imagine an energy-sink dependent on the potential energy, which in electrical networks is the same as an inverse resistance but in energy bond graphs it can be useful to view them as two different kinds.

The idea is that energy bond graphs contain the same tools as electrical networks and a few more, it is formulated in a way to give it more diversity and more 'modeling power', but unfortunately this also makes it more abstract and un-intuitive. This thesis will not include the complete exhaustive presentation of the energy bond formalism, instead refer to Christiansen [1979, 1993] in Danish, or Christiansen [2003] in English for a deeper explanation.

One underlying assumption in the energy bond technique as well as in electrical networks is the use of linear response theory. For all elements in the energy bond graph it is assumed that the two associated variables of the energy bond are aligned in a linear relation such that the output from the element is given by a linear relation of the input with the response function of the element. In the simple case that may just be a product, for instance voltage loss is given by resistance times current, but more generally for time-dependent variables the linear relation is given as a convolution-integral of the input with the response function. Not all effects in the elastic tube are linear effects, see for instance section 4.2.1, but through the use of transformations of variables and a knowledge of how the model is solved in the end the linear response principle is observed.

An important topic is the way energy bonds are connected. Naturally an energy bond must lead to each of the elements of the model but sometimes two or more bonds need to be joined. In electrical networks this would be done either by serial or parallel connections, which are governed by Kirchhoff's laws. In energy bond graphs Kirchhoff's laws are represented with two new elements: The O-junction, ⟐, where potential is conserved and the current obeys Kirchhoff's first law; "the sum of currents into a node equals zero", this equals to a parallel connection. The X-junction, ⊗, where current is conserved and potential obeys Kirchhoff's second law; "the sum of potential differences around a closed loop equals zero", this equals to a serial connection.

The transmission line in figure 1.3 is converted into the network shown in figure 4.1 using the energy bond graphs.

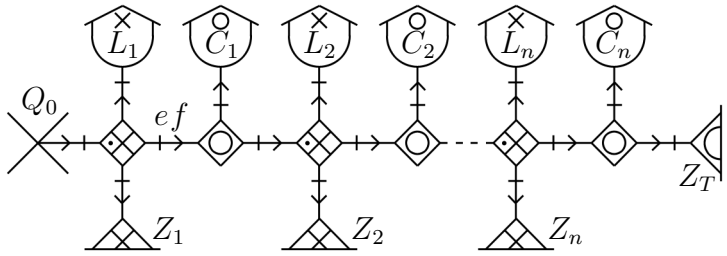

Figure 4.1: The energy bond graph representation of the transmission line as a model for the liquid flow in an elastic tube.

In figure 4.1 ⏀ is the icon for a potential energy storage, C (a capacitor), ⏁ is the icon for a kinetic energy storage, L (an inductor), ⏢ is the icon for a an energy leak, Z (a resistor, R is used for radius), and ⏦ is the icon for another type of energy leak (admittance which is the inverse of impedance), it is used when the intention is to indicate that current is lost while voltage is conserved, in the equations admittance and impedance will look basically the same way however. Finally ⨯ is the current input to the system. In addition there is also a symbol for a voltage input, ◯, which will become relevant during the setup of the tubular heart model in section 7.5.

Each section of the transmission line corresponds to a section of elastic tube with length, Δx. The potential in the model, e, is the pressure in a section, P [Pa], and current, f, is the volume flow, Q [m^3/s], which makes the charge, q, the excess volume of a section, ΔV [m^3], when it expands under the pressure. In the following the word 'section' will be used to refer to such a portion of the tube.

4.2 The cylindric model

The model presented herein is a model for the liquid flow in an elastic tube, essentially it is an expansion of the transmission line constructed in the process of explaining each of the elements in figure 4.1, though the elements in the beginning and the end of the transmission line will not be explained here.

Presently the mean of each of the elements is only explained through words but with a mathematical analysis of this meaning it will be demonstrated how an expression for each element can be calculated. In the following this analysis is completed for each of the three basic elements of figure 4.1 with the use of material from chapter 3 under the assumption that the modeled elastic tube has a circular cross-section.

It is assumed for the construction of the tube that it is divided into N smaller sections of tube and that for each section, n, the elements of that section describe the physical properties of elasticity, mass of inertia, and resistance to the flow from one section to the next. This underlying discretization is the basis for the model and in section 5.6.4 it is tested if the model is convergent for the number of sections.

Each section is described with a dynamic radius, r_n, which has the equilibrium value, R_n, when flow and pressure difference are zero. The section has cross-sectional area, πr_n^2, which gives the dynamic volume $V_n = \pi r_n^2 \Delta x$, where Δx is the length of the section. Furthermore the liquid in each section has pressure, P_n, and the flow, Q_n, is defined as the volume of liquid flowing from section n to section $n + 1$.

4.2.1 Elasticity of the tube wall

The capacity to contain an excess volume of liquid for each section of the tube is a function of the elasticity of the tube wall. This is modeled through the potential energy storage (a capacitance in the energy bond graph), when an extra volume of liquid is pumped into a section of the tube the wall expands until the high pressure is balanced by the elastic force.

The excess volume of liquid is ΔV_n but since the section is modeled as a hollow cylinder with a circular cross-section and with constant length, Δx, it is easier to describe the excess volume of section n with the radial change, $\Delta r_n = r_n - R_n$, where R_n is the equilibrium radius of the section. The elastic force of section n is given by equation 3.18,

$$F_n = \frac{\Delta x E h}{R_n} \left(r_n - R_n \right), \tag{4.1}$$

where E is Young's modulus and h is the thickness of the tube wall. Integrate this

force from R_n to r_n to get a potential energy and integrate over the circumference to get the total potential energy stored in the section when the walls expand from R_n to r_n,

$$U_n = \int_{R_n}^{r_n} \frac{\Delta x E h}{R_n} (r - R_n) 2\pi dr = \pi \frac{\Delta x E h}{R_n} (r_n - R_n)^2 . \tag{4.2}$$

This expression is inserted into definition of the potential energy of a capacitor, $U = \frac{1}{2}\Delta r_n^2 / C_n$, which shows that the capacitance, C_n, is given by,

$$C_n = \frac{R_n}{2\pi \Delta x E h}. \tag{4.3}$$

Notice that this is not the capacitance compared to the original charge and potential variables, i.e. ΔV_n and P_n. The excess volume, ΔV_n, has been transformed to radial expansion, $q_n = \Delta r_n$, and pressure has been transformed to $e_n = \Delta r_n / C_n = 2\pi F_n$. To use the expression for the capacitance in equation 4.3 it is necessary to insert a transformer in front of each potential energy storage of the model in figure 4.1.

The rule for use of transformers in energy bond graphs is the same as for electrical networks, it is a variable transformation that transforms current and potential to a new set of current and potential. A transformation ratio, T_n, is multiplied with the potential to find the new potential, while the current is divided by T_n. Thus current and potential changes but the energy flow remains the same. When the new current and potential are transformed back to their original values the multiplication and division are reversed. In this case the transformation ratio is calculated through the volume expansion of section n, which must be equal to,

$$\Delta V_n = \pi \Delta x \left(r_n^2 - R_n^2 \right) = \pi \Delta x (r_n + R_n) \Delta r_n \approx 2\pi \Delta x \; r_n \; \Delta r_n, \tag{4.4}$$

which makes the transformation ratio equal to $T_n = 2\pi r_n \Delta x$, but notice the approximation at the end of equation 4.4 where it is assumed that the radial changes are sufficiently small such that $r_n + R_n$ can be approximated by $2r_n$.

The pressure response to the volume change in section n can be calculated by using the transformation ratio,

$$P_n = \frac{2\pi F_n}{2\pi r_n \Delta x} = E h \frac{r_n - R_n}{r_n R_n} = \frac{E h}{R_n} \frac{\Delta r_n}{r_n}, \tag{4.5}$$

and thus the capacitance in the original charge and potential variables can be calculated,

$$C_n' = \frac{\Delta V_n}{P_n} = \frac{2\pi \Delta x R_n r_n^2 \Delta r_n}{E h \Delta r_n} = \frac{2\pi \Delta x R_n}{E h} r_n^2. \tag{4.6}$$

4.2.2 Inertia of the liquid

Assuming volume flow and pressure are pulsatile functions inertia of the liquid becomes a factor in the model, this is modeled by the kinetic energy storage (the inductance) in the transmission line.

The inertia is a function of the mass of liquid, but since it is a function designed to react to the flow between section n and section $n+1$ the mass of liquid is defined as a mean between the two sections,

$$M_n = \rho \Delta x \pi r_n r_{n+1}, \tag{4.7}$$

where $r_n r_{n+1}$ is the square of the geometric mean between the radii of section n and section $n+1$, in some ways this can be thought of as the mass of an intermediate section with cross-sectional area, $\pi r_n r_{n+1}$. The utilization of the geometric mean as well as the approximation in equation 4.4 are chosen over the arithmetic mean to eliminate sums in the model under the assumption that dimensional variations are reasonably small.

With the geometric mean cross-sectional area the mean laminar flow velocity of the liquid is defined,

$$v_n = \frac{Q_n}{\pi r_n r_{n+1}}, \tag{4.8}$$

with Q_n being the volume flow from section n to section $n+1$.

The definition of mass and velocity allows for an expression of the kinetic energy of the liquid,

$$E_n = \psi \frac{1}{2} M_n v_n^2 = \psi \frac{\rho \Delta x \pi r_n r_{n+1}}{2 \left(\pi r_n r_{n+1}\right)^2} Q_n^2 = \psi \frac{\rho \Delta x}{2 \pi r_n r_{n+1}} Q_n^2 \,, \tag{4.9}$$

where ψ is an inertia correction factor, which is decided by the cross-sectional velocity profile of the liquid flow (see section 3.8). $\psi = 1$ corresponds to the case of a flat velocity profile where all liquid layers move with velocity, v_n, while $\psi = 4/3$ corresponds to normal Poiseuille flow. Further down in section 4.3.3 the meaning of the inertia correction factor will be investigated.

The next step relies on the energy bond technique and linear response theory. When potential and current variables are chosen their product should be that of energy transferred per time, which means that the product of charge and potential will be that of an energy, which is used for potential energy in capacitors like above. In the same way kinetic energy is found as the product of current and momentum, where momentum is defined as the time-integration of the potential.

Define a momentum of flow, p'_n, with units [kg/m·s] such that the derivative of the energy with respect to this momentum is,

$$\frac{\partial E_n}{\partial p'_n} = Q_n, \tag{4.10}$$

which makes p'_n,

$$p'_n = \psi \frac{\rho \Delta x}{\pi r_n r_{n+1}} Q_n = \psi \rho \Delta x v_n. \tag{4.11}$$

The kinetic energy can then be written as a function of the momentum,

$$E_n = \frac{1}{\psi} \frac{\pi r_n r_{n+1}}{2\rho \Delta x} {p'_n}^2. \tag{4.12}$$

By using the momentum definition of the kinetic energy, $E_n = \frac{1}{2}{p'_n}^2 / L_n$, it is now possible to find the inductance, L_n, of the model,

$$L_n = \psi \frac{\rho \Delta x}{\pi r_n r_{n+1}}. \tag{4.13}$$

4.2.3 Poiseuille resistance

The last element of the energy bond graph in figure 4.1 is the impedance, Z_n. This impedance is typically a resistance to movement, in this case a resistance to the flow caused by friction and the viscosity of the liquid, creating a drop in hydrodynamic pressure. In most cases this resistance is modeled by a Poiseuille relation so that the definition of the impedance exactly satisfies the Poiseuille equation (equation 3.11) though in some cases there may be additional terms to the impedance.

The Poiseuille resistance to the flow between section n and section $n+1$ is defined,

$$Z_n = \frac{\Delta P_n}{Q_n} = \frac{8\eta \Delta x}{\pi r_n^2 r_{n+1}^2}, \tag{4.14}$$

where η is the dynamic viscosity of the liquid, ΔP is the pressure loss from section n to section $n+1$, and $r_n r_{n+1}$ is the square of the geometric mean between the radii of section n and section $n+1$.

As mentioned earlier, the liquid does not flow with an exact Poiseuille parabolic flow profile, which is assumed in section 3.4. Because of the pulsating pressure and volume flow, the parabolic flow profile never has time to settle completely. Instead the flow profile appears to be more flat and squared, see for instance Nichols and O'Rourke [1998, p. 39].

Therefore the Poiseuille equation does not give the complete description of impedance in this model, an investigation of the impedance of the pulsatile flow profile will be given in section 4.3.3, and furthermore section 4.3.2 will detail another impedance term given by the curvature of the tube.

4.2.4 The Bernoulli effect

All elements of the energy bond graph in figure 4.1 are now described, the first and the last element in the figure are to be considered as boundary conditions for the model and as such they will change according to the use of the model, for instance on section 5.2 they are completely absent. The simple explanation of the elements is complete, but there is more to be done in constructing the cylindric tube model.

Notice how the dynamic radius, r_n, is included in the expression for all the elements of the model, but at the same time r_n is part of the charge variable at the untransformed capacitance, $\Delta r_n = r_n - R_n$. It seems that there is a coupling between the elements, which should be explored.

Let the total energy of the transmission line be named E, it will be a sum of potential and kinetic energies of all the sections of the tube. The derivative of E with respect to the charge variable, Δr_n, will yield the potential variable. This reveals a relation between charge and potential, which is not directly reflected in the model,

$$\begin{aligned}
\frac{\partial E}{\partial r_n} &= \frac{\partial \left(U_n + E_{n-1} + E_n\right)}{\partial r_n} \\
&= 2\pi F_n + \frac{1}{\psi}\frac{\pi}{2\rho\Delta x}\left(r_{n-1}{p'_{n-1}}^2 + r_{n+1}{p'_n}^2\right) \\
&= 2\pi r_n \Delta x \left(P_n + \frac{\rho}{4\psi}\left(\frac{r_{n-1}}{r_n}v_{n-1}^2 + \frac{r_{n+1}}{r_n}v_n^2\right)\right). \qquad (4.15)
\end{aligned}$$

Notice that the factor, $2\pi r_n \Delta x$, is the transformation ratio, T_n, from the section 4.2.1. It is seen that the potential is not only composed of the pressure, which was specified from the start, but also has two extra terms coming from the kinetic energy. Overall expression 4.15 bear a certain likeness to the Bernoulli equation (equation 3.17), with the two extra terms being some sort of kinetic pressure. This connection to the Bernoulli equation will be investigated further below.

Furthermore it is clear that the capacitance and the inductance of the model are not independent of each other, both are functions of the dynamic radius and the radius is itself a variable of the section. Thus write the dynamic radius as a function of the capacitance,

$$r_n = \sqrt{C'_n \frac{Eh}{2\pi\Delta x R_n}}, \qquad (4.16)$$

which makes it obvious that the inductance can be written as a function of the capacitance,

$$L_n = \psi \frac{\rho \Delta x}{\pi r_n r_{n+1}} = \psi \frac{2\rho \Delta x^2}{E\tau} \sqrt{\frac{R_n R_{n+1}}{C'_n C'_{n+1}}}. \tag{4.17}$$

The inductance depends on the capacitance of the section and the capacitance of the next section, which makes sense since the capacitance models how much liquid each section can hold (under the given pressure), and the inductance models the inertia of the total amount of liquid flowing from one section to the next. Mathematically this is not a problem for the model, but physically it is desirable to have all elements described as independent physical constants and let current and potential be the only variables of the system.

The almost-Bernoulli relation of equation 4.15 and the inter-dependency of the elements point to the fact that this model is still incomplete, there are hidden qualities of the model that need to be explicitly reflected in the energy bond graph. To do this, a new momentum variable is introduced by inserting a transformer in front of the inductance in the energy bond diagram in figure 4.1. Mathematically this corresponds to a transformation of variables by the transformation ratio, $\sqrt{r_n r_{n+1}/R_n R_{n+1}}$, which gives the momentum,

$$p_n = \sqrt{\frac{r_n r_{n+1}}{R_n R_{n+1}}} p'_n = \sqrt{\frac{r_n r_{n+1}}{R_n R_{n+1}}} \psi \rho \Delta x v_n. \tag{4.18}$$

This yields a new expression for the kinetic energy,

$$E_n = \frac{1}{\psi} \frac{\pi r_n r_{n+1}}{2\rho \Delta x} \left(\sqrt{\frac{R_n R_{n+1}}{r_n r_{n+1}}} p_n \right)^2 = \frac{1}{\psi} \frac{\pi R_n R_{n+1}}{2\rho \Delta x} p_n^2, \tag{4.19}$$

and hence also a new r_n-independent expression for the inductance,

$$L_n = \frac{p_n^2}{2E_n} = \psi \frac{\rho \Delta x}{\pi R_n R_{n+1}}. \tag{4.20}$$

In the definition of the new momentum of flow it is interesting to observe what this means for the potential input to the inductance, this is found by taking the time-derivative of the momentum,

$$\begin{aligned} \frac{dp_n}{dt} &= \sqrt{\frac{r_n r_{n+1}}{R_n R_{n+1}}} \frac{dp'_n}{dt} + \frac{1}{2} \frac{p'_n}{\sqrt{R_n R_{n+1}}} \left(\sqrt{\frac{r_{n+1}}{r_n}} \frac{dr_n}{dt} + \sqrt{\frac{r_n}{r_{n+1}}} \frac{dr_{n+1}}{dt} \right) \\ &= \sqrt{\frac{r_n r_{n+1}}{R_n R_{n+1}}} \frac{dp'_n}{dt} + \frac{1}{2} \frac{p_n}{\sqrt{r_n r_{n+1}}} \left(\sqrt{\frac{r_{n+1}}{r_n}} \frac{dr_n}{dt} + \sqrt{\frac{r_n}{r_{n+1}}} \frac{dr_{n+1}}{dt} \right) \\ &= \sqrt{\frac{r_n r_{n+1}}{R_n R_{n+1}}} \frac{dp'_n}{dt} + \frac{p_n}{2r_n} \frac{dr_n}{dt} + \frac{p_n}{2r_{n+1}} \frac{dr_{n+1}}{dt}. \end{aligned} \tag{4.21}$$

Notice here that the input potential to the inductance comes partially from the transformed momentum and partially from two other sources. The time-derivative of the dynamic radius is the current into the capacitance of the system, and so by the transformation of the momentum it has become clear that the input potential to the inductance has contributions from the current at the capacitors on either side of the inductance. The current is however changed from current to potential through the ratio, $p_n/2r_n$ on the lower side and $p_n/2r_{n+1}$ on the upper side.

With this restructuring of the transmission line the energy derivative from equation 4.15 can be redone,

$$\begin{aligned}\frac{\partial E}{\partial r_n} &= 2\pi F_n + \frac{1}{\psi}\frac{\pi}{2\rho\Delta x}\left(r_{n-1}{p'_{n-1}}^2 + r_{n+1}{p'_n}^2\right) \\ &= 2\pi F_n + \frac{1}{\psi}\frac{\pi}{2\rho\Delta x}\left(\frac{R_{n-1}R_n}{r_n}p_{n-1}^2 + \frac{R_nR_{n+1}}{r_n}p_n^2\right) \\ &= 2\pi F_n + \frac{p_{n-1}}{2r_n}\frac{p_{n-1}}{L_{n-1}} + \frac{p_n}{2r_n}\frac{p_n}{L_n}, \end{aligned} \tag{4.22}$$

which corresponds exactly to the output potential from the capacitance plus two contributions from the inductances on either side that have been converted through the relations $p_{n-1}/2r_n$ and $p_n/2r_n$. In other words this is the potential given by the derivative of the total energy with respects to the charge variable, Δr_n, it has the units of force and through the transformation ratio $2\pi\Delta x r_n$ the driving pressure for section n is found,

$$\begin{aligned}P_n &= \frac{1}{2\pi\Delta x r_n}\left(2\pi F_n + \frac{p_{n-1}}{2r_n}\frac{p_{n-1}}{L_{n-1}} + \frac{p_n}{2r_n}\frac{p_n}{L_n}\right) \\ &= \frac{F_n}{\Delta x r_n} + \frac{1}{2\pi\Delta x r_n}\left(r_{n-1}\frac{\psi\pi\rho\Delta x}{2}v_{n-1}^2 + r_{n+1}\frac{\psi\pi\rho\Delta x}{2}v_n^2\right) \\ &= \frac{F_n}{\Delta x r_n} + \psi\frac{r_{n-1}}{2r_n}\frac{1}{2}\rho v_{n-1}^2 + \psi\frac{r_{n+1}}{2r_n}\frac{1}{2}\rho v_n^2. \end{aligned} \tag{4.23}$$

From this equation it can be seen that the driving pressure consists of the hydrodynamic pressure, $F_n/\Delta x r_n$, and a 'kinetic pressure' that is consistent with the Bernoulli equation except that it is calculated as an average of the inflow and outflow velocities of a section of the tube and weighted by the ratio of the radius to the radii of the adjacent sections.

4.3 Additional effects

With the Bernoulli coupling the cylindric tube model has come so far that it is operational, as specified in the descriptions above the energy bond graph has been modified from that of the transmission line in figure 4.1 through use of variable transformations to the energy bond graph in figure 4.2.

In the figure it is still possible to see the basic setup consisting of a capacitance, inductance and a resistor, but in addition the triangle symbols represent the transformation of variables mentioned in equation 4.4 and 4.18 and the fish-shaped symbols represent another set of variable transformations presented in equation 4.22, though these gyrators as they are called have the special effect that they transform current to potential and vice versa.

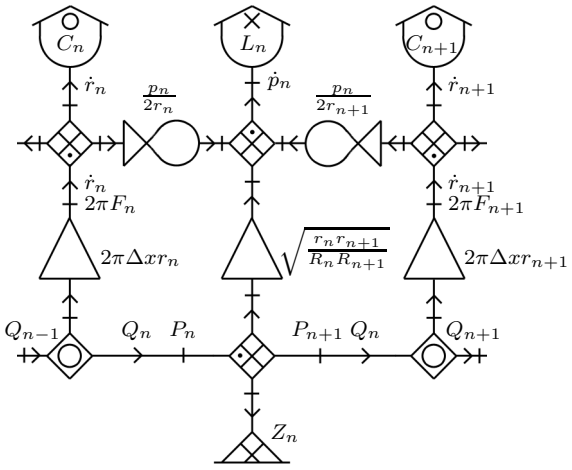

Figure 4.2: The energy bond graph of the expansion to the transmission line. The figure only shows one and a half section in the transmission line, but notice that the elements of the section have been switched around compared to figure 4.1 so that the potential storage comes before the kinetic storage.

The definitions of elastic capacitance, inertia of mass, Poiseuille resistance and the Bernoulli effect constitute the core effects of the model, but the model is still in the rough. The next step is to improve the model with additional effects that increase the model's applicability in relation to the liquid flow in an elastic tube: the longitudinal tensions of the tube counteracting lengthwise discrepancies between different radii of neighboring sections, the resistance induced by tube curvature on the pressure and flow, and the Womersley theory for pulsatile pressure and flow. The three effects will be presented one by one and explained how they are implemented in the model.

4.3.1 Longitudinal shear tensions

One adjustment to the model comes from the logical fact that when the radius of one section of the tube is increased the wall of the section will pull the walls of the neighboring sections. The sections are not independent and thus the radius increase is not only a function of the liquid volume of the section itself but also a function of the radii of the neighboring sections. This interaction of the radii of the various sections is governed by the elastic forces tangential to the tube, which are described as shear tensions of the tube wall.

The shear tensions of the tube wall describe the wall's response to a skew deformation when one section's surface area becomes larger than its neighbor's, but as all skew deformations can be transformed into right angle deformations the shear tensions will also describe the wall's response to a longitudinal strain of its length. As such this addition to the model is also supposed to reflect how the periodic pressure waves produce longitudinal stresses in the tube, even though the length of the tube is fixed in the model. Therefore this addition to the model will have a more ad hoc character compared to the previous model elements.

When the radii of two neighboring sections differ from their resting values by unequal increments a force will act between them trying to pull the difference towards zero. This force, which has both tangential and longitudinal composites, is proportional to the difference in radial change between the sections and it is given by the shear modulus, G, which for isotropic materials is one third of Young's modulus (since the shear modulus models a one dimensional response while Young's modulus has three dimensions). The calculation of the elastic force, F_{sn}, is analogue to the elastic force for the radius expansions in section 4.2.1,

$$F_{sn} = \frac{Gh\sqrt{R_n R_{n+1}}}{\Delta x}\left(\Delta r_{n+1} - \Delta r_n\right), \tag{4.24}$$

where $\sqrt{R_n R_{n+1}}$ is the geometric mean between the resting radii of the two neighboring sections. This force is integrated over the circumference (multiply with 2π) and integrated over the difference from Δr_n to Δr_{n+1},

$$\begin{aligned} U_{sn} &= \int_{\Delta r_n}^{\Delta r_{n+1}} 2\pi \frac{Gh\sqrt{R_n R_{n+1}}}{\Delta x}\left(\Delta r_{n+1} - \Delta r'\right) d\Delta r' \\ &= \frac{\pi Gh\sqrt{R_n R_{n+1}}}{\Delta x}\left(\Delta r_{n+1} - \Delta r_n\right)^2. \end{aligned} \tag{4.25}$$

Insert the energy from equation 4.25 into the formula for the potential energy of a capacitor, $U_{sn} = \frac{1}{2}\left(\Delta r_{n+1} - \Delta r_n\right)^2 / C_{sn}$, to find the capacitance,

$$C_{sn} = \frac{\Delta x}{2\pi G h \sqrt{R_n R_{n+1}}}. \tag{4.26}$$

The capacitance, C_{sn}, models the elastic attraction between two neighboring sections, for a soft tube the capacitance is high and the radii of neighboring sections are allowed to diverge more easily.

On the other hand diverging radii of neighboring sections will also cause friction inside the tube wall. Friction equals loss of energy thus an resistance is needed to model the shear tensions of the wall, with impedance proportional to the difference in radial change between the two sections.

In the model the impedance, Z_{sn}, is an ad hoc determined constant, which is given from the desire that oscillations with frequencies above 100 Hz should be damped. The impedance is determined through the fact that the period of an oscillation in an RC-circuit is given by $T = Z_{sn}C_{sn}$, which by insertion of the desired period, $T = 0.01$ seconds, yields the impedance, $Z_{sn} = T/C_{sn}$.

4.3.2 Curvature of the tube

Another addition to the model is the resistance given by the curvature of the tube. When liquid flows through a bent tube a lot of interesting things happen and it is clear that the standard Poiseuille equation will not fully describe the flow, even if it is still laminar, in fact it has been demonstrated that the location of maximum axial velocity shifts towards the outer wall of a curved tube [Berger et al., 1983].

Even more interesting is the establishment of so called secondary flow where liquid performs a rotating motion at right angles to the axis of the tube. This secondary flow is a consequence of the centrifugal pressure gradient in the bent tube acting together with the friction of the tube walls, it is generally superimposed upon the main flow and is present in both laminar and turbulent flows [Crane Co., 1982].

Generally the flow through a bent tube depends on only two characteristics of the bend, the angle of the bend and its curvature. These are compared to the Reynolds number of the flow to establish if the bend is 'smooth' in relation to the flow [Crane Co., 1982]. If the bend is too sharp eddies will form at the inner wall, which will impact flow before and mainly after the bend and increase energy loss in the bend. For higher Reynolds numbers the turbulent flow will cover more area of the bent tube.

Despite of these phenomena the main effect of a bent tube on the liquid flow is a loss of energy, which can be seen as a pressure drop from the frontal to distal end of the bend. In general a pressure drop in the tube is given by Darcy's equation,

$$\Delta P = f\frac{\Delta x}{2R}\frac{\rho v^2}{2}, \tag{4.27}$$

where Δx is the length of tube and R is its radius, ρ is the density of the liquid and v is the typical velocity of the liquid through the tube. The typical velocity of the liquid is unspecified in Darcy's equation to the extent that it is the same velocity as used in the definition of the Reynolds number and generally it is taken to be the mean velocity, $v = Q/\pi R^2$.

The quantity f in equation 4.27 is the friction factor, which details the energy loss of the flow through that particular length of tube. For a straight tube the friction factor is dependent on the Reynolds number, for laminar flow ($Re < 1000$) the friction factor is a function of the Reynolds number alone, $f = \frac{32}{Re} = \frac{32\eta}{\rho v R}$,

$$\Delta P = \frac{32\eta}{\rho v R}\frac{\Delta x}{2R}\frac{\rho v^2}{2} = \frac{8\eta\Delta x v}{R^2} = \frac{8\eta\Delta x}{\pi R^4}Q, \tag{4.28}$$

thus Darcy's equation becomes the Poiseuille equation.

For completely turbulent flow ($Re > 2000$) the friction factor is a function of the Reynolds number as well as the roughness of the tube wall. There is no simple equation that governs friction factors in this regime but the Blasius law seems to be a good approximation for the lower bounds of turbulent friction factors in a completely smooth tube [Keller, 1978, p. 49],

$$f_{turbulent} = \frac{0.316}{\sqrt[4]{2Re}}. \tag{4.29}$$

For $Re \in [1000; 2000]$ the flow can be either laminar or turbulent, and thus the friction factor may vary between the values of the friction factors of laminar and turbulent flow as the lower and upper bound [Crane Co., 1982].

For any sort of circumstance imposed on the tube, such as bends, contractions, valves and branches, there is a corresponding friction factor, which will give the pressure loss for that instance. Collectively these pressure losses are known as minor losses. For each instance the friction factor will be an empirical number that has to be found experimentally but common engineering practice dictates that it will be sufficient to extrapolate from known values of likened effects [Crane Co., 1982].

The clever thing about writing the pressure loss with Darcy's equation is that friction coefficients are cumulative by definition, and thus the pressure loss associated with the flow through a curved tube will be defined,

$$\Delta P = (f_L + f_B)\frac{\Delta x}{2R}\frac{\rho v^2}{2}, \tag{4.30}$$

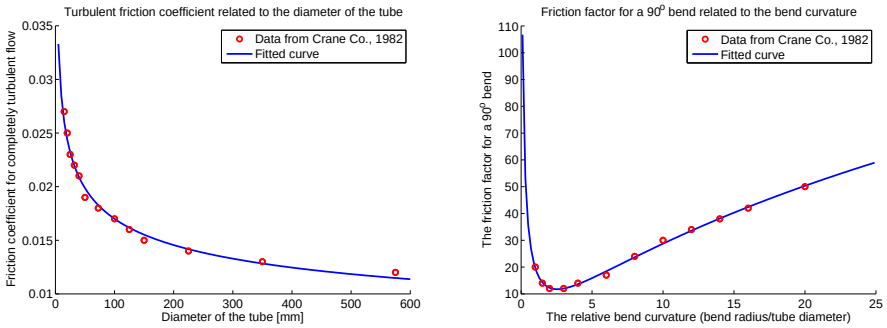

Figure 4.3: Data from Crane Co. [1982] table A-26 and A-29. To the left the friction coefficient for completely turbulent flow, f_T, together with a power function fit. To the right the friction factor for a $90°$ bend, K_B, as a function of the relative bend curvature, defined as radius of curvature relative to the tube diameter, R_B/d.

where f_L is the friction coefficient associated with the length of the curved tube, by default laminar flow is assumed in this thesis, thus f_L is set to $f_L = 32/Re$, and f_B is the friction coefficient associated with a bend in the tube, given by the curvature and the angle of the bend.

The friction coefficient of a bend is a number that has to be found empirically or through charts in engineering manuals. The approach through Darcy's equation to these sorts of problems is something quite common for engineers in the plumbing industry and from their field the curves in figure 4.3 are obtained. In this approach the friction coefficient of a bend is described through the product of three functions,

$$f_B = \xi(\theta) \cdot K_B(R_B/d) \cdot f_T(d). \tag{4.31}$$

Starting from the rear of equation 4.31, f_T is the friction coefficient for completely turbulent flow, that is, when the velocity of the liquid is high enough to produce Reynolds numbers far above 2000. According to Crane Co. [1982] f_T is solely a function of the diameter of the tube, d, and it is easy to see that for density, viscosity and flow velocity sufficient to reach the completely turbulent regime the Reynolds number becomes a function of the tube dimension alone. Therefore, despite the flow is not necessarily turbulent in the bend it is customary to model the friction coefficients relative to the friction coefficient for completely turbulent flow. From the fit in figure 4.3 f_T is found as a power function of tube diameter,

$$f_T = 0.05 \cdot d^{-0.22}, \tag{4.32}$$

which fits very well with Blasius law (equation 4.29).

K_B is the friction factor that is multiplied to f_T for a tube bend of exactly $90°$. Plumbers work mostly with right angle fittings and thus the data comes from measurement of pressure loss through those. Different fittings can have different curvature, and thus K_B is a function of the relative curvature defined as the curvature radius for the center-line of the tube bend, R_B, relative to the tube diameter, d. Figure 4.3 shows data from Crane Co. [1982], the data is fitted to the function,

$$K_B(R_B/d) = 9.07\,(\ln(R_B/d))^2 - 16.93\,\ln(R_B/d) + 19.64. \tag{4.33}$$

The final function of equation 4.31, $\xi(\theta)$, is the angular factor for bend angles different from $90°$. The angle of the bend, θ, is defined as the angle between the directions of the tube before and after the bend, thus a straight tube would have $\theta = 0°$. Keller [1978, p. 49] defines the function,

$$\xi(\theta) = 0.042 \cdot \theta^{0.69}. \tag{4.34}$$

In the end the friction factor, $f = f_L + f_B = 32/Re + \xi K_B f_T$, lets Darcy's equation be converted to the Poiseuille equation plus an extra term,

$$\begin{aligned}
\Delta P &= \frac{8\eta\Delta x}{\pi R^4}Q + \xi K_B f_T \frac{\Delta x}{2R}\frac{\rho v^2}{2} \\
&= \frac{8\eta\Delta x}{\pi R^4}Q + \left(0.018\left(\ln\frac{R_B}{d}\right)^2 - 0.034\ln\frac{R_B}{d} + 0.039\right)\frac{\theta^{0.69}}{d^{0.22}}\frac{\Delta x}{2R}\frac{\rho v^2}{2} \\
&= \frac{8\eta\Delta x}{\pi R^4}Q + \left(3.9\left(\ln\frac{R_B}{d}\right)^2 - 7.3\ln\frac{R_B}{d} + 8.4\right)10^{-3}\frac{\rho\Delta x\theta^{0.69}}{\pi^2 R^{5.22}}Q^2.
\end{aligned} \tag{4.35}$$

As can be seen in equation 4.35 the last term is quadratic with respect to the flow. Thus it do not directly fit into the linear approach of the energy bond formalism.

With the curvature of the tube two distinct frictional effects are defined in the relation between flow and pressure, and equation 4.35 demonstrates quite simply that they will be serially coupled in the energy bond graph. The first frictional effect is the Poiseuille resistance, which has already been described, the other is the friction of the bend. In the energy bond graph the friction will be represented by an impedance symbol, Z_B, that links a pressure loss to the flow rate,

$$Z_{Bn} = \frac{\Delta P_n}{Q_n} = \xi K_B f_T \frac{\rho\Delta x Q_n}{4\pi^2\sqrt{r_n r_{n+1}}^5}. \tag{4.36}$$

In terms of the energy bond formalism, which relies on linear response theory, this equation is erroneous; the volume flow is not allowed to be part of the response

function while it is input to the function. Instead notice that this equation has resemblance to the momentum of the flow defined in equation 4.18,

$$p_n = \sqrt{\frac{r_n r_{n+1}}{R_n R_{n+1}}} p'_n = \psi \sqrt{\frac{r_n r_{n+1}}{R_n R_{n+1}}} \frac{\rho \Delta x}{\pi r_n r_{n+1}} Q_n, \tag{4.37}$$

and thus the impedance of the bend can be written using the momentum rather than the flow (where the numerical value of the momentum is used because the impedance should cause a loss of energy independent of the direction of flow),

$$Z_{Bn} = \frac{\Delta P_n}{Q_n} = \frac{\xi K_B f_T}{\psi} \frac{\sqrt{R_n R_{n+1}}}{4\pi r_n^2 r_{n+1}^2} |p_n|. \tag{4.38}$$

Equation 4.38 defines the additional friction of the bend as a relation between pressure loss to volume flow. Interestingly this impedance is proportional to the numerical value of the momentum of the flow, thus it grows when flow is accelerated, which is very interesting in relation to pulsating flow and pressure.

4.3.3 Womersley theory

The final addition to the model it the inclusion of Womersley theory to express the influence by the velocity profile on the nature of the flow in a tube.

With regards to the behavior of regular pulsating blood flow it has been argued by many physicians and researchers that the Poiseuille equation is not the best description for the interrelation between volume flow and pressure gradient when both are pulsating with time, see for instance the list of restrictions in section 3.4. Such was also the view of mathematician John R. Womersley who in the 1950'ies struck a productive cooperation with the established doctor of physiology Donald A. McDonald, and together they became a very important chapter in the history of blood flow research [Nichols and O'Rourke, 2008].

Womersley's approach to the problem of pulsatile blood flow was to analyze the Navier-Stokes equation under assumptions applicable to blood in the arteries.

Under the simple assumption that the pressure gradient, ∇P, and the flow velocity field, $\mathbf{v}$, are both unchanged with time the Navier-Stokes equation of incompressible liquid,

$$\rho \left(\frac{\partial \mathbf{v}}{\partial t} + \mathbf{v} \cdot \nabla \mathbf{v} \right) = -\nabla P + \eta \nabla^2 \mathbf{v} + \mathbf{f}, \tag{4.39}$$

with ρ, η and $\mathbf{f}$ being liquid density, dynamic viscosity and external forces on the infinitesimal liquid volume respectively, under the restrictions of a cylindrical tube is written,

$$\frac{d^2\mathbf{v}}{dr^2} + \frac{1}{r}\frac{d\mathbf{v}}{dr} + \frac{1}{\eta}\frac{\Delta P}{\Delta x} = 0, \tag{4.40}$$

where $\nabla P = \Delta P/\Delta x$ is the pressure gradient found by subtracting pressures at two different points on the longitudinal axis of the tube and dividing by the distance between them, Δx.

Notice that pressure may change with the longitudinal axis of the tube, the pressure gradient is a constant, whereas the flow velocity may change with the radial position in the tube but not with the longitudinal coordinate. The solution to this equation gives the flow velocity, $v(r) = \frac{\Delta P}{4\eta\Delta x}\left(R^2 - r^2\right)$, where R is the radius of the tube, and with volume flow defined as the integral, $Q = 2\pi\int_0^R v(r)rdr$, the Poiseuille equation is achieved,

$$Q = \frac{\pi R^4}{8\eta\Delta x}\Delta P. \tag{4.41}$$

In contrast Womersley allowed both flow velocity field and pressure gradient to vary with time, though pressure is radially constant and the velocity field is unchanged with the longitudinal coordinate, which yields the following equation,

$$\frac{\partial^2\mathbf{v}}{\partial r^2} + \frac{1}{r}\frac{\partial\mathbf{v}}{\partial r} - \frac{\rho}{\eta}\frac{\partial\mathbf{v}}{\partial t} + \frac{\Delta P(t)}{\eta\Delta x} = 0. \tag{4.42}$$

Assume the time variant pressure difference has a constant and a varying term, $\Delta P(t) = \Delta P_0 + \widetilde{\Delta P}(t)$, with $\widetilde{\Delta P}(0) = 0$ and $\widetilde{\Delta P}(T) = \widetilde{\Delta P}(0)$ for some $T > 0$. Due to linearity a simple particular solution to the constant term will be the Poiseuille equation, $v_0(r) = \frac{\Delta P_0}{4\eta\Delta x}\left(R^2 - r^2\right)$. The complete solution to equation 4.42 will be given on the form,

$$\begin{aligned} v(r,t) &= \sum_{n=1}^{\infty}\left(A_n J_0\left(r\sqrt{-k_n}\right) + B_n Y_0\left(r\sqrt{-k_n}\right)\right)e^{k_n\frac{\eta}{\rho}t} \\ &\quad + \left(\int_0^t \frac{\widetilde{\Delta P}(\tau)}{\rho\Delta x}d\tau\right) + \frac{\Delta P_0}{4\eta\Delta x}\left(R^2 - r^2\right), \end{aligned} \tag{4.43}$$

where J_0 and Y_0 are Bessel functions of the first and second kinds of order zero, however the limit, $\lim_{z\to 0} Y_0(z) = -\infty$, forces $B_n = 0$ for a real solution. Furthermore the boundary condition $v(R,t) = 0$ forces $A_n = \frac{-a_n}{\rho\Delta x J_0\left(R\sqrt{-k_n}\right)}$, where a_n is a new arbitrary constant that will be determined later, so that,

$$v(r,t) = \sum_{n=1}^{\infty}\frac{-a_n}{\rho\Delta x}\frac{J_0\left(r\sqrt{-k_n}\right)}{J_0\left(R\sqrt{-k_n}\right)}e^{k_n\frac{\eta}{\rho}t} + \int_0^t\frac{\widetilde{\Delta P}(\tau)}{\rho\Delta x}d\tau + \frac{\Delta P_0}{4\eta\Delta x}\left(R^2 - r^2\right). \tag{4.44}$$

The equation is rewritten with the definition of volume flow,

$$\begin{aligned} Q(t) &= 2\pi \int_0^R \sum_{n=1}^{\infty} \frac{-a_n}{\rho \Delta x} \frac{J_0\left(r\sqrt{-k_n}\right)}{J_0\left(R\sqrt{-k_n}\right)} e^{k_n \frac{\eta}{\rho} t} r dr \\ &\quad + 2\pi \int_0^R r \int_0^t \frac{\widetilde{\Delta P}(\tau)}{\rho \Delta x} d\tau dr + 2\pi \int_0^R \frac{\Delta P_0}{4\eta \Delta x} \left(R^2 - r^2\right) r dr \\ &= \sum_{n=1}^{\infty} \frac{-a_n 2\pi R}{\rho \Delta x \sqrt{-k_n}} \frac{J_1\left(R\sqrt{-k_n}\right)}{J_0\left(R\sqrt{-k_n}\right)} e^{k_n \frac{\eta}{\rho} t} + \frac{\pi R^2}{\rho \Delta x} \int_0^t \widetilde{\Delta P}(\tau) d\tau + \frac{\pi R^4}{8\eta \Delta x} \Delta P_0. \end{aligned} \tag{4.45}$$

The obvious case suggests itself that volume flow and pressure gradient inside the blood vessels can be described with a Fourier series, which was exactly one of the questions in the research by Womersley and McDonald [Nichols and O'Rourke, 2008]. Assume that the pressure difference is a periodic function, with angular frequency, ω, described with the Fourier series,

$$\widetilde{\Delta P}(t) = \sum_{n=1}^{\infty} \Delta P_n e^{in\omega t}. \tag{4.46}$$

The no-slip boundary condition, $v(R,t) = 0$, will then enforce $a_n = \frac{\Delta P_n}{in\omega}$ and $k_n = in\omega \frac{\rho}{\eta}$. Thus the oscillating volume flow becomes

$$\begin{aligned} Q(t) &= \sum_{n=1}^{\infty} \frac{-\Delta P_n 2\pi R}{in\omega \rho \Delta x \sqrt{-in\omega \frac{\rho}{\eta}}} \frac{J_1\left(R\sqrt{-in\omega \frac{\rho}{\eta}}\right)}{J_0\left(R\sqrt{-in\omega \frac{\rho}{\eta}}\right)} e^{in\omega t} \\ &\quad + \sum_{n=1}^{\infty} \frac{\pi R^2}{in\omega \rho \Delta x} \Delta P_n e^{in\omega t} + \frac{\pi R^4}{8\eta \Delta x} \Delta P_0 \\ &= \sum_{n=1}^{\infty} \frac{\pi R^2}{\rho \Delta x} \frac{\Delta P_n}{in\omega} \left(1 - \frac{2}{R\sqrt{-in\omega \frac{\rho}{\eta}}} \frac{J_1\left(R\sqrt{-in\omega \frac{\rho}{\eta}}\right)}{J_0\left(R\sqrt{-in\omega \frac{\rho}{\eta}}\right)}\right) e^{in\omega t} + \frac{\pi R^4}{8\eta \Delta x} \Delta P_0 \\ &= \frac{\pi R^4}{\eta \Delta x} \left[\sum_{n=1}^{\infty} \frac{-\Delta P_n}{R^2 \sqrt{-in\omega \frac{\rho}{\eta}^2}} \left(1 - \frac{2}{R\sqrt{-in\omega \frac{\rho}{\eta}}} \frac{J_1\left(R\sqrt{-in\omega \frac{\rho}{\eta}}\right)}{J_0\left(R\sqrt{-in\omega \frac{\rho}{\eta}}\right)}\right) e^{in\omega t} \right. \\ &\quad \left. + \frac{\Delta P_0}{8} \right]. \end{aligned} \tag{4.47}$$

From equation 4.47 it is clear that the relation between volume flow and pressure gradient is much more complex than the Poiseuille equation, specifically the relation depends on the angular frequency. To analyze this relation Womersley defined the non-dimensional parameter popularly known as the Womersley number [Womersley, 1955b],

$$\alpha = R\sqrt{\omega\frac{\rho}{\eta}}. \tag{4.48}$$

With the Womersley number examine the oscillating part of the volume flow, that is, the constant term $Q_0 = \frac{\pi R^4}{8\eta\Delta x}\Delta P_0$ is disregarded for the moment. Specifically of interest is the function inside the brackets in equation 4.47,

$$f(\alpha, n) = 1 - \frac{2}{\alpha\sqrt{-in}}\frac{J_1\left(\alpha\sqrt{-in}\right)}{J_0\left(\alpha\sqrt{-in}\right)}, \tag{4.49}$$

$f(\alpha, n)$ is a complex function with $\mathrm{Re}f(\alpha, n) \in [0, 1]$ and $\mathrm{Im}f(\alpha, n) \geq 0$ and with $\lim_{n\to\infty} f(\alpha, n) = 1{+}0i$. Womersley recognized that the behavior of $f(\alpha, n)$ could generally be divided into three cases:

For $\alpha < 1$ and for n small $f(\alpha, n) \approx 0 + 0i$. In this case the lowest line of equation 4.47 is of interest; recognize that the function $\frac{f(\alpha,n)}{in\alpha^2} \approx \frac{1}{8} + 0i$ for small values of n and goes to zero for higher values of n. As could be expected for low values of α equation 4.47 approaches the Poiseuille equation, this let Womersley conclude that for small frequencies the oscillating flow is dominated by friction, through one period the flow will have time to establish a parabolic flow profile, which is sufficiently described with the Poiseuille equation [Womersley, 1955b].

For $\alpha > 10$ the function $f(\alpha, n) \approx 1 + 0i$ for all values of n. In this case the middle line of equation 4.47 is of interest; recognize that with $f(\alpha, n)$ basically a constant, the flow is given by a relation to the integral of the pressure difference, which by definition is the momentum of the flow, $\widetilde{p}(t)$. Therefore with high values of α the oscillating volume flow is dominated by inertia and in simple terms it can be approximated with the equation,

$$Q(t) = \frac{\pi R^2}{\rho\Delta x}\widetilde{p}(t). \tag{4.50}$$

In the intermediate regime, $1 < \alpha < 10$, the oscillating volume flow is neither completely dominated by friction or inertia, and the function $f(\alpha, n)$ has a significant imaginary part. Unfortunately for Womersley blood flow in the larger mammalian and human arteries tend to fall inside this range [Womersley, 1955a].

To give a tangible solution for the volume flow approximate $f(\alpha, n)$ with n to the first order,

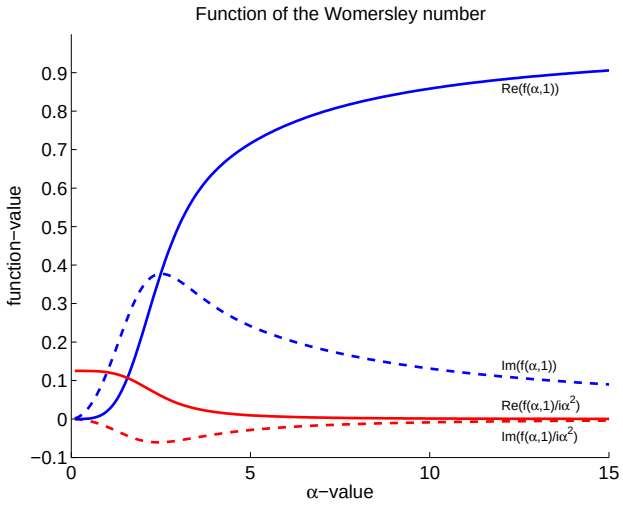

Figure 4.4: The function $f(\alpha, n) = 1 - \frac{2}{\alpha\sqrt{-in}} \frac{J_1\left(\alpha\sqrt{-in}\right)}{J_0\left(\alpha\sqrt{-in}\right)}$ for $n = 1$ as the defining function for the time variant pressure and volume flow.

$$f(\alpha, 1) = 1 - \frac{2}{\alpha\sqrt{-i}} \frac{J_1\left(\alpha\sqrt{-i}\right)}{J_0\left(\alpha\sqrt{-i}\right)}, \tag{4.51}$$

as figure 4.4 demonstrates this function is almost zero for $\alpha < 1$ and nearly constant and real for $\alpha > 10$. For higher orders of n the transition from zero to one will only be more steep. With this function define an approximate solution to the time variant volume flow given by equation 4.45 through a combination of frictional and inertial effects (still without the constant term),

$$\begin{aligned} Q(t) &\approx \frac{\pi R^2}{\rho \Delta x} \left(1 - \frac{2}{\alpha\sqrt{-i}} \frac{J_1\left(\alpha\sqrt{-i}\right)}{J_0\left(\alpha\sqrt{-i}\right)}\right) \widetilde{p}(t) \\ &\approx \frac{\pi R^4}{\eta \Delta x} \frac{1}{i\alpha^2} \left(1 - \frac{2}{\alpha\sqrt{-i}} \frac{J_1\left(\alpha\sqrt{-i}\right)}{J_0\left(\alpha\sqrt{-i}\right)}\right) \widetilde{\Delta P}(t). \end{aligned} \tag{4.52}$$

Depending on the scale of α either of the two lines of equation 4.52 may be chosen as the approximation to the time variant volume flow.

Furthermore, rearranging equation 4.52 yields the relation,

$$\frac{\eta \Delta x}{\pi R^4} \left(8 + \Psi(\alpha)\right) Q(t) = \frac{\eta}{\rho} \frac{1}{R^2} i\alpha^2 \widetilde{p}(t), \tag{4.53}$$

where

$$\Psi(\alpha) = \frac{i\alpha^2}{1 - \frac{2}{\alpha\sqrt{-i}}\frac{J_1\left(\alpha\sqrt{-i}\right)}{J_0\left(\alpha\sqrt{-i}\right)}} - 8, \tag{4.54}$$

and where $\alpha^2 = R^2\omega\frac{\rho}{\eta}$ so that the right hand side can be replaced by the time variant pressure difference. In this way equation 4.53 shows that the pressure difference is made of two terms, one Poiseuille term defined by the low frequency limit of the function $\frac{1}{i\alpha^2}f(\alpha, 1)$ and one other term defined by the function $\Psi(\alpha)$. Name the Poiseuille term $\widetilde{\Delta P}_p(t)$ and the other term $\widetilde{\Delta P}_\psi(t)$,

$$\frac{\eta\Delta x}{\pi R^4}\left(8 + \Psi(\alpha)\right)Q(t) = \widetilde{\Delta P}_p(t) + \frac{\eta}{\rho}\frac{1}{R^2}i\alpha^2\widetilde{p_\psi}(t), \tag{4.55}$$

where $\widetilde{p_\psi}(t)$ is the momentum referring to $\widetilde{\Delta P}_\psi(t)$. The Poiseuille term cancels out of the relation by use of Poiseuille's equation, which leaves the expression,

$$\begin{aligned} \frac{\eta\Delta x}{\pi R^4}\Psi(\alpha)Q(t) &= \frac{\eta}{\rho}\frac{1}{R^2}i\alpha^2\widetilde{p_\psi}(t) \\ \frac{\rho\Delta x}{\pi R^2}\psi(\alpha)Q(t) &= \widetilde{p_\psi}(t). \end{aligned} \tag{4.56}$$

The function $\psi(\alpha)$ is defined,

$$\psi(\alpha) = \frac{1}{1 - \frac{2}{\alpha\sqrt{-i}}\frac{J_1\left(\alpha\sqrt{-i}\right)}{J_0\left(\alpha\sqrt{-i}\right)}} - \frac{8}{i\alpha^2}, \tag{4.57}$$

and gives the magnitude of the extra term in equation 4.55 for any value of α. As figure 4.5 demonstrates $\psi(\alpha)$ is a complex function with real values in the range from 1 for high values of α to $4/3$ for low values of α and with imaginary values different from zero only in the transition, notably for α-values from 1 to 10.

For higher orders of n in equation 4.49 a similar result is obtained, assuming that cross-terms are negligible, for each n a function like $\psi(\alpha)$ can be defined, which will have real values in the range from 1 to $4/3$ and imaginary values different from zero only in the transition. The transition itself will only be sharper for higher values of n.

Thus it is assumed that the function $\psi(\alpha)$ for $n = 1$ is a sufficient approximation and that the complete description of the volume flow to pressure gradient can be described with a Poiseuille term of the pressure difference plus a momentum term given by the function $\psi(\alpha)$,

$$Q(t) = \frac{\pi R^4}{8\eta\Delta x}\Delta P(t) + \frac{1}{\psi(\alpha)}\frac{\pi R^2}{\rho\Delta x}\widetilde{p_\psi}(t). \tag{4.58}$$

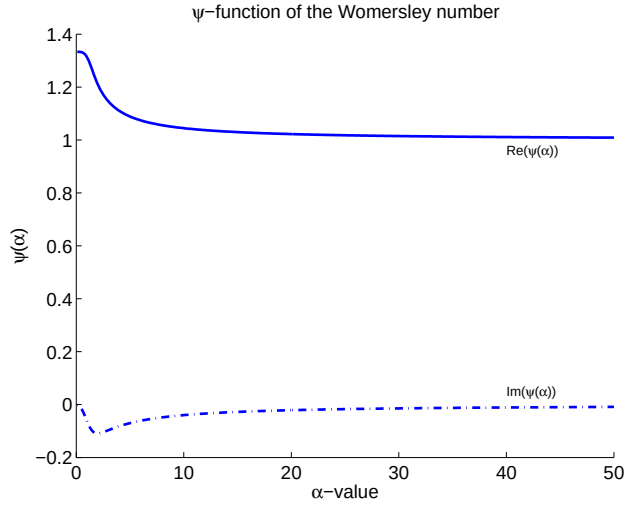

Figure 4.5: The function $\psi(\alpha) = \frac{1}{1-\frac{2}{\alpha\sqrt{-i}}\frac{J_1(\alpha\sqrt{-i})}{J_0(\alpha\sqrt{-i})}} - \frac{8}{i\alpha^2}$ as the defining function for the extra momentum contribution to the time variant pressure and volume flow.

Equation 4.58 reveals how the inertia of the liquid depends on the flow profile, which was discussed in section 3.8, and demonstrates how the inductance defined in section 4.2.2 is modified with the function $\psi(\alpha)$ defined in equation 4.57.

4.4 The use of the model

The Womersley factor concludes the last addition to the model and reveals how the factor ψ introduced in section 4.2.2 is given by at function found by the solution of the Navier-Stokes equations under the assumptions of a pulsatile flow and pressure.

With the additions of shear tensions, curvature resistance and the Womersley factor to the model the energy bond graph will be changed as shown in figure 4.6, both the capacitance and impedance of the shear tensions are visible at the top of the model, and the resistance from curvature is visible below, while the Womersley factor is not directly visible in the model as it is a factor in the calculation of the inductance, L_n.

It is apparent that this model is non-linear and that none of the elements in the model are directly constant compared to the pressure and volume flow, the dynamic radius seems to play an important role in their relations as well as the momentum of flow. Since the value of some elements depend on parameters defined as output from other elements in the energy bond graph it is not possible

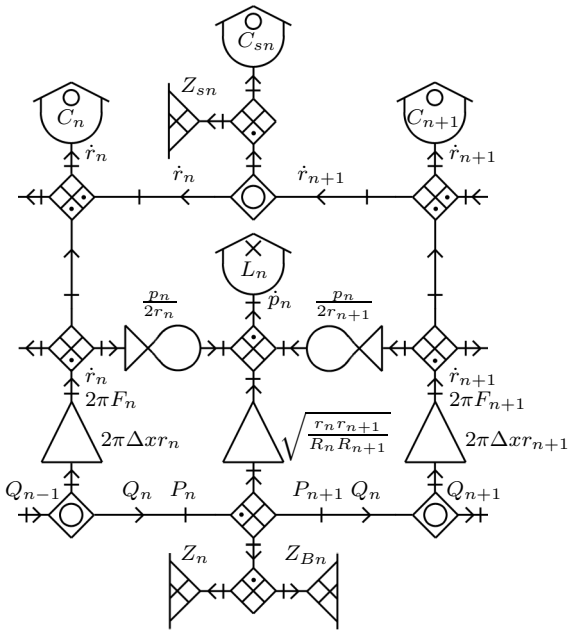

Figure 4.6: The final appearance of the energy bond graph for the cylindrical model. The standard layout of the transmission line is still an important factor in the model, but it has been changed to better describe liquid flow in an elastic tube. The capacitance and resistance, C_{sn} and Z_{sn}, are secondary effects to reduce the flexibility of the arterial wall, while the resistance Z_{Bn} is included to model the resistance induced by the curvature of the tube.

to make a simple simulation of the model of the kind normally understood from energy bond graphs or electrical networks. Instead an approximative simulation procedure must be constructed by a Runge-Kutta iteration of the variables of the model.

For this iterative solution procedure the rates of change of the radius and the momentum of the flow are used for a progressive numerical Runge-Kutta solution of their respective differential equations to find their state variables as functions of time, and from those the variables of pressure and flow are calculated.

The time-dependent values of pressure and volume flow are used as dummy variables in the calculations of the rates of change of radial change and momentum of the flow, it is useful to identify those before calculating the rates of change. In the energy bond graph in figure 4.6 the volume flow, Q_n, is given by the back-transformed output from the inductance, L_n,

$$Q_n = \frac{p_n}{L_n}\sqrt{\frac{r_n r_{n+1}}{R_n R_{n+1}}}. \tag{4.59}$$

Likewise the pressure is given by the output from the capacitance, C_n, but also from the adjacent capacitances, C_{sn}, and their related resistances, Z_{sn}. In addition the Bernoulli effect adds contributions from the adjoined inductances, L_{n-1} and L_n, through the gyration ratios, $\frac{p_{n-1}}{2r_n}$ and $\frac{p_n}{2r_n}$. All this is transformed back by the transformation ratio, $2\pi\Delta x r_n$. This corresponds to the combined potential in the first O-junction of the network,

$$\begin{aligned} P_n &= \frac{1}{2\pi\Delta x r_n}\Big(\frac{r_n - R_n}{C_n} + \frac{r_n - r_{n-1}}{C_{sn-1}} + Z_{sn-1}\left(\frac{dr_n}{dt} - \frac{dr_{n-1}}{dt}\right) \\ &\quad -\frac{r_{n+1} - r_n}{C_{sn}} - Z_{sn}\left(\frac{dr_{n+1}}{dt} - \frac{dr_n}{dt}\right) + \frac{p_{n-1}}{2r_n}\frac{p_{n-1}}{L_{n-1}} + \frac{p_n}{2r_n}\frac{p_n}{L_n}\Big). \end{aligned} \tag{4.60}$$

The rate of change for the radius of a section of the tube is the current variable in the left vertical branch of the energy bond graph in figure 4.6, which constitute the input to the capacitance, C_n. This current variable is given by the transformation, $2\pi\Delta x r_n$, of the current variable below the first transformer in the network, and this current is given as the difference between inflow and outflow to the o-junction in the network. This corresponds to the fact that the change in radius is found by the change in volume given by the difference in volume flow in relation to the surface area of the section,

$$\frac{dr_n}{dt} = \frac{Q_{n-1} - Q_n}{2\pi\Delta x r_n} = \frac{1}{2\pi\Delta x r_n}\left(\frac{p_{n-1}}{L_{n-1}}\sqrt{\frac{r_{n-1}r_n}{R_{n-1}R_n}} - \frac{p_n}{L_n}\sqrt{\frac{r_n r_{n+1}}{R_n R_{n+1}}}\right). \tag{4.61}$$

In the same way the rate of change for the momentum of the flow is the input to the inductance, L_n, this is a potential variable and thus it is found by adding all the incoming potential contributions to the X-junction in front of the inductance. The incoming potential is firstly given by the rate of change of radii of the bordering sections that is changed into a potential through the gyrators, and secondly it is given by the transformation of the pressure difference given by the difference in pressure between two neighboring sections minus the loss from the Poiseuille resistance and the resistance due to curvature. Combined, the rate of change of the momentum is calculated from the transformation of the pressure difference between the the two sections with two contributions from the Bernoulli effect,

$$
\begin{aligned}
\frac{dp_n}{dt} &= \sqrt{\frac{r_n r_{n+1}}{R_n R_{n+1}}}\left(P'_n - P'_{n+1} - \left(\frac{8\eta\Delta x}{\pi r_n^2 r_{n+1}^2} + \frac{\xi K_B f_T}{\psi(\alpha)}\frac{\sqrt{R_n R_{n+1}}}{4\pi r_n^2 r_{n+1}^2}|p_n|\right)Q_n\right) \\
&\quad + \frac{p_n}{2r_n}\frac{dr_n}{dt} + \frac{p_n}{2r_{n+1}}\frac{dr_{n+1}}{dt} \\
&= \sqrt{\frac{r_n r_{n+1}}{R_n R_{n+1}}}\left[\frac{1}{2\pi\Delta x r_n}\left(\frac{r_n - R_n}{C_n} + \frac{r_n - r_{n-1}}{C_{sn-1}} + Z_{sn-1}\left(\frac{dr_n}{dt} - \frac{dr_{n-1}}{dt}\right)\right.\right. \\
&\quad \left. - \frac{r_{n+1} - r_n}{C_{sn}} - Z_{sn}\left(\frac{dr_{n+1}}{dt} - \frac{dr_n}{dt}\right) + \frac{p_{n-1}}{2r_n}\frac{p_{n-1}}{L_{n-1}} + \frac{p_n}{2r_n}\frac{p_n}{L_n}\right) \\
&\quad - \frac{1}{2\pi\Delta x r_{n+1}}\left(\frac{r_{n+1} - R_{n+1}}{C_{n+1}} + \frac{r_{n+1} - r_n}{C_{sn}} + Z_{sn}\left(\frac{dr_{n+1}}{dt} - \frac{dr_n}{dt}\right)\right. \\
&\quad \left.\left. - \frac{r_{n+2} - r_{n+1}}{C_{sn+1}} - Z_{sn+1}\left(\frac{dr_{n+2}}{dt} - \frac{dr_{n+1}}{dt}\right) + \frac{p_n}{2r_{n+1}}\frac{p_n}{L_n} + \frac{p_{n+1}}{2r_{n+1}}\frac{p_{n+1}}{L_{n+1}}\right)\right. \\
&\quad \left. - \frac{8\eta\Delta x}{\pi r_n^2 r_{n+1}^2}\sqrt{\frac{r_n r_{n+1}}{R_n R_{n+1}}}\frac{p_n}{L_n} - \frac{\xi K_B f_T}{\psi(\alpha)}\frac{\sqrt{R_n R_{n+1}}}{4\pi r_n^2 r_{n+1}^2}|p_n|\sqrt{\frac{r_n r_{n+1}}{R_n R_{n+1}}}\frac{p_n}{L_n}\right] \\
&\quad + \frac{p_n}{2r_n}\frac{dr_n}{dt} + \frac{p_n}{2r_{n+1}}\frac{dr_{n+1}}{dt}. \qquad (4.62)
\end{aligned}
$$

The rates of change of dynamic radius and momentum of flow are the fundamental equations of the model. If N is the number of sections in the model the rates of change will constitute a system of $2N$ non-linear differential equations, iterated trough a Runge-Kutta algorithm they yield the time-variant functions of radius and momentum for all sections of the model, which subsequently can be used to find the time dependent functions of flow and pressure for all sections of the model. This will be the solution to the model.

4.5 The continuous limit

An interesting feature of the cylindric tube model worth examination is how the model behaves when the equations go to the continuous limit by letting Δx approach zero. In other words, will the equations of the model approach the continuous equations for liquid transport when the model goes from a finite element model to a continuous model. This section is devoted to this question.

Consider the rates of change for a section of the tube, insert the expressions for L_n, C_n, C_{sn} and Z_{sn} to have the equations described with only radius, momentum and material constants,

$$\frac{dr_n}{dt} = \frac{1}{2\pi\Delta x r_n}\left(\frac{\pi R_{n-1}R_n p_{n-1}}{\psi(\alpha)\rho\Delta x}\sqrt{\frac{r_{n-1}r_n}{R_{n-1}R_n}} - \frac{\pi R_n R_{n+1}p_n}{\psi(\alpha)\rho\Delta x}\sqrt{\frac{r_n r_{n+1}}{R_n R_{n+1}}}\right), \tag{4.63}$$

$$\begin{aligned}
\frac{dp_n}{dt} &= \sqrt{\frac{r_n r_{n+1}}{R_n R_{n+1}}}\Bigg[\frac{1}{2\pi\Delta x r_n}\Bigg(2\pi\Delta x Eh\frac{r_n - R_n}{R_n} \\
&+2\pi Gh\sqrt{R_n R_{n-1}}\frac{(r_n - R_n) - (r_{n-1} - R_{n-1})}{\Delta x} \\
&+\frac{0.01\cdot 2\pi Gh\sqrt{R_n R_{n-1}}}{\Delta x}\left(\frac{dr_n}{dt} - \frac{dr_{n-1}}{dt}\right) \\
&-2\pi Gh\sqrt{R_n R_{n+1}}\frac{(r_{n+1} - R_{n+1}) - (r_n - R_n)}{\Delta x} \\
&-\frac{0.01\cdot 2\pi Gh\sqrt{R_n R_{n01}}}{\Delta x}\left(\frac{dr_{n+1}}{dt} - \frac{dr_n}{dt}\right) \\
&+\frac{\pi R_n R_{n-1}p_{n-1}^2}{2r_n\psi(\alpha)\rho\Delta x} + \frac{\pi R_n R_{n+1}p_n^2}{2r_n\psi(\alpha)\rho\Delta x}\Bigg) \\
&-\frac{1}{2\pi\Delta x r_{n+1}}\Bigg(2\pi\Delta x Eh\frac{r_{n+1} - R_{n+1}}{R_{n+1}} \\
&+2\pi Gh\sqrt{R_n R_{n+1}}\frac{(r_{n+1} - R_{n+1}) - (r_n - R_n)}{\Delta x} \\
&+\frac{0.01\cdot 2\pi Gh\sqrt{R_n R_{n+1}}}{\Delta x}\left(\frac{dr_{n+1}}{dt} - \frac{dr_n}{dt}\right) \\
&-2\pi Gh\sqrt{R_{n+1} R_{n+1}}\frac{(r_{n+2} - R_{n+1}) - (r_{n+1} - R_{n+1})}{\Delta x} \\
&-\frac{0.01\cdot 2\pi Gh\sqrt{R_{n+1} R_{n+2}}}{\Delta x}\left(\frac{dr_{n+2}}{dt} - \frac{dr_{n+1}}{dt}\right) \\
&+\frac{\pi R_n R_{n+1}p_n^2}{2r_{n+1}\psi(\alpha)\rho\Delta x} + \frac{\pi R_{n+1}R_{n+2}p_{n+1}^2}{2r_{n+1}\psi(\alpha)\rho\Delta x}\Bigg) \\
&-\frac{8\eta\Delta x}{\pi r_n^2 r_{n+1}^2}\frac{\pi R_n R_{n+1}p_n}{\psi(\alpha)\rho\Delta x}\sqrt{\frac{r_n r_{n+1}}{R_n R_{n+1}}} \\
&-\frac{\xi K_B f_T}{\psi(\alpha)^2\rho\Delta x}\frac{\sqrt{R_n R_{n+1}}}{4\pi r_n^2 r_{n+1}^2}\sqrt{\frac{r_n r_{n+1}}{R_n R_{n+1}}}\pi R_n R_{n+1}p_n^2\Bigg] \\
&+\frac{p_n}{2r_n}\frac{dr_n}{dt} + \frac{p_n}{2r_{n+1}}\frac{dr_{n+1}}{dt},
\end{aligned} \tag{4.64}$$

but notice that p_n is also dependent on Δx with the relation

$$p_n = \sqrt{\frac{r_n r_{n+1}}{R_n R_{n+1}}}\psi(\alpha)\rho\Delta x v_n. \tag{4.65}$$

To find the continuous limit for the equations use the variables r_n and v_n, which will be defined as functions of space and time, $r(x,t)$ and $v(x,t)$. Let the arterial section n be described by the position x_0, thus the equation for the rate of change of $r(x_0,t)$ becomes

$$\begin{aligned}
\frac{\partial r(x_0,t)}{\partial t} &= \frac{1}{2\pi\Delta x r(x_0,t)}\Bigg(\frac{\pi R(x_0-\Delta x)R(x_0)}{\psi(\alpha)\rho\Delta x}\sqrt{\frac{r(x_0-\Delta x,t)r(x_0,t)}{R(x_0-\Delta x)R(x_0)}} \\
&\quad \cdot\sqrt{\frac{r(x_0-\Delta x,t)r(x_0,t)}{R(x_0-\Delta x)R(x_0)}}\psi(\alpha)\rho\Delta x v(x_0-\Delta x,t) \\
&\quad -\frac{\pi R(x_0)R(x_0+\Delta x)}{\psi(\alpha)\rho\Delta x}\sqrt{\frac{r(x_0,t)r(x_0+\Delta x,t)}{R(x_0)R(x_0+\Delta x)}} \\
&\quad \cdot\sqrt{\frac{r(x_0,t)r(x_0+\Delta x,t)}{R(x_0)R(x_0+\Delta x)}}\psi(\alpha)\rho\Delta x v(x_0,t)\Bigg) \\
&= \frac{1}{2\Delta x}\left(r(x_0-\Delta x,t)v(x_0-\Delta x,t) - r(x_0+\Delta x,t)v(x_0,t)\right) \\
&= \frac{1}{2\Delta x}\Bigg(r(x_0-\Delta x,t)v(x_0-\Delta x,t) \\
&\quad -r(x_0+\Delta x,t)\left(v(x_0+\Delta x,t) - \Delta x\frac{\partial v(x_0,t)}{\partial x}\right)\Bigg),
\end{aligned} \tag{4.66}$$

where the last step in the equation comes from a first-order Taylor expansion of $v(x_0,t)$. Next, let Δx approach zero

$$\begin{aligned}
\frac{\partial r(x_0,t)}{\partial t} &= -\frac{1}{2}\lim_{\Delta x\to 0}\frac{r(x_0,t)v(x_0,t) - r(x_0-\Delta x,t)v(x_0-\Delta x,t)}{\Delta x} \\
&\quad -\frac{1}{2}\lim_{\Delta x\to 0}\frac{r(x_0+\Delta x,t)v(x_0+\Delta x,t) - r(x_0,t)v(x_0,t)}{\Delta x} \\
&\quad +\frac{1}{2}r(x_0,t)\frac{\partial v(x_0,t)}{\partial x} \\
&= -\frac{\partial}{\partial x}\left(r(x_0,t)v(x_0,t)\right) + \frac{1}{2}r(x_0,t)\frac{\partial v(x_0,t)}{\partial x} \\
&= -v(x_0,t)\frac{\partial r(x_0,t)}{\partial x} - \frac{1}{2}r(x_0,t)\frac{\partial v(x_0,t)}{\partial x}.
\end{aligned} \tag{4.67}$$

Though it may be hard to see, this corresponds exactly to a one-dimensional continuity equation for volume in the tube, $\frac{\partial V}{\partial t} = -\frac{\partial}{\partial x}(V \cdot v)$. The volume can be written as $V = \pi r^2 s$, where s is an infinitesimal length of the tube, put this volume directly into the continuity equation and observe that the result will be equation 4.67,

$$\begin{aligned}
\frac{\partial}{\partial t}\left(\pi s r^2(x,t)\right) &= -\frac{\partial}{\partial x}\left(\pi s r^2(x,t) v(x,t)\right) \qquad \Rightarrow \\
2r(x,t)\frac{\partial r}{\partial t} &= -2r(x,t)v(x,t)\frac{\partial r}{\partial x} - r^2(x,t)\frac{\partial v}{\partial x} \qquad \Rightarrow \\
\frac{\partial r}{\partial t} &= -v(x,t)\frac{\partial r}{\partial x} - \frac{1}{2}r(x,t)\frac{\partial v}{\partial x}. \qquad (4.68)
\end{aligned}$$

For the rate of change of the momentum something similar can be done, though it will not be pretty. Start with equation 4.64 and insert the definition of the momentum of flow with respect to the mean velocity (equation 4.65),

$$\begin{aligned}
&\frac{\psi(\alpha)\rho\Delta x}{\sqrt{R_n R_{n+1}}}\frac{d}{dt}\left(\sqrt{r_n r_{n+1}} v_n\right) = \\
&\sqrt{\frac{r_n r_{n+1}}{R_n R_{n+1}}}\Bigg[\frac{1}{2\pi\Delta x r_n}\Bigg(2\pi\Delta x E h\frac{r_n - R_n}{R_n} \\
&+2\pi G h\sqrt{R_n R_{n-1}}\frac{(r_n - R_n) - (r_{n-1} - R_{n-1})}{\Delta x} \\
&+\frac{0.01\cdot 2\pi G h\sqrt{R_n R_{n-1}}}{\Delta x}\left(\frac{dr_n}{dt} - \frac{dr_{n-1}}{dt}\right) \\
&-2\pi G h\sqrt{R_n R_{n+1}}\frac{(r_{n+1} - R_{n+1}) - (r_n - R_n)}{\Delta x} \\
&-\frac{0.01\cdot 2\pi G h\sqrt{R_n R_{n+1}}}{\Delta x}\left(\frac{dr_{n+1}}{dt} - \frac{dr_n}{dt}\right) \\
&+\frac{\pi r_n r_{n-1}\left(\psi(\alpha)\rho\Delta x\right)^2 v_{n-1}^2}{2r_n\psi(\alpha)\rho\Delta x} + \frac{\pi r_n r_{n+1}\left(\psi(\alpha)\rho\Delta x\right)^2 v_n^2}{2r_n\psi(\alpha)\rho\Delta x}\Bigg) \\
&-\frac{1}{2\pi\Delta x r_{n+1}}\Bigg(2\pi\Delta x E h\frac{r_{n+1} - R_{n+1}}{R_{n+1}} \\
&+2\pi G h\sqrt{R_n R_{n+1}}\frac{(r_{n+1} - R_{n+1}) - (r_n - R_n)}{\Delta x} \\
&+\frac{0.01\cdot 2\pi G h\sqrt{R_n R_{n+1}}}{\Delta x}\left(\frac{dr_{n+1}}{dt} - \frac{dr_n}{dt}\right) \\
&-2\pi G h\sqrt{R_{n+1} R_{n+2}}\frac{(r_{n+2} - R_{n+2}) - (r_{n+1} - R_{n+1})}{\Delta x}
\end{aligned}$$

$$
\begin{aligned}
&-\frac{0.01\cdot 2\pi Gh\sqrt{R_{n+1}R_{n+2}}}{\Delta x}\left(\frac{dr_{n+2}}{dt}-\frac{dr_{n+1}}{dt}\right)\\
&+\frac{\pi r_n r_{n+1}\left(\psi(\alpha)\rho\Delta x\right)^2 v_n^2}{2r_{n+1}\psi(\alpha)\rho\Delta x}+\frac{\pi r_{n+1}r_{n+2}\left(\psi(\alpha)\rho\Delta x\right)^2 v_{n+1}^2}{2r_{n+1}\psi(\alpha)\rho\Delta x}\Big)\\
&-\frac{8\eta\Delta x}{\pi r_n^2 r_{n+1}^2}\frac{\pi\sqrt{R_nR_{n+1}}\sqrt{r_nr_{n+1}}\psi(\alpha)\rho\Delta x v_n}{\psi(\alpha)\rho\Delta x}\sqrt{\frac{r_nr_{n+1}}{R_nR_{n+1}}}\\
&-\frac{\rho\Delta x\xi K_B f_T}{4}\frac{1}{\sqrt{r_nr_{n+1}}}v_n^2\Big]\\
&+\sqrt{\frac{r_nr_{n+1}}{R_nR_{n+1}}}\frac{\psi(\alpha)\rho\Delta x v_n}{2r_n}\frac{dr_n}{dt}+\sqrt{\frac{r_nr_{n+1}}{R_nR_{n+1}}}\frac{\psi(\alpha)\rho\Delta x v_n}{2r_{n+1}}\frac{dr_{n+1}}{dt}.
\end{aligned}
\tag{4.69}
$$

Rearrange the expression and define the radius and mean velocity as functions of position and time, $r(x,t)$ and $v(x,t)$, with x_0 once again being the position of the n'th section of the tube,

$$
\begin{aligned}
\frac{\partial}{\partial t}\left(\sqrt{r(x_0,t)r(x_0+\Delta x,t)}v(x_0,t)\right) &= \sqrt{r(x_0,t)r(x_0+\Delta x,t)}\Big[\\
&\frac{-Eh}{\psi(\alpha)\rho\Delta x}\left(\frac{r(x_0+\Delta x,t)-R(x_0+\Delta x)}{r(x_0+\Delta x,t)R(x_0+\Delta x)}-\frac{r(x_0,t)-R(x_0)}{r(x_0,t)R(x_0)}\right)\\
&+\frac{Gh}{\psi(\alpha)\rho}\Big[\frac{\sqrt{R(x_0)R(x_0-\Delta x)}}{\Delta x r(x_0,t)}\\
&\qquad\cdot\frac{(r(x_0,t)-R(x_0))-(r(x_0-\Delta x,t)-R(x_0-\Delta x))}{\Delta x^2}\\
&\quad-\frac{\sqrt{R(x_0)R(x_0+\Delta x)}}{\Delta x r(x_0+\Delta x,t)}\\
&\qquad\cdot\frac{(r(x_0+\Delta x,t)-R(x_0+\Delta x))-(r(x_0,t)-R(x_0))}{\Delta x^2}\\
&\quad-\frac{\sqrt{R(x_0)R(x_0+\Delta x)}}{\Delta x r(x_0,t)}\\
&\qquad\cdot\frac{(r(x_0+\Delta x,t)-R(x_0+\Delta x))-(r(x_0,t)-R(x_0))}{\Delta x^2}\\
&\quad+\frac{\sqrt{R(x_0+\Delta x)R(x_0+2\Delta x)}}{\Delta x r(x_0+\Delta x,t)}\frac{1}{\Delta x^2}\Big(r(x_0+2\Delta x,t)\\
&\qquad -R(x_0+2\Delta x)-r(x_0+\Delta x,t)+R(x_0+\Delta x)\Big)\Big]
\end{aligned}
$$

$$
\begin{aligned}
&+\frac{0.01Gh}{\psi(\alpha)\rho}\Bigg[\frac{\sqrt{R(x_0)R(x_0-\Delta x)}}{\Delta x^3 r(x_0,t)}\left(\frac{\partial r(x_0,t)}{\partial t}-\frac{\partial r(x_0-\Delta x,t)}{\partial t}\right)\\
&\quad-\frac{\sqrt{R(x_0)R(x_0+\Delta x)}}{\Delta x^3 r(x_0+\Delta x,t)}\left(\frac{\partial r(x_0+\Delta x,t)}{\partial t}-\frac{\partial r(x_0,t)}{\partial t}\right)\\
&\quad-\frac{\sqrt{R(x_0)R(x_0+\Delta x)}}{\Delta x^3 r(x_0,t)}\left(\frac{\partial r(x_0+\Delta x,t)}{\partial t}-\frac{\partial r(x_0,t)}{\partial t}\right)\\
&\quad+\frac{\sqrt{R(x_0+\Delta x)R(x_0+2\Delta x)}}{\Delta x^3 r(x_0+\Delta x,t)}\\
&\qquad\cdot\left(\frac{\partial r(x_0+2\Delta x,t)}{\partial t}-\frac{\partial r(x_0+\Delta x,t)}{\partial t}\right)\Bigg]\\
&+\frac{r(x_0-\Delta x,t)v^2(x_0-\Delta x,t)}{4\Delta x r(x_0,t)}+\frac{r(x_0+\Delta x,t)v^2(x_0,t)}{4\Delta x r(x_0,t)}\\
&-\frac{r(x_0,t)v^2(x_0,t)}{4\Delta x r(x_0+\Delta x,t)}-\frac{r(x_0+2\Delta x,t)v^2(x_0+\Delta x,t)}{4\Delta x r(x_0+\Delta x,t)}\\
&-\frac{8\eta}{\psi(\alpha)\rho}\frac{v(x_0,t)}{r(x_0,t)r(x_0+\Delta x,t)}\\
&-\frac{\xi K_B f_T}{4\psi(\alpha)}\frac{1}{\sqrt{r(x_0,t)r(x_0+\Delta x,t)}}v^2(x_0,t)\Bigg]\\
&+\sqrt{r(x_0,t)r(x_0+\Delta x,t)}\frac{v(x_0,t)}{2r(x_0,t)}\frac{\partial r(x_0,t)}{\partial t}\\
&+\sqrt{r(x_0,t)r(x_0+\Delta x,t)}\frac{v(x_0,t)}{2r(x_0+\Delta x,t)}\frac{\partial r(x_0+\Delta x,t)}{\partial t}. \qquad (4.70)
\end{aligned}
$$

Let Δx go to zero,

$$
\begin{aligned}
\frac{\partial}{\partial t}\left(r(x_0,t)v(x_0,t)\right) &= -\frac{Eh}{\psi(\alpha)\rho}r(x_0,t)\frac{\partial}{\partial x}\left(\frac{r(x_0,t)-R(x_0)}{r(x_0,t)R(x_0)}\right)\\
&\quad+\frac{Gh}{\psi(\alpha)\rho}r(x_0,t)\frac{\partial}{\partial x}\left(\frac{R(x_0)}{r(x_0,t)}\right)\frac{\partial^2}{\partial x^2}\left(r(x_0,t)-R(x_0)\right)\\
&\quad+\frac{0.01Gh}{\psi(\alpha)\rho}r(x_0,t)\frac{\partial}{\partial x}\left(\frac{R(x_0)}{r(x_0,t)}\right)\frac{\partial^2}{\partial x^2}\left(\frac{\partial r(x_0,t)}{\partial t}\right)\\
&\quad-\frac{1}{2}\frac{\partial}{\partial x}\left(r(x_0,t)v^2(x_0,t)\right)-\frac{8\eta}{\psi(\alpha)\rho}\frac{v(x_0,t)}{r(x_0,t)}\\
&\quad-\frac{\xi K_B f_T}{4\psi(\alpha)}v^2(x_0,t)+v(x_0,t)\frac{\partial r(x_0,t)}{\partial t}. \qquad (4.71)
\end{aligned}
$$

This expression can be rewritten to,

$$\begin{aligned}\frac{\partial v(x_0,t)}{\partial t} &= -\frac{Eh}{\psi(\alpha)\rho}\left(\frac{1}{r^2(x_0,t)}\frac{\partial r(x_0,t)}{\partial x}-\frac{1}{R^2(x_0)}\frac{dR(x_0)}{dx}\right)\\ &+\frac{Gh}{\psi(\alpha)\rho}\frac{\partial}{\partial x}\left(\frac{R(x_0)}{r(x_0,t)}\right)\frac{\partial^2}{\partial x^2}\left(r(x_0,t)-R(x_0)\right)\\ &+\frac{0.01Gh}{\psi(\alpha)\rho}\frac{\partial}{\partial x}\left(\frac{R(x_0)}{r(x_0,t)}\right)\frac{\partial^2}{\partial x^2}\left(\frac{\partial r(x_0,t)}{\partial t}\right)\\ &-\frac{1}{2}\frac{v^2(x_0,t)}{r(x_0,t)}\frac{\partial r(x_0,t)}{\partial x}-v(x_0,t)\frac{\partial v(x_0,t)}{\partial x}\\ &-\frac{8\eta}{\psi(\alpha)\rho}\frac{v(x_0,t)}{r^2(x_0,t)}-\frac{\xi K_B f_T}{4\psi(\alpha)}\frac{v^2(x_0,t)}{r(x_0,t)}.\end{aligned} \tag{4.72}$$

The pressure, P_n, can be rewritten in a similar way, expressed as a function, $P(x,t)$, of x and t, where the point x_0 corresponds to the center of section n,

$$\begin{aligned}P(x_0,t) &= Eh\frac{r(x_0,t)-R(x_0)}{R(x_0)}+\frac{Gh\sqrt{R(x_0)R(x_0-\Delta x)}}{\Delta x r(x_0,t)}\\ &\cdot\frac{(r(x_0,t)-R(x_0))-(r(x_0-\Delta x,t)-R(x_0-\Delta x))}{\Delta x}\\ &+\frac{0.01Gh\sqrt{R(x_0)R(x_0-\Delta x)}}{\Delta x^2 r(x_0,t)}\left(\frac{\partial r(x_0,t)}{\partial t}-\frac{\partial r(x_0-\Delta x,t)}{\partial t}\right)\\ &-\frac{Gh\sqrt{R(x_0)R(x_0+\Delta x)}}{\Delta x r(x_0,t)}\\ &\cdot\frac{(r(x_0+\Delta x,t)-R(x_0+\Delta x))-(r(x_0,t)-R(x_0))}{\Delta x}\\ &-\frac{0.01Gh\sqrt{R(x_0)R(x_0+\Delta x)}}{\Delta x^2 r(x_0,t)}\left(\frac{\partial r(x_0+\Delta x,t)}{\partial t}-\frac{\partial r(x_0,t)}{\partial t}\right)\\ &+\frac{\psi(\alpha)\rho r(x_0-\Delta x,t)v^2(x_0-\Delta x,t)}{4r(x_0,t)}\\ &+\frac{\psi(\alpha)\rho r(x_0+\Delta x,t)v^2(x_0,t)}{4r(x_0,t)},\end{aligned} \tag{4.73}$$

which makes it interesting to calculate the pressure difference for a single section,

$$
\begin{aligned}
&\frac{P(x_0+\Delta x,t)-P(x_0,t)}{\Delta x} \quad = \\
&\quad \frac{Eh}{\Delta x}\left(\frac{r(x_0+\Delta x,t)-R(x_0+\Delta x)}{r(x_0+\Delta x,t)R(x_0+\Delta x)}-\frac{r(x_0,t)-R(x_0)}{r(x_0,t)R(x_0)}\right) \\
&\quad +\frac{Gh\sqrt{R(x_0)R(x_0+\Delta x)}}{\Delta x^2 r(x_0,t)} \\
&\qquad \cdot\frac{(r(x_0+\Delta x,t)-R(x_0+\Delta x))-(r(x_0,t)-R(x_0))}{\Delta x} \\
&\quad -\frac{Gh\sqrt{R(x_0+\Delta x)R(x_0+2\Delta x)}}{\Delta x^2 r(x_0+\Delta x,t)}\frac{1}{\Delta x}\Big(r(x_0+2\Delta x,t) \\
&\qquad -R(x_0+2\Delta x)-r(x_0+\Delta x,t)+R(x_0+\Delta x)\Big) \\
&\quad -\frac{Gh\sqrt{R(x_0-\Delta x)R(x_0)}}{\Delta x^2 r(x_0,t)} \\
&\qquad \cdot\frac{(r(x_0,t)-R(x_0))-(r(x_0-\Delta x,t)-R(x_0-\Delta x))}{\Delta x} \\
&\quad +\frac{Gh\sqrt{R(x_0)R(x_0+\Delta x)}}{\Delta x^2 r(x_0,t)} \\
&\qquad \cdot\frac{(r(x_0+\Delta x,t)-R(x_0+\Delta x))-(r(x_0,t)-R(x_0))}{\Delta x} \\
&\quad +\frac{0.01Gh\sqrt{R(x_0)R(x_0+\Delta x)}}{\Delta x^3 r(x_0+\Delta x,t)}\left(\frac{\partial r(x_0+\Delta x,t)}{\partial t}-\frac{\partial r(x_0,t)}{\partial t}\right) \\
&\quad -\frac{0.01Gh\sqrt{R(x_0+\Delta x)R(x_0+2\Delta x)}}{\Delta x^3 r(x_0+\Delta x,t)} \\
&\qquad \cdot\left(\frac{\partial r(x_0+2\Delta x,t)}{\partial t}-\frac{\partial r(x_0+\Delta x,t)}{\partial t}\right) \\
&\quad -\frac{0.01Gh\sqrt{R(x_0)R(x_0-\Delta x)}}{\Delta x^3 r(x_0,t)}\left(\frac{\partial r(x_0,t)}{\partial t}-\frac{\partial r(x_0-\Delta x,t)}{\partial t}\right) \\
&\quad +\frac{0.01Gh\sqrt{R(x_0)R(x_0+\Delta x)}}{\Delta x^3 r(x_0,t)}\left(\frac{\partial r(x_0+\Delta x,t)}{\partial t}-\frac{\partial r(x_0,t)}{\partial t}\right) \\
&\quad +\frac{\psi(\alpha)\rho r(x_0,t)v^2(x_0,t)}{\Delta x 4r(x_0+\Delta x,t)}-\frac{\psi(\alpha)\rho r(x_0-\Delta x,t)v^2(x_0,t)}{\Delta x 4r(x_0,t)} \\
&\quad +\frac{\psi(\alpha)\rho r(x_0+2\Delta x,t)v^2(x_0+\Delta x,t)}{\Delta x 4r(x_0+\Delta x,t)}-\frac{\psi(\alpha)\rho r(x_0+\Delta x,t)v^2(x_0,t)}{\Delta x 4r(x_0,t)},
\end{aligned}
$$

(4.74)

which for Δx going to zero becomes,

$$\begin{aligned}\frac{\partial P(x_0,t)}{\partial x} &= Eh\left(\frac{1}{r^2(x_0,t)}\frac{\partial r(x_0,t)}{\partial x}-\frac{1}{R^2(x_0)}\frac{dR(x_0)}{dx}\right)\\ &\quad -Gh\frac{\partial}{\partial x}\left(\frac{R(x_0)}{r(x_0,t)}\right)\frac{\partial^2}{\partial x^2}\left(r(x_0,t)-R(x_0)\right)\\ &\quad -0.01Gh\frac{\partial}{\partial x}\left(\frac{R(x_0)}{r(x_0,t)}\right)\frac{\partial^2}{\partial x^2}\left(\frac{\partial r(x_0,t)}{\partial t}\right)\\ &\quad +\frac{\psi(\alpha)\rho}{2r(x_0,t)}\frac{\partial}{\partial x}\left(r(x_0,t)v^2(x_0,t)\right). \qquad (4.75)\end{aligned}$$

Thus when equation 4.72 and equation 4.75 are compared it is seen that

$$\psi(\alpha)\rho\frac{\partial v(x_0,t)}{\partial t}=-\frac{\partial P(x_0,t)}{\partial x}-8\eta\frac{v(x_0,t)}{r^2(x_0,t)}-\frac{\xi K_B f_T\rho}{4}\frac{v^2(x_0,t)}{r(x_0,t)}. \qquad (4.76)$$

Equation 4.76 is a special version of Navier-Stokes equations (equation 3.2) known as the Euler equation, with the addition of the Womersley inertia correction factor, $\psi(\alpha)$, and two frictional terms coming from Poiseuille resistance and resistance due to curvature. The Euler equation explicitly express the momentum conservation of liquid flow, and it is seen from equation 4.76 that the momentum defined as $\psi(\alpha)\rho v(x,t)$ is influenced by three factors: the pressure gradient, the Poiseuille resistance and the resistance from curvature of the tube. All in all, it is clear that the model in the continuous limit yields a set of equations that are well-known descriptions of liquid flow.

Chapter 5

Case: Liebau's Ring

For the case of the embryonic chick heart the measurement data and the overall research practice are of a very visual character, the doctors and researchers are interested in images and films that illustrate the qualitative behavior of the heart and combined with their knowledge of medicine and physiology hold a lot of information to them. This provides the models in this thesis with nice images for a qualitative comparison but it does however leave them without any empirical measurement data for a necessary quantitative validation.

Therefore a quantitative validation of the models is sought for externally to the case of the embryonic chick heart. The choice has fallen on a classical case of valveless flow phenomena: Liebau's ring. The name is not universal, in the reports it is called many things from closed loop and closed elastic tube-system to simply a valveless pumping system, however as an exemplar demonstrating a physical principle of valveless pumping it deserves a name of its own.

It is an elegantly simple case where two rubber tubes of different elastic materials are joined together end-to-end to form a torus filled with liquid, see figure 5.1. Induced with a periodic pinching at a single point on one of the tubes a mean flow is formed through the ring.

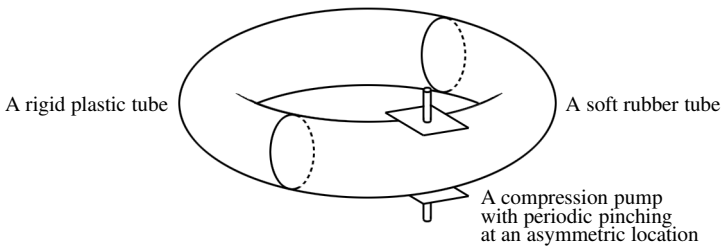

Figure 5.1: An illustration of the fundamental setup of Liebau's ring.

5.1 The story of Liebau's ring

Liebau's ring is named after the German doctor Gerhart Liebau who in the 1950'ies demonstrated a series of valveless flow phenomena that had never been seen before his time [Männer et al., 2010].

Valveless flow refers to specially constructed situations where flow is induced in an elastic tube via external changes to the conditions of the tube, without internal valves in the tube to guide the flow, for instance through a compression of the tube radius. It is expected that valveless flow can provide some explanation to the flow in the veins, and to optimization of current CPR methods [Hoeben, 2009], and also biologists have found invertebrate and vertebrate with valveless circulatory systems [Larsen et al., 2006], and then of course there is the embryonic heart.

Until the 1950'ies valveless flow was primarily associated with a peristaltic pumping mechanism, such as a sliding or sequential compression of a tube along the direction of the desired flow. Though in the 19th century Franciscus Donders proposed the possibility of the respiratory system acting as an at that time undiscovered pumping mechanism to aid venous return in the circulatory system [Noordergraaf et al., 2006]. The resulting discussion between Donders and others remained inconclusive, but in 1954 inspired by this idea Gerhart Liebau proposed a pumping mechanism; a periodic squeezing of the tube at a singular point, which on average would induce a directional flow Liebau [1954].

Liebau proposed that such a valveless pumping mechanism could account for some of the energetic mismatch between heart pump pressure and peripherally measured blood pressure. To demonstrate the effects of the pumping mechanism Liebau [1954] proposed an experiment with two tanks connected by an elastic rubber tube, one tank was positioned higher than the other, but by pressing on the rubber tube with a certain frequency it would be possible to pump liquid from the lower tank to the higher.

A year later in 1955 Gerhart Liebau constructed a series of other cases where a single periodic pinching on the outside of the tube would create a mean flow, among those examples were Liebau's ring [Manopoulos et al., 2006]. The ring is ideally constructed of two pieces of tube with equal length and radius but with different rigidity, the tubes are glued together end-to-end to form a ring, actually a torus, with the inside filled with liquid. When the ring is held horizontally and a harmonic oscillating external compression of the tube is applied to an asymmetric point on the ring (ie. not midways on the tubes) a mean flow will form round in the ring. Among other things this mean flow depends on the frequency of the pressure oscillations and at certain critical frequencies the flow will change direction.

This sort of periodic compression pumping has later been known as the Liebau effect or more generally impedance induced pumping since the general idea behind the mechanism is that the periodic compressions create waves of pressure and liquid displacement that interact with the impedance of the tube, if the compression pump is positioned at a point with a difference in impedance from left to right a mean flow will follow from the complicated interaction between the periodic compressions and the impedance mismatch.

Liebau proposed his models as suggestions to the functionality of the cardiovascular system and the discussion raised by Donders, but it was mathematicians and engineers that caught the interest in the phenomenon of impedance induced pumping. Thus the Liebau effect has had little or no influence on physiological research [Männer et al., 2010]. For a full historical review of the mathematical research in Liebau's ring refer to Manopoulos et al. [2006].

5.2 Setup of a model of Liebau's ring

Besides the quantitative validation of the model another reason to include the simulation of Liebau's ring into this thesis is that it will function as a fast way to demonstrate the necessary steps needed to adapt the model to a specific simulation case: boundary conditions, parameter estimation, a tracing of the tube, and a pumping mechanism.

Boundary conditions refer to what happens at the ends of the tube. The endpoints are very defining for the impedance of the tube, such that it is generally stated that the tube ends should have a impedance mismatch to produce a Liebau flow in the tube [Männer et al., 2010]. Though in reality it is the impedance of the tube together with the impedance at the tube ends that should have a mismatch, which becomes very clear in the case of Liebau's ring where the boundary condition of one tube is simply just another tube of the same length, the two tubes are joined end to end to form a ring. The boundary condition is cyclic.

A parameter estimation is necessary to obtain values for parameters of the model. Not that many parameters are needed for the model to function - primarily three parameters: density, ρ, and viscosity, η, of the liquid and Young's modulus, E, for the softness of the tube wall. Secondarily some extra parameters are nice to have: the outside pressure, P_0, sets a baseline for the pressure plots, the typical period of a cardiac cycle, T, gives an indication of the relevant frequencies, and the thickness of the tube wall, h, can in many ways be thought of as a model parameter also. Thirdly the boundary conditions and pumping mechanism will typically have parameters of their own.

In the case of Liebau's ring the parameters used for the simulation are found in [Snitker et al., 2000] and [Ottesen, 2003], which contain measurement data from an experiment with a ring consisting of one latex and one PVC tube filled with water ($\rho = 10^3$ kg/m^3, $\eta = 10^{-3}$ Pa·s). Ideally the only difference between the two tubes should be their softness, though that is not a necessary condition, and in the physical experiment the PVC tube is both smaller and thicker: The latex tube has thickness $h_\alpha = 0.001$ m and Young's modulus $E_\alpha = 4.1 \cdot 10^5$ N/m^2 while the PVC tube has thickness $h_\beta = 0.003$ m and Young's modulus $E_\beta = 4.3 \cdot 10^5$ N/m^2.

The tracing of the tube is necessary to find the resting radius at all points in the tube, the length of the tube, and the curvature of the tube. The tracing is also used to determine a suitable division into sections for the model, in the case of Liebau's ring this only refers to a suitable number of identical sections, but for the more complicated heart models the sections need not be identical.

Let the model of Liebau's ring be described with $N = 60$ sections. The first $N/2$ sections will be that of the latex tube described with thickness h_α and Young's modulus E_α and the last $N/2$ sections will be that of the PVC tube with thickness h_β and Young's modulus E_β. Young's modulus and the thickness are factors in the expressions for C_n, C_{sn} and Z_{sn}.

Furthermore let the first $N/2$ sections be described with a radius of $R_n = 0.01$ m and the next $N/2$ sections with a radius of $R_n = 0.008$ m as the PVC tube is slightly thinner than the latex tube. The cyclic boundary conditions transform section 0 to section N and section $N + 1$ to section 1. Each tube have an exact length of 0.5 m combining to form a ring with a circumference, $l = 1.0$ m. The radius of curvature will be universal for all sections, $R_B = \frac{l}{2\pi}$, and likewise for the bend angle, $\theta = \frac{360^\circ}{N}$.

Finally the pumping mechanism is important to complete the model setup. The equations of the model will be described by the equations in section 4.4 of chapter 4, except for the sections where the pumping mechanism affects the tube. According to Ottesen [2003] the compression pump is described with a reduction of the cross-sectional area, $A(t, x)$, in both time and space. The duration of the compression is 10% of the period while $A(t, x)$ is equal to the resting cross-sectional area, A_0, for the remaining 90% of the period. Spatially the compression area is localized to 10% of the soft latex tube only. The compression pump is described by the equation,

$$A(t, x) = A_0 - (A_0 - A_{min}) \sin\left(\frac{\pi}{0.1T} t\right) \sin\left(\frac{\pi}{0.1 l_\alpha} x\right) \tag{5.1}$$

for $((t \bmod T), (x \bmod l)) \in [0, 0.1T[\times[0, 0.1l_\alpha[$ and $A(t, x) = A_0$ else, where T is the period, $l_\alpha = 0.5$ m is the length of the soft latex tube, and A_{min} is the minimum cross-sectional area achieved during the compression cycle, defined such that the compression ratio, $c = \frac{A_0 - A_{min}}{A_0}$, is set to 25% if nothing else is mentioned.

In the model in this thesis radius is the defining variable, not cross-sectional area, thus a similar equation is defined,

$$R(t,x) = \sqrt{R_0^2 - (R_0^2 - R_{min}^2)\sin\left(\frac{\pi}{0.1T}t\right)\sin\left(\frac{\pi}{0.1l_\alpha}x\right)} \tag{5.2}$$

for $((t \bmod T),(x \bmod l)) \in [0, 0.1T[\times[0, 0.1l_\alpha[$ and $R(t,x) = R_0$ else, where R_0 is the resting radius and where the minimum radius during a compression cycle is defined, $R_{min} = R_0\sqrt{1-c}$.

Implemented into the model where each section is defined with a uniform radius the above sinusoidal spatial compression of the tube will not be possible. Instead define a pinching mechanism involving a number tube sections, defined as the pinching site, such that the minimum radius of each section of the pinching site is defined so the overall pinching mechanism approximates the sinusoidal compression profile of equation 5.2. The minimum radius of each section of the pinching site is defined as,

$$R_{min,m} = R_{0,m}\sqrt{1 - c\sin\left(\pi\frac{m}{M+1}\right)}, \tag{5.3}$$

where $m = 1, \ldots, M$ is the index number for the sections included in the pinching site and M is the total number of sections in the pinching site, and where $R_{0,m}$ is the equilibrium radius of the section for the tube at rest. Then the compression for each section of the pinching mechanism is found as a function of time,

$$R_m(t) = \sqrt{R_{0,m}^2 - \left(R_{0,m}^2 - R_{min,m}^2\right)\sin\left(\frac{\pi f}{0.1}t\right)}, \tag{5.4}$$

for $t \bmod T \in [0, 0.1/f[$ and $R_m(t) = R_{0,m}$ else, where f is the frequency of the pinching mechanism.

The pinching mechanism produces a problem for the simulations of the model since a time-dependent radius is sought for through its derivative in a Runge-Kutta algorithm, while the pumping mechanism defines the radius directly as a function of time. Therefore the radius of those sections affected by the pumping mechanism is removed from the algorithm and overwritten with the radius defined by equation 5.2. This will create some apparent numerical effects in the sections where the pinching site is positioned because of discrepancies between the time solution of the Runge-Kutta algorithm and the function given by equation 5.2. These effects will not disturb the solution of the equations by the Runge-Kutta algorithm they are merely artifacts of the brute force implementation of the pumping mechanism into the computer algorithm.

5.3 Frequency spectrum of Liebau's ring

It is postulated that the Liebau effect is caused by a mismatch of impedance to the left and right compared to the position of the pinching site, which creates a difference in reflection of the pressure waves induced by the periodic pinching.

The pressure waves are induced by the periodic compression at the pinching site and travel round in the ring as a function of the elastic modules and dimensions of the two tubes. At two locations the pressure waves are reflected because of the sharp change in elasticity and tube dimensions; exactly at the junctions between the tubes. The mismatch between reflected waves creates asymmetry in the ring, which should be the cause of the Liebau effect. If that is the case, resonance between reflected pressure waves and the pumping mechanism should amplify the effect.

From the Moens-Korteweg equation (see section 3.7) the velocity of the pressure wave is,

$$v_\alpha = \sqrt{\frac{E_\alpha h_\alpha}{2R_\alpha \rho \psi}} \qquad \text{and} \qquad v_\beta = \sqrt{\frac{E_\beta h_\beta}{2R_\beta \rho \psi}}, \tag{5.5}$$

where R_α is the radius of the latex tube and R_β is the radius of the PVC tube, notice the factor ψ multiplied to the density as explained in section 3.8.

With parameters described in section 5.2 and $\psi = 1.03$, which corresponds roughly to frequencies from 2 to 4 Hz, the pressure wave velocity $v_\alpha = 4.46$ m/s is achieved for the soft tube and $v_\beta = 8.80$ m/s for the rigid tube. Correspondingly Ottesen [2003] reports $v_\alpha = 5.22$ m/s and $v_\beta = 10.37$ m/s by use of a modified Moens-Korteweg equation similar to the functions in equation 5.5 without ψ but multiplied with a factor $2/\sqrt{3}$, which corresponds $\sqrt{\psi}$ for a flow with Poiseuille profile, $\psi = 4/3$.

The pressure wave velocity gives a relation between the distance the wave needs to travel and the travel time. Seen in relation to the period of oscillations it is clear that if travel time and period match the pressure wave will encounter positive interference.

The interaction between pressure waves in the system is a function of both the position of the pinching site and the frequency of the pinching; in the simple case two reflected waves are identified in the system: one pressure wave reflected at the junction left of the pinching site and another pressure wave reflected at the junction right of the pinching site. These will be referred to as first order reflections.

But the pressure waves are not only reflected at the junctions between the tubes, they are also transmitted across the junctions. Reflection and transmission will happen every time the pressure wave crosses a junction between the two tubes, thus a reflected wave from the second junction in the path of the wave will

also be present as well as higher orders of reflected waves, however for each order of reflections the energy of the pressure wave will be split between the reflected and the transmitted wave and so only the first three orders of reflections will be considered here.

For the first order reflected wave the distance the wave needs to travel left to reach the left junction is l_p, while the distance it needs to travel right is $\frac{1}{2}l - l_p$, with l_p being the distance to the center of the pinching site from the left junction. These reflected waves will resonate with the pump oscillations if the travel time from the pinching site to the junction corresponds to $\frac{2j-1}{4}$ of the oscillation period, with j being an integer number,

$$f_{1,left} = \frac{2j-1}{4}\frac{v_\alpha}{l_p} \qquad \text{and} \qquad f_{1,right} = \frac{2j-1}{4}\frac{v_\alpha}{\frac{1}{2}l - l_p}. \tag{5.6}$$

For the second order reflected wave similar arguments apply except that these waves travel both through the soft and the rigid tube,

$$\begin{aligned} f_{2,left} &= \frac{2j-1}{4}\frac{v_\alpha v_\beta}{l_p v_\beta + \frac{1}{2}l v_\alpha} \qquad \text{and} \\ f_{2,right} &= \frac{2j-1}{4}\frac{v_\alpha v_\beta}{\left(\frac{1}{2}l - l_p\right) v_\beta + \frac{1}{2}l v_\alpha}. \end{aligned} \tag{5.7}$$

A third order reflected wave is reflected at the third junction in the path of the wave, thus it actually completes a full circle in the ring before being reflected,

$$\begin{aligned} f_{3,left} &= \frac{2j-1}{4}\frac{v_\alpha v_\beta}{(\frac{1}{2}l + l_p)v_\beta + \frac{1}{2}l v_\alpha} \qquad \text{and} \\ f_{3,right} &= \frac{2j-1}{4}\frac{v_\alpha v_\beta}{(l - l_p)\, v_\beta + \frac{1}{2}l v_\alpha}. \end{aligned} \tag{5.8}$$

However for the third order reflected wave an additional possibility exist where the wave is reflected twice inside the rigid tube, $f^*_{3,left}$ and $f^*_{3,right}$,

$$\begin{aligned} f^*_{3,left} &= \frac{2j-1}{4}\frac{v_\alpha v_\beta}{l_p v_\beta + l v_\alpha} \qquad \text{and} \\ f^*_{3,right} &= \frac{2j-1}{4}\frac{v_\alpha v_\beta}{\left(\frac{1}{2}l - l_p\right) v_\beta + l v_\alpha}. \end{aligned} \tag{5.9}$$

In this manner a multitude of different reflected waves exist for higher orders of reflections.

Furthermore since waves are transmitted across the junctions there will also be pressure waves that travel a full circle round in the ring. Those waves have other conditions for resonance; the distance the wave needs to travel through either tube is $\frac{1}{2}l$, and for the waves to be resonant the time it takes to travel round the ring must be a whole number of periods, jT, which gives the condition for the resonance frequencies,

$$f_{circle} = \frac{j}{\frac{1}{2}l\left(\frac{1}{v_\alpha} + \frac{1}{v_\beta}\right)}. \tag{5.10}$$

In addition if the travel time corresponds to $(j - \frac{1}{2})T$ the transmitted pressure waves will also experience resonance, though not as powerful, in fact due to the wave-form of the pinching mechanism a transmitted wave with a period corresponding to twice the travel time round the ring will appear as a wave with twice the frequency but with less power. Similarly it is possible to find transmitted waves with periods corresponding to other "simple factors" of the travel time.

If one pressure wave is resonant with the pinching oscillations it will be attenuated compared to the other waves and dominate the system. For the reflected waves this domination will create a pressure pulse traveling in a certain direction round in the ring, which should be associated with an amplified mean flow in the system. Resonance for the transmitted wave traveling a full circle in the system will create symmetric waves in the system. These waves does not depend on position of the pinching site and thus they should never be associated with mean flow, otherwise it would be possible to have mean flow when the pinching site is positioned symmetrically in the system. This hypothesis will be tested in section 5.4.3.

Let the parameters of the model be the same as defined above in section 5.2 and let ψ have the approximate value $\psi = 1.03$, which corresponds roughly to the frequency range used by Ottesen [2003]. Let furthermore the distance from the center of the pinching site to the left junction be $l_p = 10$ cm, which corresponds to the simulations by Ottesen [2003] and experimental measurements by Snitker et al. [2000], then resonance frequencies for the reflected and transmitted waves can be calculated, they may be found in table 5.1.

As it is seen in table 5.1 the spectrum of resonance frequencies for different wave modes is very complicated and it is generally difficult to predict the effect a given frequency will have on the flow in the system. For instance the first order resonance, $f_{1,right} = 2.78$ Hz, and the resonance of the transmitted wave, $f_{\frac{1}{2},circle} = 2.96$ Hz, lie very close to each other, and in between them a third order resonance is found, $f_{3,right} = 2.90$ Hz. $f_{1,right}$ is the first mode of reflected waves from the right and should produce a clear mean flow while $f_{\frac{1}{2},circle}$ is the first standing mode of the transmitted wave corresponding one half of a period, which should possibly have a nullifying effect on the mean flow.

j	$f_{1,left}$	$f_{1,right}$	$f_{2,left}$	$f_{2,right}$	f_{circle}
1	11.23 Hz	2.78 Hz	3.16 Hz	1.70 Hz	5.95 Hz
2	33.46 Hz	8.41 Hz	9.54 Hz	5.14 Hz	11.93 Hz
j	$f_{3,left}$	$f_{3,right}$	$f^*_{3,left}$	$f^*_{3,right}$	$f_{\frac{1}{2},circle}$
1	1.29 Hz	0.95 Hz	1.83 Hz	1.22 Hz	2.96 Hz
2	3.93 Hz	2.90 Hz	5.54 Hz	3.69 Hz	8.94 Hz

Table 5.1: The resonance frequencies for the reflected and transmitted pressure waves in Liebau's ring with $\rho = 10^3$ kg/m^3, $\eta = 10^{-3}$ Pa·s and elastic modules of the tubes $E_\alpha = 4.1 \cdot 10^5$ N/m^2, $E_\beta = 4.3 \cdot 10^5$ N/m^2. The dimensions of the tubes are $R_\alpha = 0.01$ m, $R_\beta = 0.008$ m, $h_\alpha = 0.001$ m , $h_\beta = 0.003$ m and length of each tube $\frac{1}{2}l = 0.5$ m, with the pinching site positioned 0.1 m from the left junction on the soft tube.

Furthermore it should be noted that the pressure waves traveling in the system are not normal sinusoidal waves; the pumping mechanism only compress the tube for one tenth of the period and so it creates pressure pulse waves, which demonstrate a significantly other pattern of interference that does not include the possibility of destructive interference.

Whenever a pressure pulse wave travels across a section of the tube the liquid inside will be displaced slightly according to the moving pressure gradient. So when the pressure pulse waves from the pumping mechanism are reflected by the impedance given by the dimensions and stiffness of the two tubes, a mismatch of reflected pressure pulse waves ensues and those reflected waves (resonating with the pumping mechanism or not) create an uneven displacement of liquid in the ring, which is the Liebau effect.

5.4 Model results

Liebau's ring is used to test and validate the energy bond model presented in chapter 4, the case is selected especially because all the elements of the model, even curvature, are expressed in a fairly simple way in the ring, as such it is the perfect test scenario for the model.

The simulation results of the mean flow in Liebau's ring are compared to the experimental results of Snitker et al. [2000] and simulation results obtained through use of another one-dimensional mathematical model involving an average of the Navier-Stokes equations by Ottesen [2003]. This comparison is detailed in section 5.5.

Before the comparison and a subsequent investigation of the model parts the results of the simulations will be presented and investigated here.

5.4.1 Model programming

The model of Liebau's ring is setup up according to the equations presented in section 4.4, detailing the differential equations for the dynamic radius and momentum of flow for each section of the model. The elements of the model are calculated as described in chapter 4 with the material parameters presented in section 5.2, with the compression pump described by equation 5.4 and with a cyclic boundary condition such that section $N + 1$ equals to section 1.

The model is programmed in MatLab v. 7.5 (copyright The MathWorks Inc.) and makes use of MatLab's inherent 'ode45' Runge-Kutta algorithm to iterate the differential equations of r_n and p_n. After the end of the 'ode45'-solver the values of P_n and Q_n are calculated through equation 4.59 and 4.60. For some simulations mean values are calculated by integrating over a whole number of periods and dividing with time. The programs used in the simulations are presented in appendix A.

A simulation involving $N = 60$ sections with a periodic compression pump at frequency $f = 2.06$ Hz (like the simulation presented in figure 5.2) and fifty periods of iterations took 120 seconds of CPU-time on a computer with a 2.93 GHz CPU and 1.86 GB ram, of these 107 seconds was used by the 'ode45'-solver, which divided 44 seconds to the solver-algorithm itself and 62 seconds to the calculation of r_n and p_n, and the remains to other functions. The 'ode45'-solver reported 21119 successful iteration steps and 3515 failed attempts, which may have taken up time for the solver. It took less than 3 seconds to calculate P_n and Q_n and more than 10 seconds to save the data.

5.4.2 Oscillations in time

The simulation results are obtained with a pinching pump similar to the one described by Ottesen [2003] and detailed for the implementation into the model in section 5.2, which also explains the setup and parameter values of the model for Liebau's ring. For most of the simulations the center of the pinching site is positioned 10 cm from the left junction, which is comparable to both [Ottesen, 2003] and [Snitker et al., 2000]. An example of the results of a simulation with frequency, $f = 2.06$ Hz, is visible in figure 5.2.

The figure demonstrates what appears to be very violent and erratic oscillations of all functions in the simulation, but for instance the oscillations of the radius ranges between 0.92 cm and 1.05 cm, that is the tube's radius varies with 1.3 mm, which seems reasonable. On the other hand the oscillations of flow ranges from -150 cm^3/s to almost 200 cm^3/s, that is about 100 times the mean flow, -1.78 cm^3/s. Correspondingly Ottesen [2003] reports flow oscillations about 16 times the mean flow.

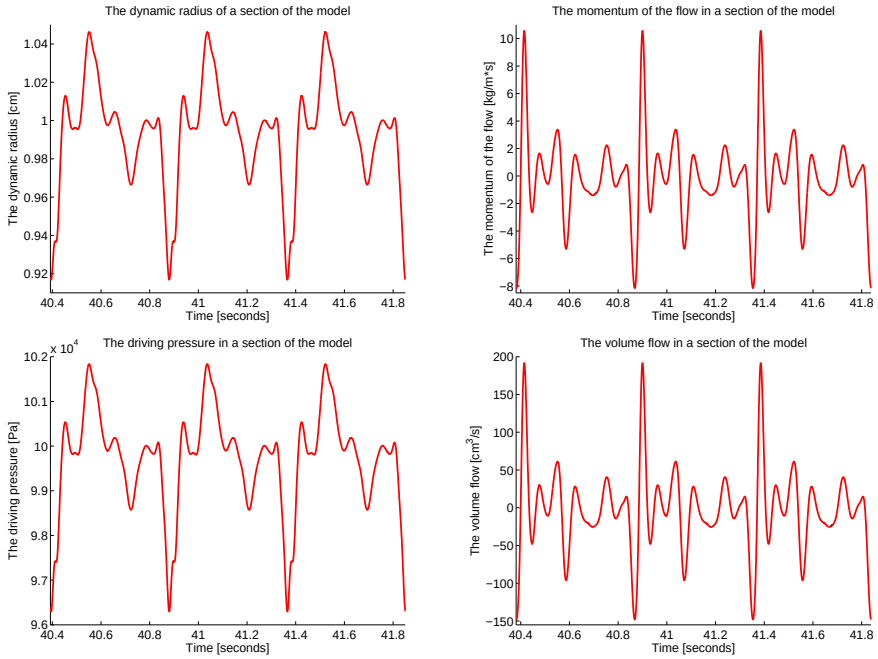

Figure 5.2: Three periods of a simulation of Liebau's ring at frequency, $f = 2.06$ Hz with the center of pinching site 10 cm from the left junction. Top left a plot of the oscillations in radius of the soft tube with mean radius, 0.993 cm. Top right a plot of the oscillations of the momentum of flow with average momentum, $-9.52 \cdot 10^{-2}$ kg/m·s. Bottom left the pressure oscillations with mean pressure, $9.97 \cdot 10^4$ Pa. Bottom right the volume flow oscillations with mean flow, -1.78 cm^3/s.

Notice how the graphs of the oscillations appear to be paired; radius compares to pressure and momentum compares to flow. In the energy bond graph, figure 4.6, radius is proportional to the force on the tube walls which is given by the pressure divided by the transformation ratio, $2\pi\Delta x r_n$, so for small changes, radius will appear to be proportional to pressure. In the same way flow is proportional to momentum as long as the changes in radius are small, while pressure is proportional to the derivative of the momentum, and flow is proportional to the derivative of radius.

All of the oscillations are dependent on the tube dimensions and may vary from section to section, for radius and momentum the mean values are also strongly dependent on tube dimensions while the mean value of pressure appears to be less dependent and the mean value of flow is a universal number for all sections of the tube, given that oscillations have found a dynamic equilibrium. Thus the mean of radius and momentum may vary strongly from section to section, especially since

the radius of the soft and the rigid tube differs, while mean pressure varies only little depending on the section, with the strongest variance observed in the rigid tube. The mean pressure of the soft tube will be regarded as almost invariant and specifically reported for the section opposite to the pinching site from the middle of the soft tube.

The mean pressure with $9.97 \cdot 10^4$ Pa is a little lower than the equilibrium pressure, set to atmospheric pressure, $P_0 = 10^5$ Pa. This may seem counter-intuitive as reduction of volume, or in this case a reduction of radius, is typically associated with an increase in pressure. But this argument only holds if energy is locally contained, instead an increase in pressure will induce an increase in radius, and similarly for decreases; the mean radius is a little lower than equilibrium radius, 0.7 %, thus the mean pressure is a little lower than equilibrium pressure, 0.3 %.

But shouldn't the pressure increase when the pinching compress the tube, where does that missing pressure go? It is converted to kinetic energy through Bernoulli's equation. The kinetic energy defines the flow oscillations, and the mean kinetic energy will define the mean flow. Furthermore with the oscillations of the flow energy dissipates through the Poiseuille resistance and the curvature resistance, effectively due to friction.

The mean flow with -1.78 cm^3/s is much less compared to the flow oscillations. The total volume inside the ring is 257.6 cm^3 at equilibrium so a flow of nearly 200 cm^3/s would mean that the liquid moves almost a full circle in one second, though this only lasts for a moment it is clear that it takes a lot of energy to accelerate the liquid to such velocities, energy that is supplied by the pressure oscillations. On the other hand, the mean flow compares to a mean flow velocity, 0.56 cm/s, so even though the oscillations are massive the liquid moves quite slowly round in the ring.

5.4.3 The no-flow condition

An important condition to test for the model of Liebau's ring is if the flow is truly zero when the pinching site is placed symmetrically in the system, ie. centrally on the soft tube. As explained the Liebau effect is attributed to the mismatch between reflected pressure waves in the system, but if the pinching site is placed symmetrically no mismatch is encountered, and thus no flow.

Therefore a test of the no-flow condition is significant to prove that the model is in accordance with the simplest physical conditions of the system, or, if not, to investigate what could be causing an eventual error.

Figure 5.3 shows the plots of flow and pressure from a simulations using the model setup described in section 5.2 with the number of sections $N = 50$ and with the 3 sections wide pinching site situated in section 12, 13 and 14, which is centrally on the soft tube of the ring.

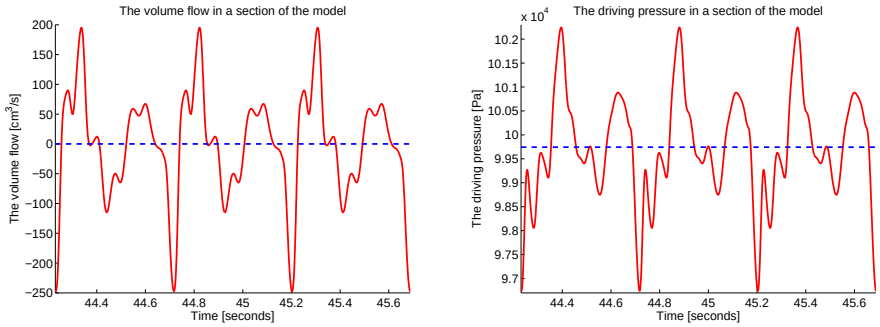

Figure 5.3: Three periods of a numerical test of the model with the number of sections $N = 50$ and the three sections pinching site centered at section 13, midways on the soft tube. Model setup as defined in section 5.2. Both flow and pressure oscillations are very dramatic, while mean flow is almost zero, $1.67 \cdot 10^{-4}$ cm^3/s, and mean pressure drops a little compared to atmospheric pressure, $9.97 \cdot 10^4$ Pa.

As the figure demonstrates the mean flow is only $1.67 \cdot 10^{-4}$ cm^3/s despite the range of oscillations reach from -250 to 200 cm^3/s. Clearly this proves that the model is in accordance with the no-flow condition, the minimal deviation from zero flow must be attributed to numerical effects in the model or in the computation of the mean.

Additionally figure 5.3 demonstrates a drop in the mean pressure compared to pressure at time zero, which is set to atmospheric pressure, $P_0 = 10^5$ Pa. The mean pressure drops to $9.97 \cdot 10^4$ Pa though no mean flow is observed, which means that the mean kinetic energy is zero. This reveals that the greatest leak in pressure actually comes from the Poiseuille and curvature resistances that dissipate energy due to the flow oscillations.

An interesting question regarding the no-flow condition is, if the transmitted wave that travels round the ring is capable of inducing flow. Because this wave is independent of the position of the pinching site it should be able to induce flow when the pinching site is positioned symmetrically in the system, if this is the case.

There are two possible cases that should be tested; the transmitted wave encounters resonance and the transmitted wave does not encounter resonance. The last case is tested in figure 5.3 as the frequency, $f = 2.06$ Hz does not correspond to any resonance modes of the transmitted wave, no flow is observed in that case. The first case is visible in figure 5.4.

In the figure flow oscillations are visible for transmitted waves with periods corresponding to once or twice the travel time round the ring, none of them produce any mean flow. Figure 5.3 and 5.4 should be enough to prove that the trans-

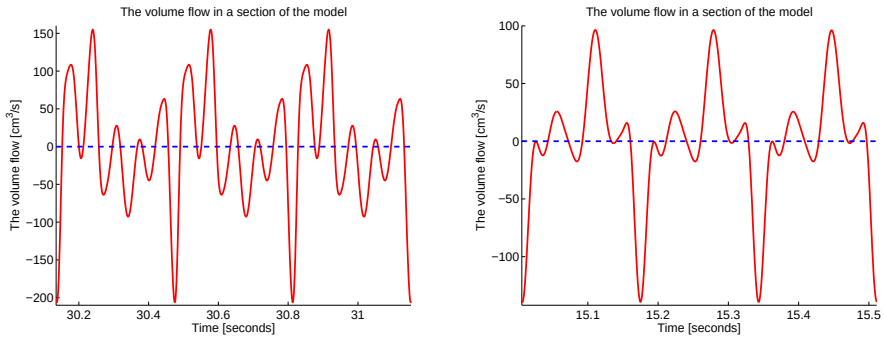

Figure 5.4: Three periods of a numerical test of the model with $N = 50$ sections and the three sections pinching site centered at section 13. Model setup is defined in section 5.2. On the left is a simulation with $f = 2.96$ Hz, corresponding to the travel time round the ring equal to the half of a period, yielding a mean flow of $6.49 \cdot 10^{-4}$ cm^3/s. On the right is a simulation with $f = 5.95$ Hz, corresponding to the travel time round the ring equal to a full period, yielding a mean flow equal to $6.51 \cdot 10^{-4}$ cm^3/s. Mean flow in both simulations is effectively zero safe for numerical effects.

mitted wave does not induce flow in the system, the mean flow must come from the reflected waves.

Notice how the range of flow oscillations are greater in figure 5.3, lesser in the left plot of figure 5.4 and least in the right plot. All three plots are made for section 20 of a model with 50 sections and with the pinching site centered at section 13, but the oscillations can vary a lot from section to section and depending on the frequency. The plots in figure 5.4 correspond to modes where the transmitted wave encounters resonance, thus a standing wave is created with antinode at the pinching site, so the full oscillations are not visible in those plots. In the plot of figure 5.3 the frequency does not correspond to any modes of standing waves, so it is a more complicated picture of the transmitted and reflected waves in the system.

5.4.4 The frequency scan

In relation to the Liebau effect the interesting question is how the dynamical flow and pressure oscillations lead to conditions that produce a mean flow round in the ring, and how that situation depends upon a number of different factors. As discussed in section 5.3 one of those factors is the frequency of the periodic compressions of the tube, which will induce pressure waves in the system and at certain frequencies these pressure waves will resonate with the periodic pinching mechanism, as presented in table 5.1.

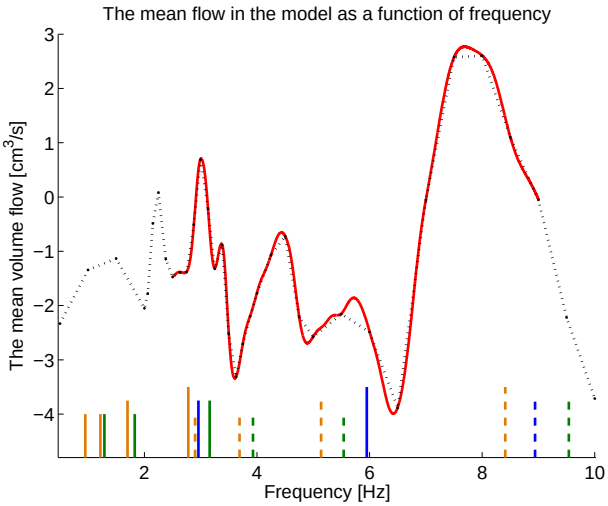

Figure 5.5: A frequency scan of the mean flow in the ring with setup as described in section 5.2. The solid curve represent a series of simulations with much finer resolution in the frequency range that due to long computation time of simulations with longer periods does not extend all the way to the low frequency range, but as shown by the figure the coarser resolution scan (dotted curve) demonstrates the features of the frequency spectrum reasonably well. Several of the resonance frequencies defined in table 5.1 are visible in the graph as small markers in the bottom of the plot; green markers are right reflected waves and yellow are left reflected waves, the size of the markers refer to the reflection order, and the dashed markers refer to $j = 2$ in table 5.1.

Naturally it will be interesting to investigate exactly how these resonance frequencies affect the mean flow for the system. To make a frequency scan of the system the program from appendix A is changed so that for any array of frequencies it will iterate the equations for 70 periods of time and afterwards calculate the mean values by integrating over the last twenty periods and dividing with time, assuming the system have found its dynamic equilibrium at that time. This is not shown in the appendix. This time consuming procedure gives the frequency spectrum for mean values of r_n, p_n, P_n and Q_n for every frequency in the array, which is visible in figure 5.5.

As is visible in the figure the mean flow is primarily negative for the frequency spectrum, that is the flow moves from the larger part of the soft tube towards the shorter part. This corresponds to the assumption that in the low frequency range the right reflected pressure waves will generally be dominant, as the distance they have to travel is longer and thus their travel time will be better compatible with the period of the compressions. At higher frequencies more resonance modes of the

left reflected waves may come into play such that the distribution between positive and negative mean flow may be more even.

At certain frequencies the spectrum demonstrate clear peaks where the mean flow is either intensified, nullified or it changes direction, most of these appear to correspond roughly to the resonance frequencies identified in table 5.1.

The resonance frequencies of 2.78 Hz, 3.16 Hz, 3.69 Hz, 5.14 Hz and 5.54 Hz can be clearly identified, and with some imagination also the resonances at 1.70 Hz and 1.83 Hz. The frequencies of 3.16 Hz and 5.54 Hz correspond to the resonance of left reflected waves that change the mean flow to a positive direction. This also helps to identify the resonance at 1.83 Hz, which should be shifted a little higher to fit with the graph. The other resonances correspond to right reflected waves that increase the mean flow in the negative direction.

Additionally unidentified peaks are visible in figure 5.5, likely corresponding to reflection patterns not identified in section 5.3. Specifically for frequencies larger than 6 Hz it does not appear as if the identified resonances can explain the graph of the mean flow.

Furthermore the mean flow is not only dependent on the resonance of pressure waves with the compression pump, for most parts of the frequency spectrum the mean flow is produced from interference between reflected and transmitted pressure pulse waves, with the the resonances being situations that are easily identifiable and should dominate the system at their respective frequencies. The pressure pulse waves have several modes of interference, it is quite possible that several reflected waves resonates to amplify each other and even if no waves resonate at a certain frequency they will not terminate each other either due to the nature of the pulse waves. Generally at a given frequency it is very difficult to predict the exact value of the mean flow from the complicated interaction of pressure waves.

5.4.5 Position of the pinching site

From the premise given in the calculation of the resonance frequencies in table 5.1 it is clear that the observed mean flow will depend on the position of the pinching site, especially since it is proven in section 5.4.3 that the transmitted pressure wave, which is site-independent, does not produce any mean flow. Thus it will be interesting to observe how the simulation results change when the position of the compression pump is moved. For that reason the program from appendix A is changed just like in section 5.4.4 though this time the mean values are computed as a function of the position of the pinching site.

Figure 5.6 shows a plot of the mean flow as a function of the position of the pinching site in the ring. One thing that is clear to see in the figure is the symmetry between the two halves of each tube, when the pinching site is moved to the opposite site from the middle of the tube flow is reversed but of equal magnitude.

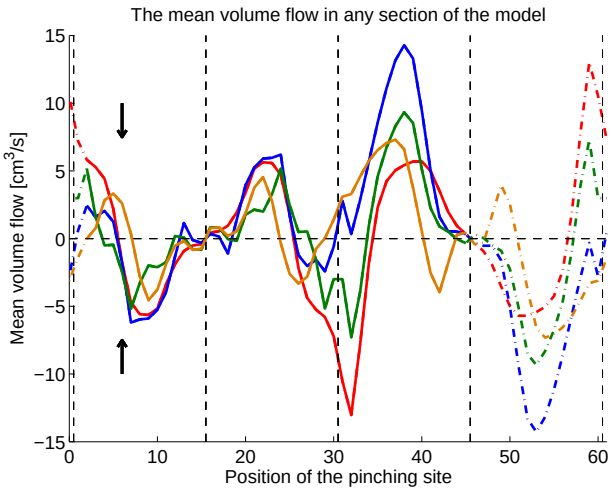

Figure 5.6: A set of simulations with $N = 60$ sections where the pinching site has been moved around to any position of two tubes, model setup as described in section 5.2. In the plot the mean flow is visible for frequencies of 2.06 Hz (red curve), 4.00 Hz (blue curve), 6.00 Hz (green curve) and 8.00 Hz (yellow curve), the dashed part of the curves are reconstructions from other parts of the curves. The dotted lines separate the tubes into four quarters, the first two quarters belong to the soft tube and the other two to the rigid tube. The two black arrows mark the position of the pinching site for all other simulations presented in this thesis, except the ones in section 5.4.3 of course.

One other thing that is clearly visible in the figure is the dependency between frequency and the position of the pinching site. At low frequency it appears that there is only one optimal position of the pinching site, about one third of the length from the junction between the two tubes, but with higher frequencies that optimal position moves closer to the junctions and other positions appear in relation to the shortening of the wavelength for higher frequencies.

It must be that the site of the compression pump should fit with the distance that the traveling pressure waves are able to cover in a whole number of periods going from the pinching site to a point of reflection and back, such that the sites of optimal mean flow are the positions for which a wave of that frequency encounters resonance in the ring. As such it is clear that the position of the pinching site selected for all the other simulations, marked by the arrows in figure 5.6, will not see the maximum Liebau effect possible with the two tubes for the chosen frequencies.

In the report by Snitker et al. [2000] it is claimed how positioning the pumping mechanism exactly at the junction between the two tubes produces the highest mean flow with a frequency, $f = 2.06$ Hz. From that it is speculated that this will be the case for all frequencies. While figure 5.6 confirms the first result it also proves that for other frequencies the mean flow may be less, even zero.

Positioning the pinching site at the junction between the tubes is a special case because it effectively removes one of the possible reflection sites for the waves in the tube, this completely changes the system and for that reason no more time will be spent with that case here. Similarly figure 5.6 demonstrate that higher mean flows may be achieved by pressing on the rigid tube, for a pinching mechanism designed for pressing the soft tube. This comes only natural since the increased thickness and elastic module of the rigid tube makes it harder to compress it, in this way more energy is spent to compress the tube to a compression ratio of 25 %, thus the waves in the system contain more energy yielding a higher pressure and displacement amplitude. No more time will be spent on that case either.

With that the basic phenomena in the simulations of Liebau's ring are presented. In the following focus will be put on a comparison of the simulation results to other reports and specific elements of the model will be examined to test the validity, stability and performance of the model.

5.5 Comparison to other results

The simulations of Liebau's ring are compared to another set of simulations by Ottesen [2003] and to experimental measurements by Snitker et al. [2000].

The experiments by Snitker et al. [2000] measures the mean velocity of the flow in Liebau's ring, specifically pertaining to different compositions of tube materials and the position of the pump in relation to the junctions between the tubes. The experiments involve an external physical pump that is connected to Liebau's ring through as small tube, it works by producing an excess volume of liquid inside the ring, which will then induce the flow. The frequency of the pump is 2.06 Hz in all reported experiments.

The simulation results by Ottesen [2003] are based on a one-dimensional averaging of the Navier-Stokes equations into a system of differential equations, which are solved using the eigenvalue method and simulated using Richtmeyer's two step version of Lax-Wendroff's method. The pumping mechanism used in these simulations is described in equation 5.1 and simulation results are specifically reported for the frequency range from 2.5 Hz to 3.5 Hz.

The setup and pinching mechanism of Ottesen is the same as used for the simulations of Liebau's ring here, so results will be comparable to the extend that in the data by Ottesen the system is subjected to a small pressure increase before starting the pumping mechanism. This high pressure should not have much

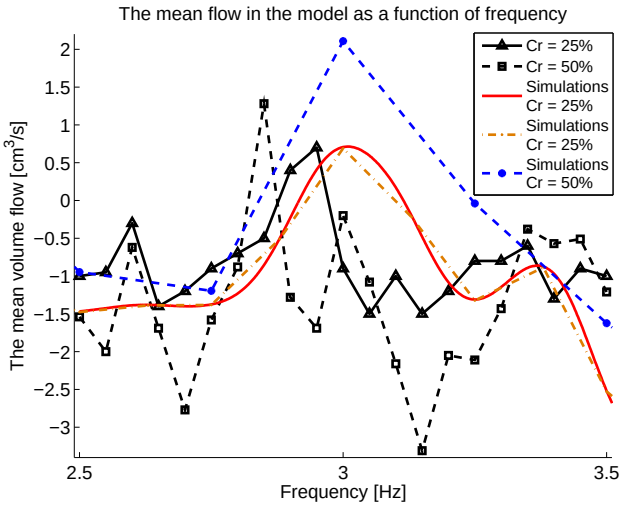

Figure 5.7: Comparison of the mean flow from the simulations of Liebau's ring to data from Ottesen [2003] (square and triangle plots). The simulations are made with $N = 60$ and setup as described in section 5.2, though one set is made with compression ratio $c = 25$ % (solid and dash-dotted curve as presented in figure 5.5) and another is made with compression ratio $c = 50$ % (dashed curve).

influence on the observed Liebau effect as demonstrated in section 5.5.1.

Figure 5.7 shows a comparison between mean flow of the simulations to data supplied in by Ottesen [2003]. The figure compares the mean flow for simulations with a compression ratio 25 % and 50 %, where the compression ratio is defined by the compression of cross-sectional area, $c = \frac{A_0 - A_{min}}{A_0}$, according to the setup in section 5.2.

There seem to be good correspondence between the registered mean flow from the two sets of simulation data when the compression ratio, c, is set to 25 %, to the point that deviances can be ascribed to difference in modeling and simulation procedure. Both sets of data has mean flow about -1.0 to -1.5 cm^3/s for most parts of the frequency range, but in the vicinity of 2.79 Hz, 2.97 Hz and 3.17 Hz something happens, corresponding to resonance modes defined in table 5.1.

For the compression ratio, c, set to 50 % the comparability is more unclear. The mean flow is still in the vicinity of -1.0 to -1.5 cm^3/s in the low and high frequency end while something else happens in the frequency band around 3.0 Hz. The mean flow by Ottesen appear to change direction around the resonances in this interval, which is also the case in the simulations of the model, though not in the same way. It appears as if the simulations at $c = 25\%$ have good comparability, yet the lack of data points makes comparison uncertain for higher compression rates.

Comparison to the results by Snitker et al. [2000] is more complicated. Their experiment consisted of two tubes clamped together and an external pump set into the system through a T-junction and a third tube. The pump consists of a compliant plastic bag that is periodically compressed to pump an excess volume into the system, and through the compliance of the bag it is gradually refilled such that the total volume of liquid pumped into the system during one period is zero.

The pump employed in this experiment has an active duration of $1/4$ of the period and a relaxation duration of $3/4$ of the period, the frequency is set to 2.06 Hz for all measurements, and the excess volume pumped into the system the active duration is estimated between 10 - 12 cm^3. Unfortunately Snitker et al. [2000] fail to measure compliance of the pump, so a reconstruction will not be attempted here. It is however possible to make a crude modification of the pumping mechanism in the model to compare with Snitker, such that an excess volume is periodically injected and removed not relying on compliance, using the equation,

$$V(t) = V_{total}\left(1 - \cos\left(\frac{2\pi}{\tau}t\right)\right), \tag{5.11}$$

for $(t \mod T) \in [0, \tau[$ and $V(t) = 0$ else, where τ it the active duration as a fraction of the period and V_{total} is the total volume of fluid pumped into the system during the active duration.

The excess volume is added to the volume flow between two sections of the model as a function of time by means of its derivative,

$$\frac{dV}{dt} = V_{total}\frac{2\pi}{\tau}\sin\left(\frac{2\pi}{\tau}t\right), \tag{5.12}$$

for $(t \mod T) \in [0, \tau[$ and $\frac{dV}{dt} = 0$ else.

The excess volume pump periodically injects a volume of 10 - 12 cm^3 into the system, correspondingly the pinching mechanism defined by equation 5.2 and implemented into a model with $N = 60$ sections while the pinching site is 3 sections wide compresses the tube with a volume of 3.2 cm^3 for a compression ratio of 25 % and with a volume of 6.3 cm^3 with a compression ratio of 50 %. The pinching mechanism needs to compress the tube with a compression ratio of 80 % or more to compare with the excess volume pump.

Snitker et al. [2000] measure the flow velocity in the ring by timing the movement of small plastic balls suspended in the water inside the tubes, specifically in the rigid PVC tube, which is transparent. Explained in the report is the concern to find a material for the plastic balls that would remain suspended in the liquid and neither sink or float, eventually folded pieces of plastic bags was used. Due to the volume of the plastic balls compared to the velocity profile the balls will experience a velocity gradient and thus they will tend to migrate towards the center of the tube where the velocity is highest in an effect similar to the one encountered

by blood cells [Meier, 1987], though the rugged shape of the folded pieces of plastic could disrupt this migration at times. Thus it is expected that the velocity measured by Snitker et al. [2000] is the peak velocity inside the tube.

Assuming the flow has a Poiseuille velocity profile the measured velocity corresponds to the mean volume flow,

$$Q = 2\pi \int_0^R V_{max} \left(1 - \frac{r^2}{R^2}\right) r\, dr = \frac{\pi R^2}{2} V_{max}, \tag{5.13}$$

which is half of the volume flow achieved under the assumption of a flat velocity profile. The flow however has a Womersley velocity profile, which means that the corresponding flow lies in the interval from $\frac{1}{2}\pi R^2 V_{max}$ to $\pi R^2 V_{max}$.

From an experiment involving two tubes as described in section 5.2 and with a volume pump positioned 10 cm from the left junction Snitker et al. [2000] obtain a flow velocity equal to 5.0 ± 0.5 cm/s, corresponding to a flow from 5.0 ± 0.5 to 10.0 ± 1.0 cm^3/s.

Correspondingly simulations with the pinching mechanism from section 5.2 yield mean flows of -1.78 cm^3/s, -1.31 cm^3/s and -0.92 cm^3/s for compression ratios of 25 %, 50% and 75 % respectively. And for a simulation with the above setup and an excess volume pump as suggested by equation 5.12 a mean flow of 3.1 cm^3/s is obtained if the activity duration is set to one tenth of the period as suggested by Ottesen [2003] while a mean flow of only 0.3 is obtained if the activity duration is set to one fourth of the period, much lower than the measured flow rate.

5.5.1 High pressure results

The results by Snitker et al. [2000] were achieved for a system with high pressure, obtained by injecting 10 or 20 cm^3 of liquid into the system and letting it relax before setting the liquid into motion with the volume pump. It is reported that the system would not function satisfactory with atmospheric pressure, as the velocities measured had a large spread in magnitude and did not demonstrate any systematic behavior.

To compare with those results a set of simulations are prepared where a single section of the tube is dilated to accommodate either 10 or 20 cm^3 of extra volume, and the system is allowed to relax such that all the sections of the model will have a slightly dilated radius compared to equilibrium radius. When the system has found its new stable condition the pumping mechanism is started with the use of the excess volume pump from equation 5.12. A comparison of flow and pressure of three simulations involving 10 cm^3 extra volume, 20 cm^3 extra volume, and no extra volume is visible on figure 5.8.

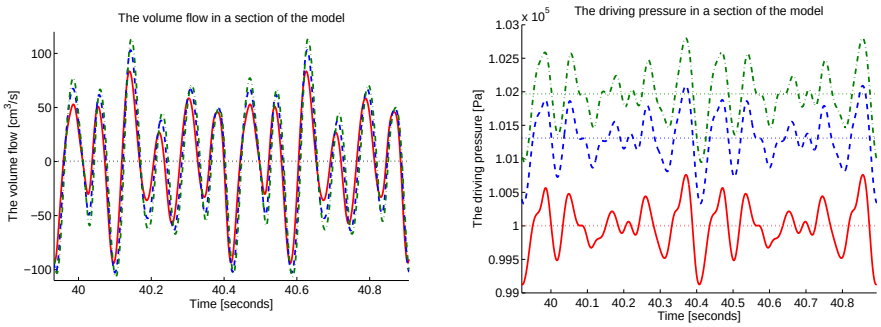

Figure 5.8: A comparison of simulations with the excess volume pump at frequency $f = 2.06$ Hz: One simulation without higher pressure (solid curve), one simulation with 10 cm^3 extra liquid volume (dashed curve) and one with 20 cm^3 extra volume (dash-dotted curve), the increased volume before the onset of the excess volume pump will increase the equilibrium pressure inside the tube. On the left is a plot of the volume flow oscillations; all three simulations follow the same curve, except that amplitude increases with the higher pressure. On the right is a plot of the pressure oscillations; the curves are nearly identical, except that the higher pressure shifts the curve towards higher values.

As the figure demonstrates the simulations at higher pressure are not really that different from the normal simulation: The amplitude on the flow oscillations increase with higher pressure, and the pressure oscillations are naturally shifted towards higher pressure.

It is noticeable on figure 5.8 that the mean pressure is almost constant under the application of the excess volume pump, while it decreases under the use of the pinching mechanism explained in section 5.2. For the simulations with 0, 10 and 20 cm^3 extra volume the mean pressure is $1.0001 \cdot 10^5$ Pa, $1.0131 \cdot 10^5$ Pa and $1.0197 \cdot 10^5$ Pa respectively, while the corresponding equilibrium pressures are 10^5 Pa, $1.0119 \cdot 10^5$ Pa and $1.0199 \cdot 10^5$ Pa. The differences between equilibrium and mean pressures are 100 Pa or less with a tendency to increase rather than decrease, this may be an indication that the two pumping mechanisms are not comparable at all.

A further comparison of the mean flow produced by the excess volume pump to that produced by the pinching mechanism and the data by Ottesen [2003] is visible on figure 5.9. Furthermore the reported flow velocities by Snitker et al. [2000] are drawn on the figure as vertical bars, calculated into volume flow through equation 5.13. It is clear that flow corresponding to the observed velocities is much larger than any computed flow from the models.

According to Snitker et al. [2000] the difference between experiments with 10

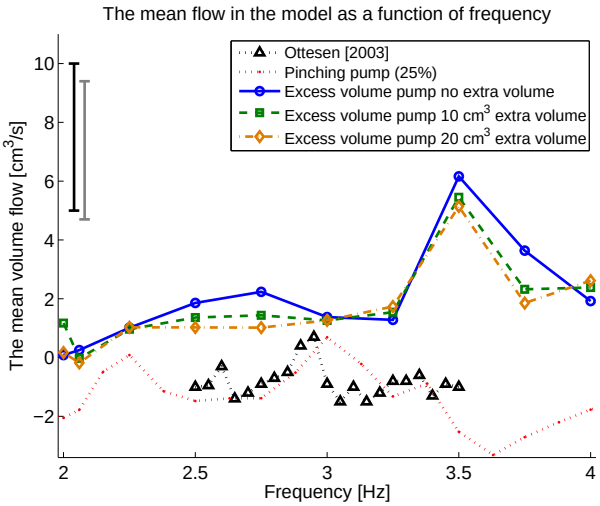

Figure 5.9: Comparison of the mean flow from the simulations with the excess volume pump with those of the pinching mechanism (red dotted curve) and data from Ottesen [2003] (black dotted curve) and the reported velocities from Snitker et al. [2000] calculated into an interval for the volume flow. The black bar is the volume flow for their experiment with 10 cm^3 extra volume of liquid, ranging from 5.0 to 10.0 cm^3/s, and the gray bar is the volume flow for their experiment with 20 cm^3 extra volume of liquid, ranging from 4.7 to 9.4 cm^3/s. Though it is demonstrated that the excess volume pump is capable of producing flow in the range reported by Snitker et al. [2000] explicitly at $f = 2.06$ Hz it produces nearly no flow at all.

and 20 cm^3 extra volume injected prior to the start of the pumping is a decrease in velocity for the higher pressure measurement, though for other of their measurements the higher pressure demonstrates a higher velocity. Generally that picture is confirmed here, the simulation with 20 cm^3 extra volume constituting higher pressure will sometimes exhibit a lower mean flow and sometimes a higher, compared to the other simulations. In figure 5.9 this is proved to be dependent on frequency, but it may as well depend on a number of other things, for instance the position of the pump on the ring, which seems to be the case for Snitker et al. [2000].

The frequency spectrum demonstrated for the simulations with the excess volume pump does not particularly resemble that of the pinching mechanism, in some ways they appear to be mirror images of each other, but the most notable peak of the excess volume spectrum at $f = 3.5$ Hz is not recognized in the spectrum of the pinching mechanism. Furthermore it appears there is a minor peak at $f = 2.06$ Hz for the simulations at higher pressure, which is not observed for any of the simulations involving the pinching mechanism.

Many things point to the fact that the pumping mechanisms are fundamentally

different and incomparable, it has been reported many times for instance by Ottesen [2003] that the observed Liebau effect depends on the method of pumping applied, which is confirmed by figure 5.9. In fact according to Yang and Wang [2010] valveless systems that differ in configuration or operation conditions (down to the frequency of compression) may rely entirely upon different mechanisms to pump fluids.

The excess volume pump involved in the simulations is a very poor resemblance of the pump applied by Snitker et al. [2000] due to the fact that the simulated pump actively refills instead of passively though its compliance, in the simulations the pump interacts with the tube by 'magically' introducing an excess volume in the tube while the real pump has a whole other range of interaction possibilities not accounted for by the model.

Constructing a hybrid pumping mechanism that works like the excess volume pump but with the activity duration of the pinching mechanism (1/10 of the period instead of 1/4 of the period) does not improve the comparison, even through the hybrid pump will produce 10 cm^3 excess liquid volume for only one tenth of the period corresponding to the pinching mechanism with an 80 % compression ratio, which compress a volume equal to 1.01 cm^3 for one tenth of the period. The spectrum of the mean flow mostly resembles that of the other excess volume simulations, but with more modes of resonance. Thus the difference in pumping mechanisms can not be explained only by the difference of activity duration.

The conclusion is that the model is not able to reproduce the data from Snitker et al. [2000], mainly out of a lack of information about the pumping mechanism used in the experiment. Many things are unclear about the experiment: the estimation of elastic modulus of the wall of the tubes, the estimation of mean velocity based on the timing of plastic balls in the liquid, disturbance of momentum oscillations by the plastic balls, which could produce a more smooth mean flow, but in the end it all comes down to the pumping mechanism. The pumping mechanism is extremely important for the observed Liebau effect to the point that it is almost impossible to compare two cases if not the pumping mechanisms are comparable.

5.6 Testing model parts

One huge advantage of the application of energy bond networks in the modeling is the possibility to add or remove effects in the model just as a set of building blocks. This makes it very easy to construct tests of the model to estimate the importance of different model elements.

The model is constructed in basically two steps; one step involving the fundamental elements of elastic compliance, liquid inertia and flow resistance, and another step involving three additional elements of the model: Womersley theory, shear forces in the tube and curvature of the tube. As these three last elements carry additional assumptions about the behavior of the flow and elasticity of the tube and sometimes deliberately are left out in reports of valveless flow models, see for instance [Manopoulos et al., 2006] or [Azer and Peskin, 2007], it will be interesting to inspect what influence the elements or their absence will have on the simulations of Liebau's ring.

5.6.1 Womersley theory

Many reports point to the assumption that Womersley theory does not have much influence on the flow, for instance Azer and Peskin [2007] state that the results of their simulations involving Womersley theory are similar to other models assuming other shapes of the velocity profile, though some simulations may show greater effect of the velocity profile, specifically if they involve a Poiseuille velocity profile. In a similar fashion Manopoulos et al. [2006] argue that for high Womersley numbers the inertia correction factor, ψ, is close to unity and in order to eliminate parameters from their model they assume $\psi = 1$ in all their simulations.

With frequencies in the range from 1 to 5 Hz and the model setup described in section 5.2 the real values of the inertia correction factor lies in the range from 1.07 to 1.03, thus $\psi = 1$ is a fair simplification of this model, though not in general. On the other hand setting $\psi = 4/3$ in assumption of a Poiseuille profile may be interesting for the model, figure 5.10 shows a comparison of simulations involving a standard Womersley profile, a flat profile, $\psi = 1$, and a Poiseuille profile, $\psi = 4/3$.

From the figure it is clear that the difference in results between simulations with a regular Womersley profile and with a flat velocity profile, $\psi = 1$, are minimal. The results obtained with at Poiseuille profile, $\psi = 4/3$, are different from the other two. It is clear from the left plot of figure 5.10 that the liquid has higher inertia as the oscillations are slower, for each period the graph appears to skip an oscillation compared to the other two. On the right plot of figure 5.10 it is visible that the mean flow of the Poiseuille profile follows the same general curve as the other two, it is only shifted to lower frequencies. This is not coincidental, in fact equation 5.5 states how the velocity of the pressure wave depends on ψ and the resonance frequencies are generally proportional to this velocity, therefore the whole spectrum of the simulations are multiplied with a factor, $\sqrt{1/\psi} = \sqrt{3/4} \approx 0.87$.

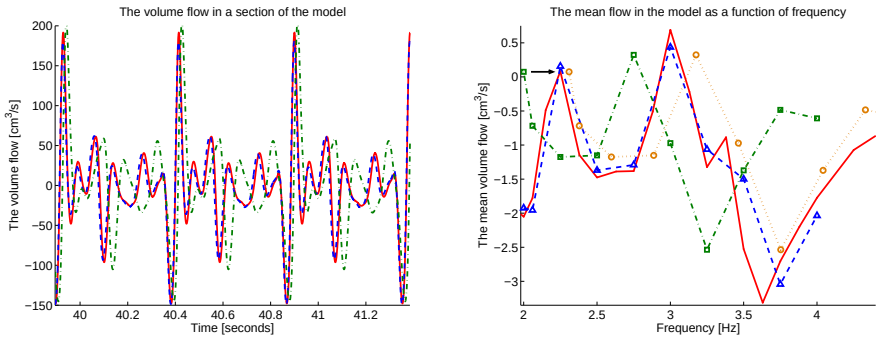

Figure 5.10: A comparison of simulations with different configuration of the inertia correction factor: regular Womersley profile (solid curve), flat velocity profile (dashed curve), and Poiseuille profile (dash-dotted curve). On the left is a plot of the oscillations of flow, $f = 2.06$ Hz, it is visible how the flat profile and the Womersley profile produce almost similar results, while the oscillations are slower for the Poiseuille profile due to higher inertia. On the right is a plot of the mean volume flow, once again the flat profile and Womersley profile are in good accordance while the Poiseuille profile is not, if however the plot of the Poiseuille profile is scaled with a factor, $\sqrt{4/3}$, towards higher frequencies (as marked by the arrow) it is seen that the shape of the new dotted curve is in much better agreement with the other two.

Generally Womersley theory does not mean much for the magnitude of the simulations of pulsating flow it does however have an effect on oscillations and the frequency spectrum of the mean flow.

5.6.2 Shear tensions

In the model the shear strain between tube sections are added as an ad hoc improvement to the model in order to include longitudinal shear effects in the tube. In section 4.3.1 it is explained how these effects are modeled through the use of a capacitor representing shear elasticity and an impedance representing energy loss in the tube wall.

The elements were added to the model after preliminary investigations proved that a single-capacitance elasticity did not produce accurate results for the model, as such they represent several effects in the model of the tube. Naturally the simplest effect is the binding of sections to their neighbors such that the deformation of each section is not independent, physically the elements represent a longitudinal stress-strain relation coming from the fact that the tube will attempt to minimize length stretches of surface area resulting from the dilation or contraction of

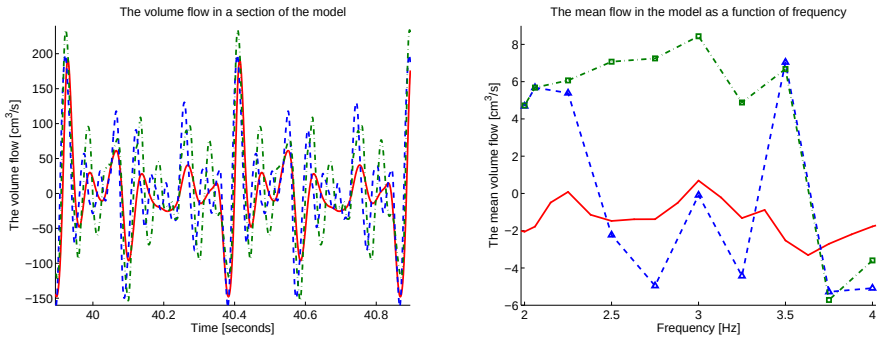

Figure 5.11: A comparison of simulations with normal shear effects (solid curve), shear effects with no damping (dashed curve), and no shear effects at all (dash-dotted curve). On the left is a plot of the oscillations of volume flow at frequency $f = 2.06$, it is clear how the simulations without damping or shear effects experience much wilder oscillations. On the right is a plot of the mean volume flow as a function of frequency, it is interesting how the simulations without damping or shear effects seem to follow each other at low and high frequencies, while frequencies near the resonances of 2.79 Hz, 2.97 Hz and 3.17 Hz seem to separate the two curves.

tube sections, and through the energy loss the elements model the fact that the tube walls are not ideally elastic, energy is lost in the wall due to internal friction.

With the shear capacity described as in equation 4.26, $C_{sn} = \frac{\Delta x}{2\pi G h \sqrt{R_n R_{n+1}}}$, where $G = E/3$ is the shear modulus, and the model setup as detailed in section 5.2 the values of the capacity are $C_{sn} = 1.94 \cdot 10^{-3}$ m/N for the soft tube and $C_{sn} = 0.77 \cdot 10^{-3}$ m/N for the rigid tube. With the maximum dilation-distance between two sections equal to 1.3 mm as described in section 5.4.2 for a simulation with frequency $f = 2.06$, the capacity yields a maximum force equal to 0.67 N for the soft tube and 1.69 N for the rigid tube. For comparison the capacitance reacting to radial expansion of a section yields 2.79 N for the soft tube and 10.98 N for the rigid tube for the same dilation. Thus the shear forces are between 1/7 to 1/4 weaker than the radial forces.

Additionally the impedance, defined as $Z_{sn} = T/C_{sn}$ where $T = 0.01$ s is the period of eigenfrequencies in the combination of capacitance and impedance added to the model with inclusion of the shear effects. Z_{sn} yields a resistance equal to $0.52 \cdot 10^3$ N·s/m for the soft tube and $1.30 \cdot 10^3$ N·s/m for the rigid tube, depending on the speed of radius oscillations of the neighboring sections the impedance will produce a force to dampen the oscillations.

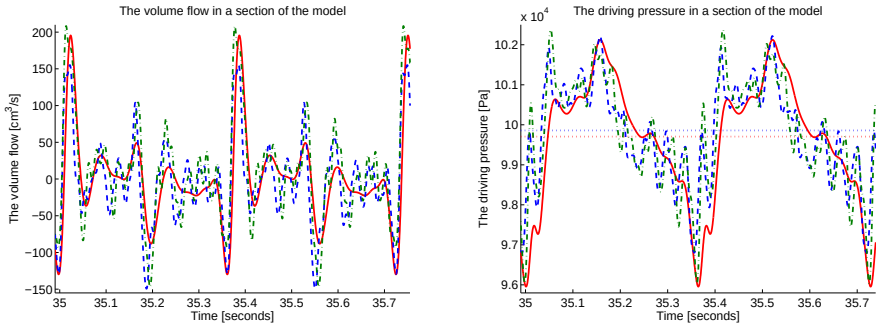

Figure 5.12: A comparison of simulations at frequency $f = 2.75$ Hz with normal shear effects (solid curve), shear effects with no damping (dashed curve), and no shear effects at all (dash-dotted curve). On the left is a plot of the flow, the wildness of the oscillations is confirmed, which makes it very hard to determine what causes the big difference in mean velocities at the frequency. On the right is a plot of the pressure, which similarly project wildness when undamped or without shear effects, the oscillations of the two curves are almost identical and follows the pressure curve of the normal simulation. However, their mean pressure is closer to the equilibrium value than for the normal simulation. From this it would appear that it is the damping effect that matters most for the oscillations of pressure.

Figure 5.11 and 5.12 shows graphs of three simulations: one simulation with normal shear effects included, one simulation without shear impedance, $Z_{sn} = 0$, and one simulation with both shear capacitance and impedance removed, the latter is achieved by setting $C_{sn} = 10^{10}$ m/N such that the shear effect will be nearly non-existent.

The figures demonstrate how the oscillations of volume flow and pressure become wilder when the impedance or the shear effect is removed; both the amplitude and number of oscillations per period increase. The oscillating curves of the simulations without damping and without shear effects appear to follow each other for most of the period and it is unclear what exactly causes the major difference in mean flow between the two, at $f = 2.75$ Hz the simulation without damping has a mean flow of -4.96 cm^3/s while the other has a mean flow of 7.25 cm^3/s.

The mean flow of the simulations without damping and without shear effects are almost in complete agreement for low frequencies until $f = 2.25$ Hz and again for high frequencies from $f = 3.50$ Hz and up. In the intermediate range the simulation without shear effects remain with a high positive mean flow while the other becomes negative and almost seems to follow the curve of the regular simulations with shear effects included. In that intermediate frequency range at

least three resonance frequencies have been determined at 2.79 Hz, 2.97 Hz and 3.17 Hz, it appears as if the simulation without damping is strongly reacting to those resonances while the other is almost not affected. This makes sense as the pressure wave travels as a function of the elasticity of the tube, when the shear elasticity is removed from the model the circumstances for the pressure wave is changed dramatically, on the other hand when only the damping is removed the effect of the pressure wave resonances will be seen much clearer.

The shear effect may be implemented as an ad hoc addition to the model, but it models a real physical effect in the tube; the longitudinal elasticity, which is not covered by the standard radial elasticity in the model. The longitudinal elasticity is important for the propagation of pressure waves in the system. Moreover the damping of oscillations in the wall models a real effect of friction in the tube generating heat from the oscillations, thereby higher frequency oscillations are damped, which seem to be the defining discrepancy between curves of the pressure oscillations. From figure 5.11 and 5.12 it is clear to see that both damping and shear elasticity has a major effect on the simulations.

5.6.3 Tube curvature

Curvature of the tubes in Liebau's ring is a condition that is quite obvious; of all the cases proposed by Gerhart Liebau in his papers Liebau's ring is not the simplest, yet because of the curvature of the ring it is an interesting case for this model.

Curvature adds another resistance to the flow but this resistance does not only depend on the radius, as is the case for the Poiseuille resistance, it also depends on the momentum of the flow. For flow of small momentum the impedance is insignificantly small an may be ignored but for flow of higher momentum it may become more influential than the Poiseuille resistance.

For pulsatile flow the resistance depends on the oscillations of momentum, which may be important for the Liebau effect as the flow momentum is the integral of the pressure wave. It is however common to ignore the effects of curvature in models of Liebau's ring, it is for instance done by both Ottesen [2003] and Manopoulos et al. [2006].

The resistance due to curvature is defined in equation 4.38 and while the coefficients $\alpha K_B f_T/\psi$ adds up to 0.38 for the soft tube and 0.49 for the rigid tube and momentum oscillations have a magnitude of about 10 kg/m·s the relation defined by the radii of the tube yields $7.96 \cdot 10^4$ m^{-3} for the soft tube and $1.55 \cdot 10^5$ m^{-3} for the rigid tube, which can make the resistance explode at times of high numerical momentum.

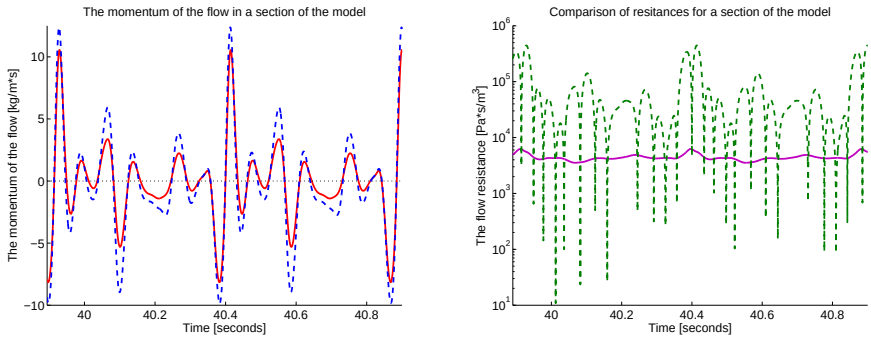

Figure 5.13: On the right is a comparison of the momentum of simulations with normal implementation of curvature (solid curve) and without curvature resistance (dashed curve) at frequency $f = 2.06$ Hz, it is clear how the oscillations without curvature resistance express a larger amplitude. On the right is a comparison of the Poiseuille resistance (solid curve) to the curvature resistance (dashed curve) for a standard simulation at $f = 2.06$ Hz (notice the logarithmic axis), the curvature resistance increase and decrease in relation to the oscillations of the momentum, while the Poiseuille resistance is much more stable.

Figure 5.13 and 5.14 show the comparison of two types of simulations: one normal simulation with curvature resistance included and another one without curvature, effectively achieved by setting the bending angle of each section to zero.

The figures demonstrate how the resistance due to curvature is much more dynamic compared to the Poiseuille resistance. The resistance from curvature increases and decreases in accordance with the numerical value of the momentum of flow but most of the time it is larger than the Poiseuille resistance, sometimes even with a factor 10 or more.

The damping of the curvature has a large effect on the oscillations of all the variables of the simulation; the amplitude is decreased yet the shape of the curve is almost similar for simulations with and without curvature, for the flow and the momentum without curvature the curves are shifted to higher or lower values depending on the frequency compared to the curves of normal flow and momentum, which creates a dramatic effect for the mean flow, especially in the vicinity of resonance frequencies. It is possible to identify resonances from table 5.1 at 2.79 - 3.17 Hz, 5.13 Hz, 9.50 Hz and possibly also at 1.71 Hz though it is unclear what happens at the lower frequencies.

It is clear that the curvature of the tube has a large effect on the oscillating flow and pressure waves of the model, and that it is very important for the observation of Liebau phenomena in the tube. Without the curvature the observed Liebau

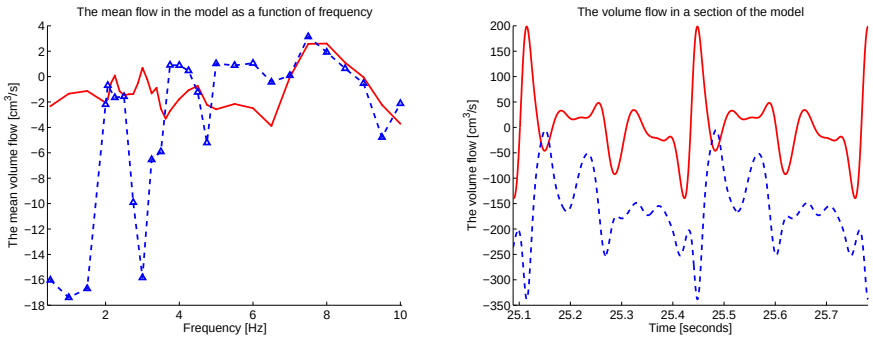

Figure 5.14: A comparison of simulations with normal implementation of curvature (solid curve) and without curvature resistance (dashed curve). On the left is a comparison of the mean flows as a function of frequency, the mean flow without curvature has much higher numerical values that the flow with curvature, the dashed curve has been divided by 10 in order to make the comparison, the mean flow without curvature still appears to respond to resonance effects in the frequency spectrum. On the right is a plot of the flow oscillations at frequency $f = 3.0$ Hz, the curves have an almost similar appearance except that the mean flow without curvature lies much lower.

effect is many times larger, this alone is a proof that curvature effects may not be ignored in the model.

Overall it is clear that the damping effects are what defines the observation of the Liebau effect in the model, both the damping from friction in the walls of the tube and the damping from the curvature of the tube are very important for the observed curves of oscillating flow and pressure and in the end for the mean flow through the system. While the shear elasticity of the tube wall and the Womersley inertia correction factor are not inconsequential to the outcome of the simulations it is clearly the damping and resulting energy loss from the shear effects or the tube curvature that has the most influence.

5.6.4 Difference in the number of sections

Another interesting question about the model is its stability pertaining to the number of sections, N, that are used in the simulations. All the above simulations except those of section 5.4.3 are made for $N = 60$ sections of the model, which gives a section length, $\Delta x = 1.67$ cm. Here four simulations will be compared involving 20, 40, 60 and 80 sections.

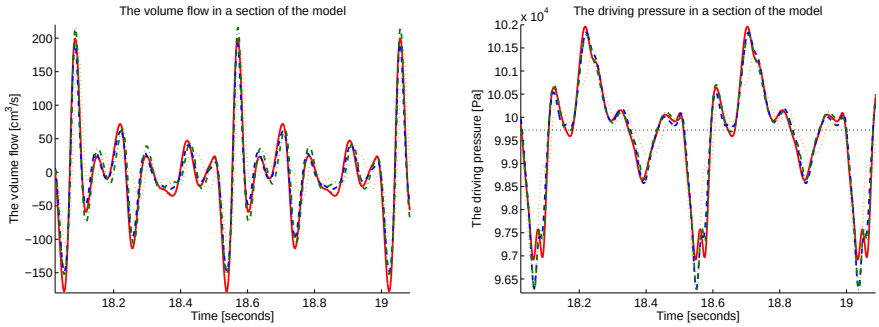

Figure 5.15: A comparison of simulations involving 80 sections (solid curve), 60 sections (dashed curve), 40 sections (dash-dotted curve) and 20 sections (dotted curve) at frequency $f = 2.06$ Hz. On the left is a plot of the flow oscillations, some differences are visible between the simulations, especially for the simulation with 20 sections. On the right is a plot of the pressure oscillations, some differences, especially for for the simulation with 20 sections, are also visible here. However, as the horizontal line indicates the mean pressure is the same for all simulations, $9.97 \cdot 10^4$ Pa.

When changing the number of sections it is simultaneously needed to change the position of the pinching pump and how many sections it covers. For the simulation involving 60 sections the pinching site is 3 sections wide and centered on the sixth section from the left. Naturally the pinching site will be 1, 2 and 4 sections wide for the simulations involving 20, 40 and 80 sections, while the position of the site is at section 2 for the simulation involving 20 sections, at section 4 and 5 for the simulation involving 40 sections, and at section 7, 8, 9 and 10 for the simulation involving 80 sections. The positions of the pinching site does not correlate completely for the four simulations.

Figure 5.15 shows a comparison of the four simulations through graphs of the oscillations of flow and pressure. It is visible how the curves in both graphs generally follow the same path but with minor deviations mostly at the peak of the oscillations, especially the curve for the simulation involving 20 sections seems to deviate from the others.

The mean pressure is similar for all the simulations, $9.97 \cdot 10^4$ Pa, but that is not the case for the mean flow: the calculations of the mean flow yielded 2.67 cm^3/s, -2.86 cm^3/s, -1.78 cm^3/s and -4.01 cm^3/s for the simulations involving 20, 40, 60 and 80 sections respectively.

The large differences in mean flow between the simulations may seem disheartening for the model stability but it is explained with the differences in compression profile. As defined by equation 5.3 the compression profile defined by

the minimum radius for each section of the pinching site depends on the number of sections included in the pinching site, which again depends on the number of sections included in the model, as it is the intention that the pinching site covers one tenth of the soft tube comparative to [Ottesen, 2003].

Therefore the compression profile will look different for each of the four simulations: For the first two it will be a square profile, for the third and fourth simulation it will be a staircase. Generally the more sections in the pinching site the better it will approximate a sinusoidal profile.

Ottesen [2003] reports a preliminary investigation that showed that the compression profile and the speed of the compressions are very influential to the direction and magnitude of the observed mean flow, which seems to be the case here.

Furthermore the compressed volume is different for each simulation; for the simulations involving 20, 40, 60 and 80 sections the compressed volume equals to 3.9 cm^3, 3.4 cm^3, 3.2 cm^3 and 3.0 cm^3 respectively. As this is the volume that is displaced by the pinching mechanism it will probably have some influence on the mean flow, though it does not appear to be in any systematic way.

Finally the numerical calculation of the mean flow may experience higher uncertainties when the number of sections is reduced. Already the computation of the mean relies on an algorithm to find an exact number of periods in the time-data, which are not spaced with equal time steps, and a numerical integration of the data for each of the variables based on a mean between right and left Riemann sums. Possibly this procedure becomes unstable with less sections in the model.

Though based on figure 5.15 it is seen that the oscillations follow the same general curves, which is an indication that the dynamics in the system is the same independent of the number os sections. Naturally more sections would produce better results, however the computation time is longer and even more problematic, a simulation with too many sections produce too much data for the computer to handle.

5.7 Conclusion to the case of Liebau's ring

The results of the simulations of Liebau's ring did not produce an exact validation of the cylindric model. As indicated by the comparison of results Liebau's ring is a complicated case where many different factors have influence on the observations of the Liebau effect; from the material properties of the tube to the frequency, shape and position of the pumping mechanism down to the very way the model is built.

Though it was not possible to reproduce data from Snitker et al. [2000] and the simulations by Ottesen [2003] only partially agree with the simulations using the pinching mechanism with compression ratio at 25 % and 50 %, the explanation for the discrepancies is clear; it all lies in the pumping mechanism, even for the comparison with the simulation data by Ottesen [2003] the pinching mechanism is only an approximation and as demonstrated in section 5.6.4 even pinching sites with different number of sections are hard to compare. Because the pumping mechanisms are not comparable it is only possible to make a partial comparison of experimental and simulation data.

On the other hand the simulations of Liebau's ring demonstrate the strengths of the cylindric model and the way it is built. Because of the modular construction of the model it is possible to compare the effect of different additions to the model and decide how they each influence the observation of flow and pressure in the model. It is clear from those observations that the impedance in the model has a very large influence on the observed Liebau effect.

All in all the simulations of Liebau's ring makes it clear that the model is able to handle complicated flow phenomena, that would not be possible with a Windkessel or transmission line model. The difference is that the Liebau effect is a non-linear phenomenon that would not be visible in a linear model, and even though the cylindric model is built from the principle of linear response theory inherent in the energy bond technique the composition of elements and transformations in the model grants it non-linear qualities.

Chapter 6

Construction of the Eccentric Tube Models

In this chapter the model constructed in chapter 4 will be expanded to have an elliptic cross-section, and by the end of the chapter to a layered model with an elliptic inner layer and circular outer layer following the observations of section 2.3.

The models herein will be referred to as the elliptic model, as the first model has an elliptic cross-section, and the embedded model, since the final step of the modeling procedure will be as an elliptic tube embedded inside a cylindric. Occasionally they may also be referred to as the eccentric models because elastic compliance and cross-sectional contraction are eccentric, as opposed to concentric compliance and cross-sectional contraction, which is the case for the model presented in chapter 4.

The modeling procedure in this chapter follows the same basic steps as in chapter 4 on the basis of the energy bond theory; at first the fundamental elements of elasticity, inertia and impedance are defined, then additional content of shear forces, tube curvature and Womersley theory is included and the characteristic equations of the model are derived, finally as an extra step in the modeling procedure in this chapter the embedded model will be constructed as an additional structure for the elliptic model.

6.1 The ellipse

An ellipse can be described by its major and minor semi-axis, a and b respectively, when $a = b$ the ellipse becomes a circle. A parameter describing an ellipse's deviance from a circle is known as the eccentricity,

$$\epsilon = \sqrt{\frac{a^2 - b^2}{a^2}} = \sqrt{1 - \left(\frac{b}{a}\right)^2}, \tag{6.1}$$

the range of ϵ belongs to $[0, 1[$, when $\epsilon = 0$ the ellipse is a a circle and with increasing ϵ the skewness of the ellipse increases. With $\epsilon = 1$ the ellipse degenerates.

The area of an ellipse is described simply by the formula $A = \pi ab$.

The ellipse is parameterized by $x = a\cos\theta$ and $y = b\sin\theta$ with $\theta \in [0, 2\pi]$. Thus the perimeter of the ellipse is described by the complete elliptic integral of the second kind,

$$\begin{aligned} C &= \int_0^{2\pi} \sqrt{a^2 \sin^2\theta + b^2 \cos^2\theta}\, d\theta \\ &= a \int_0^{2\pi} \sqrt{1 - \epsilon^2 \cos^2\theta}\, d\theta \\ &= 2\pi a \left[1 - \left(\frac{1}{2}\right)^2 \epsilon^2 - \left(\frac{1 \cdot 3}{2 \cdot 4}\right)^2 \frac{\epsilon^4}{3} - \left(\frac{1 \cdot 3 \cdot 5}{2 \cdot 4 \cdot 6}\right)^2 \frac{\epsilon^6}{5} - \ldots\right]. \end{aligned} \tag{6.2}$$

Approximations to the perimeter of the ellipse is a classic question of advanced geometry that have entertained many mathematicians over the centuries, the trick is to find an approximation that works well for the entire range of ϵ. One of the more prominent mathematicians who have attempted this is Ramanujan, who in 1914 suggested the formulas [Barnard et al., 2001],

$$C \approx \pi \left(3(a+b) - \sqrt{(3a+b)(a+3b)}\right), \tag{6.3}$$

or even better for a wider range of ϵ,

$$C \approx \pi(a+b)\left(1 + \frac{3\left(\frac{a-b}{a+b}\right)^2}{10 + \sqrt{4 - 3\left(\frac{a-b}{a+b}\right)^2}}\right). \tag{6.4}$$

6.2 The elliptic model

In the construction of the elliptic model it is assumed that the elastic tube is divided longitudinally into a finite number of tube sections. For each section, n, the model describe the physical properties pertaining to the liquid flow, pressure and elasticity of the tube section.

Each section is described with an elliptic cross-section given by the relation $\pi a_n b_n$ of the two semi-axes of the ellipse (henceforth known as the major and

minor axis of the ellipse). The equilibrium values of the major and minor axis of section n of the model are A_n and B_n respectively, which gives the equilibrium volume of the section, $\pi A_n B_n \Delta x$, where Δx is the length of a section of the tube.

The liquid inside the tube is described with a pressure, P_n, for each section of the tube and a volume flow, Q_n, for the volume of liquid flowing from section n to section $n+1$. Another quantity that will be important later in the modeling procedure is the momentum of flow, p_n, which by energy bond definitions is given by the integral of pressure and through the inertia of the liquid is proportional to the flow.

By the end of the modeling procedure differential equations for the change in the major axis, a_n, minor axis, b_n, and flow momentum, p_n, will be the characteristic equations for the elliptic model.

6.2.1 Elasticity of the tube wall

The elastic properties of each tube section is associated with the pressure response to a change in the volume of the tube. The volume of a section of the tube is a function of the dynamic major and minor axis, a_n and b_n, that will change as the tube deforms. Let the dynamical volume be the function, $V_n(a_n, b_n) = \pi a_n b_n \Delta x$, and by partial derivatives the change in volume is given by the change in the axes of the elliptic cross section,

$$dV_n = \frac{\partial V_n}{\partial a_n} da_n + \frac{\partial V_n}{\partial b_n} db_n = \pi \Delta x (b_n da_n + a_n db_n). \tag{6.5}$$

Thus the elasticity will be associated with the pressure response to the length-changes of the major axis from A_n to a_n and of the minor axis from B_n to b_n. The change of the axes of the elliptic cross-section will produce a change of the surface area of the wall of the tube, and the elasticity of the wall will produce a tension force in response to those changes.

The surface area of a section of the elliptic tube is given by the second elliptic integral,

$$s_n = \Delta x \int_0^{2\pi} \sqrt{a_n^2 \sin^2\theta + b_n^2 \cos^2\theta}\; d\theta, \tag{6.6}$$

with S_n being the corresponding equilibrium surface area given by A_n and B_n. Thus the change in surface area will be given by the change of the axes,

$$\begin{aligned} ds_n &= \Delta x \int_0^{2\pi} \frac{a_n \sin^2\theta}{\sqrt{a_n^2 \sin^2\theta + b_n^2 \cos^2\theta}}\; d\theta\; da_n \\ &\quad + \Delta x \int_0^{2\pi} \frac{b_n \cos^2\theta}{\sqrt{a_n^2 \sin^2\theta + b_n^2 \cos^2\theta}}\; d\theta\; db_n. \end{aligned} \tag{6.7}$$

The response to this surface area change is a surface tension, σ_n, which is given by the elastic modulus of the tube wall times the relative change in surface area. The elastic modulus is given by the thickness of the tube wall, h, times Young's modulus for the material of the tube wall, E. It is assumed that changes in the thickness of the tube wall due to stretch of the surface are small to the point of insignificance and that Young's modulus is uniform throughout the elliptic surface wall and throughout the tube in general. Therefore the surface tension will be,

$$\sigma_n = Eh\frac{\Delta s_n}{S_n}, \tag{6.8}$$

where Δs_n is an approximation to the infinitesimal ds_n, ie. $ds_n \approx s_n - S_n = \Delta s_n$.

By definition surface tension equals the derivative of surface energy with respect to surface area, so to get the total potential energy stored in the surface from the change in surface area integrate the surface tension from S_n to s_n,

$$U_{\sigma n} = \int_{S_n}^{s_n} \frac{Eh}{S_n}\left(s - S_n\right) ds = \frac{Eh}{2S_n}\left(s_n - S_n\right)^2. \tag{6.9}$$

This expression compares to the potential energy of a capacitor, $U_{\sigma n} = \frac{1}{2}\Delta s_n^2 / C_{\sigma n}$, which defines the elastic capacitance of the surface tension, $C_{\sigma n}$,

$$C_{\sigma n} = \frac{S_n}{Eh}. \tag{6.10}$$

This is the elastic capacitance of the surface in relation to the variables of surface area and surface tension, to get the capacitance in relation to the variables of axial length and force (or even volume and pressure) a transformation of coordinates is required.

The surface tension is by assumption uniform throughout the surface area, but when it is multiplied with the infinitesimal surface area segment and the curvature at a specific point on the surface an elastic reaction force perpendicular to the surface is obtained, which details how much the surface counteracts an area increase at that particular point.

The integrand of equation 6.6 gives the area of any segment of the surface, $\Delta x\sqrt{a_n^2 \sin^2\theta + b_n^2 \cos^2\theta}$. The surface curvature of an ellipse with parametrization $(a_n \cos\theta, b_n \sin\theta)$ is for any point on the surface given by the relation [Pressley, 2001],

$$\kappa(\theta) = \frac{a_n b_n}{\sqrt{a_n^2 \sin^2\theta + b_n^2 \cos^2\theta}^3}. \tag{6.11}$$

The product of these three is the reaction force at any given point on the surface to an increase in surface area,

$$F = a_n b_n \Delta x E h \frac{\sqrt{a_n^2 \sin^2\theta + b_n^2 \cos^2\theta}}{\sqrt{a_n^2 \sin^2\theta + b_n^2 \cos^2\theta}^3} \frac{\Delta s_n}{S_n}. \tag{6.12}$$

In order to separate the force into composites reacting in the direction of the axes of the ellipse multiply F with the cosine to the angle, ϕ, between the force vector and the horizontal plane to find the horizontal component in direction of the major axis, and similarly multiply with the sine to the angle to find the vertical component in direction of the minor axis. In terms of the parametrization of the ellipse the sine and cosine is given as (notice that $\theta \neq \phi$),

$$\sin\phi = \frac{a_n \sin\theta}{\sqrt{a_n^2 \sin^2\theta + b_n^2 \cos^2\theta}}, \tag{6.13}$$

$$\cos\phi = \frac{b_n \cos\theta}{\sqrt{a_n^2 \sin^2\theta + b_n^2 \cos^2\theta}}. \tag{6.14}$$

To find the total force working in the horizontal direction each horizontal force component must be integrated over the angle ϕ from $-\pi/2$ to $\pi/2$, and similarly each vertical force component must be integrated from 0 to π to find the total vertical force.

Due to symmetry of the ellipse the boundary values of ϕ and θ are identical and the integral only needs to cover one quarter of the elliptic curve, thus the two integrals can be computed with the help of the simpler integrals of the product between the infinitesimal area segment, $\Delta x\sqrt{a_n^2 \sin^2\theta + b_n^2 \cos^2\theta}d\theta$, the curvature of the ellipse, and the angles given by equation 6.13 and 6.14,

$$\begin{aligned} I_a &= \Delta x a_n b_n^2 \int_0^{\pi/2} \frac{\cos\theta}{\sqrt{a_n^2 \sin^2\theta + b_n^2 \cos^2\theta}} \frac{\sqrt{a_n^2 \sin^2\theta + b_n^2 \cos^2\theta}}{\sqrt{a_n^2 \sin^2\theta + b_n^2 \cos^2\theta}^3} d\theta \\ &= \Delta x \left(1-\epsilon^2\right) \int_0^{\pi/2} \frac{\cos\theta}{\sqrt{1-\epsilon^2\cos^2\theta}^3} d\theta = \Delta x \frac{1-\epsilon^2}{1-\epsilon^2} = \Delta x, \end{aligned} \tag{6.15}$$

$$\begin{aligned} I_b &= \Delta x a_n^2 b_n \int_0^{\pi/2} \frac{\sin\theta}{\sqrt{a_n^2 \sin^2\theta + b_n^2 \cos^2\theta}} \frac{\sqrt{a_n^2 \sin^2\theta + b_n^2 \cos^2\theta}}{\sqrt{a_n^2 \sin^2\theta + b_n^2 \cos^2\theta}^3} d\theta \\ &= \Delta x \sqrt{1-\epsilon^2} \int_0^{\pi/2} \frac{\sin\theta}{\sqrt{1-\epsilon^2\cos^2\theta}^3} d\theta = \Delta x \frac{\sqrt{1-\epsilon^2}}{\sqrt{1-\epsilon^2}} = \Delta x. \end{aligned} \tag{6.16}$$

The product of the surface tension and one of these two integrals gives the horizontal or vertical force reaction to a change of the surface area,

$$F_{\sigma an} = 2I_a\sigma_n = \frac{2\Delta xEh}{S_n}\Delta s_n \quad , \quad F_{\sigma bn} = 2I_b\sigma_n = \frac{2\Delta xEh}{S_n}\Delta s_n. \tag{6.17}$$

To find the force response to a change in the length of the major axis multiply F_{an} with the surface change relative to the length-change of the axis, that is the partial derivative of s_n with respect to a_n. And likewise for the force response to a change of the minor axis,

$$\begin{aligned} F_{\sigma an} &= \frac{2\Delta xEh}{S_n}\frac{\partial s_n}{\partial a_n}\Delta a_n \\ &= \frac{2\Delta x^2Eh}{S_n}\int_0^{2\pi}\frac{a_n\sin^2\theta}{\sqrt{a_n^2\sin^2\theta + b_n^2\cos^2\theta}}\,d\theta\;\Delta a_n, \end{aligned} \tag{6.18}$$

$$\begin{aligned} F_{\sigma bn} &= \frac{2\Delta xEh}{S_n}\frac{\partial s_n}{\partial b_n}\Delta b_n \\ &= \frac{2\Delta x^2Eh}{S_n}\int_0^{2\pi}\frac{b_n\cos^2\theta}{\sqrt{a_n^2\sin^2\theta + b_n^2\cos^2\theta}}\,d\theta\;\Delta b_n, \end{aligned} \tag{6.19}$$

where the partial derivatives of s_n are found through equation 6.7, and where $\Delta a_n = a_n - A_n$ and $\Delta b_n = b_n - B_n$ are approximations to the infinitesimals da_n and db_n.

Notice that in relation to energy bond conventions the forces defined by equation 6.18 and 6.19 are not the effort variables comparable to Δa_n and Δb_n of the energy bond model. For example, choose Δa_n as one variable of the energy bond then the corresponding effort variable is defined as $e_{\sigma an} = T_1(T_1\Delta a_n + T_2\Delta b_n)/C_{\sigma n}$, where T_1 and T_2 are coordinate transformation ratios defined by the integrals in equation 6.7; $T_1 = \partial s_n/\partial a_n$ and $T_2 = \partial s_n/\partial b_n$. In the case of a circular cross-section this would lead to an effort $e_{\sigma an} = \pi F_{\sigma an}$, though for an ellipse it is more complicated.

As stated earlier the volume of a section of the tube is computed as the length of the section, Δx, times the cross-sectional area, so that $V_n = \pi\Delta x\ a_nb_n$. It follows directly from its partial derivative that a change of the volume comes from the separate changes of the axes,

$$dV_n = \pi\Delta x\left(b_nda_n + a_ndb_n\right), \tag{6.20}$$

where each term in the equation can be considered as an individual volume change where one axis is constrained and the other is changed,

$$\Delta V_{an} = \pi \Delta x b_n (a_n - A_n), \tag{6.21}$$
$$\Delta V_{bn} = \pi \Delta x a_n (b_n - B_n). \tag{6.22}$$

The total change of the volume of a section is made as a sum of the individual volume changes from the change in the axes of the elliptic cross-section. Furthermore equations 6.21 and 6.22 detail how the change in the lengths of the axes is transformed to a volume change.

The volume change gives rise to the dynamical pressure coming from the tension force from the walls of the tube. The increase in pressure associated with the change of volume is according to the energy bond graph given through the effort comparative to the length-change of the axes, $e_{an} = T_1(T_1\Delta a_n + T_2\Delta b_n)/C_n$ and $e_{bn} = T_2(T_1\Delta a_n + T_2\Delta b_n)/C_n$, which are transformed into the pressure by applying the coordinate transformation found in equations 6.21 and 6.22,

$$P_{an} = \frac{e_{an}}{\pi \Delta x b_n} = \frac{Eh}{\pi \Delta x S_n b_n} \frac{\partial s_n}{\partial a_n} \left(\frac{\partial s_n}{\partial a_n} \Delta a_n + \frac{\partial s_n}{\partial b_n} \Delta b_n \right), \tag{6.23}$$
$$P_{bn} = \frac{e_{bn}}{\pi \Delta x a_n} = \frac{Eh}{\pi \Delta x S_n a_n} \frac{\partial s_n}{\partial b_n} \left(\frac{\partial s_n}{\partial a_n} \Delta a_n + \frac{\partial s_n}{\partial b_n} \Delta b_n \right). \tag{6.24}$$

The pressure given by equations 6.23 and 6.24 must be the same for both axes as it is simply the dynamic pressure, $P_n = P_{an} = P_{bn}$. Setting these two equations equal to each other gives two possibilities. The first possible outcome is the relation,

$$\frac{1}{b_n} \frac{\partial s_n}{\partial a_n} = \frac{1}{a_n} \frac{\partial s_n}{\partial b_n}, \tag{6.25}$$

which looks very satisfying but it only applies if $a_n = b_n$, that is if the elliptic cross-section is a circle. This condition is not sufficient for the elliptic tube, though it gives an opportunity to check if the resulting capacitance fits with the capacitance of the cylindric tube by referring to section 4.2.1,

$$\begin{aligned} C_n' &= \frac{\Delta v_n}{P_n} \\ &= \frac{\pi \Delta x \left(b_n \Delta a_n + a_n \Delta b_n \right)}{\frac{Eh}{\pi \Delta x S_n b_n} \frac{\partial s_n}{\partial a_n} \left(\frac{\partial s_n}{\partial a_n} \Delta a_n + \frac{\partial s_n}{\partial b_n} \Delta b_n \right)} \\ &= \pi^2 \Delta x^2 \frac{S_n}{Eh} \frac{b_n \Delta a_n + a_n \Delta b_n}{\left(\frac{\partial s_n}{\partial a_n} \right)^2 \left(\Delta a_n + \frac{a_n}{b_n} \Delta b_n \right)} b_n \\ &= \frac{S_n}{Eh} \left(\frac{\pi \Delta x}{\frac{\partial s_n}{\partial a_n}} \right)^2 b_n^2, \end{aligned} \tag{6.26}$$

which fits with equation 4.6 for the capacitance of the circular tube, when $a_n = b_n$.

The other possibility by setting equation 6.23 equal to 6.24 is the dynamical relation,

$$\frac{\partial s_n}{\partial a_n}\Delta a_n = -\frac{\partial s_n}{\partial b_n}\Delta b_n, \tag{6.27}$$

which gives a relation between the surface increase resulting from a change of the major axis compared to the likewise increase from a change of the minor axis, but held against equation 6.7 it is clear that it leads to $ds_n = 0$, which implies that the axial lengths can only be changed in such a way that the surface area is held constant.

The conclusion is that the description of the elasticity is not yet completed. It lies implicit in the current description of the elasticity that even though the cross-section of the tube can be elliptically deformed its preferred state will be that of a circular cross-section, and only in its circular configuration will the tube actually change its surface area through the relation in equation 6.25. In order to complete this description another elastic property must be included; a structural shear elasticity that will retain the preference of an elliptic cross-section with a certain eccentricity $\epsilon_n = \sqrt{1 - b_n^2/a_n^2}$.

A change of eccentricity of the elliptic cross-section will be described as a shear deformation of the tube, and the tube will naturally have an elastic response to such deformations as well. Shear deformations are described in the terms of the change of angles in the internal structure of the body under circumstances where the volume of the body is held constant.

The forces on the principal axes of the ellipse puts the elliptic tube under conditions of 'pure shear', which is defined as equivalent to a combination of tension and compression stresses at right angles to each other [Feynman et al., 1964, sec. 38-4]. Pure shear can be visualized by picturing the sheared body inscribed inside a rectangular shape and then focus on the change in the angle between the two diagonals of the rectangle when the shape of the body is changed. For an elliptic body such a rectangle is easily described with length $2a_n$ and height $2b_n$, and thus the angle between the diagonals will be $\phi_n = 2\arctan(b_n/a_n)$.

When the length of an axis is changed, the rectangle will change accordingly, and so will the angle between the diagonals. The change in this angle is the shear strain, γ_n, and it can be found through the derivative [Feynman et al., 1964, sec. 38-2],

$$\begin{aligned} \gamma_n &= d\phi_n = \left(\frac{2}{1 + b_n^2/a_n^2}\right)\left(\frac{-b_n}{a_n^2}da_n + \frac{1}{a_n}db_n\right) \\ &= \left(\frac{2a_n b_n}{a_n^2 + b_n^2}\right)\left(\frac{1}{b_n}db_n - \frac{1}{a_n}da_n\right), \end{aligned} \tag{6.28}$$

which naturally can be ascribed to the changes of a_n and b_n.

In fact it would be more correct to name the tangent of the angle change as the shear strain, $\gamma_n = \tan d\phi_n$, but this will violate the linear response doctrine of the energy bond formalism (see section 4.1) and generally it is hardly ever applied since for small angle changes $\tan d\phi_n \approx d\phi_n$.

Structurally it is specified that the elliptic configuration of least potential energy is described by the angle, $\Phi_n = 2\arctan(B_n/A_n)$, which identifies the state of zero shear strain, $\gamma_{n0} = 0$. Whenever the elliptic cross-section attains another shape shear forces will try to counter the deformation and return the shape of the ellipse to its minimum energy state.

The elastic reaction to the shear strain is the shear stress, τ_n, it is defined proportionally to the strain and the constant of proportionality is the shear modulus, G. The shear modulus has the same units as Young's modulus and in many simple cases it will be defined as one third of Young's modulus, $G = E/3$, though it is typically a little bit less.

The shear stress details the amount of tension the elliptic tube will be under when it is deformed, when multiplied with the volume of the tube wall. Given by the thickness of the wall, h, times the surface area, the potential energy stored in the tube by the shear deformation is achieved,

$$u_{\gamma n} = Gh\ d\gamma_n\ \Delta x \int_0^{2\pi} \sqrt{A_n^2 \sin^2\theta + B_n^2 \cos^2\theta} d\theta = GhS_n\ d\gamma_n. \tag{6.29}$$

With the changes in shear strain approximated by the difference $d\gamma_n = \gamma_n - \gamma_{n0}$ this expression is integrated over the total shear strain from γ_{n0} to γ_n in order to find the total potential energy,

$$U_{\gamma n} = \int_{\gamma_{n0}}^{\gamma_n} GhS_n\left(\gamma - \gamma_{n0}\right) d\gamma = \frac{GhS_n}{2}\left(\gamma_n - \gamma_{n0}\right)^2. \tag{6.30}$$

Through the potential energy, $U_{\gamma n} = \frac{1}{2}\Delta\gamma_n^2/C_{\gamma n}$, the capacitance is defined

$$C_{\gamma n} = \frac{1}{GhS_n}. \tag{6.31}$$

Thus another contribution is added to the force that changes the length of the axes of the elliptic cross-section, namely that of the structural shear elasticity, which can be found by applying the transformation ratios between the shear strain and the change of the axes of the ellipse defined in equation 6.28 to the capacitance of the structural elasticity in equation 6.31,

$$F_{\gamma an} = GhS_n \left(\frac{2a_n b_n}{a_n^2 + b_n^2}\right)^2 \frac{1}{a_n}\left(\frac{1}{a_n}\Delta a_n - \frac{1}{b_n}\Delta b_n\right), \tag{6.32}$$

$$F_{\gamma bn} = -GhS_n \left(\frac{2a_n b_n}{a_n^2 + b_n^2}\right)^2 \frac{1}{b_n}\left(\frac{1}{a_n}\Delta a_n - \frac{1}{b_n}\Delta b_n\right). \tag{6.33}$$

Together the structural shear elasticity and the surface area elasticity define the elastic properties of the elliptic cross-section of the tube. The combined elastic force is the sum of forces from these two elastic properties, which will add a term, $F_{\gamma an}/\pi\Delta x b_n$, to the pressure in equation 6.23 and another term, $F_{\gamma bn}/\pi\Delta x a_n$, to equation 6.24, thus expanding the expression for the pressure, which will be explored later in equation 6.95.

6.2.2 Inertia of the liquid

The inductance of the model is a representation of the inertia of mass that the liquid in the tube posses on the acceleration of flow. In in the model the hydrodynamic pressure is defined in the center of a section, but the flow is calculated at the crossing between two sections. Therefore, to know the inertia of the flow the mass of liquid needs to be defined as an average mass between two sections of the model,

$$M_n = \rho\Delta x\pi\sqrt{a_n a_{n+1}}\sqrt{b_n b_{n+1}}, \tag{6.34}$$

where ρ is the density of the liquid and $\sqrt{a_n a_{n+1}}$ is a geometric mean between the major axis of a section and the major axis of the next section (the geometric mean is chosen over the arithmetic mean for practical reasons, which should be apparent when it is squared further down).

Define the mean velocity of the liquid as the volume flow divided by the cross-sectional area,

$$v_n = \frac{Q_n}{\pi\sqrt{a_n a_{n+1}}\sqrt{b_n b_{n+1}}}. \tag{6.35}$$

The kinetic energy of the flow in a section is defined as one-half mass times velocity squared,

$$\begin{aligned} E_n &= \psi\frac{1}{2}M_n v_n^2 = \psi\frac{\rho\Delta x\pi\sqrt{a_n a_{n+1}}\sqrt{b_n b_{n+1}}}{2\left(\pi\sqrt{a_n a_{n+1}}\sqrt{b_n b_{n+1}}\right)^2}Q_n^2 \\ &= \psi\frac{\rho\Delta x}{2\pi\sqrt{a_n a_{n+1}}\sqrt{b_n b_{n+1}}}Q_n^2, \end{aligned} \tag{6.36}$$

where ψ is the inertia correction factor specified by the Womersley number in the elliptical regime, which will be investigated further in section 6.3.3.

Through energy bond techniques every energy bond will be associated with two variables whose product will be the energy conveyed per time, but it is possible to transform one of these to a new variable so that the product will only be the energy - for the volume flow the associated transformed variable is the momentum of the flow.

Define a momentum function such that the derivative of the kinetic energy with respect to this momentum is the volume flow,

$$\frac{\partial E_n}{\partial p'_n} = Q_n, \tag{6.37}$$

which makes the momentum, p'_n,

$$p'_n = \psi \frac{\rho \Delta x}{\pi \sqrt{a_n a_{n+1}} \sqrt{b_n b_{n+1}}} Q_n = \psi \rho \Delta x v_n. \tag{6.38}$$

This can be proved by substituting the momentum into the equation for the kinetic energy,

$$\begin{aligned} E_n &= \psi \frac{\rho \Delta x}{2\pi \sqrt{a_n a_{n+1}} \sqrt{b_n b_{n+1}}} \left(\frac{\pi \sqrt{a_n a_{n+1}} \sqrt{b_n b_{n+1}}}{\psi \rho \Delta x} \right)^2 {p'_n}^2 \\ &= \frac{1}{2} \frac{\pi \sqrt{a_n a_{n+1}} \sqrt{b_n b_{n+1}}}{\psi \rho \Delta x} {p'_n}^2, \end{aligned} \tag{6.39}$$

and taking the derivative with respect to p'_n,

$$\frac{\partial E_n}{\partial p'_n} = \frac{\pi \sqrt{a_n a_{n+1}} \sqrt{b_n b_{n+1}}}{\psi \rho \Delta x} p'_n = Q_n. \tag{6.40}$$

Furthermore equation 6.39 can be used to define the inductance of the model, L_n, through the definition of the energy of a self-inductor, $E_n = \frac{1}{2} {p'_n}^2 / L_n$,

$$L_n = \psi \frac{\rho \Delta x}{\pi \sqrt{a_n a_{n+1}} \sqrt{b_n b_{n+1}}}. \tag{6.41}$$

6.2.3 Poiseuille resistance

The resistance of the model is defined through the Poiseuille equation, which is reinvented for a tube with an elliptical cross-section. To rephrase, Poiseuille flow is defined as steady laminar pressure driven flow of a non-compressible liquid, thus most of the terms of the general Navier-Stokes equation are discarded, which makes it into the much simpler Poisson equation,

$$\nabla P(x) = \eta \nabla^2 v(a, b), \tag{6.42}$$

in the coordinates (a, b, x), where a and b refer to the cross-sectional dimension in direction of the major and minor axis, and where x is the longitudinal coordinate along the length of the tube. The pressure, $P(x)$, only depends on longitudinal dimension and the velocity, $v(a, b)$, is steady and thus only depends on the cross-sectional dimensions. η is the dynamic viscosity of the liquid.

Given the assumption that the flow is driven by a pressure difference between the endpoints of the tube, the left hand side of equation 6.42 is simply the pressure difference over the length,

$$-\frac{\Delta P}{\eta \Delta x} = \frac{\partial^2 v}{\partial a^2} + \frac{\partial^2 v}{\partial b^2}, \tag{6.43}$$

where Δx is the length between the endpoints of the tube and $-\Delta P$ is the pressure difference taken as negative since the pressure in the frontal end of the tube needs to be higher in order to drive the flow towards the distal end.

A unique solution to this partial differential equation is found through the constants A, B and K,

$$v(a,b) = \frac{\Delta P}{\eta \Delta x} K \left(1 - \frac{a^2}{A^2} - \frac{b^2}{B^2}\right), \tag{6.44}$$

where A and B are the major and minor axis of the elliptic cross-section (not related to the equilibrium axes A_n and B_n just yet), fulfilling the simple boundary conditions, $v(A,0) = v(0,B) = 0$. The general no-slip boundary condition is given through the constant K,

$$K = \frac{A^2 B^2}{2\left(A^2 + B^2\right)}. \tag{6.45}$$

From equation 6.44 the flow rate through the tube is defined as the integral of the velocity taken over the cross-sectional area,

$$\begin{aligned} Q &= \int_{a,b} v(a,b)\, db\, da \\ &= \frac{\Delta P}{\eta \Delta x} \frac{A^2 B^2}{2\left(A^2 + B^2\right)} 4 \int_0^A \int_0^{B\sqrt{1-a^2/A^2}} \left(1 - \frac{a^2}{A^2} - \frac{b^2}{B^2}\right) db\, da \\ &= \frac{\Delta P}{\eta \Delta x} \frac{A^2 B^2}{2\left(A^2 + B^2\right)} 4 \frac{\pi AB}{8} = \frac{\pi}{4} \frac{\Delta P}{\eta \Delta x} \frac{A^3 B^3}{A^2 + B^2}. \end{aligned} \tag{6.46}$$

Therefore the Poiseuille resistance of the elliptical tube becomes

$$Z = \frac{\Delta P}{Q} = \frac{4}{\pi} \frac{\eta \Delta x \left(A^2 + B^2\right)}{A^3 B^3}. \tag{6.47}$$

In the terms of the model the flow is defined between two neighboring sections through the use of the geometric mean between the axes of the two sections, $\sqrt{a_n a_{n+1}}$, thus the Poiseuille resistance will have the following equation in the model, parallel to equation 4.14,

$$Z_n = \frac{\Delta P_n}{Q_n} = \frac{4}{\pi} \frac{\eta \Delta x \left(a_n a_{n+1} + b_n b_{n+1}\right)}{\sqrt{a_n a_{n+1}}^3 \sqrt{b_n b_{n+1}}^3}. \tag{6.48}$$

6.2.4 The Bernoulli effect

The total energy in the tube is given by the sum of potential and kinetic energy, which are again given by the sum of potential energy, U_n, and kinetic energy, E_n, for each section. When taking the derivative of the total energy of the model with respect to a certain charge variable (for instance Δa_n) the associated potential variable is achieved (notice that for all the terms in the sum of the total energy, only four are dependent on a_n),

$$\begin{aligned}
\frac{\partial E}{\partial a_n} &= \frac{\partial}{\partial a_n}\left(U_{\sigma an} + U_{\gamma an} + E_{n-1} + E_n\right) \\
&= \frac{Eh}{S_n}\frac{\partial s_n}{\partial a_n}\left(\frac{\partial s_n}{\partial a_n}\Delta a_n + \frac{\partial s_n}{\partial b_n}\Delta b_n\right) \\
&\quad + GhS_n\left(\frac{2a_nb_n}{a_n^2+b_n^2}\right)^2\frac{1}{a_n}\left(\frac{1}{a_n}\Delta a_n - \frac{1}{b_n}\Delta b_n\right) \\
&\quad + \frac{\partial}{\partial a_n}\left(\frac{\pi\sqrt{a_{n-1}a_n}\sqrt{b_{n-1}b_n}}{2\psi\rho\Delta x}{p'_{n-1}}^2 + \frac{\pi\sqrt{a_na_{n+1}}\sqrt{b_nb_{n+1}}}{2\psi\rho\Delta x}{p'_n}^2\right),
\end{aligned} \tag{6.49}$$

by definition the two first terms of this equation is equal to $\pi\Delta x b_n P_n$, which makes this complicated expression more simple,

$$\begin{aligned}
\frac{\partial E}{\partial a_n} &= \pi\Delta x b_n P_n + \frac{\pi}{4\psi\rho\Delta x}\left(\sqrt{\frac{a_{n-1}}{a_n}}\sqrt{b_{n-1}b_n}{p'_{n-1}}^2 + \sqrt{\frac{a_{n+1}}{a_n}}\sqrt{b_nb_{n+1}}{p'_n}^2\right) \\
&= \pi\Delta x b_n P_n + \frac{\pi\psi\rho\Delta x}{4}\left(\sqrt{\frac{a_{n-1}}{a_n}}\sqrt{b_{n-1}b_n}v_{n-1}^2 + \sqrt{\frac{a_{n+1}}{a_n}}\sqrt{b_nb_{n+1}}v_n^2\right) \\
&= \pi\Delta x b_n\left(P_n + \frac{\psi\rho}{4}\left(\sqrt{\frac{a_{n-1}}{a_n}}\sqrt{\frac{b_{n-1}}{b_n}}v_{n-1}^2 + \sqrt{\frac{a_{n+1}}{a_n}}\sqrt{\frac{b_{n+1}}{b_n}}v_n^2\right)\right).
\end{aligned} \tag{6.50}$$

It is clear that the potential variable is not only the transformed pressure, as would be expected, two other terms also offer contributions to the potential. A similar expression would result from taking the derivative with respects to b_n. To investigate those extra terms redefine the momentum from equation 6.38,

$$p_n = \sqrt{\frac{\sqrt{a_na_{n+1}}\sqrt{b_nb_{n+1}}}{\sqrt{A_nA_{n+1}}\sqrt{B_nB_{n+1}}}}\,p'_n. \tag{6.51}$$

This transforms the kinetic energy,

$$\begin{aligned} E_n &= \frac{\pi\sqrt{a_n a_{n+1}}\sqrt{b_n b_{n+1}}}{2\psi\rho\Delta x}\left(\sqrt{\frac{\sqrt{A_n A_{n+1}}\sqrt{B_n B_{n+1}}}{\sqrt{a_n a_{n+1}}\sqrt{b_n b_{n+1}}}}p_n\right)^2 \\ &= \frac{1}{\psi}\frac{\pi\sqrt{A_n A_{n+1}}\sqrt{B_n B_{n+1}}}{2\rho\Delta x}p_n^2, \end{aligned} \tag{6.52}$$

which in turn transforms the inductance,

$$L_n = \psi\frac{\rho\Delta x}{\pi\sqrt{A_n A_{n+1}}\sqrt{B_n B_{n+1}}}. \tag{6.53}$$

The new definition of the momentum of flow given by equation 6.51 is investigated by taking its time-derivative (this should give the potential at the inductance),

$$\begin{aligned} \frac{dp_n}{dt} &= \sqrt{\frac{\sqrt{a_n a_{n+1}}\sqrt{b_n b_{n+1}}}{\sqrt{A_n A_{n+1}}\sqrt{B_n B_{n+1}}}}\frac{dp'_n}{dt} \\ &\quad + \frac{1}{2}\frac{p'_n}{\sqrt{\sqrt{A_n A_{n+1}}\sqrt{B_n B_{n+1}}}}\sqrt{\frac{\sqrt{b_n b_{n+1}}}{\sqrt{a_n a_{n+1}}}} \\ &\qquad \cdot\left(\frac{1}{2}\sqrt{\frac{a_{n+1}}{a_n}}\frac{da_n}{dt} + \frac{1}{2}\sqrt{\frac{a_n}{a_{n+1}}}\frac{da_{n+1}}{dt}\right) \\ &\quad + \frac{1}{2}\frac{p'_n}{\sqrt{\sqrt{A_n A_{n+1}}\sqrt{B_n B_{n+1}}}}\sqrt{\frac{\sqrt{a_n a_{n+1}}}{\sqrt{b_n b_{n+1}}}} \\ &\qquad \cdot\left(\frac{1}{2}\sqrt{\frac{b_{n+1}}{b_n}}\frac{db_n}{dt} + \frac{1}{2}\sqrt{\frac{b_n}{b_{n+1}}}\frac{db_{n+1}}{dt}\right) \\ &= \sqrt{\frac{\sqrt{a_n a_{n+1}}\sqrt{b_n b_{n+1}}}{\sqrt{A_n A_{n+1}}\sqrt{B_n B_{n+1}}}}\frac{dp'_n}{dt} \\ &\quad + \frac{1}{4}\frac{p_n}{\sqrt{a_n a_{n+1}}}\left(\sqrt{\frac{a_{n+1}}{a_n}}\frac{da_n}{dt} + \sqrt{\frac{a_n}{a_{n+1}}}\frac{da_{n+1}}{dt}\right) \\ &\quad + \frac{1}{4}\frac{p_n}{\sqrt{b_n b_{n+1}}}\left(\sqrt{\frac{b_{n+1}}{b_n}}\frac{db_n}{dt} + \sqrt{\frac{b_n}{b_{n+1}}}\frac{db_{n+1}}{dt}\right). \end{aligned} \tag{6.54}$$

In the end the derivative of the momentum is achieved,

$$\begin{aligned} \frac{dp_n}{dt} &= \sqrt{\frac{\sqrt{a_n a_{n+1}}\sqrt{b_n b_{n+1}}}{\sqrt{A_n A_{n+1}}\sqrt{B_n B_{n+1}}}}\frac{dp'_n}{dt} \\ &\quad + \frac{p_n}{4a_n}\frac{da_n}{dt} + \frac{p_n}{4a_{n+1}}\frac{da_{n+1}}{dt} + \frac{p_n}{4b_n}\frac{db_n}{dt} + \frac{p_n}{4b_{n+1}}\frac{db_{n+1}}{dt}. \end{aligned} \tag{6.55}$$

It is clear that the momentum derivative here comes from the transformed derivative of the original momentum together with four other terms that actually coincide with the length-changes of the axes of the two neighboring sections, between which the momentum is calculated. The time-derivative of an axis, da_n/dt, is a current input to the combined elastic capacitance of a section, and it is converted through a new connection to the potential at the inductance.

With that result the derivative of the total energy is investigated once more,

$$\begin{aligned}\frac{\partial E}{\partial a_n} &= \pi\Delta x b_n P_n + \frac{1}{\psi}\frac{\pi}{4\rho\Delta x}\left(\sqrt{\frac{a_{n-1}}{a_n}}\sqrt{b_{n-1}b_n}{p'_{n-1}}^2 + \sqrt{\frac{a_{n+1}}{a_n}}\sqrt{b_n b_{n+1}}{p'_n}^2\right)\\ &= \pi\Delta x b_n P_n\\ &\quad + \frac{1}{\psi}\frac{\pi}{4\rho\Delta x}\left(\frac{\sqrt{A_{n-1}A_n}\sqrt{B_{n-1}B_n}}{a_n}p_{n-1}^2 + \frac{\sqrt{A_n A_{n+1}}\sqrt{B_n B_{n+1}}}{a_n}p_n^2\right)\\ &= \pi\Delta x b_n P_n + \frac{p_{n-1}}{4a_n}\frac{p_{n-1}}{L_{n-1}} + \frac{p_n}{4a_n}\frac{p_n}{L_n}, \end{aligned} \tag{6.56}$$

and likewise for the energy derivative with respects to b_n,

$$\frac{\partial E}{\partial b_n} = \pi\Delta x a_n P_n + \frac{p_{n-1}}{4b_n}\frac{p_{n-1}}{L_{n-1}} + \frac{p_n}{4b_n}\frac{p_n}{L_n}. \tag{6.57}$$

These two equations clearly support the idea that a connection must exist in the model between the elastic forces and the inertia of the flow. This connection given by the potential and kinetic energies in the tube is in accordance with the Bernoulli equation discussed in section 3.5.

6.3 Additional effects

With the surface area elasticity and structural shear elasticity, the inertia of mass and the Poiseuille resistance the core elements of the model is defined and with the Bernoulli effect the connection between potential and kinetic energy of the model is given with the transformation of variables. The model now includes the fundamental physical principles of the liquid flow in an elastic elliptic tube, but it is not done yet.

To further improve the model the next step include three additional effects that increase the model's applicability in relation to liquid flow in an elastic tube: the longitudinal elasticity of the tube to counteract a lengthwise increase in surface area of the tube and to create inter-dependency of the axial lengths between the sections, the minor loss resistance affecting the pressure when the flow runs through a curved tube, and the Womersley theory of pulsatile flow and pressure. These additions are presented one by one and it is explained how that effect is included in the elliptic model.

6.3.1 Longitudinal shear tensions

The first adjustment to the model is a term that describes the shear tensions longitudinal along the length of the tube. This term is more an ad hoc approximation than a theoretical founded addition to the model. As such the term does not accommodate for changes in the length of the tube but only for differences in the cross-sectional area between sections.

The shear tensions extend between two neighboring sections of the tube and depend on the perimeter of the elliptic cross-section of the tube. As the shear tensions are defined on the intersection between two tube sections they rely on a mean equilibrium perimeter based on the geometric mean between the axes of the two neighboring sections, $\sqrt{A_n A_{n+1}}$ and $\sqrt{B_n B_{n+1}}$. In most cases these will be equal to A_n and B_n, but not if the tube is tapered, in any case the mean perimeter is defined,

$$\Omega_n = \int_0^{2\pi} \sqrt{A_n A_{n+1} \sin^2\theta + B_n B_{n+1} \cos^2\theta}\, d\theta. \tag{6.58}$$

Define the elastic force of section n relative to section $n+1$ when one section has the length of one of its axes stretched in relation to the other section, this force is proportional to the change in length between the axes, inversely proportional to the length of one section, and proportional to half the perimeter of the ellipse (tension forces only apply where the ellipse is stretched). The proportionality factor is the thickness of the tube wall times the shear modulus (where shear modulus here is defined as, $G = E/3$),

$$F_{san} = \frac{Gh}{2\Delta x}\Omega_n \left((a_{n+1} - A_{n+1}) - (a_n - A_n)\right), \tag{6.59}$$

$$F_{sbn} = \frac{Gh}{2\Delta x}\Omega_n \left((b_{n+1} - B_{n+1}) - (b_n - B_n)\right). \tag{6.60}$$

Integrate the force over the length change of the major axis to get the potential energy of the shear tensions,

$$\begin{aligned} U_{san} &= \int_{a_n - A_n}^{a_{n+1} - A_{n+1}} \frac{Gh}{2\Delta x}\Omega_n \left((a_{n+1} - A_{n+1}) - \Delta a\right) d\Delta a \\ &= \frac{Gh}{4\Delta x}\Omega_n \left((a_{n+1} - A_{n+1}) - (a_n - A_n)\right)^2, \end{aligned} \tag{6.61}$$

and likewise for the change of the minor axis,

$$U_{sbn} = \frac{Gh}{4\Delta x}\Omega_n \left((b_{n+1} - B_{n+1}) - (b_n - B_n)\right)^2. \tag{6.62}$$

Use the definition of potential energy of a capacitor to find the capacitance of the shear elasticity, $U_{san} = \frac{1}{2}\left(\Delta a_{n+1} - \Delta a_n\right)^2 / C_{san}$,

$$C_{sn} = C_{san} = C_{sbn} = \frac{\Delta x}{Gh}\frac{2}{\Omega_n}. \tag{6.63}$$

Furthermore these shear tensions should be damped so that there is a small energy loss from friction in the tube wall given by the changes in cross-sectional area. This is modeled by a resistance in series with the capacitance, the value of this resistance is decided from the relation of the characteristic period of an RC-circuit, $T = Z_s C_s$, such that all oscillations with frequencies above 100 Hz are be damped,

$$Z_{sn} = \frac{T}{C_{sn}} = \frac{0.01\,\mathrm{s}}{C_{sn}}. \tag{6.64}$$

6.3.2 Curvature of the tube

The second addition to the model is the resistance induced by the curvature of the tube, which cause a pressure loss proportional to the product of flow and momentum of the flow.

The curvature resistance is a representative of the so called minor losses, which cover a range of special conditions that produce resistance and energy loss in the liquid flow, dependent on the external conditions presented by the tube. Some of the typical minor losses are bends, branches and valves in the tubes, but it is clear that for the elliptic tube another condition could be relevant, namely the twisting of the tube. That condition is not included in the model, and so it is implicitly assumed that the tube does not twist or that twisting produce a minor loss, which is small enough to be ignored.

When the tube curves many interesting things happen for the flow, if the flow has too high Reynolds number the curve may induce turbulence in the flow, even though the flow in straight tubes may be laminar, the curve introduces secondary flow in the tube, which makes the liquid rotate in the tube, but the most interesting effect in this case is the resistance introduced by the tube curvature. This resistance is caused by increased friction in the tube and it is generally dependent on only two things, the curvature of the tube and the angle of the bend.

The friction of af bent tube is defined as a loss of pressure in relation to the flow velocity given by Darcy's equation,

$$\Delta P = f\frac{\Delta x}{2R}\frac{\rho v^2}{2}, \tag{6.65}$$

which is defined for a cylindric tube, given by the radius, R.

To find how a bend on a tube with elliptic cross-section effects pressure loss in the tube Darcy's equation is changed to fit an elliptic regime. The length of the tube, Δx, the flow velocity, v, and the friction factor, f, is defined as usual, but the radius of the tube is changed to fit with the axes of the ellipse.

The radius, R, in Darcy's equation is by definition the region of change defined in the expression of the Reynolds number, equation 3.4, and it refers to a characteristic region in which a change of flow can occur, incidentally it is equal to the radius in the cylindric tube but in the elliptic tube it will be more complicated. The characteristic length, l_c, is given as an intermediate value between A and B, the axes of the ellipse, defined by the relation,

$$l_c = \frac{AB}{\sqrt{\frac{A^2+B^2}{2}}}. \tag{6.66}$$

Thus the elliptic Darcy's equation becomes,

$$\Delta P = f\frac{\rho\Delta x}{4}\sqrt{\frac{A^2+B^2}{2A^2B^2}}v^2. \tag{6.67}$$

By insertion of the friction factor, $f = 32/Re$, for steady laminar flow the Poiseuille equation is achieved (remember that the flow is defined as $Q = \pi AB \cdot v$ in the elliptic tube),

$$\Delta P = \frac{32\eta}{\rho v}\sqrt{\frac{A^2+B^2}{2A^2B^2}}\frac{\rho\Delta x}{4}\sqrt{\frac{A^2+B^2}{2A^2B^2}}v^2 = \frac{4\eta\Delta x}{\pi}\frac{A^2+B^2}{A^3B^3}Q, \tag{6.68}$$

thus proving that the characteristic length defined in equation 6.66 fits in the scheme of Darcy's equation.

The friction of the bend of the elliptic tube is found through the elliptic analogue to equation 4.30,

$$\Delta P = (f_L + f_B)\frac{\rho\Delta x}{4}\sqrt{\frac{A^2+B^2}{2A^2B^2}}v^2, \tag{6.69}$$

where f_L is the friction factor for the length of the tube defined $f_L = 32/Re$ and f_B is the friction factor of a bend of the tube defined analogously to equation 4.31,

$$f_B = \xi(\theta) \cdot K_B(R_B/2l_c) \cdot f_T(2l_c), \tag{6.70}$$

where $f_T(2l_c)$ is the friction coefficient for completely turbulent flow, which is the base that all minor loss coefficients are calculated from, even if the flow in the specific case is not turbulent, $K_B(R_B/2l_c)$ is a friction factor for a bend of exactly $90°$, dependent on the radius of curvature, R_B, relative to the characteristic length, and $\xi(\theta)$ is an angular factor for bend angles less than $90°$.

In the typical case of a cylindrical tube f_T and K_B are dependent on the diameter of the tube, and it can be argued that the length l_c should not be used for determination of the numeric values of the functions in equation 6.70 instead of diameter, but in fact these functions are themselves approximations relative to a length that appears to be the characteristic length of the Reynolds number. A more elegant approach would be if it were possible to dissolve the bend into 'bend composites' relative to the directions of the major and minor axes of the elliptic cross-section, but the data from Crane Co. [1982] does not support such an approach.

The pressure loss in the elliptic bend will be given by the sum,

$$\Delta P = \frac{4\eta\Delta x}{\pi}\frac{A^2+B^2}{A^3B^3}Q + \xi K_B f_T \frac{\rho\Delta x}{4\pi^2}\sqrt{\frac{A^2+B^2}{2}}\frac{1}{A^3B^3}Q^2, \tag{6.71}$$

where f_T is the friction coefficient for completely turbulent flow defined in equation 4.32, K_B is defined as a function of the radius of curvature, R_B, by equation 4.33, and $\xi(\theta)$ is defined by equation 4.34.

In terms of resistance to the flow in the energy bond model, the Poiseuille resistance is already defined, but the resistance of the bend, Z_B, becomes,

$$Z_{Bn} = \frac{\Delta P_n}{Q_n} = \xi K_B f_T \frac{\rho\Delta x Q_n}{4\sqrt{2}\pi^2}\frac{\sqrt{a_n a_{n+1}+b_n b_{n+1}}}{\sqrt{a_n a_{n+1}}^3\sqrt{b_n b_{n+1}}^3}, \tag{6.72}$$

and with the definition of the momentum of the flow,

$$p_n = \sqrt{\frac{\sqrt{a_n a_{n+1}}\sqrt{b_n b_{n+1}}}{\sqrt{A_n A_{n+1}}\sqrt{B_n B_{n+1}}}}\psi\frac{\rho\Delta x}{\pi\sqrt{a_n a_{n+1}}\sqrt{b_n b_{n+1}}}Q_n, \tag{6.73}$$

the flow is eliminated from the equation to give the final resistance of the bend usable in the energy bond model (where the numerical value of the momentum is used because impedance should cause a loss of energy independent of the direction of flow),

$$Z_{Bn} = \frac{\Delta P_n}{Q_n} = \frac{\xi K_B f_T}{\psi}\frac{1}{4\pi}\sqrt{\frac{\sqrt{A_n A_{n+1}}\sqrt{B_n B_{n+1}}}{\sqrt{a_n a_{n+1}}^5\sqrt{b_n b_{n+1}}^5}}\sqrt{\frac{a_n a_{n+1}+b_n b_{n+1}}{2}}|p_n|. \tag{6.74}$$

Equation 6.74 defines the friction of the bend of the elliptic tube as a relation between pressure loss to volume flow. This impedance may be an approximation from the data from Crane Co. [1982] for cylindric tubes, but interestingly it is proportional to the momentum of the flow, which means that the impedance grows when the flow is accelerated. This is very interesting in relation to the pulsating flow and pressure in the embryonic heart.

6.3.3 Womersley theory

Finally the addition of Womersley theory concerning the influence of the velocity profile on the inertia of the flow is included in the elliptic model. Womersley's approach to the pulsating Navier-Stokes equation must be constructed with an elliptic geometry. The procedure follows the same steps as in section 4.3.3.

Define the Navier-Stokes equation for the elliptic system under similar assumptions as equation 4.42, the flow is laminar and incompressible but both flow velocity field and pressure gradient are functions of time, furthermore pressure gradient is invariant on the cross-section of the tube and the velocity field is unchanged with the longitudinal coordinate,

$$\frac{\partial^2 \mathbf{v}}{\partial a^2} + \frac{\partial^2 \mathbf{v}}{\partial b^2} - \frac{\rho}{\eta}\frac{\partial \mathbf{v}}{\partial t} + \frac{\Delta P(t)}{\eta \Delta x} = 0, \tag{6.75}$$

where a and b are the cross-sectional coordinates of the elliptic tube in relation to major and minor axis respectively. Similar to the procedure for the cylindric tube it is assumed that the time variant pressure difference $\Delta P(t)$ consists of a constant term, ΔP_0, and an oscillating term, $\widetilde{\Delta P}(t)$. The differential equation will have a particular solution of the constant term that is coincident with the elliptic Poiseuille equation, for now the existence of this particular solution is ignored, focus is put on the oscillating pressure term. The general solution to equation 6.75 is

$$\begin{aligned} v(a,b,t) &= \sum_{n=1}^{\infty} \left(\lambda_n^1 e^{\sqrt{k_n}a} + \lambda_n^2 e^{-\sqrt{k_n}a}\right)\left(\lambda_n^3 e^{\sqrt{l_n}b} + \lambda_n^4 e^{-\sqrt{l_n}b}\right) e^{\frac{\eta}{\rho}(k_n+l_n)t} \\ &\quad + \int \frac{\widetilde{\Delta P}(t)}{\rho \Delta x} dt + \lambda_0. \end{aligned} \tag{6.76}$$

$v(a,b,t)$ must obey the no-slip boundary condition, $v(A\cos\theta, B\sin\theta, t) = 0$, for any $\theta \in [0; 2\pi]$, where A and B are the major and minor axis of the elliptic cross-section, this will force the constant $\lambda_0 = 0$. Furthermore it is logically assumed that the velocity profile is a symmetric function on the elliptic domain, thus equation 6.76 is rewritten,

$$\begin{aligned} v(a,b,t) &= \sum_{n=1}^{\infty} \frac{\mu_n}{\rho \Delta x}\left(e^{\sqrt{k_n}a} + e^{-\sqrt{k_n}a}\right)\left(e^{\sqrt{l_n}b} + e^{-\sqrt{l_n}b}\right) e^{\frac{\eta}{\rho}(k_n+l_n)t} \\ &\quad + \int \frac{\widetilde{\Delta P}(t)}{\rho \Delta x} dt, \end{aligned} \tag{6.77}$$

where μ_n is a sequence of constants that will ensure that $v(A\cos\theta, B\sin\theta, t) = 0$.

Notice that it is not possible to find constants such that each term in the sum will be zero on the boundary, it is the infinite sum that will be zero while each term of the sum is different from zero for $(a, b) = (A\cos\theta, B\sin\theta)$.

Assume that the pressure difference is an oscillating function with angular frequency, ω, that can be written as the Fourier series,

$$\widetilde{\Delta P}(t) = \sum_{n=1}^{\infty} \Delta P_n e^{in\omega t}. \tag{6.78}$$

The pressure equation forces a condition on the exponents, $k_n + l_n = in\omega\frac{\rho}{\eta}$, and a suitable solution is found to be,

$$k_n = in\omega\frac{\rho}{\eta}\frac{B^2}{A^2+B^2} \qquad \text{and} \qquad l_n = in\omega\frac{\rho}{\eta}\frac{A^2}{A^2+B^2}, \tag{6.79}$$

hence $v(a, b, t)$ becomes,

$$\begin{aligned} v(a,b,t) &= \sum_{n=1}^{\infty} \frac{1}{\rho\Delta x}\frac{\Delta P_n}{in\omega}\left[1-\mu_n\left(e^{\frac{a}{A}\sqrt{in\omega\frac{\rho}{\eta}\frac{A^2B^2}{A^2+B^2}}}+e^{-\frac{a}{A}\sqrt{in\omega\frac{\rho}{\eta}\frac{A^2B^2}{A^2+B^2}}}\right)\right. \\ &\quad \left.\cdot\left(e^{\frac{b}{B}\sqrt{in\omega\frac{\rho}{\eta}\frac{A^2B^2}{A^2+B^2}}}+e^{-\frac{b}{B}\sqrt{in\omega\frac{\rho}{\eta}\frac{A^2B^2}{A^2+B^2}}}\right)\right]e^{in\omega t}. \end{aligned} \tag{6.80}$$

With the calculation of the flow velocity in the elliptic domain in equation 6.80 an elliptic parallel to the Womersley number is suggested; choose the elliptic Womersley number corresponding to the standard Womersley number for $A = B$,

$$\alpha_e = \sqrt{\omega\frac{\rho}{\eta}\frac{2A^2B^2}{A^2+B^2}}. \tag{6.81}$$

Notice further that the inside the two brackets of equation 6.80 contains the hyperbolic cosine function, this will become important when the volume flow is computed as the cross-sectional integral of the flow velocity, as the Taylor series approximation to the hyperbolic functions will be employed to solve the integral,

$$\begin{aligned} Q(t) &= 4\int_0^A\int_0^{B\sqrt{1-a^2/A^2}} v(a,b,t)\,dbda \\ &= \sum_{n=1}^{\infty}\frac{1}{\rho\Delta x}\frac{\Delta P_n}{in\omega}e^{in\omega t}\left[4\int_0^A\int_0^{B\sqrt{1-a^2/A^2}} 1\;dbda\right. \\ &\quad \left.-4\mu_n\int_0^A\int_0^{B\sqrt{1-a^2/A^2}} 4\cosh\left(\frac{a}{A}\alpha_e\sqrt{\frac{in}{2}}\right)\cosh\left(\frac{b}{B}\alpha_e\sqrt{\frac{in}{2}}\right)dbda\right] \end{aligned}$$

$$
\begin{aligned}
&= \sum_{n=1}^{\infty} \frac{1}{\rho\Delta x}\frac{\Delta P_n}{in\omega}e^{in\omega t}\Bigg[\pi AB \\
&\quad -4\mu_n \frac{4B}{\alpha_e\sqrt{\frac{in}{2}}}\int_0^A \sum_{m=0}^{\infty}\frac{\left(\frac{a\alpha_e}{A}\sqrt{\frac{in}{2}}\right)^{2m}}{(2m)!}\sum_{l=0}^{\infty}\frac{\left(\frac{\sqrt{A^2-a^2}\alpha_e}{A}\sqrt{\frac{in}{2}}\right)^{2l+1}}{(2l+1)!}da\Bigg] \\
&= \sum_{n=1}^{\infty}\frac{\pi AB}{\rho\Delta x}\frac{\Delta P_n}{in\omega}e^{in\omega t}\left[1-4\mu_n\sum_{m=1}^{\infty}\frac{\left(\alpha_e\sqrt{\frac{in}{2}}\right)^{2m}}{2^m}\frac{1}{(m+1)!\,m!}\right] \\
&= \sum_{n=1}^{\infty}\frac{\pi AB}{\rho\Delta x}\frac{\Delta P_n}{in\omega}\left[1-4\mu_n\frac{J_1\left(\alpha_e\sqrt{-in}\right)}{\alpha_e\sqrt{-in}}\right]e^{in\omega t}. \qquad (6.82)
\end{aligned}
$$

Equation 6.82 shows a remarkable resemblance to equation 4.47 for the oscillating flow in the cylindric tube, in fact when μ_n is set to $\mu_n = \frac{1}{4J_0(\alpha_e\sqrt{-in})}$ it shows that $v(A\cos\theta, B\sin\theta, t) = 0$. Thus the oscillating flow becomes,

$$
\begin{aligned}
Q(t) &= \sum_{n=1}^{\infty}\frac{\pi AB}{\rho\Delta x}\frac{\Delta P_n}{in\omega}\left[1-\frac{1}{\alpha_e\sqrt{-in}}\frac{J_1\left(\alpha_e\sqrt{-in}\right)}{J_0\left(\alpha_e\sqrt{-in}\right)}\right]e^{in\omega t} \\
&= \frac{2\pi A^3B^3}{\eta\Delta x(A^2+B^2)}\sum_{n=1}^{\infty}\frac{\Delta P_n}{in\alpha_e^2}\left[1-\frac{1}{\alpha_e\sqrt{-in}}\frac{J_1\left(\alpha_e\sqrt{-in}\right)}{J_0\left(\alpha_e\sqrt{-in}\right)}\right]e^{in\omega t}, \qquad (6.83)
\end{aligned}
$$

where J_0 and J_1 are the Bessel functions of the first kind of order zero and one.

The bracketed function in equation 6.83 is $f(\alpha, n)$ from equation 4.49 only with the elliptic Womersley number, α_e,

$$
f(\alpha_e, n) = 1 - \frac{1}{\alpha_e\sqrt{-in}}\frac{J_1\left(\alpha_e\sqrt{-in}\right)}{J_0\left(\alpha_e\sqrt{-in}\right)}. \qquad (6.84)
$$

The earlier analysis of the function revealed that for low values of the Womersley number $f(\alpha_e, n)$ is close to zero for all values of n, and thus the function in the lower line of equation 6.83 is close to $1/8$ making the flow dominated by the Poiseuille resistance, and for high values of α_e the function $f(\alpha_e, n)$ is close to 1 for all values of n making the flow dominated by inertia.

For any n the function $f(\alpha_e, n)$ behaves in a similar fashion, only the transition from 0 to 1 becomes steeper for higher values of n, thus it is assumed that equation 6.83 can be approximated by,

$$
\begin{aligned}
Q(t) &\approx \frac{\pi AB}{\rho\Delta x}f(\alpha_e, 1)\sum_{n=1}^{\infty}\frac{\Delta P_n}{in\omega}e^{in\omega t} \\
&\approx \frac{2\pi A^3B^3}{\eta\Delta x(A^2+B^2)}\frac{f(\alpha_e, 1)}{i\alpha_e^2}\sum_{n=1}^{\infty}\Delta P_n e^{in\omega t}. \qquad (6.85)
\end{aligned}
$$

In the equation $\widetilde{\Delta P}(t) = \sum_{n=1}^{\infty} \Delta P_n e^{in\omega t}$ is the time variant pressure difference and $p(t) = \sum_{n=1}^{\infty} \frac{\Delta P_n}{in\omega} e^{in\omega t}$ is the momentum of the oscillating flow. Thus,

$$\frac{\eta \Delta x (A^2 + B^2)}{2\pi A^3 B^3} \left(8 + \Psi(\alpha_e)\right) Q(t) \approx \frac{\eta}{\rho} \frac{A^2 + B^2}{2A^2 B^2} i\alpha_e^2 \, p(t), \tag{6.86}$$

where $\Psi(\alpha_e)$ is defined $\Psi(\alpha_e) = \frac{i\alpha_e^2}{f(\alpha_e,1)} - 8$. Notice that the right hand side of this equation is actually equal to $\widetilde{\Delta P}(t) = i\omega p(t)$ and thus the equation demonstrates that the pressure difference is made up of two terms, one Poiseuille term, $\widetilde{\Delta P}_p(t)$, and one other term, $\widetilde{\Delta P}_\psi(t)$,

$$\frac{\eta \Delta x (A^2 + B^2)}{2\pi A^3 B^3} \left(8 + \Psi(\alpha_e)\right) Q(t) \approx \widetilde{\Delta P}_p(t) + \frac{\eta}{\rho} \frac{A^2 + B^2}{2A^2 B^2} i\alpha_e^2 \, p_\psi(t), \tag{6.87}$$

where $p_\psi(t)$ is the momentum referring to $\widetilde{\Delta P}_\psi(t)$. The Poiseuille terms on each side of the equation cancel out and leaves the relation,

$$\begin{aligned} \frac{\eta \Delta x (A^2 + B^2)}{2\pi A^3 B^3} \Psi(\alpha_e) Q(t) &\approx \frac{\eta}{\rho} \frac{A^2 + B^2}{2A^2 B^2} i\alpha_e^2 \, p_\psi(t) \\ \frac{\rho \Delta x}{\pi A B} \psi(\alpha_e) Q(t) &\approx p_\psi(t), \end{aligned} \tag{6.88}$$

where the function $\psi(\alpha_e)$ is defined,

$$\psi(\alpha_e) = \frac{1}{1 - \frac{2}{\alpha_e \sqrt{-i}} \frac{J_1\left(\alpha_e \sqrt{-i}\right)}{J_0\left(\alpha_e \sqrt{-i}\right)}} - \frac{8}{i\alpha_e^2}. \tag{6.89}$$

The function $\psi(\alpha_e)$ is the exact same as $\psi(\alpha)$ in equation 4.57 for the cylindric tube. It has real values in the range from 1 for high values of α_e to $4/3$ for low values of α_e and complex values different from zero only in the transition, which lies in the domain from $\alpha_e = 1$ to $\alpha_e = 10$.

For higher orders of n the same calculations can be made and assuming cross-terms can be ignored a function similar to $\psi(\alpha_e)$ can be defined for each n, with values in the range from 1 to $4/3$. The transition from 1 to $4/3$ will only be more steep for higher values of n.

Thus it may be assumed that the function $\psi(\alpha_e)$ for $n = 1$ is a sufficient approximation so that the complete description of the time variant volume flow may be described through a Poiseuille term of the pressure difference, where the particular solution that was ignored at first is brought back into the complete solution, together with a momentum term modified by the function $\psi(\alpha_e)$,

$$Q(t) = \frac{\pi A^3 B^3}{4\eta \Delta x (A^2 + B^2)} \Delta P(t) + \frac{1}{\psi(\alpha_e)} \frac{\pi A B}{\rho \Delta x} p(t). \tag{6.90}$$

Equation 6.90 demonstrates that the solution to a Navier-Stokes equation for time-oscillating velocity field and pressure gradient ends with a volume flow described by the Poiseuille equation with addition of a momentum term where the inertia of the liquid has been modified by the function $\psi(\alpha_e)$ defined by equation 6.89. This result matches the result achieved for the cylindric tube in section 4.3.3 and defines the function multiplied to the inductance in section 6.2.2.

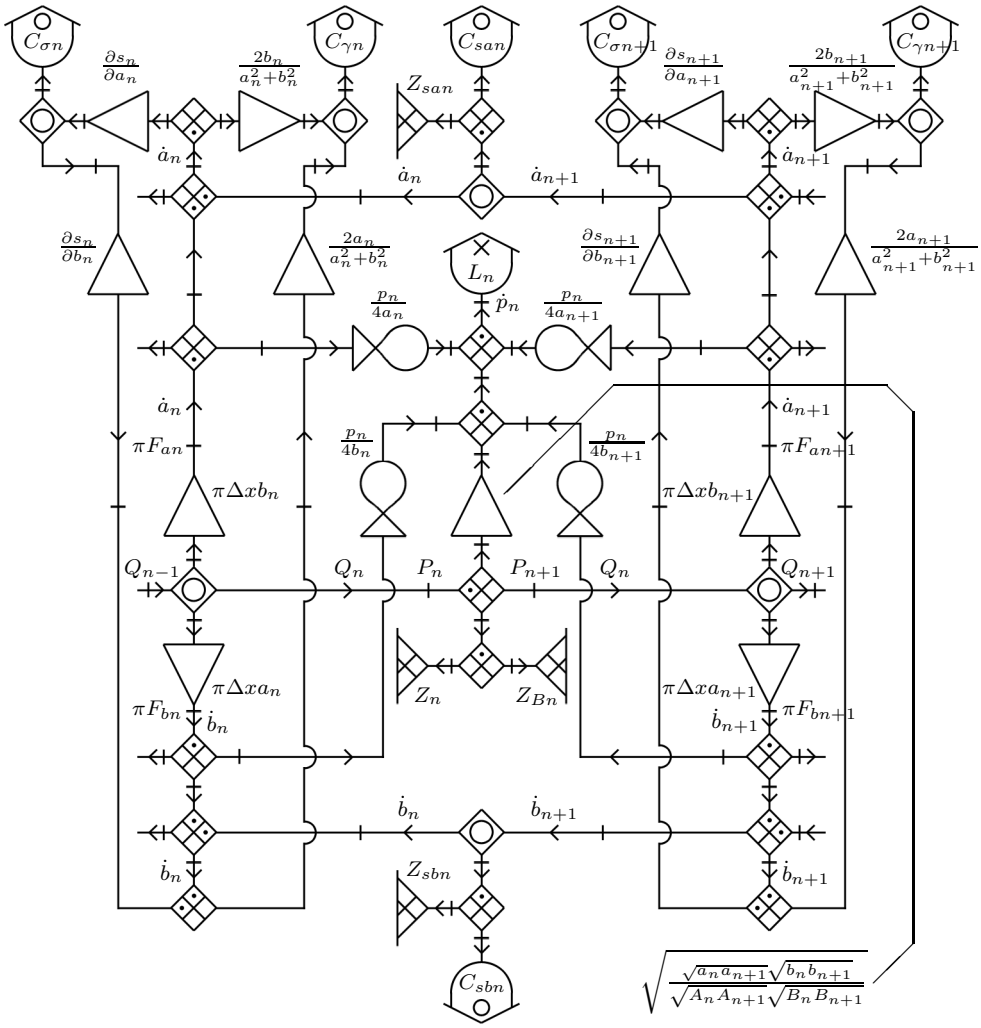

Figure 6.1: The schematic appearance of the elliptic tube model. Notice how the branches of a_n and b_n are joined through the capacitances $C_{\sigma n}$ and $C_{\gamma n}$.

6.4 The use of the model

With the last additions of the longitudinal shear tensions, the resistance due to curvature and the Womersley theory to the elliptic model the energy bond graph that represents the model will have an appearance as shown in figure 6.1.

The energy bond graph is split into two branches, one for a_n and one for b_n, but they are joined again through the capacitances $C_{\sigma n}$ and $C_{\gamma n}$ shown at the top of the figure. Additionally the capacitances and impedances of the shear tensions join one section to its neighbors, and the resistance from the curvature of the tube, Z_{Bn}, is added next to the Poiseuille resistance, Z_n. The Womersley factor is not visible in the model, as it is a factor in the calculation of the inductance, L_n.

The model is used for numerical computations of the flow inside an elastic tube or blood vessel, the computations are iterations through a Runge-Kutta algorithm of the rates of change of the length of the axes and the momentum of flow for each section of the model.

For each section specify the volume flow, Q_n, given by the output from the inertia relation defined in section 6.2.2 and redefined with equation 6.51 and 6.53,

$$Q_n = \frac{p_n}{L_n}\sqrt{\frac{\sqrt{a_n a_{n+1}}\sqrt{b_n b_{n+1}}}{\sqrt{A_n A_{n+1}}\sqrt{B_n B_{n+1}}}}, \tag{6.91}$$

and the dynamical pressure, P_n, which for the change in a_n is given by the combination of elastic forces, equation 6.18 and 6.32 from section 6.2.1, together with the shear tensions from equation 6.59 and the two Bernoulli terms from equation 6.56, all transformed with the ratio $\pi\Delta x b_n$ (equivalently the pressure can be calculated through the change of b_n),

$$\begin{aligned}
P_n \;=\; & \frac{1}{\pi\Delta x b_n}\Bigg[\frac{\partial s_n}{\partial a_n}\left(\frac{\partial s_n}{\partial a_n}\frac{a_n - A_n}{C_{\sigma n}} + \frac{\partial s_n}{\partial b_n}\frac{b_n - B_n}{C_{\sigma n}}\right) \\
& + \left(\frac{2a_n b_n}{a_n^2 + b_n^2}\right)^2 \frac{1}{a_n}\left(\frac{1}{a_n}\frac{a_n - A_n}{C_{\gamma n}} - \frac{1}{b_n}\frac{b_n - B_n}{C_{\gamma n}}\right) \\
& + \frac{(a_n - A_n) - (a_{n-1} - A_{n-1})}{C_{sn-1}} + Z_{sn-1}\left(\frac{da_n}{dt} - \frac{da_{n-1}}{dt}\right) \\
& - \frac{(a_{n+1} - A_{n+1}) - (a_n - A_n)}{C_{sn}} - Z_{sn}\left(\frac{da_{n+1}}{dt} - \frac{da_n}{dt}\right) \\
& + \frac{p_{n-1}}{4a_n}\frac{p_{n-1}}{L_{n-1}} + \frac{p_n}{4a_n}\frac{p_n}{L_n}\Bigg]
\end{aligned}$$

$$
\begin{aligned}
= \quad & \frac{1}{\pi\Delta x a_n}\Bigg[\frac{\partial s_n}{\partial b_n}\left(\frac{\partial s_n}{\partial a_n}\frac{a_n - A_n}{C_{\sigma n}} + \frac{\partial s_n}{\partial b_n}\frac{b_n - B_n}{C_{\sigma n}}\right) \\
& - \left(\frac{2a_n b_n}{a_n^2 + b_n^2}\right)^2 \frac{1}{b_n}\left(\frac{1}{a_n}\frac{a_n - A_n}{C_{\gamma n}} - \frac{1}{b_n}\frac{b_n - B_n}{C_{\gamma n}}\right) \\
& + \frac{(b_n - B_n) - (b_{n-1} - B_{n-1})}{C_{sn-1}} + Z_{sn-1}\left(\frac{db_n}{dt} - \frac{db_{n-1}}{dt}\right) \\
& - \frac{(b_{n+1} - B_{n+1}) - (b_n - B_n)}{C_{sn}} - Z_{sn}\left(\frac{db_{n+1}}{dt} - \frac{db_n}{dt}\right) \\
& + \frac{p_{n-1}}{4b_n}\frac{p_{n-1}}{L_{n-1}} + \frac{p_n}{4b_n}\frac{p_n}{L_n}\Bigg].
\end{aligned} \tag{6.92}
$$

With the definition of volume flow the changes of the length of the axes can be described with a simple inflow minus outflow relation, but still the resulting volume change must be divided into changes of the two axes according to the relation given by equation 6.20,

$$\pi\Delta x b_n \frac{da_n}{dt} + \pi\Delta x a_n \frac{db_n}{dt} = Q_{n-1} - Q_n. \tag{6.93}$$

To solve this equation use the rule that the pressure is uniform in the energy bond graph, $P_n = P_{an} = P_{bn}$, which gives a relation between the axial changes,

$$\frac{da_n}{dt} = \chi \frac{db_n}{dt}, \tag{6.94}$$

referring to the end of section 6.2.1 χ is given as,

$$\chi = \frac{\frac{1}{b_n}\frac{\partial s_n}{\partial a_n}\frac{\partial s_n}{\partial b_n} - \frac{1}{a_n}\left(\frac{\partial s_n}{\partial b_n}\right)^2 - \frac{2}{3}S_n^2\left(\frac{2a_n b_n}{a_n^2+b_n^2}\right)^2 \frac{1}{a_n b_n}\frac{1}{b_n}}{\frac{1}{a_n}\frac{\partial s_n}{\partial a_n}\frac{\partial s_n}{\partial b_n} - \frac{1}{b_n}\left(\frac{\partial s_n}{\partial a_n}\right)^2 - \frac{2}{3}S_n^2\left(\frac{2a_n b_n}{a_n^2+b_n^2}\right)^2 \frac{1}{a_n b_n}\frac{1}{a_n}}, \tag{6.95}$$

where secondary effects of the longitudinal shear tensions are ignored. Alternatively, in some cases the secondary effects may be important as the primary effects will not show truthful behavior, such as a circular tube with an eccentric deformation, which could be interesting for Liebau's ring in chapter 5. In those cases χ may be given by,

$$
\begin{aligned}
\chi \quad = \quad & \Bigg[\frac{1}{C_{\sigma n}}\frac{\partial s_n}{\partial b_n}\left(\frac{1}{a_n}\frac{\partial s_n}{\partial b_n} - \frac{1}{b_n}\frac{\partial s_n}{\partial a_n}\right) + \frac{1}{C_{\gamma n}}\frac{2}{a_n b_n^2}\left(\frac{2a_n b_n}{a_n^2 + b_n^2}\right)^2 \\
& + \frac{1}{C_{sn-1}}\frac{1}{a_n}\left(1 - \frac{\partial b_{n-1}}{\partial b_n}\right)\frac{1}{C_{sn}}\frac{1}{a_n}\left(1 - \frac{\partial b_{n+1}}{\partial b_n}\right)\Bigg]
\end{aligned}
$$

$$/\left[\frac{1}{C_{\sigma n}}\frac{\partial s_n}{\partial a_n}\left(\frac{1}{b_n}\frac{\partial s_n}{\partial a_n}-\frac{1}{a_n}\frac{\partial s_n}{\partial b_n}\right)+\frac{1}{C_{\gamma n}}\frac{2}{a_n^2 b_n}\left(\frac{2a_n b_n}{a_n^2+b_n^2}\right)^2\right.$$
$$\left.+\frac{1}{C_{sn-1}}\frac{1}{b_n}\left(1-\frac{\partial a_{n-1}}{\partial a_n}\right)+\frac{1}{C_{sn}}\frac{1}{b_n}\left(1-\frac{\partial a_{n+1}}{\partial a_n}\right)\right], \tag{6.96}$$

where the partial derivatives such as $\frac{\partial a_{n-1}}{\partial a_n}$ have to be approximated by functions of a_n and a_{n-1}. By use of the implicit function theorem if a continuous differentiable function f exist on an open space, (a_n, a_{n-1}), such that $f(a_n, a_{n-1}) = 0$ yet its partial derivatives are different from zero, then that function defines a_{n-1} as a function a_n and through its derivatives,

$$\frac{\partial a_{n-1}}{\partial a_n} = -\frac{\frac{\partial f}{\partial a_n}}{\frac{\partial f}{\partial a_{n-1}}}. \tag{6.97}$$

Such a function could be the function $f(a_n, a_{n-1}) = e^{\frac{-1}{(a_n - a_{n-1})^2}}$, which for a_{n-1} close to a_n is close to zero. With the derivatives, $\frac{\partial f}{\partial a_n} = 2e^{\frac{-1}{(a_n - a_{n-1})^2}}(a_n - a_{n-1})^{-3}$ and $\frac{\partial f}{\partial a_{n-1}} = -2e^{\frac{-1}{(a_n - a_{n-1})^2}}(a_n - a_{n-1})^{-3}$, the implicit partial derivative is found,

$$\frac{\partial a_{n-1}}{\partial a_n} = -\frac{2e^{-(a_n - a_{n-1})^{-2}}(a_n - a_{n-1})^{-3}}{-2e^{-(a_n - a_{n-1})^{-2}}(a_n - a_{n-1})^{-3}} = 1. \tag{6.98}$$

Thus for variations between the axes of the different sections the partial derivatives may simply be approximated with 1, which will remove the effect of the derivatives in equation 6.96, thus proving that the equation 6.95 is a good approximation in the first place. Though to see the effect of the shear elasticity and thus induce elliptic variations in a cylindric tube in the computations, the partial derivatives are instead approximated with $\frac{\partial a_{n-1}}{\partial a_n} = 1 - \delta$, where δ is a small number depending on the sign of $a_n - a_{n-1}$.

The use of secondary effects in the computations heavily increase computation time, and will not be used except to see necessary eccentric behavior in a non-eccentric tube.

The resulting rate of change for the axes will be as follows,

$$\frac{da_n}{dt} = \frac{Q_{n-1} - Q_n}{\pi \Delta x}\frac{\chi}{a_n + \chi b_n}, \tag{6.99}$$

$$\frac{db_n}{dt} = \frac{Q_{n-1} - Q_n}{\pi \Delta x}\frac{1}{a_n + \chi b_n}. \tag{6.100}$$

Finally the rate of change of the momentum is calculated as the pressure difference minus friction losses from the Poiseuille resistance given by equation 6.48 and the resistance due to tube curvature given by equation 6.74 plus the four extra terms from the Bernoulli effect given by equation 6.55,

$$\begin{aligned}\frac{dp_n}{dt} &= \sqrt{\frac{\sqrt{a_n a_{n+1}}\sqrt{b_n b_{n+1}}}{\sqrt{A_n A_{n+1}}\sqrt{B_n B_{n+1}}}}\left[P_n - P_{n+1} - \frac{4}{\pi}\frac{\eta\Delta x\,(a_n a_{n+1} + b_n b_{n+1})}{\sqrt{a_n a_{n+1}}^3\sqrt{b_n b_{n+1}}^3}Q_n\right.\\ &\quad\left.+\frac{\xi K_B f_T}{\psi(\alpha_e)}\frac{1}{4\pi}\sqrt{\frac{\sqrt{A_n A_{n+1}}\sqrt{B_n B_{n+1}}}{\sqrt{a_n a_{n+1}}^5\sqrt{b_n b_{n+1}}^5}}\sqrt{\frac{a_n a_{n+1} + b_n b_{n+1}}{2}}|p_n|Q_n\right]\\ &\quad+\frac{p_n}{4a_n}\frac{da_n}{dt} + \frac{p_n}{4a_{n+1}}\frac{da_{n+1}}{dt} + \frac{p_n}{4b_n}\frac{db_n}{dt} + \frac{p_n}{4b_{n+1}}\frac{db_{n+1}}{dt}. \qquad (6.101)\end{aligned}$$

The rates of change of the length of the axes and momentum of flow are the three fundamental equations of the model. If N is the number of sections in the model the rates of change will constitute a system of $3N$ non-linear differential equations, iterated trough a Runge-Kutta algorithm they yield the time-variant functions of major and minor axis and for the momentum of flow for all sections, which subsequently can be used to find the time dependent functions of flow and pressure for all sections of the model. This will be the solution to the elliptic model.

6.5 The embedded tube model

As an extension to the elliptic tube model another addition is included to make a model suitable for describing the embryonic heart, as such the elliptic tube model is changed to the embedded tube model.

At certain stages of the embryonic development the embryonic heart is constructed in a very ‘simple’ way relative to our normal understanding of a beating heart, as a length of tube with a muscle that periodically contracts its outer radius.

The construction of the heart tube is layered. The inner layer of the tube is called the endocardium it has an almost elliptic cross-section and is very flexible, the outer layer of the tube known as the myocardium has an almost concentric cross-section and is strongly elastic. Between the inner and outer layer of the tube walls is an easily-deformable elastic gelatinous material known as the cardiac jelly.

The purpose of the cardiac jelly is to convey the muscular contractions of the outside myocardium to the inside volume of the tube, in such a way that a relatively small contraction of the outside layer of the tube contracts the inside elliptical cross-section to almost total occlusion.

The idea in the embedded model is to construct a layered structure consisting of a soft elastic tube of elliptic cross-section embedded inside a stronger elastic tube of circular cross-section. In the space between the two tubes an easily-deformable elastic material resides to convey the periodic contractions of the outer tube into the inner tube.

This will be an approximation to the embryonic heart as the inner lumen of the heart is only approximately elliptic and the outer perimeter is not entirely circular, in addition when the the outer layer of the embryonic heart contracts it achieves an almost complete closure of the lumen of the inner tube, which will not be possible in this model.

6.5.1 The tubular cross-section

The layered cross-section of the tube is described through the radius of the outside layer, r_n, and the major and minor axes of the the inner elliptic layer, a_n and b_n, for each section of the tube. However the inner layer is embedded into the outer concentric tube in such a way that the major axis of the ellipse is equal to the radius of the outside layer, $a_n = r_n$.

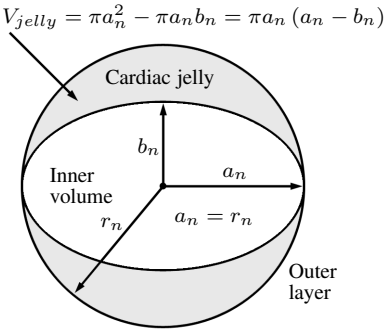

Figure 6.2: The cross-section of the layered tube.

The elastic properties of this complex tube is described with four cross-sectional compliances and at least two inter-sectional. The four cross-sectional compliances come from the elasticity of the concentric outer layer, C_{rn}, the elasticity of the elliptic inner layer, which according to section 6.2.1 must be divided into a compliance for the change of the surface area, $C_{\sigma n}$, and one for the shear deformation of the elliptic layer, $C_{\gamma n}$, and the fourth compliance comes from the elastic properties of the cardiac jelly, C_{jn}. The inter-sectional compliances are related to the shear stress along the length of the tube and will be described by the longitudinal shear tensions from section 6.3.1.

6.5.2 Elasticity of the tube wall

Following the procedure in section 6.2.1 the elasticity of the inner and outer layer can be calculated through the potential energy stored by a deformation of the layer. This energy is given by the pressure on the layer integrated over volume change, which is unfortunately not a linear relation.

To make it linear the variables are transformed from volume change to a change in the axes of the inner ellipse, and then the energy is given by the integral of the surface-specific elastic modulus, the surface area, the curvature of the surface and the deformation of the axes.

For the outer circular layer this relation is quite simple, since both surface area and curvature are simple functions in a circular scheme, thus the increase in energy will be given as in section 4.2.1,

$$U_{rn} = \int_{-\frac{\pi}{2}}^{\frac{\pi}{2}} \int_{A_n}^{a_n} \frac{\Delta x E_{out} h_{out}}{A_n} (a - A_n)\, da d\theta = \frac{\pi}{2} \frac{\Delta x E_{out} h_{out}}{A_n} (a_n - A_n)^2 , \tag{6.102}$$

where surface-specific elastic modulus is given by the thickness of the outer layer, h_{out}, times Young's modulus for that type of material, E_{out}. The equilibrium radius for the tube at rest is A_n and Δx is the length of section n of the tube.

Notice that the energy is only integrated over the arc from $-\pi/2$ to $\pi/2$ in contradiction to how it is done in the cylindric model in section 4.2.1. This is due to the fact that the effort of the energy bond related to the changes of the major axis only covers half of the force related to one section, $e_{rn} = \pi F_{rn}$, whereas the effort of the concentric model is equal to the full force on a section, $e_n = 2\pi F_n$.

Given the expression for the potential energy of a capacitor, $U_{rn} = \frac{1}{2}\Delta a_n^2 / C_{rn}$, this defines the capacitance associated with the length-change of the radius of the outer layer,

$$C_{rn} = \frac{A_n}{\pi \Delta x E_{out} h_{out}}. \tag{6.103}$$

The force subjected by this capacitance is simply computed as the change in the radius of the outer layer divided by the capacitance (and divided by π because of the relation of force to effort, $e_{rn} = \pi F_{rn}$),

$$F_{rn} = \frac{\Delta x E_{out} h_{out}}{A_n} \Delta a_n, \tag{6.104}$$

the interesting part about this force is that it only affects the radius of the outer layer, that is the major axis of the inner elliptic layer. This is in contrast to all the other forces in the model.

For the axes of the inner elliptic layer the relation is more complicated because the surface area and surface curvature are much more complicated functions, furthermore a change of the axes will produce shear forces in the elliptic layer, which must also be taken into account.

The process of finding the elastic forces from a deformation of the elliptic layer is described in section 6.2.1. The end result is a pair of coupled forces, where two forces acts on the major axis of the ellipse,

$$F_{\sigma an} = \frac{E_{in}h_{in}}{S_n}\frac{\partial s_n}{\partial a_n}\left(\frac{\partial s_n}{\partial a_n}\Delta a_n + \frac{\partial s_n}{\partial b_n}\Delta b_n\right), \tag{6.105}$$

$$F_{\gamma an} = G_{in}h_{in}S_n\left(\frac{2a_nb_n}{a_n^2+b_n^2}\right)^2\frac{1}{a_n}\left(\frac{1}{a_n}\Delta a_n - \frac{1}{b_n}\Delta b_n\right), \tag{6.106}$$

and two other forces, one proper and one shear, acts on the minor axis,

$$F_{\sigma bn} = \frac{E_{in}h_{in}}{S_n}\frac{\partial s_n}{\partial b_n}\left(\frac{\partial s_n}{\partial a_n}\Delta a_n + \frac{\partial s_n}{\partial b_n}\Delta b_n\right), \tag{6.107}$$

$$F_{\gamma bn} = -G_{in}h_{in}S_n\left(\frac{2a_nb_n}{a_n^2+b_n^2}\right)^2\frac{1}{b_n}\left(\frac{1}{a_n}\Delta a_n - \frac{1}{b_n}\Delta b_n\right), \tag{6.108}$$

where h_{in} is the thickness of the inner elliptic layer, E_{in} is Young's modulus, and G_{in} is the shear modulus for the layer. The surface area of section n of the elliptic layer is described through the second elliptic integral,

$$s_n = \Delta x\int_0^{2\pi}\sqrt{a_n^2\sin^2\theta + b_n^2\cos^2\theta}\,d\theta, \tag{6.109}$$

where S_n is the corresponding equilibrium surface area, and where $\partial s_n/\partial a_n$ and $\partial s_n/\partial b_n$ are its derivatives with respect to the axial changes.

The forth elasticity comes from the volume deformation of the elastic material between the two layers, the cardiac jelly. The volume of the space between the layers is a function of the difference between the volume of the outer layer, $\Delta x\pi a_n^2$, and the volume of the inner elliptic layer, $\Delta x\pi a_nb_n$ yielding the volume of the cardiac jelly, $V_{jn} = \Delta x\pi(a_n^2 - a_nb_n)$. Thus the volume change will be,

$$dV_{jn} = \Delta x\pi\left((2a_n - b_n)da_n - a_ndb_n\right). \tag{6.110}$$

Transform from a_n to a_n^* by applying the transformation relation,

$$da_n = \frac{a_n}{2a_n - b_n}da_n^*, \tag{6.111}$$

which gives a symmetric expression for the volume change,

$$dV_{jn} = \Delta x\pi a_n\left(da_n^* - db_n\right). \tag{6.112}$$

The increased pressure inside the cardiac jelly is given by the relative volume change, that is the change in volume compared to the original volume,

$$dP_n = K\frac{dV_{jn}}{V_{j0}} = K\frac{dV_{jn}}{\Delta x\pi\left(A_n^2 - A_nB_n\right)}, \tag{6.113}$$

where K is an unspecific elastic modulus of the cardiac jelly. It is clear that the elastic modulus involved in this expression will have both proper and shear qualities corresponding to the complicated deformation of the arc-shaped volume inhabited by the cardiac jelly, in this thesis it is assumed that the elastic modulus used can be approximated by a single constant similar to Youngs modulus, though further investigation may clarify this question.

Let $\Delta P_n = P_n - P_0$ and $\Delta V_{jn} = V_{jn} - V_{j0}$ be the first order approximations to the infinitesimals of equation 6.113, then integrate the pressure over the volume increase from V_{j0} to V_{jn} to get the potential energy,

$$\begin{aligned} U_{jn} &= \int \Delta P_n dV_{jn} = \int_{V_{j0}}^{V_{jn}} \frac{K}{\Delta x\pi(A_n^2 - A_nB_n)}\left(V - V_{j0}\right)dV \\ &= \frac{K}{2\Delta x\pi\left(A_n^2 - A_nB_n\right)}\left(V_{jn} - V_{j0}\right)^2. \end{aligned} \tag{6.114}$$

By the expression for the potential energy of a capacitor, $U_{jn} = \frac{1}{2}\delta V_{jn}^2/C_{jn}$, the capacitance is defined,

$$C_{jn} = \frac{\Delta x\pi(A_n^2 - A_nB_n)}{K}. \tag{6.115}$$

The forces subjected to the layers of the tube by the elasticity of the cardiac jelly is paired similarly to the elastic forces given in section 6.2.1, one for the minor axis of the ellipse and one for the major axis. The forces are found by tracing backwards through the equations, thus the force on the major axis becomes,

$$F_{jan} = -\Delta x\pi(2a_n - b_n)\frac{K}{A_n^2 - A_nB_n}\left((2a_n - b_n)\Delta a_n - a_n\Delta b_n\right), \tag{6.116}$$

and the force on the minor axis,

$$F_{jbn} = \Delta x\pi a_n\frac{K}{A_n^2 - A_nB_n}\left((2a_n - b_n)\Delta a_n - a_n\Delta b_n\right). \tag{6.117}$$

Thereby all four cross-sectional elastic properties have been described, but notice how the first did only produce one force on the outside layer whereas the other three produced paired forces on the major and minor axis respectively.

The intersectional elasticity is given by the longitudinal shear tensions described in section 6.3.1. The first, C_{san}, is made from a combination of the elasticity of the outer layer and the elasticity of the elliptic inner layer and thus also refers to section 4.3.1,

$$C_{san} = \frac{2\Delta x}{4\pi G_{out} h_{out} \sqrt{A_n A_{n+1}} + G_{in} h_{in} \Omega_n}, \tag{6.118}$$

and the second, C_{sbn}, comes alone from the elasticity of the inner layer,

$$C_{sbn} = \frac{2\Delta x}{G_{in} h_{in} \Omega_n}, \tag{6.119}$$

where Ω_n is the geometric mean surface area between two neighboring tube sections defined by equation 6.58 and G_{in} and G_{out} are the shear modulus of the wall layers, equal to one third of Young's modulus.

As described in section 6.3.1 the longitudinal shear tensions are accompanied by a damping resistance, $Z_{san} = T/C_{san}$ and $Z_{sbn} = T/C_{sbn}$, where $T = 0.01$ s is the characteristic time of the RC-circuit made up by the capacitance and impedance in serial coupling in the energy bond graph.

6.5.3 The use of the model

With the description of the four cross-sectional elastic capacitances and the longitudinal shear tensions the total elastic properties of the tube is described. In addition the embedded model is equipped with an inductance representing the inertia, L_n, with the Womersley inertia correction factor, $\psi(\alpha_e)$, a Poiseuille resistance, Z_n, and a resistance due to curvature of the tube, Z_{Bn}. The energy bond graph of this complicated model is shown in figure 6.3.

The model is used for numerical computations of the flow inside an complicated elastic tube or in the embryonic heart, the computations are iterations through a Runge-Kutta algorithm of the derivatives of the length of the axes and the momentum for each section of the model.

For each section specify the volume flow, Q_n,

$$Q_n = \frac{p_n}{L_n} \sqrt{\frac{\sqrt{a_n a_{n+1}} \sqrt{b_n b_{n+1}}}{\sqrt{A_n A_{n+1}} \sqrt{B_n B_{n+1}}}}, \tag{6.120}$$

and the dynamical pressure, P_n,

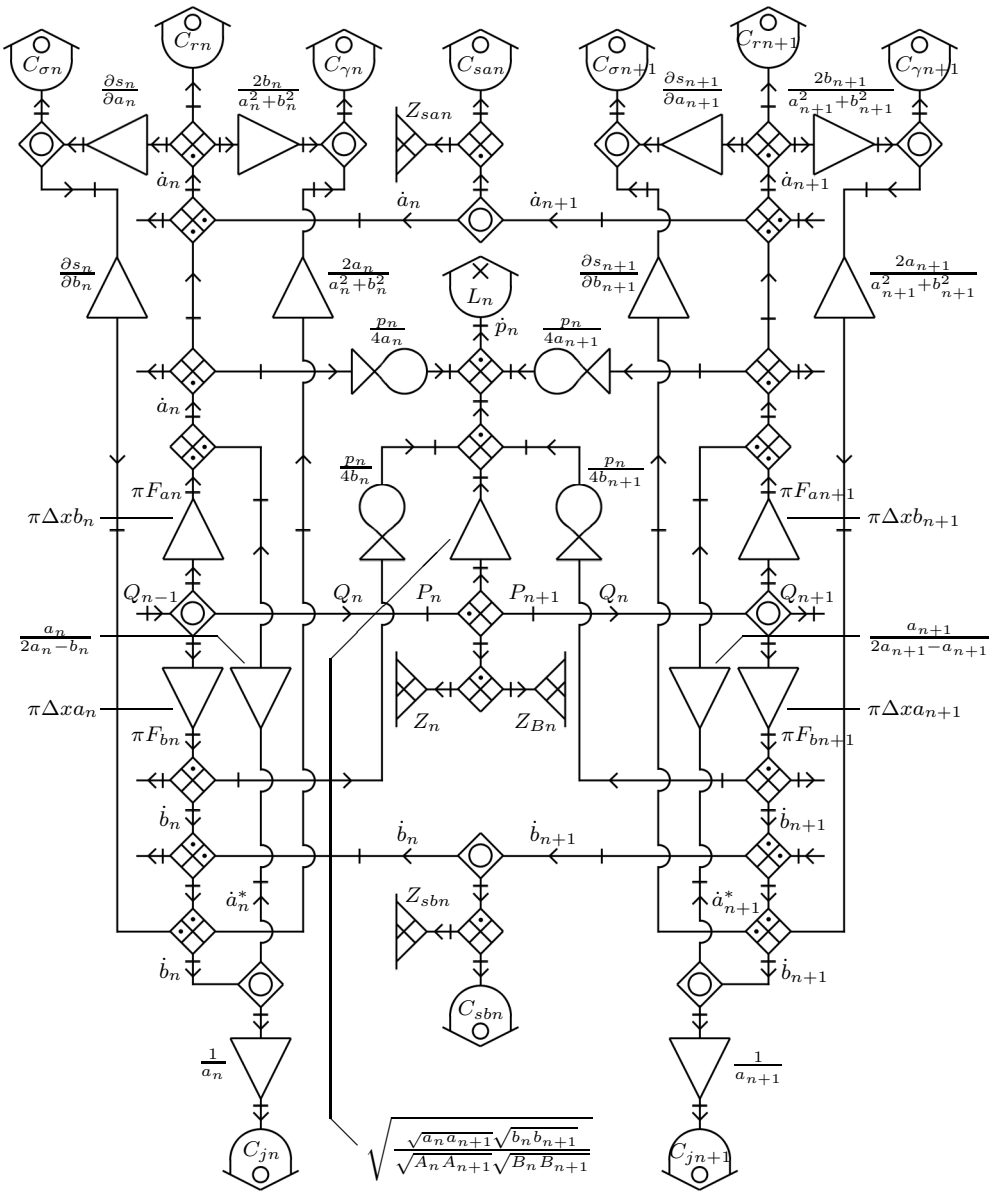

Figure 6.3: The schematic appearance of the embedded tube model. The branches of a_n and b_n are joined through three energy bonds; one for the surface area specific compliance, $C_{\sigma n}$, one for the surface structural shear compliance $C_{\gamma n}$ and one for the volume specific compliance of the cardiac jelly, C_{jn}. Additionally the compliance of the outer myocardial layer is represented through C_{rn}.

$$
\begin{aligned}
P_n &= \frac{1}{\pi\Delta x b_n}\Bigg[\frac{a_n - A_n}{C_{rn}} + \frac{\partial s_n}{\partial a_n}\left(\frac{\partial s_n}{\partial a_n}\frac{a_n - A_n}{C_{\sigma n}} + \frac{\partial s_n}{\partial b_n}\frac{b_n - B_n}{C_{\sigma n}}\right) \\
&\quad + \left(\frac{2a_n b_n}{a_n^2 + b_n^2}\right)^2 \frac{1}{a_n}\left(\frac{1}{a_n}\frac{a_n - A_n}{C_{\gamma n}} - \frac{1}{b_n}\frac{b_n - B_n}{C_{\gamma n}}\right) \\
&\quad - (\Delta x\pi)^2(2a_n - b_n)\left((2a_n - b_n)\frac{a_n - A_n}{C_{jn}} - a_n\frac{b_n - B_n}{C_{jn}}\right) \\
&\quad + \frac{(a_n - A_n) - (a_{n-1} - A_{n-1})}{C_{sn-1}} + Z_{sn-1}\left(\frac{da_n}{dt} - \frac{da_{n-1}}{dt}\right) \\
&\quad - \frac{(a_{n+1} - A_{n+1}) - (a_n - A_n)}{C_{sn}} - Z_{sn}\left(\frac{da_{n+1}}{dt} - \frac{da_n}{dt}\right) \\
&\quad + \frac{p_{n-1}}{4a_n}\frac{p_{n-1}}{L_{n-1}} + \frac{p_n}{4a_n}\frac{p_n}{L_n}\Bigg] \\
&= \frac{1}{\pi\Delta x a_n}\Bigg[\frac{\partial s_n}{\partial b_n}\left(\frac{\partial s_n}{\partial a_n}\frac{a_n - A_n}{C_{\sigma n}} + \frac{\partial s_n}{\partial b_n}\frac{b_n - B_n}{C_{\sigma n}}\right) \\
&\quad - \left(\frac{2a_n b_n}{a_n^2 + b_n^2}\right)^2 \frac{1}{b_n}\left(\frac{1}{a_n}\frac{a_n - A_n}{C_{\gamma n}} - \frac{1}{b_n}\frac{b_n - B_n}{C_{\gamma n}}\right) \\
&\quad + (\Delta x\pi)^2 a_n\left((2a_n - b_n)\frac{a_n - A_n}{C_{jn}} - a_n\frac{b_n - B_n}{C_{jn}}\right) \\
&\quad + \frac{(b_n - B_n) - (b_{n-1} - B_{n-1})}{C_{sn-1}} + Z_{sn-1}\left(\frac{db_n}{dt} - \frac{db_{n-1}}{dt}\right) \\
&\quad - \frac{(b_{n+1} - B_{n+1}) - (b_n - B_n)}{C_{sn}} - Z_{sn}\left(\frac{db_{n+1}}{dt} - \frac{db_n}{dt}\right) \\
&\quad + \frac{p_{n-1}}{4b_n}\frac{p_{n-1}}{L_{n-1}} + \frac{p_n}{4b_n}\frac{p_n}{L_n}\Bigg].
\end{aligned} \tag{6.121}
$$

With the definition of volume flow the changes of the volume per section can be described with a simple inflow minus outflow relation,

$$
\pi\Delta x b_n\frac{da_n}{dt} + \pi\Delta x a_n\frac{db_n}{dt} = Q_{n-1} - Q_n. \tag{6.122}
$$

Unfortunately the axial changes can not be derived from this equation alone, a further condition of the pressure is needed. In the model the pressure can be described through two ways as demonstrated in equation 6.121, which gives a relation between the axial changes, $\frac{da_n}{dt} = \chi\frac{db_n}{dt}$, with χ given by,

$$\chi = \frac{\frac{1}{2}\left(\frac{b_n}{a_n}\left(\frac{\partial s_n}{\partial b_n}\right)^2 - \frac{\partial s_n}{\partial a_n}\frac{\partial s_n}{\partial b_n}\right) + \frac{S_n^2}{3}\left(\frac{2a_nb_n}{a_n^2+b_n^2}\right)^2\frac{1}{a_nb_n} + \frac{\pi\Delta x K S_n}{E_{in}h_{in}}\frac{a_n^2}{A_n^2-A_nB_n}}{\frac{1}{2}\left(\left(\frac{\partial s_n}{\partial a_n}\right)^2 - \frac{b_n}{a_n}\frac{\partial s_n}{\partial a_n}\frac{\partial s_n}{\partial b_n}\right) + \frac{S_n^2}{3}\left(\frac{2b_n}{a_n^2+b_n^2}\right)^2 + \frac{\pi\Delta x K S_n}{E_{in}h_{in}}\frac{a_n(2a_n-b_n)}{A_n^2-A_nB_n} + \frac{\pi\Delta x E_{out}h_{out}S_n}{2E_{in}h_{in}A_n}}, \tag{6.123}$$

which gives the resulting rate of change for the axes,

$$\frac{da_n}{dt} = \frac{Q_{n-1}-Q_n}{\pi\Delta x}\frac{\chi}{a_n+\chi b_n}, \tag{6.124}$$

$$\frac{db_n}{dt} = \frac{Q_{n-1}-Q_n}{\pi\Delta x}\frac{1}{a_n+\chi b_n}. \tag{6.125}$$

Notice that in section 6.4 another more complicated procedure for calculating χ was introduced for the cases where the simple approach would not suffice, but given the already eccentric construction of the embedded model with an asymmetric distribution of the cardiac jelly that procedure will not be necessary here.

The rate of change of the momentum is calculated as the pressure difference minus friction loss plus the contributions from the Bernoulli coupling,

$$\begin{aligned}\frac{dp_n}{dt} &= \sqrt{\frac{\sqrt{a_na_{n+1}}\sqrt{b_nb_{n+1}}}{\sqrt{A_nA_{n+1}}\sqrt{B_nB_{n+1}}}}\left[P_n - P_{n+1} - \frac{4}{\pi}\frac{\eta\Delta x\,(a_na_{n+1}+b_nb_{n+1})}{\sqrt{a_na_{n+1}}^3\sqrt{b_nb_{n+1}}^3}Q_n\right.\\ &\quad\left.-\frac{\xi K_B f_T}{\psi(\alpha_e)}\frac{1}{4\pi}\sqrt{\frac{\sqrt{A_nA_{n+1}}\sqrt{B_nB_{n+1}}}{\sqrt{a_na_{n+1}}^5\sqrt{b_nb_{n+1}}^5}}\sqrt{\frac{a_na_{n+1}+b_nb_{n+1}}{2}}|p_n|Q_n\right]\\ &\quad+\frac{p_n}{4a_n}\frac{da_n}{dt} + \frac{p_n}{4a_{n+1}}\frac{da_{n+1}}{dt} + \frac{p_n}{4b_n}\frac{db_n}{dt} + \frac{p_n}{4b_{n+1}}\frac{db_{n+1}}{dt}.\end{aligned} \tag{6.126}$$

The three derivatives, $\frac{da_n}{dt}$, $\frac{db_n}{dt}$ and $\frac{dp_n}{dt}$ constitute a system of $3N$ non-linear differential equations, where N is the number of sections in the model. A solution to this system of differential equations is found numerically using a Runge-Kutta algorithm, which yields the time-dependent functions of the axes and momentum for each section of the model, subsequently the functions of flow and pressure is found through the use of equation 6.120 and 6.121. The set of all five time-dependent functions of the axial lengths, momentum of flow, pressure and volume flow is a complete solution to the embedded model.

Chapter 7

The Embryonic Heart Model

As specified in chapter 2 the embryonic heart is formed as a simple straight elastic tube that gradually twists and turns during the Hamburger and Hamilton development stages (HH-stages) 10 to 24. During this process known as cardiac looping the heart starts beating at HH-stage 10 and from the different looping procedures and overall growth of the embryo the liquid flow will experience great changes in heart rate, stroke volume, tubular dimensions and physical parameters (among other things) during the following HH-stages.

It was argued in section 2.2 that the interesting stages of the tubular heart are HH-stage 10 with the onset of cardiac looping and the beating of the heart, HH-stage 12 when the looping heart has formed in the shape of a 'c' and a stable flow rate is observed, HH-stage 14 when the looping heart has formed in the shape of an 's' and the primitive atrium is fully developed, and HH-stage 16 with a fully s-shaped heart that includes all the cardiac segments of the looping heart. These are the four stages of the tubular that will be the focus of this chapter.

In the following a model for the embryonic heart tube will be setup following the four steps introduced in section 5.2, though here it will make more sense to include them in a different order: First a tracing of the heart tube, then boundary conditions, parameter estimation, and finally the pumping mechanism.

7.1 Tracing of the embryonic heart

Acquisition of accurate numbers for the dimensions of the heart tube is unfortunately a problem for embryological research, in vivo imaging techniques are still at a very early stage of development and the embryonic heart so small that only approximal data is available - and usually in the form of images rather than numerical values. So far the acquisition of dimensional data has not been the focus of embryological research although it is of great importance for the understanding of

the pumping function of the tubular embryonic heart, due to its small dimensions the circulatory system of the embryo has just been regarded as a vascular system that shows flow at low Reynolds numbers.

In order to make a tracing of the embryonic heart loop the following values are needed: length of each of the cardiac segments (left and right ventricle, primitive atrium, outflow tract etc.), end-diastole diameter at defining points along the heart tube preferably a few measurements for each cardiac segment, measurements of end-diastole inner lumen of the heart tube or a measurement of the percentage that cardiac jelly take of the cross-sectional area of the heart tube (for each of the cardiac segments), thickness of the outer myocardial layer and the inner endocardial layer, and curvature of the heart, which is not necessarily uniform.

The paper by Männer [2000] includes a number of very nice in ovo (in the egg) images of embryonic hearts in the relevant stages of development using scanning electron microscopy, see figure 2.1, from which it is possible to estimate approximal external lengths and diameters (assuming that width in the images can be translated directly to diameter in the model) of the observed cardiac segments, the data is presented in table 7.1.

In addition to the data presented in table 7.1 it is possible to estimate an approximate radius of curvature for the looping heart at the beginning of dextral looping (HH-stage 10) from Männer [2000] fig. 1.D. The heart appears to have an almost uniform radius of curvature, $R_B = 550$ μm, from the venous pole to the outflow tract. Due to the complicated three dimensional looping at later stages it was not possible to make similar estimates for HH-stage 12, 14 or 16.

Additionally some dimensional data can be found in various papers from experimental embryological research, below table 7.2 to 7.5 list some dimensional measurements and model estimations found in the embryological literature. The combined tracing of the looping heart with dimensional data from table table 7.1 and tables 7.2 to 7.5 is shown on figures 7.1 to 7.4, which include the sketches of the embryonic heart at the appropriate stages.

The disagreement of the reported dimensional values is notable, for instance table 7.5 lists five different measurements of the outside dimension of the HH-stage 16 ventricle, which under the simple assumption of a circular cross section gives the following diameters for the ventricle 240 μm, 250 μm, 256 μm, 542 μm, and 800 μm, especially the measurements of outside perimeter and cross-sectional area from table 7.3, 7.4 and 7.5 seem to suggest diameters twice the size of other corresponding numbers.

For HH-stage 16 a much larger set of dimensional information is needed to complete the model with all the cardiac segments present compared to the other stages, and even though this stage is the most researched of the four some numbers are still missing, most importantly the thickness of the myocardial layer and the radius of curvature for the heart tube. Both are possible to estimate from knowledge of the surrounding stages.

Stages	HH-10	HH-12	HH-14	HH-16*
Lengths				
Sinus venosis	50 μm**	70 μm	170 μm	230 μm
Primitive atrium		200 μm	230 μm	470 μm
Left ventricle	130 μm	270 μm	480 μm	700 μm
Right ventricle	250 μm	370 μm	500 μm	500 μm
Proximal outflow tract***	230 μm	250 μm	230 μm	270 μm
Distal outflow tract***			100 μm	170 μm
Diameters				
Left vein	150 μm	130 μm	250 μm	200 μm
Right vein	100 μm	130 μm	250 μm	200 μm
Sinus venosis	330 μm**	350 μm	450 μm	470 μm
Venous pole	300 μm	330 μm	250 μm	370 μm
Central atrium		320 μm	270 μm	370 μm
Upper atrium		280 μm	270 μm	350 μm
Atrioventricular canal			250 μm	330 μm
Lower left ventricle		250 μm	280 μm	380 μm
Central left ventricle	270 μm	250 μm	350 μm	470 μm
Upper left ventricle			330 μm	400 μm
Left lateral furrow	250 μm	250 μm	320 μm	350 μm
Lower right ventricle			330 μm	350 μm
Central right ventricle	250 μm	230 μm	320 μm	350 μm
Upper right ventricle		170 μm	250 μm	300 μm
Conoventricular sulcus	200 μm	150 μm	200 μm	270 μm
Proximal outflow tract***	170 μm	150 μm	200 μm	250 μm
Distal outflow tract***		150 μm	180 μm	200 μm
Arterial outlet	120 μm	130 μm	130 μm	170 μm

Table 7.1: Estimated external dimensions of the early stages of the looping embryonic heart based on images from Männer [2000] fig. 1.D (HH-stage 10), fig. 1.G (HH-stage 12), fig. 3.A and 3.A´ (HH-stage 14), fig. 3.C, 3.C´, 4.A, 4.A´ and 4.A´´ (HH-stage 16). (*) Notice that at HH-stage 16 the looping heart makes it difficult to estimate some dimensions due to perspective in the images. (**) At HH-stage 10 the heart has not yet developed the sinus venosis of the later stages, here it is merely used to describe the inflow portion of the heart tube. (***) In cardiac morphology research it is debated at what stages the conus and truncus part of the outflow tract is formed [Martinsen, 2005], therefore the proximal and distal outflow tract are not meant as reference to those specific cardiac segments, they refer only to the dimensions of the outflow tract present at the particular stage.

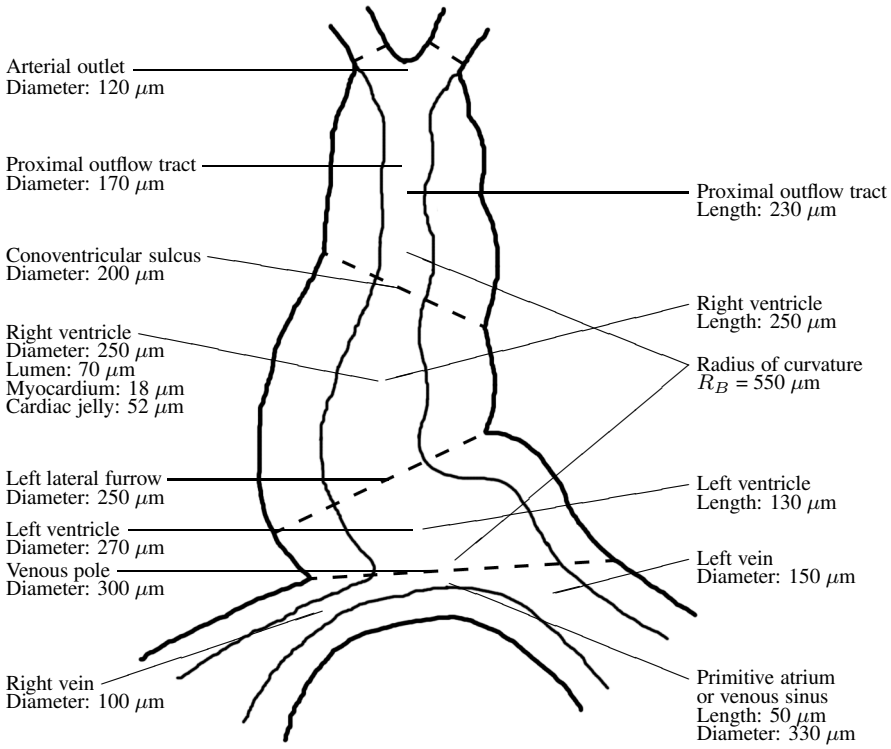

Figure 7.1: A sketch of the HH-stage 10 embryonic heart with all the found dimensional values noted on the figure.

HH-stage 10	Dimension	Reference
Length of the heart tube	500 μm	[Latacha et al., 2005]
Length of the heart tube	700 μm	[Taber, 2006b]
External diameter of the ventricle	200 μm	[Latacha et al., 2005]
External diameter of the ventricle	200 μm	[Taber, 2006b]
Lumen diameter of the ventricle	70 μm	[Latacha et al., 2005]
Thickness of the myocardial layer	18 μm	[Latacha et al., 2005]
Thickness of the myocardial layer	18 μm	[Taber, 2006b]
Thickness of the cardiac jelly	47 μm	[Latacha et al., 2005]
Thickness of the cardiac jelly	56 μm	[Taber, 2006b]

Table 7.2: Reports of HH-stage 10 embryonic heart dimensions. In addition Taber [1998] reports that the thickness of the myocardial layer is two cells thick whereas the thickness of the endocardial layer is one cell thick. Notice however that all three articles assumes a more or less concentric position of the cardiac jelly and inner lumen of the heart tube.

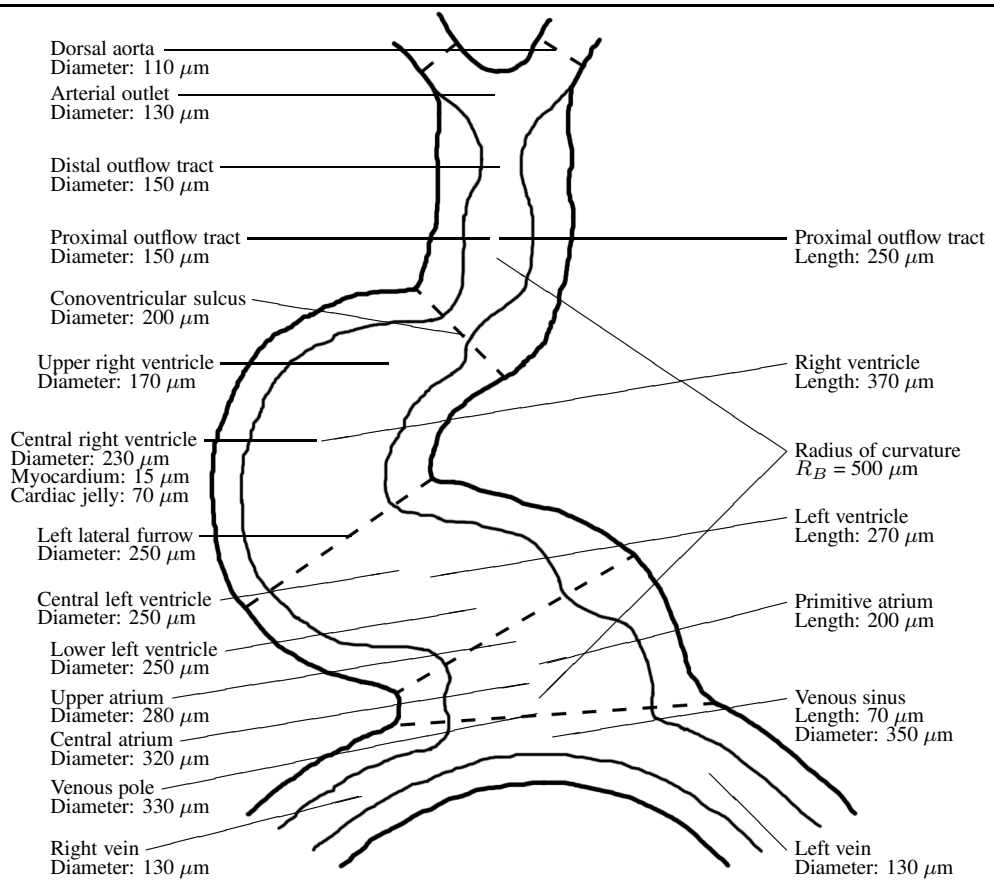

Figure 7.2: A sketch of the HH-stage 12 embryonic heart with all the found dimensional values noted on the figure. Notice the thickness of the cardiac jelly, Zamir et al. [2003] estimate the thickness to around 90 % of the tube radius but from images by Männer et al. [2008] the thickness seems to be closer to 50 %.

HH-stage 12	Dimension	Reference
Outer radius of the heart tube	150 μm	[Zamir et al., 2003]
Outside perimeter of the ventricle	1800$\pm$30 μm	[Keller et al., 1990]
Cross-sectional area of the ventricle	0.23$\pm$0.01 mm^2	[Keller et al., 1990]
Outer diameter of the outflow tract	290$\pm$10 μm	[Keller et al., 1990]
Diameter, atrioventricular canal	500 μm	[Hu et al., 1991]
Cross-sectional area of the aorta	0.01$\pm$0.002 mm^2	[Hu and Clark, 1989]
Inner radius of the heart tube	25 μm	[Zamir et al., 2003]
Thickness of the myocardial layer	15 μm	[Zamir et al., 2003]
Thickness of the cardiac jelly	135 μm	[Zamir et al., 2003]
Radius of curvature, heart tube	500 μm	[Zamir et al., 2003]

Table 7.3: Reports of HH-stage 12 embryonic heart dimensions. In addition the statement from Taber [1998] that the myocardial layer is two cells thick and the endocardial layer only one still holds for HH-stage 12, while Hu and Clark [1989] report the myocardium to be around 3-5 cells thick and the endocardium 1.

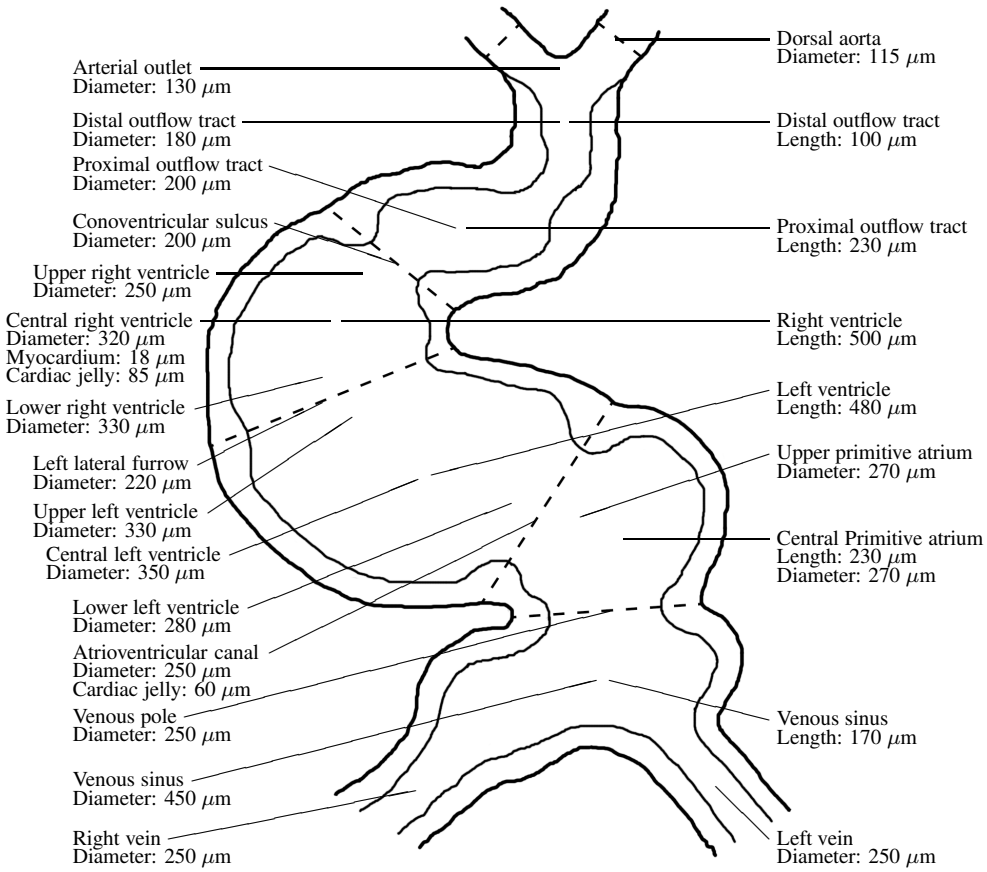

Figure 7.3: A sketch of the HH-stage 14 embryonic heart with all the found dimensional values noted on the figure. A measure of the radius of curvature is missing for this stage, therefore an average between HH-stage 12 and HH-stage 16 is used, R_B = 550 μm.

HH-stage 14	Dimension	Reference
Outside perimeter of the ventricle	2200±80 μm	[Keller et al., 1990]
Cross-sectional area of the ventricle	0.34±0.03 mm^2	[Keller et al., 1990]
Outer diameter of the outflow tract	350±10 μm	[Keller et al., 1990]
Cross-sectional area of the aorta	0.04±0.004 mm^2	[Hu and Clark, 1989]
Ventricular cardiac jelly thickness*	70-100 μm	[Männer et al., 2010]
AV-canal cardiac jelly thickness*	40-80 μm	[Männer et al., 2010]

Table 7.4: Reports of HH-stage 14 embryonic heart dimensions. For some reason numerical data for this stage of development is very scarce. (*) The thickness of the cardiac jelly is estimated from fig. 1.B in [Männer et al., 2010]. The statement from Taber [1998] that the myocardial layer is two cells thick and the endocardial layer is one cell thick still holds for HH-stage 14.

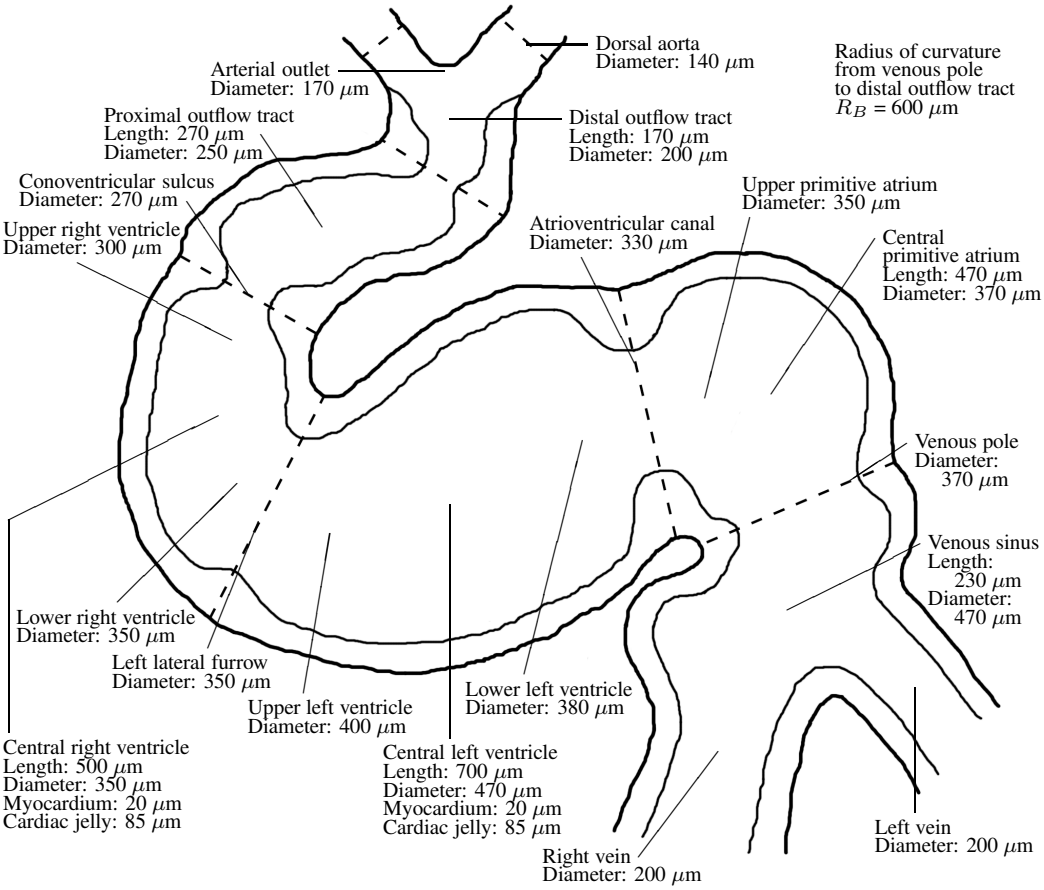

Figure 7.4: A sketch of the HH-stage 16 embryonic heart with all the found dimensional values noted on the figure.

For the thickness of the myocardial layer Taber [1998] reports that the thickness of the ventricular wall remains relatively thin with the needs of the myocardium being met entirely by diffusion from the lumen until the onset of trabeculation at HH-stage 17, and furthermore Martinsen [2005] reports that the thickness of the myocardial layer only changes slightly from 1-2 cell layers to 3-4 cell layers during the stages from HH-stage 12 to 21, thus it may be assumed that the thickness of the myocardial layer is almost constant from HH-stage 10 to HH-stage 16.

No records of the radius of curvature for a HH-stage 16 heart tube has been found, however Miller et al. [1997a] reports of a finite element model of a HH-stage 18 curved heart tube with a average radius of curvature, $R_B = 670$ μm.

HH-stage 16	Dimension	Reference
Outside radius of the ventricle	128 μm	[Taber et al., 1992]
Outside diameter, the heart tube	350 μm	[Taber et al., 1992]
Outside radius of the ventricle*	271 μm	[Lin and Taber, 1994]
Outside perimeter of the ventricle	2510$\pm$40 μm	[Keller et al., 1990]
Cross-sectional area, the ventricle	0.45$\pm$0.02 mm^2	[Keller et al., 1990]
Cross-sectional area, the ventricle	0.49 mm^2	[Miller et al., 1997a]
Outer diameter, the outflow tract	420$\pm$10 μm	[Keller et al., 1990]
Cross-sectional area of the aorta	0.06$\pm$0.004 mm^2	[Hu and Clark, 1989]
Outside perimeter of the atrium	1830 μm	[Campbell et al., 1992]
Cross-sectional area, the atrium	0.19 mm^2	[Campbell et al., 1992]
Inside radius of the ventricle*	143 μm	[Lin and Taber, 1994]
Inside diameter of the tube*	240 μm	[Miller et al., 1997a]
Thickness of the heart tube wall	128 μm	[Taber et al., 1992]
Thickness of the cardiac jelly**	85 μm	[Männer et al., 2009]

Table 7.5: Reports of HH-stage 16 embryonic heart dimensions. (*) Notice that the measures marked with an asterisk are based on a model of a concentric heart tube. (**) The thickness of the ventricular cardiac jelly is not reported directly by Männer et al. [2009] but can be measured on figure 3.B in the paper. HH-stage 16 is the final stage where the statement from Taber [1998] holds, beginning at HH-stage 17 the endocardial layer and cardiac jelly rapidly disappears in a process called trabeculation [Taber, 1998].

While this may not be an exact match for a HH-stage 16 looping heart it does give a range for radius of curvature, in fact from a comparison between HH-stage 16 and HH-stage 18 looping hearts from the figures in [Männer, 2000] the radius of curvature is probably a little less for the HH-stage 16 tube, approximately $R_B = 600$ μm.

From HH-stage 12 to 16 the cardiac jelly performs differently in the atrioventricular canal and the primitive outflow tract, the so called endocardial cushions form as an extra expansion of the cardiac jelly in those regions [Martinsen, 2005]. It is speculated that the endocardial cushions function as primitive valves in the otherwise valveless tubular heart, as they will later grow to form the heart valves of the mature heart. No reports of the exact difference between cardiac jelly thickness of the ventricle and cardiac jelly thickness of the endocardial cushions have been found, but initially suggested by Patten et al. [1948] the cushions will occlude the cardiac lumen during systole and based on the figures from that report the thickness of the cushions appears to be 3/2 - 2 times that of ventricular cardiac jelly.

7.2 Boundary conditions

As figure 7.1, 7.2 and 7.4 illustrates the relevant dimensions of the looping heart include the diameter of the caudal venous pole and an estimate of the diameter of the arterial branch at the cranial end of the embryonic heart. The model is supposed to include those two regions as the connection to the boundary conditions given by the systemic venous sinus and the arterial vascular system respectively.

The systemic venous sinus harbors the confluence of the systemic veins of the embryo, it can be regarded as a small cavity that fills passively with blood from the veins and leads the blood into the heart during diastolic filling of the atrium and ventricle. The ventricular filling mechanism is predominantly passive until HH-stage 21 [Hu et al., 1991], meaning that the ventricle is primarily filled due to a pressure difference between the venous sinus and the ventricle at diastole and that the effectiveness of the primitive atrium is still low at these stages, though it is possible to detect an increase in ventricle pressure during end diastole indicating a phase of active filling. The ratio of passive to active volume filling of the ventricle drops almost linearly from 7.89 at HH-stage 12 to 1.21 at HH-stage 18 [Hu et al., 1991].

The predominantly passive filling of the embryo indicates that the caudal boundary condition is given by the pressure at the venous sinus. According to Zahka et al. [1989] pressure at the venous sinus, 0.04 ± 0.01 mmHg, at HH-stage 21 is the lowest of an experiment with embryonic hearts from HH-stage 18 to 29. This fits well with the statement that the active filling mechanism becomes dominant at this stage, but no records of the venous sinus pressure have been found for earlier stages.

Taber et al. [1992] have measured ventricular pressure-volume loops for HH-stage 16 embryos where it is possible to characterize the filling of the ventricle from early to end diastole. The pressure-volume loops are fitted to a pressure baseline of 0 mmHg at early diastole, with a variation around ± 0.05 mmHg, where at end diastole it is close to 0.25 mmHg. This picture is confirmed by Keller et al. [1991] where it is even possible to detect a minimal kink in the pressure curve at end diastole signifying the effect of active filling. Based on the pressure curves of these two papers it would appear that the passive filling pressure (the pressure at the venous sinus) is around 0.2 mmHg, maybe even a bit lower.

For embryos of HH-stage 12, 14 and 16 Hu and Clark [1989] report an end diastolic pressure of 0.24 ± 0.02 mmHg, 0.32 ± 0.01 mmHg and 0.25 ± 0.02 mmHg respectively. This confirms the assumption above but no early diastolic pressure is measured by these authors. From Keller et al. [1991] the reported end diastolic pressures are 0.23 ± 0.01 mmHg, 0.25 ± 0.01 mmHg and 0.29 ± 0.01 mmHg for HH-stages 12, 14 and 16 respectively with a baseline of 0 mmHg early diastolic pressure for each stage. Based on these reports it would appear that a venous sinus

pressure close to 0.2 mmHg (corresponding to 26.7 Pa) is a good guess of all of these stages. No reports of pressure measurements of earlier stages than HH-stage 12 have been found but it is assumed that an average pressure of 0.2 mmHg will apply to the venous sinus of HH-stage 10 as well. It should however be noted that the heart's filling rate probably is very sensitive to this preload pressure, in accordance with observations and models of the mature heart.

Furthermore for the boundary condition at the caudal end of the embryonic heart, Männer [2008] reports that the systemic venous sinus and the mediastinal component of the primitive atrium are physically fixed to the dorsal wall of the embryonic pericardial cavity. The statement is given in the context of heart morphology and not in relation to the beating of the heart but it does indicate that conditions for the caudal end of the heart is more rigid than for the rest of the heart tube, thus it is assumed that there is a portion of the lower venous pole that does not undergo active contraction during the heart cycle and is furthermore only minimally passively contracted.

For the boundary conditions at the cranial end of the heart tube the arterial vascular system functions as a large reservoir into which the heart pumps blood with pulsatile flow and pressure. For the mature circulatory system it is common to model the vascular system with a three-element Windkessel model, with a serial connected resistance, R_c, and parallel connected capacitance and resistance, C_p and R_p, as introduced in chapter 1. Numerous reports have established this as a suitable approximation for modeling the lumped response of the mature vascular system, and it is likewise assumed to be a good description of the undeveloped vascular system, in fact Yoshigi and Keller [1996] have found the model in good accordance to flow and pressure of a HH-stage 24 vascular system. Generally however the use of a Windkessel boundary condition should be considered in relation to the application of the model; the Windkessel model will for instance typically demonstrate a misleading reflection pattern of the vascular system.

Yoshigi and Keller [1997] have performed a comparison of different Windkessel models to flow and pressure of a HH-stage 24 chick embryonic heart in frequency domain and later Yoshigi et al. [2000] compared Windkessel models with HH-stage 18 and 24 chick embryos in time domain, both projects found that the best fit was in fact obtained with a four-element Windkessel model. This model consists of a resistance, R_c, and an inductance, L_c, in serial connection and a capacitance, C_p, and another resistance, R_p, in parallel connection. R_c and L_c represent the flow resistance and inertia of the blood in the larger arteries, they are known as characteristic resistance and inertia respectively, while C_p and R_p are known as the peripheral compliance and resistance (actually compliance is the inverse of capacitance) and model the lumped compliance of the vascular system and loss of energy when leading the blood on to the veins. The Windkessel is illustrated in figure 7.8.

Assuming that the flow, $Q(t)$, and pressure, $P(t)$, are known functions time running into such a Windkessel model it is possible to estimate the values of all the elements of the model. Following Kirchhoff's laws the pressure loss is given by the pressure loss through R_c, L_c and C_p (since the pressure loss in R_p and C_p is the same), and likewise the flow spreads to the flow through R_p and C_p (since the flow through R_c and L_c is just $Q(t)$). This yields an equation for the pressure loss through C_p,

$$P_{C_p} = P(t) - R_c Q(t) - L_c \frac{dQ}{dt}, \tag{7.1}$$

and another equation for the branching of the flow,

$$Q(t) = \frac{P_{C_p}}{R_p} + C_p \frac{dP_{C_p}}{dt}, \tag{7.2}$$

combining these two equations by inserting equation 7.1 into equation 7.2 gives a differential equation in $Q(t)$ and $P(t)$,

$$\frac{dP}{dt} = -\frac{1}{R_p C_p} P(t) + \frac{R_c + R_p}{R_p C_p} Q(t) + \left(\frac{L_c}{R_p C_p} + R_c \right) \frac{dQ}{dt} + L \frac{d^2 Q}{dt^2}. \tag{7.3}$$

In the paper by Yoshigi et al. [2000] this differential equation is fitted to flow and pressure data and for a HH-stage 18 embryo the elements are found to the values $L_c = (0.378 \pm 0.12) \cdot 10^3$ g·cm^{-4}, $R_c = (0.406 \pm 0.024) \cdot 10^6$ dyn·s·cm^{-5}, $R_p = (2.16 \pm 0.12) \cdot 10^6$ dyn·s·cm^{-5} and $C_p = (0.311 \pm 0.025) \cdot 10^{-6}$ dyn^{-1}·cm^5. A similar approach could be employed here, but that would require a complete set of flow and pressure data for each of the stages, which have not been acquired.

Instead the paper by Yoshigi et al. [2000] includes detailed graphs of flow and pressure variation in the dorsal aorta, which can be transcribed to a rough set of data points, this will allow that a fitting algorithm like the one introduced in the paper be applied to reproduce the parameter values found by Yoshigi et al. [2000]. Additionally Hu and Clark [1989] have reported measurements of ventricular and arterial pressures in both systolic and diastolic configuration along with heart rate and mean dorsal aortic blood flow for HH-stages 12 to 29, assuming that the flow and pressure variation curves have a similar shape for HH-stage 12, 14, 16 and 18 it is possible to transform the transcribed data sets to fit all of those stages.

The values of the mean flow by Hu and Clark [1989] seem to be very low (almost one third) compared to the graphs by Yoshigi et al. [2000], this could be caused by a problem in their Doppler measurement technique but assuming this problem is consistent in all measurements (ie. the relative error is zero) the flow curve can be transformed by multiplication with the factor $Q_{mean}/Q_{mean,HH-18}$, where Q_{mean} refer to the mean flow at the appropriate stage.

The transcribed pressure curve is transformed using the peak systolic ventricular pressures and end diastolic vitelline arterial pressures measured by Hu and Clark [1989]. The vitelline artery is lower ranked in the arterial tree compared to the aorta, so it has peak systolic pressure much too low and end diastolic pressure just a bit too low compared to the pressure of the aorta, on the other hand the peak systolic ventricular pressure is almost similar to the systolic pressure in the dorsal aorta while the end systolic pressure is much lower. All in all the transformed pressure curve will probably have a mean pressure a bit too low compared to the pressure of the dorsal aorta, scaling the obtained pressure curve with a number slightly larger than 1 increases the fit of L_c, R_c and R_p and decreases the fit of C_p, a good scale was found to be 1.1.

Finally the period of the oscillating flow and pressure was scaled according to the heart rate period reported by Hu and Clark [1989]. The achieved data sets are naturally of poor quality compared to the original by Yoshigi et al. [2000] or any other measured data set with a higher number of data points (the transcribed data set has only 39 data points), which will make the precision of the fit worse. For comparison the HH-stage 18 embryo produced the following fit, $L_c = 0.391 \cdot 10^3$ g·cm^{-4}, $R_c = 0.322 \cdot 10^6$ dyn·s·cm^{-5}, $R_p = 1.51 \cdot 10^6$ dyn·s·cm^{-5} and $C_p = 0.297 \cdot 10^{-6}$ dyn^{-1}·cm^5. The relative deviations are 3.6%, 20.6%, 30.3% and 4.4% respectively, thus the fit of L_c and C_p falls within the listed standard deviation while R_c and R_p are 3 and 5 standard deviations away from their desired value.

For HH-stage 10 no flow and pressure is recorded in embryological literature, this is at the very beginning of the beating heart and a stable pulsating flow and pressure have yet to develop in the later stages. At the early HH-stage 9 and 10 the heart beats very irregularly but at the end of stage 10 a rhythmic contraction takes place with a frequency in the interval 0.8 - 1.2 Hz [Castenholz and Flórez-Cossio, 1972]. Furthermore Hu and Clark [1989] report in their paper that vitelline pressure increases linearly with stage while ventricular pressure and mean volume flow have a geometric increase with HH-stages. Even though the flow and pressure of HH-stage 10 hearts may be hypothetical it can be constructed through extrapolation.

With this information the four-element Windkessel model is calibrated to fit the flow and pressure data at the respective HH-stages of the embryo, the resulting calibrated parameters can be found in table 7.6.

As expected the resistance of the vascular system is higher at the earlier stages when the arteries are still very small, with the growing of arterial diameters and the mass of the vascular system the characteristic and peripheral resistances are reduced.

The embryonic vascular system is reportedly less compliant than the mature system, in fact it is so that the time constant, $\tau = R_p C_p$, which represent the decay of the pressure wave during diastole, is nearly constant in relation to the diastolic

	HH-10*	HH-12	HH-14	HH-16
L_c [kg/m^4]	$14.87 \cdot 10^8$	$6.52 \cdot 10^8$	$1.38 \cdot 10^8$	$0.75 \cdot 10^8$
R_c [Pa·s/m^3]	$5.41 \cdot 10^{11}$	$3.55 \cdot 10^{11}$	$0.86 \cdot 10^{11}$	$0.51 \cdot 10^{11}$
R_p [Pa·s/m^3]	$10.74 \cdot 10^{11}$	$9.68 \cdot 10^{11}$	$3.15 \cdot 10^{11}$	$1.87 \cdot 10^{11}$
C_p [m^3/Pa]	$0.31 \cdot 10^{-12}$	$0.36 \cdot 10^{-12}$	$1.39 \cdot 10^{-12}$	$2.21 \cdot 10^{-12}$

Table 7.6: The calibrated parameter values for a four-element Windkessel model of the vascular system given in SI-units to fit directly with the model. (*) Notice that the fitted values for the HH-stage 10 embryonic heart is based on an extrapolation from the other stages.

relaxation time for all the measured HH-stages [Yoshigi and Keller, 1996], thus when R_p is decreased at higher stages C_p is increased. Furthermore if the venous pressure (P_0 = 0.2 mmHg = 26.7 Pa) is taken as a reference to equilibrium (when the heart is not beating), an approximate equilibrium volume of the vascular system can be calculated, $V_0 = P_0 C_p$. For the HH-stage 16 embryo this gives the volume $5.9 \cdot 10^{-2}$ mm^3, which is approximately one quarter of the volume of the embryonic heart, $2.2 \cdot 10^{-1}$ mm^3. Thus the increase in C_p can be seen as an effect of the increasing volume of the vascular system.

The inertance, L_c, decreases with increasing HH-stages despite that the mass of blood is increased. This can be explained with the units of inertance, which are given by pressure over volume acceleration, but pressure is given as force per area which is again a mass times acceleration per area, the accelerations cancel and we are left with mass over area squared, but mass is density times volume which is length times area, one of the areas cancel out and in the end we are left simply with density times a length divided by an area. As we assume density is constant through all stages, the inertance is really a measure for the length of the vascular system compared to the area it covers, as the inertance is higher at the early stages it must mean that at the early stages the vascular system is actually a long an complicated tree but the dimensions of the vessels are still very small. The decreasing inertance with higher HH-stages is consistent with the findings of Yoshigi et al. [2000] and Yoshigi and Keller [1997], the latter project concluded furthermore that at least for HH-stage 24 the found inertance compares fairly to the total length of the vascular system.

7.3 Parameter estimation

The model of the embryonic heart tube needs only a very low number of material parameters, in fact only three are needed: the density of blood, ρ, the viscosity of blood, η, and Young's modulus, E, although Young's modulus is needed for each of the myocardial layer, endocardial layer and cardiac jelly.

The density of embryonic blood is reported to 1.0 g·cm^3 by [Yoshigi and Keller, 1997], due to the low hematocrit level (the volume percentage of red blood cells in the blood) in chick embryonic blood (17.7 %) the embryonic blood density is lower than for adults. For comparison the hematocrit of adult humans are around 42 %, with variance according to gender, and blood density around 1.05 g/cm^3 [Rideout, 1991, p. 78].

The viscosity of blood is even more dependent on hematocrit levels than density, in fact the suspension of red blood cells in the blood has the effect that the apparent viscosity of the blood increases with blood vessel diameter in the so called Fahraeus-Lindqvist effect [Meier, 1987], furthermore suspended blood cells will migrate towards the peak of the velocity profile in the flowing blood, this will change a regular Poiseuille flow towards a more flat flow profile [Meier, 1987]. Both of these non-Newtonian effects are strongly dependent on blood hematocrit and can be very strong in adult blood, for embryonic blood the hematocrit is sufficiently low that blood can be considered a Newtonian liquid. Meier [1987] reports a viscosity between 1 - 4·10^3 Pa·s, and Hu et al. [1991] report a kinematic viscosity of 3.8·10^{-2} cm^2/s, which with the density above equals to 3.8·10^{-}3 Pa·s.

Many authors have reported stress and strain measurements of embryonic heart tissue, especially with the focus on cardiac looping and morphology, the question is raised if cardiac looping causes residual stress in the wall of the heart tube or indeed if the process of cardiac looping is caused or enhanced by difference in wall stress or directionality in stress-strain relations. Reports indicate however that at the early embryonic stages the heart's myocardium is an isotropic material with randomly arranged sarcomeres (muscle filament) and no significant fibre architecture [Männer, 2006, Lin and Taber, 1994], furthermore the endocardium shows similar composition as the myocardium the only difference between the two layers are their thickness [Lin and Taber, 1994]. The cardiac jelly has radially oriented fibers, which may exhibit a preferred direction, but it is estimated that cardiac jelly anisotropy would have relatively little effect because of its softness compared to the myocardium [Zamir and Taber, 2004].

On the other hand Zamir et al. [2003] have measured differences in the stiffness of the heart wall under the process of dextral looping (HH-stage 12) and found that the although no significant differences were found between the outer curvature and the dorsal and ventral sides of the heart tube the inner curvature was around 2 - 3 times stiffer. Investigating this result they showed that cardiac jelly exhibit no significant difference in stiffness of the inner and outer curvature, thus it had to be a stiffness of the myocardium, and with a finite element model of the looping heart they demonstrated that this increase in myocardium stiffness could not be caused by the tube's curvature alone. Therefore it is likely that the increased stiffness is caused by a variation in the material properties in the inner curvature of the looping heart. Later Taber [2006b] concluded that the stiffness

difference may be caused by actin polymerization during cardiac looping, which causes actin (a muscle protein) to lie predominantly with a circumferential orientation near the inner curvature while there is no preferred orientation at the outer curvature, thus the assumption of isotropy likely does not hold near the inner curvature, while the residual stress field in the outer curvature of the heart loop is approximately isotropic [Zamir and Taber, 2004].

Even though the increased inner curvature stiffness of the myocardium is well known, no recordings of the stiffness is found and it is common to model the heart tube under assumption of a uniform isotropic stiffness of the entire myocardium [Zamir and Taber, 2004, Latacha et al., 2005, Taber, 2006b], which will also be the assumption here. The stiffness of the layers of embryonic heart wall are found through calibration of stress-strain measurements to the formula [Taber et al., 1995],

$$\sigma_i = \lambda_i \frac{\partial W}{\partial \lambda_i} - P \tag{7.4}$$

for $i = r, \theta, z$, where σ_i are components of the stress tensor, λ_i are the strain components in the principal directions, P is the hydrostatic pressure, and $W(\lambda_i)$ is the pseudoelastic strain-energy density function postulated by Taber et al. [1992],

$$W = \frac{A}{B}\left(e^{B\left(\lambda_r^2+\lambda_\theta^2+\lambda_z^2-3\right)} - 1\right). \tag{7.5}$$

The constants A and B in equation 7.5 are material parameters, which constitute a non-ideal small-strain elastic modulus. For a completely elastic material the material parameter A is related to Young's modulus by the relation, $E = 6A$, as long as the strains are sufficiently small [Zamir and Taber, 2004]. For both the myocardial layer and the cardiac jelly reports indicate that the stress-strain relations present fit better with this expression than with a regular Hooke's law. As such a number of reports have recorded material parameters A and B for the layers of the embryonic tube wall, parameter values can be found in table 7.7.

HH-stage	A_{MY}	B_{MY}	A_{CJ}	B_{CJ}	Reference
HH-10	10 Pa	1.2	2 Pa	0.25	[Latacha et al., 2005]
HH-12	11.1 Pa	0.49	3.0 Pa	0.30	[Zamir and Taber, 2004]
HH-16	20.0 Pa	1.1	10.0 Pa	0.10	[Lin and Taber, 1994]

Table 7.7: Parameters for the pseudoelastic strain-energy density function, the parameters A_{MY} and A_{CJ} are related to Young's modulus through the relation $E = 6A$. A_{MY} and B_{MY} refer to the elasticity of the myocardium as well as the endocardium, A_{CJ} and B_{CJ} refer to the cardiac jelly. No recordings for HH-stage 14 have been found, thus parameters for this stage will be computed as a mean between HH-stage 12 and 16.

In relation to the model of the embryonic heart it is assumed that to a first approximation the cardiac jelly (CJ) as well the myocardial (MY) and endocardial layers can be modeled as isotropic ideal elastic materials, so that Young's modulus can be found as $E = 6A$ for all layers of the tube. This gives the moduli: $E_{MY} = 60$ Pa and $E_{CJ} = 12$ Pa for HH-stage 10, $E_{MY} = 66.6$ Pa and $E_{CJ} = 18$ Pa for HH-stage 12, $E_{MY} = 93.3$ Pa and $E_{CJ} = 39$ Pa for HH-stage 14, and $E_{MY} = 120$ Pa and $E_{CJ} = 60$ Pa for HH-stage 16.

However, Zamir et al. [2003] compute a simpler model for the HH-stage 12 embryo with only one stiffness variable, where they chose Young's moduli, E_{MY} = 180 Pa and E_{CJ} = 18 Pa, arguing that the modulus of the myocardium should be one decade higher than the cardiac jelly to reflect the great difference in stiffness between the two layers. This could indicate an underestimation of myocardial stiffness or that the modulus should be around three times higher than the listed values for the myocardium when converting from the pseudoelastic strain-energy function to a regular Young's modulus, but no further evidence have pointed towards this notion.

7.4 The pumping mechanism

Finally the pumping mechanism is the big question in the modeling of the embryonic heart, what is the governing pumping principle; peristalsis or the Liebau effect, different characteristics point to different principles and as made clear by Männer et al. [2010] the answer as well as the question may not be as simple as it sounds. But before this question is addressed a description of what is recorded about the pumping mechanism is needed.

From HH-stage 10 when the embryonic heart starts beating to HH-stage 16 and 17 the myocardial layer of the heart ventricle and outflow tract undergo nearly concentric contraction during systole, while the endocardial lumen contracts in an eccentric manner where it is nearly elliptic in shape in end-diastole and slit-shaped in end-systole [Männer et al., 2008]. The eccentric contraction is caused by the uneven distribution of cardiac jelly along the original dextral and sinistral heart walls, which creates the nearly elliptic inner lumen, but in fact Männer et al. [2009] have reported that from HH-stage 13 and 14 the cardiac jelly starts to rupture with spikes reaching from the inner lumen out to the myocardial mantle, and from stage 15 to 17 much cardiac jelly has disappeared from the outer curvature of the heart loop so the inner lumen has more the shape of a bell than an ellipse at end-diastole, while it is still almost occluded at end-systole. Additionally the myocardial layer has a more eccentric contraction during these later stages.

In the modeling process the bell-shape and eccentric deformation of the myocardium at the later stages will be ignored, to a good approximation the elliptic inner lumen and a concentric deformation of the myocardial layer will cover the fundamental mechanical aspects of the tube as explained in chapter 6. Additionally the model will not be able to handle a full occlusion of the inner lumen.

Männer et al. [2009] report of a minor contraction in ventricle length during systole and Alford and Taber [2003] report of a bending and unbending of the heart tube curvature during systole, both follow from an eccentric deformation of the myocardial layer and will not be included in the models of this thesis.

As such the model will have a concentric contraction of the myocardial layer leading to an eccentric contraction of the cardiac jelly and endocardial layer, which will almost occlude the lumen of the heart tube, this is reported for a fact for both the ventricle and the outflow tract [Männer et al., 2008] and suggested for the atrioventricular canal [Männer, 2008], no reports of the contraction of atrial lumen have been found although Campbell et al. [1992] have reported active contraction curves of the myocardial layer, thus it is speculated that atrial cardiac jelly follows the same uneven distribution as ventricular cardiac jelly and the contraction level is the same.

The time function of the pumping mechanism is made up of the systolic contraction phase and the diastolic relaxation phase, together they equal one period. The period and thus also the frequency is a reference number for the pumping mechanism of the heart, even though different heart segments have different contraction and relaxation patterns their duration must always add up to exactly one period, otherwise one segment will run faster than another and the synchronization of the pumping mechanism will break down. The beating frequency of the embryonic heart is however very prone to change, even the slightest changes in the heart's environment will have effect on the frequency, as such it has become very common to report the frequency as measure of heart disturbance during experimental investigations of the embryonic heart. A range of frequencies for the various HH-stages of the heart can be found at table 7.8.

Though the frequency may change due to environment and stress of the embryonic heart the systolic contraction phase and the diastolic relaxation phase seem to change very little, when they are respectively defined as the time during which the myocardial layer contracts and the time in which it returns back to its original position [Castenholz and Flórez-Cossio, 1972]. Instead there is a third phase, the diastolic trance phase, during which the myocardial layer lies almost still, this phase varies a lot with frequency its duration is reported to lie between 410-1440 ms for HH-stage 12 to 18 [Castenholz and Flórez-Cossio, 1972].

HH-stage	Frequency	Reference
HH-10	0.8-1.2 Hz	[Castenholz and Flórez-Cossio, 1972]
HH-12	1.64 Hz	[Castenholz and Flórez-Cossio, 1972]
HH-12	1.25±0.39 Hz	[Alford and Taber, 2003]
HH-12	1.72±0.03 Hz	[Hu and Clark, 1989]
HH-12	1.32±0.10 Hz	[Keller et al., 1990]
HH-12	1.90±0.26 Hz	[Hu et al., 1991]
HH-14	1.7 Hz	[Castenholz and Flórez-Cossio, 1972]
HH-14	1.90±0.07 Hz	[Hu and Clark, 1989]
HH-14	1.93±0.08 Hz	[Keller et al., 1990]
HH-14	1.97±0.14 Hz	[Hu et al., 1991]
HH-16	2.0 Hz	[Castenholz and Flórez-Cossio, 1972]
HH-16	2.03±0.05 Hz	[Hu and Clark, 1989]
HH-16	2.00±0.07 Hz	[Keller et al., 1990]
HH-16	1.76±0.13 Hz	[Hu et al., 1991]

Table 7.8: Frequency measurements of the embryonic heart.

HH stage	Proximal contraction phase	Distal contraction phase	Proximal relaxation phase	Distal relaxation phase
HH-10	170.0±31.6 ms	228.0±41.4 ms	275.6±84.3 ms	286.0±39.3 ms
HH-12	123.7±30.4 ms	168.6±53.6 ms	193.0±66.3 ms	245.5±58.9 ms
HH-14	88.8±22.8 ms	150.1±49.2 ms	144.5±41.6 ms	145.5±46.5 ms
HH-16	109.6±17.7 ms	154.1±26.2 ms	169.2±39.2 ms	156.0±18.5 ms

Table 7.9: Duration of the systolic contraction phase and diastolic relaxation phase in the proximal and distal ends of the heart tube. Values are reported by Castenholz and Flórez-Cossio [1972].

While the systolic contraction phase and diastolic relaxation phase are invariant to changes in the heart rate they vary with the different HH-stages and they have different duration for the various heart segments. Both phases are shorter near the venous end of the heart and progressively become longer near the outflow tract and generally they both tend to become shorter for higher HH-stages. Castenholz and Flórez-Cossio [1972] have reported durations of the systolic contraction phase and the diastolic relaxation phase for the proximal and distal end of the heart tube for HH-stage 10 to 16, the data can be found in table 7.9. In addition Campbell et al. [1992] have reported atrial contraction time to 140±5 ms for HH-stage 16.

HH-stage	Contraction wave velocity	Relative diametric contraction
HH-10	$\sim$3.3 mm/s	15 %
HH-12	4.2$\pm$2.3 mm/s	24-25 %
HH-14	9.4$\pm$1.2 mm/s	26.3 %
HH-16	9.4$\pm$1.2 mm/s	24.4 %

Table 7.10: The velocity of the apparent contraction wave from the venous pole to the outflow tract and the mean relative reduction of diameter of the heart tube during contraction. Values are reported by Castenholz and Flórez-Cossio [1972].

Additionally the contraction and relaxation phases occur later in the period at the outflow tract than at the venous end of the heart, along the length of the heart tube the onset of contraction is gradually delayed so that it appears as if a contraction wave is moving from the venous end towards the outflow tract corresponding to the idea of a peristaltic pumping principle. Castenholz and Flórez-Cossio [1972] have measured the speed of this apparent contraction wave and have furthermore measured a mean diametric contraction of the outside layer for HH-stage 10 to 16, the data can be found in table 7.10. In addition Campbell et al. [1992] report a 56.2$\pm$3.0 % reduction of atrial area during contraction, corresponding to a 33.8$\pm$2.3 % diametric reduction.

The delay of contraction at the distal end of the heart tube and apparent contraction wave along the tube length give rise to a fourth phase in the characteristic contraction pattern of the myocardial layer, the so called diastolic strain phase, which is defined by an expansion of the myocardial layer. This phase is not visible at the venous end of the heart tube and most prominent at the outflow tract, where it lasts 50-100 ms and increases the diameter of the myocardial layer up to 10 %, it is therefore assumed that this phase is caused by a passive pressure wave that runs before the contraction wave of the heart tube [Castenholz and Flórez-Cossio, 1972].

To trace the contraction curve of the cardiac segments of the tubular heart three optical coherence tomography M-mode images from a HH-stage 16 embryo are supplied from a laboratory exercise made in collaboration with Jörg Männer, T. Mesud Yelbuz and Lars Thrane in 2009. The images comes from an experiment to test the image rendering and depth penetration of the OCT system during M-mode recording, see section 2.3.1, which was performed outside environmentally stable conditions for the embryo (ie. at room temperature), therefore the heart rate and ratio between contraction/relaxation phase and diastolic trance phase can not be trusted in the images. But as described by Castenholz and Flórez-Cossio [1972] the contraction and relaxation phases should be fairly unaffected. The images can be seen on figure 7.5.

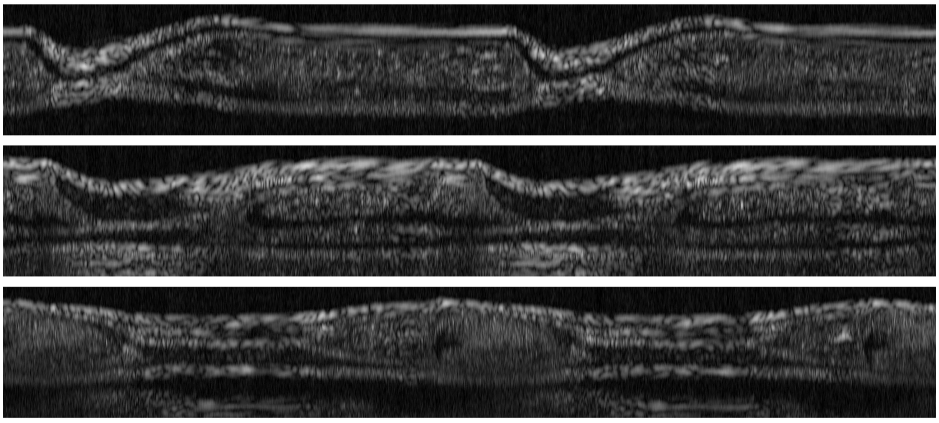

Figure 7.5: Optical Coherence Tomography (OCT) M-mode images from a HH-stage 16 embryo outside environmentally stable conditions. The images trace the diametric contraction of the heart tube as a function of time, units are not defined, at the top is a scan of the inflow region (most likely the atrioventricular canal), in the middle a scan of the ventricle, and below a scan of the proximal outflow tract. The systolic contraction phase, diastolic relaxation phase and diastolic trance phase are all easily identified but the diastolic strain phase is not recognized in these images, in addition the lower image does not show any trance phase worthy of mention.

For each of the three M-mode images the contraction pattern from start to end of contraction have been traced by simply measuring cross-sectional distance as a function pixel-number, a function is fitted to the resulting numerical arrays defined as,

$$D(t) = 1 - k_1 \sin\left(\pi k_2 \left(1 - e^{-k_3 t}\right)\right), \tag{7.6}$$

with k_1, k_2 and k_3 being the fitted parameters of the contraction function. The fitted function is then scaled according to table 7.9 and 7.10 such that the ventricular contraction function fits with the contraction ratio from table 7.10 and the other two functions are scaled accordingly. The scaling actually makes the contraction function of the inflow region fit very well with the contraction ratio reported by Campbell et al. [1992], though its duration is somewhat longer than what was reported. The fitted parameters for the HH-stage 16 embryo can be found in table 7.11 and a plot of the function can be seen on figure 7.7.

Though the systolic contraction phase and the diastolic relaxation phase are almost time-invariant to changes in the environment of the embryo the contraction may experience other changes, as a result the fitted contraction function should

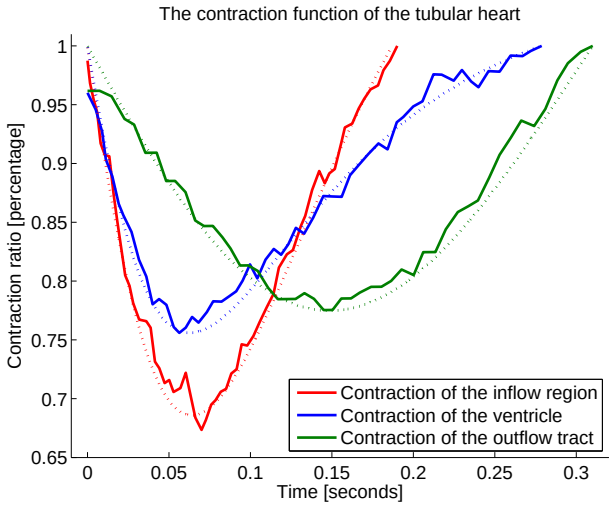

Figure 7.6: A plot of the contraction function from equation 7.6 (dotted curves) fitted to the tracings of the diametric contraction of the heart in figure 7.5 and scaled for a HH-stage 16 embryonic heart using table 7.9 and 7.10 (solid curves).

	k_1	k_2	k_3	Duration
Inflow region	31.4 %	1.35	7.24 s^{-1}	187 ms
Ventricle	24.4 %	1.06	10.11 s^{-1}	279 ms
Outflow tract	22.5 %	6.66	0.52 s^{-1}	310 ms

Table 7.11: The fitted parameters of equation 7.6 together with the fitted contraction duration for the HH-stage 16 embryonic heart.

only be seen as an approximation used in this model of the embryonic heart. Likewise the contraction function is known to be unique for each HH-stage of the embryo, but regardless of this fact the fitted function from equation 7.6 is scaled using data from table 7.9 and 7.10 for each of the embryonic stages modeled.

For each of the HH-stages modeled a contraction function is defined for each of the cardiac segmental areas: atrium, ventricle and outflow tract. It is assumed that the contraction wave moves along the heart tube with velocity defined in table 7.10 and when crossing the boundary to a new cardiac segment it changes contraction characteristics to the new contraction function. The contraction duration is furthermore only a fraction of the period and for the fraction of time outside the contraction duration the contraction is assumed to be zero.

7.5 Model setup

The model of the heart tube is defined through a tracing of the dimensions of the tubular heart, a set of boundary condition, an estimation of physical parameters and the definition of a pumping mechanism. The four steps have been carried out in the sections above, this final step combines them into a model.

The tracing of the dimensions is carried out in section 7.1, especially the lengths and diameters from table 7.1 are considered of value in this estimation, table 7.2 to 7.5 include dimensional reports from other researchers which should be seen as references to the validity of the first mentioned lengths and diameters; apparently length and size of the embryonic heart may vary and so it should be considered best to base the modeling on a complete set of data from one embryo instead of data pieced together from various authors.

The length and diameters from table 7.1 are plotted against each other, and lines are fitted between the points. Based on the reported dimensions of the cardiac jelly in table 7.2 to 7.5 an estimate of the inner lumen of the heart tube is made at similar longitudinal coordinates as the myocardial layer, lines are fitted between those points as well. Plots of this procedure is visible on figure 7.7. This make the heart tube look a little rough-edged, but no better solution has presented itself. A number of sections, N, for the model is chosen and the dimensions of each section is fitted such that each section has inner and outer dimension corresponding to the function value taken at the center of the section. This results in two arrays of outer and inner dimensions of the heart tube corresponding to the variables A_n and B_n of the model.

The radius of curvature of the heart tube is recorded in section 7.1. The tube curves from the point of the venous pole to somewhere around the middle of the outflow tract, even though it is clear that the curvature is not a constant function of the length along the heart tube it will be considered as such in this model. For each HH-stage the first and last sections of heart curvature is determined based on the total number of sections, N, and the bending angle for each section is calculated as section length divided by 2π times radius of curvature.

The boundary conditions for the heart tube are found in section 7.2, for the lower end of the heart it is defined by the venous pressure, for the upper end it is defined by a four-element Windkessel model. These two conditions can be seen depicted in the energy bond diagram in figure 7.8.

The venous boundary condition, P_0, is a pressure that will go into the model equations just like any other pressure in the model except that this pressure will define the equilibrium pressure in the heart tube, if the heart stopped beating. In addition to this condition at the lower end of the tube it is necessary to include another condition such that the heart tube is not mechanically isolated from the veins, to this end an additional 'ghost' section is added to the tube in the lower

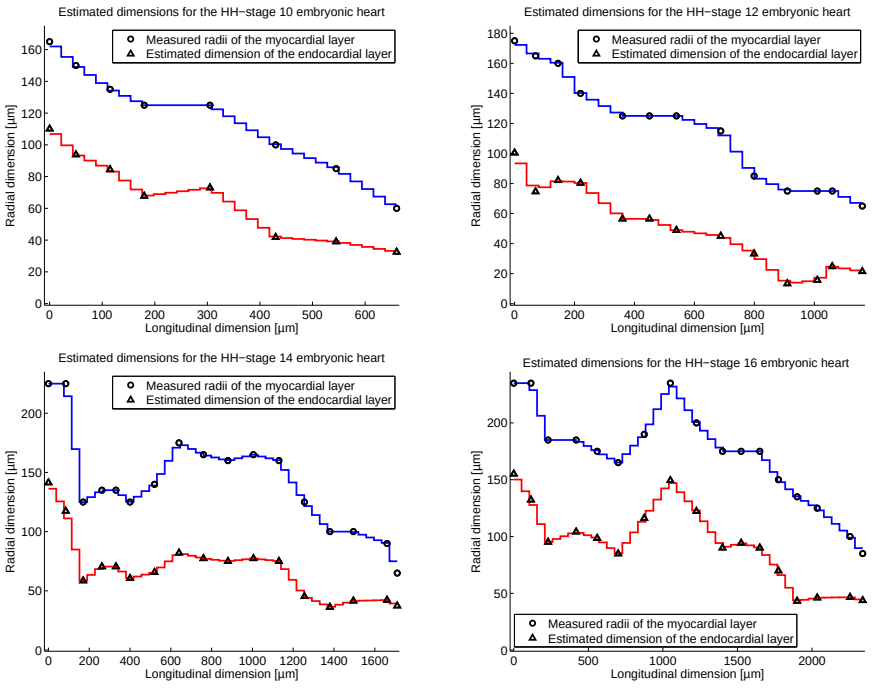

Figure 7.7: Plots showing longitudinal and radial dimensions of the heart tube for all the HH-stages modeled. The points marked in the plots comes from the measured dimensions from table 7.1 and from an estimate of the thickness of the cardiac jelly relative to the radius of the myocardial layer. The staircase functions are an illustration of the dimensional arrays used in the model, the number of sections in the model may change however.

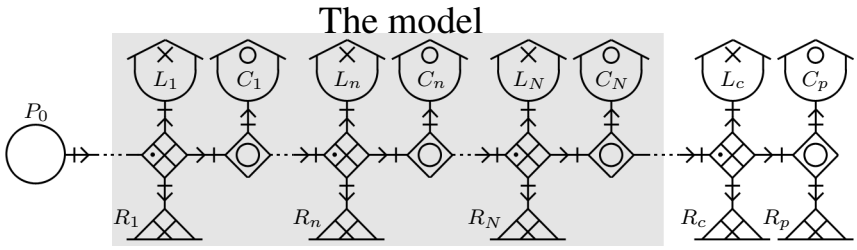

Figure 7.8: A diagram of the model with boundary conditions. The gray-shaded area is an icon for the whole complicated layered model, while P_0 is the boundary condition at the venous end and the Windkessel termination with L_c, R_c, R_p and C_p is the boundary condition at the arterial end of the heart tube.

end, this section has dimensions similar to the first section of the model except they do not vary with time, such that the variance of the first section of the model is felt relative to the 'ghost' section.

The arterial boundary condition is given by a four-element Windkessel model with parameters specified in table 7.6. In addition this boundary will also be modified with an invariant 'ghost' section that is primarily experienced through the shear tensions in the model.

The Windkessel expands the model with more equations that have to be iterated in time along with the rest of the model's equations. For both the inertance and the capacitance in the Windkessel model a function is specified such that the differential equation of that function is added to the set of equations in the Runge-Kutta algorithm step of the simulations. For the inertance it is the momentum of flow into the vascular system, M, which is the input function to the element L_c, for the capacitance it is the volume of the vascular system, V, which is the input to the element C_p. The differential equations are given by,

$$\frac{dV}{dt} = Q_{N+1} - \frac{P_{N+1}}{R_p} \tag{7.7}$$

$$\frac{dM}{dt} = P_N - P_{N+1} - R_c Q_{N+1}, \tag{7.8}$$

where P_N is the pressure in the final section of the model and Q_{N+1} and P_{N+1} are the flow and pressure in the vascular system given by the equations,

$$Q_{N+1} = \frac{V - V_0}{C_p} = \frac{V}{C_p} - P_0 \tag{7.9}$$

$$P_{N+1} = \frac{M}{L_c}. \tag{7.10}$$

V_0 is the equilibrium volume of the vascular system, which may be defined as, $V_0 = C_p P_0$, where P_0 is the equilibrium pressure corresponding to the pressure in the venous end of the model.

The parameter estimation is carried out in section 7.3 and consists only in finding values for the density of blood, $\rho = 1.0 \cdot 10^3$ kg/m^3, viscosity of blood, $\eta = 3.8 \cdot 10^{-3}$ Pa·s, and the elastic modules for the myocardium, endocardium and cardiac jelly, E_{MY}, E_{EN}, E_{CJ}, which can be found in table 7.7. There may be some uncertainty about the elastic modules as Zamir et al. [2003] argue that the ratio between myocardial and cardiac jelly stiffness should be at least one decade, which does not fit with the values in table 7.7. Some parameter variance tests may be interesting to see the difference.

The pumping mechanism is detailed in section 7.4, it is given by the heart rate found in table 7.8 and the contraction and relaxation phases found in table 7.9, which detail the duration and frequency of the contractions of the heart tube. Furthermore table 7.10 details the ratio of contraction relative to equilibrium dimensions, the table also details that the heart contractions are seen as a wave traveling from the caudal to the cranial end of the heart tube with a certain wave speed.

The exact functions of the contractions are found by a tracing of the contraction of a HH-stage 16 heart demonstrated in OCT M-mode images in figure 7.5, which are subsequently scaled in accordance to the reported values and a function is fitted to the data for all HH-stages modeled. These contraction functions (or rather their derivatives) will be added to the differential equation of the outside myocardial layer in the model and for each section they will be phase shifted in accordance with the reported wave speed of the contraction wave.

Initial values of the model will be given by the dimensions of A_n and B_n, the initial momentum of flow is assumed to be zero, $p_n = 0$ and $M = 0$, which will also entail that $V = V_0$. The heart will start from equilibrium conditions and a few periods of simulations is required for it to reach a stable cycle where all the dynamic variables of the model have found their natural levels.

Chapter 8

Simulation Results

In this chapter results of the simulations will be presented. The embryonic heart is simulated for HH-stages 10, 12, 14 and 16 according to the setup specified in chapter 7 and in addition a series of simulations for the case of Liebau's ring presented in chapter 5 is setup for the elliptic and embedded model through a modification of the setup instructions presented in section 5.2.

Through the analysis of the simulations it is attempted to give answers to the three questions posed in chapter 1. Specifically the first question is of interest for the simulations of the embryonic heart, to prove via simulation results that the models can produce data comparable to reported data of flow and pressure in the embryonic heart.

Comparability between mean flow and pressure curves of the models and the embryonic heart is important in the argumentation that models adequately describe the embryonic heart, though not all of the discussion can be decided with the comparability of data sets. The greater part of the discussion will be a comparison of the likely effects of the flow phenomena in the embryonic heart and the effects included in the model, which will be carried out in chapter 9.

For the simulations of the case of Liebau's ring with tubes of elliptic or multilayered cross-section specifically the second of the three questions in chapter 1 is of interest. The simulations are produced from a suggestion that the Liebau effect may be greater in tubes with elliptical cross-section compared to circular cross-section, or that eccentric elliptical contraction may have a higher mechanical efficiency compared to concentric contraction.

The results achieved with those simulations will only be suggestive to the embryonic heart, already research indicate that tubes with elliptical cross-section may have higher mechanical efficiency for peristaltic pumping, if the same proves true for the Liebau effect then a strong suggestion to why the embryonic heart has elliptic cross-section is presented, regardless of the pumping effect employed.

The end of the chapter will have a short analysis and conclusion to the results of the simulations, specifically regarding those two questions.

8.1 The embryonic heart simulations

Simulations of the tubular looping embryonic heart are made according to the setup described in chapter 7 and attempted for HH-stages 10, 12, 14 and 16. The attempt was not successful.

The embedded model presented in chapter 6 is employed in the simulations, specifically the equations of the rates of change of elliptic major axis, a_n, of the elliptic minor axis, b_n, and of the momentum of flow, p_n, given by equation 6.124, 6.125 and 6.126 respectively, are iterated in a Runge-Kutta algorithm to find their time-dependent variables and from those the variables of volume flow and pressure are calculated using equation 6.120 and 6.121.

The model equations are setup according to the description in chapter 7. As such the model includes a tapering three-layered curved heart tube, with cardiac jelly and an elliptic inner lumen set according to the dimensions of the heart presented in section 7.3. The pumping mechanism affects nearly the whole length of the heart tube with a contraction pattern as defined in section 7.4. That is, all the effects presented in the previous chapters are included into the simulations of the embryonic chick heart.

It has not been possible to obtain simulation results in time to include them in this thesis, at time of delivery the simulation routine is still working on its fifth week of computation. Since the simulation program has not terminated it is believed that the model actually works, but the complicated setup of the embryonic heart makes it difficult for the Runge-Kutta iteration algorithm to find convergent solutions in time, forcing it to decrease time steps to extremely small numbers in relation to its convergence criteria.

With the simulations of the case of Liebau's ring with elliptic cross-section, which will be presented in section 8.2, it is proved that the models themselves are functional, even the embedded model. Thus the problem must lie in the setup of the embryonic heart simulations. A suggestion to what causes the problems in the computations is presented below in section 8.1.1.

The simulation data would have been presented as time-oscillations of flow and pressure, specifically the outflow from the heart to the dorsal aorta and ventricular pressure curves are interesting in the time domain. Mean flow and pressure would be calculated on the basis of the oscillations, and a contraction curve of the heart tube visualized as a graphs of the time-dependent axial dimensions as a functions of the length of the tube, for each developmental stage of the embryo.

The data from the simulations of the embryonic heart would be compared to reports of aortic mean flow and ventricular pressure from the works of Castenholz and Flórez-Cossio [1972] and Hu and Clark [1989]. The comparison will not

offer a complete validation of the model as the data material is too poor, instead the comparison is meant to check the plausibility of the simulations in relation to reported data. This would have been an important link in the investigation of the first of the three questions presented in chapter 1.

8.1.1 Model programming

The programming of simulations of the embryonic heart is setup with the embedded model and uses the differential equations presented in section 6.5.3 giving the rates of change for the momentum and the elliptical axes of the inner lumen, where the major axis is also the radius of the outer myocardial layer. The setup conditions for the simulations are presented in chapter 7, and especially the boundary condition at the arterial end adds the two differential equations given by equation 7.7 to the model.

The models are divided into N sections in the simulations, where N is a specific number that fit with the measured dimensions of the embryonic heart. Not all numbers are viable, lengths and diameters of the different cardiac segments of the embryonic heart dictate the possible number of sections, which is different for the simulations of each HH-stage. The values of N used in the simulations lie in the range from 30 to 60, though smaller numbers have been used in an attempt to produce data results from the simulations. The possible values of N are are calculated and written in the programs presented in appendix B.

The cross-sectional dimensions of each section of the model are set according to a fit to the dimensions specified in section 7.1 and modified with respect to N and an overall assumption of the distribution of cardiac jelly in the heart, as such the dimensions in the simulations will appear as the staircase functions depicted in figure 7.7.

The pumping function in the simulations will be approximated by the functions depicted in figure 7.7 and applied through the derivative of the functions added to the rate of change of the major axis of the elliptic cross-section. For the pumping function the compression ratio presented in table 7.10 is a defining number, it is believed that the combination of the staircase functions of the cross-sectional axes of the tube and the compression ratio causes the problems for the computations of the model.

The model is programmed in MatLab v. 7.5 (copyright The MathWorks Inc.) and makes use of MatLab's inherent 'ode45' Runge-Kutta algorithm to iterate the differential equations of r_n and p_n and the functions V and M of the arterial boundary condition of the model. After the end of the 'ode45'-solver the values of P_n and Q_n are calculated. The programs used in the simulations are presented in appendix B.

Due to the complicated nature of the simulations is has not been possible to estimate the computation time. The 'ode45' solver is extremely time consuming for the simulations and in addition the amount of data created gives problems for MatLab's virtual memory so that a swap disk is created by MatLab; saving and loading data to such a disk uses even more time. Even if the simulation programs are changed to run for very short intervals of one period or if fewer data points are saved in the recorded simulation data the problem persists. This indicates that the problem created by the simulation programs is a problem for the 'ode45' solver itself.

8.1.2 Comparison with reported data

The simulation data from the embryonic heart would have been compared to reported data of the mean outflow from the heart to the dorsal aorta and to systolic and diastolic ventricular pressure measurements.

The outflow from the embryonic heart to the dorsal aorta is measured by Hu and Clark [1989] for HH-stages 12, 14 and 16 to the values 0.02 ± 0.004 mm^3/s, 0.08 ± 0.01 mm^3/s and 0.15 ± 0.01 mm^3/s respectively, corresponding to mean velocities of 0.86 ± 0.07 mm/s, 1.89 ± 0.12 mm/s and 2.77 ± 0.20 mm/s.

Castenholz and Flórez-Cossio [1972] measure the flow velocities in the dorsal aorta between 0.16 to 0.93 mm/s for HH-stage 12, between 0.50 to 0.80 mm/s for HH-stage 14, and up to around 3.0 mm/s for HH-stage 16. This confirms the measurements of Hu and Clark [1989] except for HH-stage 14, where they seem to disagree about a mean flow velocity between 0.70 to 1.89 mm/s.

No volume flow or mean velocity have been measured for HH-stage 10, likely because at that stage the tubular heart is still too undeveloped and the contraction pattern too irregular to decide flow conditions.

Diastolic and systolic pressure in the ventricle is measured by Hu and Clark [1989] to 0.24 ± 0.02 mmHg and 0.95 ± 0.04 mmHg for HH-stage 12, 0.32 ± 0.01 mmHg and 1.04 ± 0.04 mmHg for HH-stage 14, and 0.25 ± 0.02 mmHg and 1.15 ± 0.04 mmHg for HH-stage 16. In addition the pressure of a first-order vitelline artery is measured 0.23 ± 0.01 mmHg and 0.32 ± 0.01 mmHg for HH-stage 12, 0.35 ± 0.01 mmHg and 0.52 ± 0.02 mmHg for HH-stage 14, and 0.39 ± 0.02 mmHg and 0.62 ± 0.03 mmHg for HH-stage 16. The vitelline arterial pressure may be seen as a good approximation to the pressure at the outlet of the embryonic heart. Additionally Lin and Taber [1994] report the peak systolic pressure of the ventricle to around 1.0 mmHg, confirming the values above. The data is presented in table 8.1.

The comparison of data has not been possible since no data from the embryonic heart simulations is achieved. Though from the simulations of Liebau's ring below in section 8.2 it can be said that a mean flow in the range from 0.02 to 0.20 mm^3/s is high yet not unlikely for Liebau effect driven flow with elliptical con-

	HH-stage 12	HH-stage 14	HH-stage 16
Dorsal aortic Q_{mean} [mm^3/s]	0.02 ± 0.004	0.08 ± 0.01	0.15 ± 0.01
Ventricular $P_{diastole}$ [mmHg]	0.24 ± 0.02	0.32 ± 0.01	0.25 ± 0.02
Ventricular $P_{systole}$ [mmHg]	0.95 ± 0.04	1.04 ± 0.04	1.15 ± 0.04
Vitelline $P_{diastole}$ [mmHg]	0.23 ± 0.01	0.35 ± 0.01	0.39 ± 0.02
Vitelline $P_{systole}$ [mmHg]	0.32 ± 0.01	0.52 ± 0.02	0.62 ± 0.03
Vitelline P_{mean} [mmHg]	0.28 ± 0.01	0.40 ± 0.01	0.49 ± 0.03

Table 8.1: Experimental data of mean flow in the dorsal aorta and systolic, diastolic pressure in the ventricle and a first-order vitelline artery, and the mean vitelline pressure reported by Hu and Clark [1989]. No data from HH-stage 10 is reported.

traction. Similarly the mean pressure is increased compared equilibrium pressure, defined by the boundary condition at the venous end, $P_0 = 0.2$ mmHg, which is also seen in the simulations of Liebau's ring with elliptical contraction. Thus from a short comparison of effects it is clear that a Liebau pumping principle can not be ruled out for the embryonic heart.

8.1.3 Conclusion to the embryonic heart simulations

The simulations of the embryonic heart have not been successful. The computation time is simply too long and the amount of data to great for the computer to handle it. This may be an effect of a model setup that causes diverging effects in the simulation results, which can create problems for the 'ode45' solver in MatLab.

The modeling and simulation of the embryonic heart was expected to act as a proof of principle, to demonstrate that the embryonic heart can be described through these models. Thus it would prove that whatever details are true for the models will also be true for the embryonic heart. For instance could it be proved that Liebau pumping is more effective in a model with elliptic cross-section compared to circular cross-section, that would also count for the embryonic heart.

This is the essence in the first of the three questions in chapter 1, to provide a link between the model and the embryonic heart. Furthermore this makes the circumstances for the investigation of the third question posed in chapter 1 insecure. This will be discussed further in chapter 9.

The lack of simulation data is disappointing but as a result the simulations of an elliptic equivalent to Liebau's ring becomes even more important, despite its loose connection to the embryonic heart. Through those simulations it will be proved that the elliptic models are actually working while it is simultaneously investigated what an elliptic cross-section does for the Liebau effect in Liebau's ring.

8.2 Liebau's ring revisited

It has been suggested that tubes with elliptic cross-sections are better suited for peristaltic propulsion of liquid and some experiments indicate that this may be true [Männer et al., 2008], but so far it is not known if the same is the case for tubes with liquid flow caused by the Liebau effect. To investigate this hypothesis the case of Liebau's ring is applied to a tube of with an elliptic cross-section.

The elliptic model introduced in chapter 6 is applied with the setup of Liebau's ring introduced in section 5.2: Material parameters and dimensions are the same, the only difference is that the tube has an elliptic cross-section defined by the eccentricity $e = \sqrt{1 - B^2/A^2}$, where A and B are the equilibrium lengths of the major and minor axis.

The elliptic tube is defined such that it has cross-sectional area similar to the cylindric tube, $\pi AB = \pi R^2$, where R is the equilibrium radius of the cylindric tube. Thus as a function of the eccentricity the equilibrium lengths of the elliptic axes become,

$$A = \sqrt{R^2 \frac{1}{\sqrt{1-e^2}}} \qquad \text{and} \qquad B = \sqrt{R^2\sqrt{1-e^2}}. \tag{8.1}$$

To utilize the possibilities in the elliptic model two pumping mechanisms are applied. One pumping mechanism has concentric contraction just as described by equation 5.3 and 5.4, only with A and B substituted instead of R.

The other pumping function is specified with an elliptic contraction, such that the minor axis of the ellipse is reduced while the major axis is increased such that the compression ratio, $c = \frac{AB - A_{max}B_{min}}{AB}$, is still set to 25% just as the simulations in chapter 5. The maximum length of the major axis, A_{max}, and the minimum length of the minor axis, B_{min}, are defined,

$$\begin{aligned} A_{max,m} &= A_{0,m}\left(1 + \sqrt{c\sin\left(\pi\frac{m}{M+1}\right)}\right) \qquad \text{and} \\ B_{min,m} &= B_{0,m}\left(1 - \sqrt{c\sin\left(\pi\frac{m}{M+1}\right)}\right), \end{aligned} \tag{8.2}$$

where $m = 1, \ldots, M$ is the index number for the sections included in the pumping function and M is the total number of sections in the pumping function, and $A_{0,m}$ and $B_{0,m}$ are the length of the axes of the section for the tube at rest. Unfortunately some of the simulations were progressed without the sine-factor in equation 8.2, for those simulations the compression profile is simply $A_{max,m} = A_{0,m}(1 + \sqrt{c})$. But as shown in figure 8.2 it does not make a great difference.

The dynamic axes are then defined as functions of time,

$$\begin{aligned} A_m(t) &= A_{0,m} + (A_{max,m} - A_{0,m}) \sin\left(\frac{\pi f}{0.1} t\right) \qquad \text{and} \\ B_m(t) &= B_{0,m} - (B_{0,m} - B_{max,m}) \sin\left(\frac{\pi f}{0.1} t\right), \end{aligned} \tag{8.3}$$

for $t \bmod T \in [0, 0.1/f[$ and $A_m(t) = A_{0,m}$ and $B_m(t) = B_{0,m}$ else, where f is the frequency of the pumping function.

The simulations are made with MatLab v. 7.5 (copyright The MathWorks Inc.) and program codes can be found in appendix C.

8.2.1 An elliptic Liebau's ring

It is stated by Männer et al. [2008] that other researchers have produced results indicating that tubes with elliptic cross-sections have a higher mechanical efficiency in relation to peristaltic pumping, but it has not yet been investigated for the Liebau effect. It is however unclear from that report if the mechanical pumping mechanism in the peristaltic pumping is also of elliptical eccentric character or if it is concentric. Thus both pumping mechanisms will be investigated here. Figure 8.1 shows a comparison between an elliptic Liebau's ring with concentric contraction and with the elliptic pumping function defined in by equation 8.3.

From figure 8.1 it is clear that the elliptic deformation is far superior to the concentric contraction employed for both the tube with circular cross-section and elliptic cross-section. The induced oscillations have far greater amplitudes and do not seem to oscillate more than the oscillations of the concentric pumping. The mean flow is greater in magnitude and the mean pressure increase rather than decrease, which is the typical case for the concentric deformations.

The eccentric deformation involves a combination of shear and pure deformations while the concentric contraction is only pure, thus in order to produce a reduction of the cross-sectional area given by the compression ratio, c, the eccentric pumping function has to deform the tube more than the concentric pumping function. For a compression ratio $c = 25\%$ the length of the minor axis is halved while the length of the major axis is increased by a factor 1.5. For the concentric pump they are both only reduced by a factor 0.87.

Naturally this means that the eccentric deformation costs more energy, which is reflected in the higher oscillations in figure 8.1. The increase in energy in a section of the tube is defined as the pressure times the change in volume, $\Delta E = P\Delta V$, yet the volume change is the same with concentric and eccentric deformation, thus the ratio of energy cost between the pumping functions must be a ratio between the pressures they both produce, $\Delta E_{ecc}/\Delta E_{con} = P_{ecc}/P_{con}$.

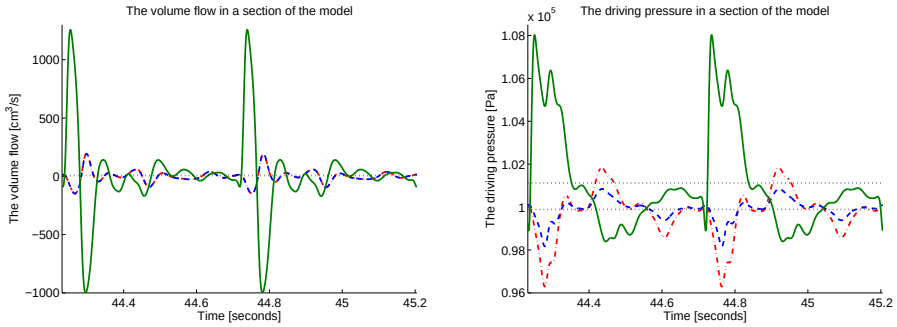

Figure 8.1: Comparison of the simulations, one cylindric tube with concentric contraction (red dash-dotted curve), one elliptic tube with concentric contraction (blue dashed curve) and one elliptic tube with eccentric contraction (green solid curve). Eccentricity in the elliptic tube is set to $e = 0.1$, only slightly elliptic. On the left is a plot of the flow oscillations, notice that two of the curves lie on top of each other, mean flow is -1.78 cm^3/s for the cylindric tube, -1.59 cm^3/s for the elliptic tube with concentric deformation and 7.11 cm^3/s for the elliptic tube with eccentric deformation. On the right is a plot of the pressure oscillations, mean pressure is $9.97 \cdot 10^4$ Pa for the cylindric and elliptic model with concentric contraction and $10.11 \cdot 10^4$ Pa for the elliptic model with eccentric deformation. It is clear that the eccentric deformation far supersedes the performance of the concentric contraction and qualitatively it gives a completely different flow.

The pressure of the elliptic model is defined in equation 6.92 and with secondary effects of the shear elasticity assumed to be insignificant the ratio between the energy requirements for the two pumping mechanisms is found to be 2.86 for the particular model setup, yet the ratio between the mean flows of the two pumping mechanisms is 4.47. Thus the eccentric deformation has higher mechanical efficiency.

Furthermore the concentric contraction appears as an essentially unrealistic pumping mechanism in Liebau's ring. In a realistic setting the pinching of the tube at an asymmetric location will never be done by contracting the radius of the tube. Instead pinching the tube by pressing it with two fingers seems much more realistic, this will create an eccentric deformation of the tube though the elliptic deformation described by equation 8.3 is probably an idealized approximation to such a deformation, and for high numbers of the eccentricity it will certainly also be unrealistic.

Figure 8.2 shows the mean flow in the tube as a function of pumping frequency for the cylindric tube, the elliptic tube with concentric contraction and the elliptic tube with eccentric deformation. It is clear that the eccentric deformation produce

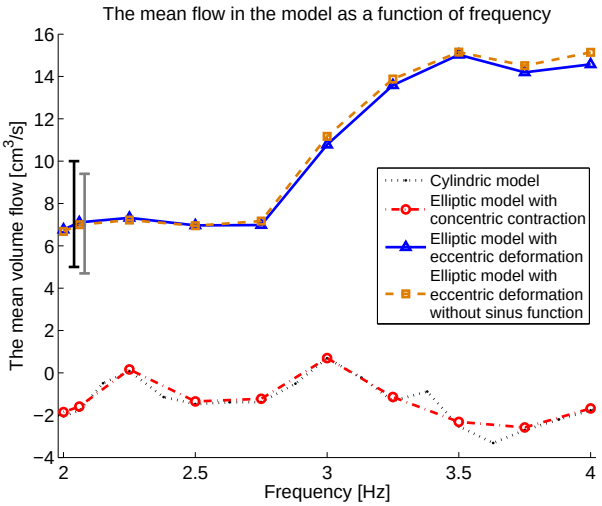

Figure 8.2: A comparison of mean flow as a function of frequency. Four series are graphed: The results of the cylindric Liebau's ring (dotted curve), the elliptic tube with concentric contraction (dash-dotted curve), the elliptic tube with eccentric deformation (solid curve) and the elliptic tube with eccentric deformation, where the sine-factor of equation 8.2 were omitted by mistake (dashed curve). Compression ratio is set to 25 % and eccentricity is 0.1 for the elliptic models. It is seen that the cylindric model and the elliptic model with concentric contraction produce results that are almost similar, which is expected since the elliptic cross-section is very close to circular. The simulations with eccentric deformation are also nearly identical, which indicate that the sine-factor in equation 8.2 has only little influence on the Liebau effect. The mean flow of those simulations is much higher than the other two, and in fact it fits perfectly with the experimental data from Snitker et al. [2000], indicated by the black and grey bars.

much higher mean flow for all frequencies, in fact considering that the eccentric deformation of the tube is a more realistic pumping function it is interesting to see that the mean flow compares to the experimental data reported by Snitker et al. [2000], which none of the simulations in chapter 5 could reproduce. Further comparison to these experimental results have no meaning as explained in section 5.5, but it illustrates clearly the difference between the pumping effects.

Furthermore it is clear that the elliptic tube with concentric contraction compares fully with the cylindric tube simulation, which is also expected since the eccentricity of 0.1 makes the elliptic cross-section very close to circular. This demonstrates that the elliptic and cylindric tube models are essentially similar in the limit when the elliptic cross-section becomes circular.

Figure 8.2 includes two simulations with the elliptic tube with eccentric cross-section; both are described by equation 8.3 though for one of them the sine-factor in equation 8.2 was accidentally omitted. The figure demonstrates that the simulations are essentially identical, only little difference is shown between them, which will be used in figure 8.3.

The frequency spectrum of the eccentric deformation appears to be different from the concentric deformation even though the tubes are similar. As it is demonstrated in section 5.3 the frequency spectrum depends on the resonance of pressure waves traveling in the tube. The speed of those pressure waves is given by the Moens-Korteweg equation, which can be calculated as a function of elasticity of the tube compared to the inertia of the liquid as specified in section 3.8. However for the elliptic tube the elasticity of the tube walls is a very complicated function and thus it is not possible to give a simple expression for the speed of the pressure waves.

Yet if the eccentricity of the elliptic cross-section is sufficiently low the Moens-Korteweg equation of the circular tube may be regarded as a suitable approximation, and thus the frequency spectrum should be approximately similar to the spectrum given in figure 5.5. Indeed it is seen that the elliptic tube with concentric contraction demonstrate almost exactly the same mean flow as the circular model in figure 8.2, but the tube with eccentric deformation does not.

This points to the conclusion that the simple picture presented in section 5.3 does not hold in the general case. The Liebau effect is not only caused by the resonance between reflected pressure waves in the system, but the nature and creation of those waves seem to have influence as well, specifically with relation to the modes of deformation of the tube. Here it seems that the eccentric deformation is defining for the spectrum such that at the previously determined resonance frequencies at 2.78 Hz, 2.96 Hz and 3.16 Hz the level of the mean flow seems to change rather than show resonance peaks.

The simulations of the elliptic Liebau's ring is made for several configurations of the eccentricity, which is demonstrated in figure 8.3. If it makes a difference to the Liebau effect that the tube is elliptic then eccentricity of the ellipse must have an influence on the effect, and for some value of the eccentricity the Liebau effect has to be optimal.

As the figure demonstrates the mean flow of the tube with concentric contractions decline with increasing eccentricity, in fact it appears to change direction with high eccentricity. It makes sense that the flow should go to zero when the eccentricity is increased as the ellipse becomes more and more stretched and thus friction is increased, though it does not explain why the flow should change direction. This could however be a numerical effect.

The mean flow of the tube with eccentric deformation increases with increasing eccentricity. This is probably a result coming from the fact that with increasing

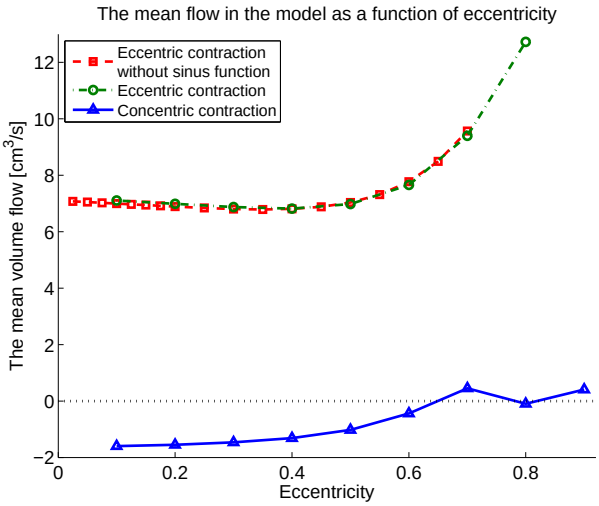

Figure 8.3: A comparison of the elliptic and concentric pumping functions as a function of the eccentricity of the cross-section of the tube. for the tube with eccentric contraction the magnitude of mean flow increases with eccentricity of the elliptic cross-section, for the concentric it goes to zero or the flow changes direction.

eccentricity the pumping function becomes increasingly unrealistic; the pumping function reduces the length of the minor axis by a factor 0.5 and increases the major axis by a factor 1.5, when the ellipse has a high eccentricity the change in the major axis of the pump becomes even greater, which is more costly in energy (the energy ratio for $e = 0.7$ equals $E_{ecc}/E_{con} = 4.10$). At extreme eccentricities this becomes absurd.

8.2.2 An embedded Liebau's ring

For the embedded model it is also possible to make a setup of Liebau's ring, this is done similarly to the cylindric and elliptic Liebau's ring, specifically concerning the cross-sectional area of the tube lumen, which is set equal to the cross-sectional area of the other models. The model has two additional modifications.

Firstly the elasticity should be specified for all three layers of the embedded model. For the outer layer the elastic modulus is specified according to section 5.2, and following the assumptions of Zamir et al. [2003] the elastic modulus of the inner layer is similar to the outer layer and the elasticity of the intermediate layer (the cardiac jelly) is one decade less. Additionally the outer layer has thickness specified as in section 5.2 while the thickness of the inner layer is half of that according to the reports of section 7.1.

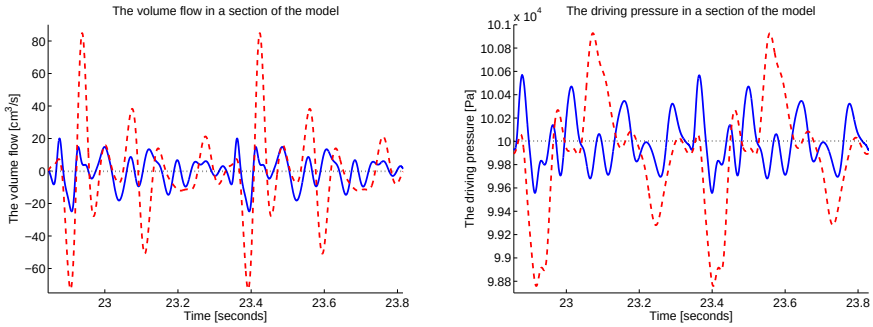

Figure 8.4: The oscillations of flow and pressure of the embedded Liebau's ring with $N = 60$ sections and a pinching function as described in section 5.2 with compression ratio, $c = 10\%$ (solid curve). The eccentricity in the simulations is set to $e = 0.3$. The results are compared to a simulation of the cylindric tube also with compression ratio, $c = 10\%$ (dashed curve). On the left the oscillations of the volume flow, which have clearly less amplitude than for the cylindric model, mean flow is computed to -0.16 cm^3/s compared to -1.04 cm^3/s for the cylindric model. On the right the oscillations of the pressure, which have also less amplitude than the cylindric model, mean pressure stays at $1.00 \cdot 10^5$ Pa. Notice that the embedded model have more oscillations than the cylindric model though they appear more damped.

Secondly the concentric pinching mechanism specified by equation 5.3 and 5.4 in section 5.2 is used to compress the outer layer of the embedded model. The computations will however not tolerate a compression ratio of 25 %, so the compression ratio is instead set to 10 %. This is possibly due of the strain produced in the intermediate layer, with a higher elastic module for this layer a higher compression ratio should be possible for the simulations, though this is not tested. Figure 8.4 shows the oscillations of a simulation with the embedded Liebau's ring.

As the figure demonstrates the time-functions of flow and pressure in the embedded tube have much less amplitude but more oscillations per period. The mean flow, -0.16 cm^3/s, is lower than for the cylindric tube, -1.04 cm^3/s, and mean pressure holds steady near the equilibrium pressure, $P_0 = 1.00 \cdot 10^5$ Pa. It appears as if the intermediate elastic layer (the cardiac jelly) acts as a form of cushion such that the contraction of the outside layer by use of the pumping function is not transmitted in full to the inside layer, that is the absolute value of the contraction of the outside layer is reduced for the inside layer, yet the relative contraction given by the compression ratio remains almost the same, for the simulation shown in figure 8.4 the inside compression ratio is 9.8 %. This will dampen the oscillations of flow and pressure and reduce the effect of the pumping function.

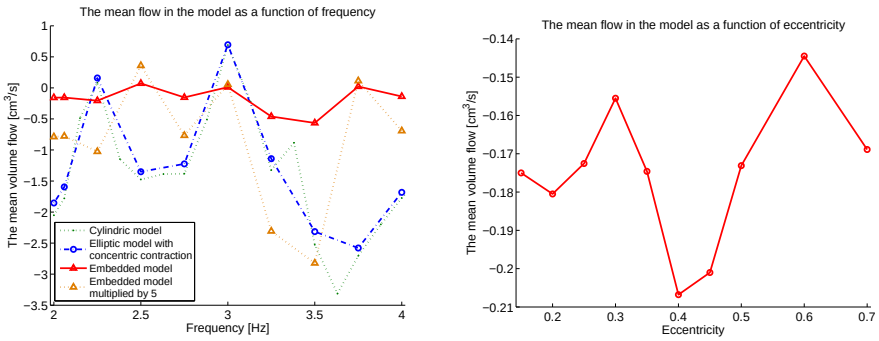

Figure 8.5: The mean flow of the embedded Liebau's ring as a function of frequency on the left and as a function of eccentricity of the lumen of the tube on the right (both solid curves). The frequency scan on the left is compared to the cylindric tube (compression ratio 25 %, dash-dotted curve) and an elliptic tube with concentric contraction (eccentricity 0.1 and compression ratio 25 %, dashed curve). The eccentricity of the embedded tube is 0.3 and the compression ratio 10 %. The mean flow is less outspoken but the frequency spectrum resembles the two other curves, which is clear to see if the function is multiplied with 5 (dotted curve). The function of eccentricity on the right demonstrates a peak in the mean flow around $e = 0.4$.

The function of the intermediate layer is according Barry [1948] to transmit contraction of the outside layer to the inside lumen, and it is clear that the elasticity of the layer will have the consequence that some of that contraction is lost as deformation of the layer. Thus the energy cost will be increased with the inclusion of this layer compared to a simple one-layer tube, for the simulations in figure 8.4 the energy ratio is $E_{emb}/E_{con} = 1.02$, between an embedded tube and a simple cylindric tube both with compression ratio, $c = 10$ %. Some of the energy usage goes to compression of the intermediate layer, which will store it as potential energy. This energy will be released again once the tube relaxes and thus it is possible that the intermediate layer will help the contracted tube to spring back to its original configuration. This could potentially be an important function of the cardiac jelly in the embryonic heart, as suggested by Männer et al. [2009].

Figure 8.5 demonstrate how the mean flow in the embedded Liebau's ring compares to frequency and eccentricity of the elliptic lumen. The function of frequency is compared to two other simulations both with compression ratio 25 %m where the compression ratio of the embedded simulation is only 10 % due to numeric reasons. It is clear that the mean flow is less as would be expected, but it can be seen that the frequency spectra of the simulations are comparable.

For the dependence on the eccentricity of the ellipse it is clear that there is an optimal eccentricity for the elliptic lumen, $e = 0.4$, for which the mean flow in the embedded tube is about one fifth of the corresponding mean flow in the cylindric tube (see figure 8.4). This was not similarly detected for the mean flow in the elliptic tube in figure 8.3, which can probably be explained through the existence of the intermediate layer for the embedded tube. It makes sense that there is an optimal distribution of this layer such that it best transmits contractions to the inner layer. Similarly it can be seen on the figure that when the eccentricity goes to zero the flow will also increase, when the embedded tube more and more resemble a normal concentric tube. In fact the eccentricity chosen for the simulations in figure 8.4 and the frequency plot, $e = 0.3$, appear to be the worst possible choice.

8.3 Conclusion to the simulation results

It is a disappointing fact that the simulations of the embryonic heart did not succeed, but the simulation results of the case of Liebau's ring with elliptic or embedded cross-section prove that the lack of simulation results for the embryonic chick heart is not caused by an error in the model; the model itself is functional. Thus the problem must lie in the setup of the embryonic simulations.

In that respect it should be noted that the differences between the simulation of the embedded Liebau's ring and the embryonic heart simulations primarily consist in the tracing of the radial dimensions of the embryonic heart through the staircase functions in figure 7.7 and the implementation of the pumping function that stretches over nearly all sections of the embryonic heart models compared to only a few sections in the Liebau simulations. Specifically it is seen in the simulation of the embedded Liebau's ring that compression ratios too large did not converge in the simulations, thus $c = 10$ % was chosen in section 8.2.2. Other differences could be the boundary conditions and the material parameters, of which especially the elastic modulus of the cardiac jelly should be considered.

On the other hand the simulations of the elliptic and embedded Liebau's ring are very successful. The simulations are made with setup according to section 5.2 with some modifications of pumping functions and assumptions about the elliptic cross-section. For a simulation of the elliptic Liebau's ring with $N = 60$ sections, eccentricity $e = 0.3$ and compression ratio $c = 0.25$ it took 67 seconds of CPU time to compute 10 periods of the model, of those were 57 used by the 'ode45' solver in MatLab that spent 43 seconds to iterate the derivatives of a_n, b_n and p_n and 13 seconds to the solver algorithm itself and the remains to other functions. It took less than 2 seconds to compute the values of P_n and Q_n and almost 5 seconds to save the data. The simulation programs can be found in appendix C.

As it was concluded in section 5.7 the pumping mechanism is very important for the behavior of flow and pressure in the system, that same conclusion can be repeated here. The eccentric pumping mechanism described with 8.2 and 8.3 appears to be superior compared to the concentric contraction employed in chapter 5. The pumping function is more energy costly but compared to the mean flow it produces, it is much more energy effective. Furthermore the energy efficiency increases with higher values of the elliptic eccentricity, which is probably an artifact of the idealized pumping mechanism that loose physical realism with high numbers of the eccentricity.

The elliptic cross-section is in itself not better suited for Liebau flow compared to circular tubes, in fact an elliptic tube with concentric contraction produces about the same mean flow as a circular tube, yet the mean flow will go towards zero when the eccentricity of the ellipse is increased as demonstrated by figure 8.3. For the embedded Liebau's ring it is however clear that there is a optimal eccentricity of the elliptic lumen such that mean flow is at its highest. The optimal eccentricity lies around $e = 0.4$ for the simulations in figure 8.5.

Thus it appears that a suggestive answer to the second of the three questions in chapter 1 is emerging. It appears that it is not the elliptic tube that will give better conditions for the Liebau effect but instead the eccentric contraction of the tube.

Chapter 9

Discussion and Final Remarks

The basis for the modeling in this thesis was that the 'simple' tubular nature of the embryonic heart made a probable case for the type of modular modeling of the flow through an elastic tube.

The purpose of the modeling is an investigation of the pulsating flow and pressure of the embryonic heart specifically with regards to the conditions of an elliptical inner lumen of the layered tube and the possibility of Liebau driven flow as opposed to peristaltic driven flow. Though of course for the modeling to answer those questions it is necessary to prove that the models adequately portray the effects of the tubular heart.

In this chapter the modeling and investigation of the embryonic heart is discussed and suggestive answers to the questions posed in chapter 1 is given. First the modeling and the assumptions made in the interpretation of the model case are discussed, then the simulations themselves and finally the questions of the elliptic tube and the proposed pumping principles.

9.1 The models

Of the three questions presented in chapter 1 the first is probably the most interesting from a mathematicians perspective: Will the complicated flow and pressure conditions exhibited by the embryonic heart be adequately modeled by the energy bond models constructed in this thesis?

The simulations with the models are discussed below but in addition a discussion of the mathematical interpretation of the characteristics of the tubular heart is found here. It is important that the limitations and assumptions the model pose on the complicated nature of the embryonic heart does not conflict with its real life behavior.

The mathematical interpretation should always simplify the modeled case, but it should not be made too simple, and on the other hand it should only be made so complex as to include the behavior investigated by the model. The mathematical interpretation of the embryonic heart needs to be adequate to see the difference that a layered elliptic cross-section does to the flow and pressure incited by peristaltic of Liebau effects, and it needs to suggest the additions and exclusions of theoretical effects in relation to the modeling procedure; for instance tube curvature is included while non-Newtonian liquid behavior is excluded.

9.1.1 Assumptions in the models

The mathematical interpretation leads to a one-dimensional model of pulsatile flow and pressure in an elastic tube, thus equating blood flow in the tubular heart with water in a rubber tube. The tube is described with a one-dimensional elasticity (two-dimensional in the elliptic case) and an ad hoc shear elastic effect, while the pulsating flow is characterized by a Womersley modified inertia, a Poiseuille resistance and a resistance due to curvature.

It could be considered if one-dimensionality is a too harsh limitation on the flow properties in the embryonic heart, so that the constructed model is not able to model blood flow satisfactorily compared to continuous fluid dynamic equations. It is known that curvature will shift the peak in the velocity profile towards the outer curvature, and other effects of the beating heart will make the velocity field non-trivial as well. Thus the assumption of a functional velocity profile may be too simple to describe the true motion of blood in the heart, even with Womersley theory. Yet the experimental measurements of flow and pressure in the heart are all one-dimensional, nowhere in the in the experimental data is there support for a model of higher dimensionality.

In the same way the elastic compliance of the tube wall is modeled with a singular Young's modulus assuming that the heart walls are isotropic pure elastic materials. While isotropy may hold true for embryos at the younger HH-stages, pure elasticity does not. Taber et al. [1992] postulate a pseudoelastic relation applicable for all layers of the embryonic heart, which has become the accepted description, and according to Miller et al. [1997b] the mechanic behavior of the heart walls is even viscoelastic. It is not known in which way the inclusion of such a pseudoelastic relation would change the model results.

The shear elastic effects of the walls are ad hoc additions to the model that are included as a representation of the physical effects in the walls, while the true effects are more complicated and require the possibility that the length of a section is variable, and in the elliptic models shear elasticity is probably even more complicated. Additionally a leak of energy is included to model friction

in the walls, thus the shear elasticity is not modeled as a pure elastic effect. In section 5.6.2 it is demonstrated how the exclusion of the shear effects will alter the model and simulations considerably; the removal of the friction will un-dampen the flow, while removal of the shear elasticity altogether will change the effects of the pressure waves in addition.

In the embedded tube model the inclusion of the elastic effects of the cardiac jelly is again modeled as a pure elastic effect, and that is probably much too simple. Firstly the elastic response will be given by a complicated interplay between bulk and shear modulus given by the geometry of the tube and the elastic tensor of the jelly. Secondly the stress-strain relationship is given by the pseudoelastic equation by Taber et al. [1992]. Thirdly the elasticity is probably followed with frictional effects just as for the shear elasticity, a fitting addition to the model would be to introduce a resistance alongside the capacitance of the cardiac jelly.

Additionally it was seen in section 8.2.2 that the compliance of the cardiac jelly dampen the contractions of the tube, such that the maximum contraction of the outer layer is reduced for the contraction of the inner layer. This reflects an entirely physical behavior as some of the energy from the contractions is stored as potential energy in the cardiac jelly (and some of the energy may be lost to friction as explained above). The potential energy of the cardiac jelly will subsequently be released when the heart relaxes, thus the cardiac jelly will help the contracted heart return to its uncontracted state (actually this is a function of the elasticity of all the layers in the tubular heart).

The inertial effects of the flow is modified with Womersley theory to include the velocity profile of pulsatile flow according to the assumption of a periodic pressure gradient in the Navier-Stokes equations. The effect of Womersley theory is investigated in section 5.6.1, and mostly consists of a shift of the frequency spectrum. However, the velocity profile may be further changed by the composition of the blood.

Blood is a two component liquid consisting blood plasma and blood cells. Blood cells can be modeled as ellipsoid deformable bodies in the liquid, and it has been proven that under a Poiseuille parabolic flow profile they will migrate towards the center of the tube and in doing that they will flatten the parabolic flow profile [Meier, 1987]. This affects the apparent inertia of the blood and in some models this is approximated with a velocity dependent viscosity coefficient, though it is not known how it affects flow with a Womersley profile.

The Womersley theory states that a standard Poiseuille resistance to the flow is used in addition to the inertial effects. It is surprising then that so many objections to the Poiseuille equation is regularly given by researchers in the field (see the list in section 3.4).

The Poiseuille resistance is a function of the viscosity, which is included as a constant in the modeling even though the high shear effect described in section 3.1 should be considered in respect to the diameter of the embryonic heart. Hu et al. [1991] reports a viscosity of $3.8{\cdot}10^{-}3$ Pa·s for embryonic blood though it is not mentioned if this is in consideration of the high shear effect. This effect, which is also known as the Fahraeus-Lindqvist effect, can alter the viscosity with a factor 1.5 to 2 depending on blood hematocrit number [Meier, 1987]. The effect is a function of the shear rates in the liquid, which are proportional to the slope of the velocity profile and under the given circumstances could probably be transformed to a function of the frequency of pulsations, and thus this effect could be added to the model as an viscosity correction factor, just as the Womersley theory gives the inertia correction factor, ψ.

The resistance to flow due to the curvature of the tube is made from engineering principles of the class of effects known as minor losses. The inclusion of the theory follows the procedure given by Crane Co. [1982] and Keller [1978], yet it is surprising how much effect the curvature has on the flow in the investigation in section 5.6.3. It may be that curvature has a very strong effect on the Liebau effect, which relies on a mismatch of pulsations to produce a mean flow, thus pulsating momentum is important in both cases, yet this does not fit with the picture that curvature is so often ignored in other models of the Liebau effect.

In addition the elliptic models and certainly the embryonic heart open up for sources of minor losses. For the embryonic heart the branching of arteries is important. For the elliptic model the twisting of the elliptic cross-section along the length of the tube will be a source for minor losses, while with regards to the curvature it makes a difference how the tube curves in relation to the elliptic cross-section. These effects are not included in the model as they are believed to be of minor influence to the character of the flow in the embryonic heart.

Finally the pumping mechanism is crudely made, both in the models of the embryonic heart and in the models of Liebau's ring. For the model of Liebau's ring equations are included in the simulation routine to overwrite the differential equations of the dynamic radius in the affected sections of the model. This is done to make an exact replication of the pumping mechanism applied by Ottesen [2003], and yet it is clear from the comparison in section 5.5 that the division into sections of the model partly ruins this emulation of sinusoidal functions used by Ottesen.

For the embryonic heart the pumping mechanism is made as concentric contractions of the outer layer of the embedded model used in the simulations. This is done though the derivative of the contraction functions specified in section 7.4, which is simply added to the rate of change of the major axis specified by equation 6.124. The concentric contractions are an approximation, it is specified by Männer et al. [2009] that the outer layer does exhibit concentric contraction, and

furthermore it is specified by Damon et al. [2009] that the contraction is not symmetric around the middle axis of the tube, instead the tube at the outer curvature of the looping heart contracts more than at the inner curvature. These asymmetric contraction effects are ignored for simplicity reasons.

9.1.2 The simulation routine

It is proven by the simulation of Liebau's ring that the computation time of the simulations is essentially short. Considering the feat done by the 'ode45' solver in MatLab v. 7.5 (copyright The MathWorks Inc.) it is remarkably fast; the Runge-Kutta iteration of more than hundred differential equations is impressive work.

This is however only when conditions for the 'ode45' solver are favorable. In the event that the setup of the model state conditions that are too complicated for the solver, for instance if it needs to check for divergence of equations, the solver is suddenly transformed to a very slow process as it constantly seeks to take lesser time steps and recheck its process. In that instance a routine that under favorable conditions would be done in an hour suddenly takes days to complete.

This problem has especially dampened the procedures with the elliptic model using the χ factor that includes shear effects of the tube wall, defined in equation 6.96, and the simulations of the embryonic heart. As a result simulation data from these routines are not achieved.

During preliminary tests of the models different pumping mechanisms were employed, for instance periodic increase in outside pressure, as well as the pumping mechanisms presented in chapter 5. It is clear that different pumping mechanisms work differently in the simulations, some are easy for the simulation routine to work with while others require much more computation time.

9.1.3 The energy bond technique

The methods employed in the modeling in this thesis proves the strengths of the energy bond technique. For many the formalism used in the technique may be unfamiliar and appear unnecessary complicated, yet the rules of the energy bond technique are given by simple linear relations that are easily comprehensible and through the connections of the energy bonds create possibilities for very complicated models. Furthermore the energy bond graphs gives a method to visualize the equations of the model, and with some practice they can be interpreted directly in place of equations.

Yet the greatest strength of the energy bond technique is the modular construction of models, which is something almost unique for the technique. It makes it possible to concentrate on singular effects of the pulsatile flow in elastic tubes one at the time during modeling, as long as it is remembered to follow the rules of the

energy bond technique, which specify how elements are connected such that physical consistency in conserved. Therefore the modeling process in chapter 4 and 6 is designed as a stepwise procedure starting with a simple principal structure of the model, which is continuously expanded with more effects and in section 9.1.1 above even more expansions are suggested.

The same modular construction plays a part when the model is tested in section 5.6. Each of the elements in the model can be picked out and examined to investigate what effect exactly this addition to the model has on the observed flow and pressure. In this way the simulations of the model becomes and active step in the model construction process, by testing model additions it is easily seen if they are made correctly and correctly included in the model. If not, they can be easily reformulated, reconnected or removed from the model.

The simulation step in the construction of the model can be a necessity as the modular construction of models in the energy bond technique is also one of the major weaknesses in the technique. Other modeling techniques are typically related to a set of assumptions for the specific model, which for instance would give a set of differential equations that are solved to construct the model. Compared to this the energy bonds are abstract and potentially out of touch with the underlying assumptions in the model.

For instance the energy bond model in this case makes an implicit assumption of the discretization of the fluid dynamical equations. The equations are discrete in space through the division into sections of the tube, where flow and pressure in the middle of a section and flow is measured between two neighboring sections. Furthermore the equations are discrete in relation to the modular construction of the model, such that one element models inertia and another resistance and so on. To make sure that the equations of the model are correlated to the fluid dynamical equations it is investigated in section 4.5 how the model equations look in the continuous limit when the length of a section becomes infinitesimal. It is seen that the model equations converge to the continuity equation and the Euler equation thus proving that the model is a true discretization of the fluid dynamical equations.

9.2 Simulations of the embryonic heart

The simulations of the embryonic heart were expected to state a proof of concept that the embryonic heart could in fact be modeled with the models in this thesis. This proof has changed form to a suggestion; it may be possible to model the embryonic heart with the models, but it is not possible to simulate the effects in the heart. At least not at present.

During the setup many assumptions were made pertaining to the dimensions and function of the embryonic heart, in fact the function of distribution of the cardiac jelly inside the heart tube visible in figure 7.7 is made from one single measurement of cardiac jelly thickness, the rest is guesswork. Therefore the simulations can never be anything more than a proof of principle; compared to measured data of flow and pressure in the embryonic heart from table 8.1 the simulations could indicate that the models capture the phenomena of the embryonic heart.

If the models should ever be used to model actual flow and pressure of the embryonic heart, measurement data is required. The lack of measurement data for the embryonic heart is problematic, despite impressing imaging techniques is employed in the study of embryonic hearts simple physical measurements of lengths and diameters are hard to find.

The setup of the embryonic heart simulations does not require many or considerably complicated material parameters; primarily the viscosity and density of blood and an elastic Young's modulus for each layer of the tube, which should all be possible to measure. In addition a set of dimensional measurements are required and an estimation of pumping function and boundary conditions. The setup in chapter 7 is reconstructed from various reports but it would increase the simulation value if all parameters could be obtained from one source.

The modeling and setup of simulations of the embryonic heart is a work that has never been attempted with this level of detail before, it is very disappointing that the simulations were not able to complete the task.

9.2.1 Problems in simulation of the embryonic heart

The explanation for the lack of simulation results is simple; the program routine in MatLab is simply not able to produce any results with the present configuration of the models. The reason for the lack of results is more complicated and may come from several sources.

It is proved in section 8.2.2 that the embedded model works perfectly under the configuration of Liebau's ring, so it is clear that the fault does not lie with the model itself. The only other option is that the problem lies with the setup of the embryonic heart simulations.

In principle four things are differently from the setup of the embryonic heart to the setup of Liebau's ring, following the simulation setup procedure in chapter 5 and 7 the four things are: the parameter estimation, the boundary conditions, the tracing of the tube, and the pumping mechanism.

The parameter estimation is naturally different. The embryonic heart is much smaller and the elastic modules much less than for the case of Liebau's ring, while density and viscosity is about the same. Specifically the elastic modulus of the cardiac jelly deserves attention. In the setup of the embryonic heart the measured

values for the elastic modulus from table 7.7 are used, which are from one half to one fifth of the corresponding elastic modules of the myocardial layer. In the setup of the embedded Liebau's ring the assumption by Zamir et al. [2003] is used, stating that the cardiac jelly should have an elastic modulus about one tenth of the myocardial layer. Despite this, it is not believed that this could be the cause of the problems.

The boundary conditions are different but should not be the cause for any computation difficulties, in fact it is probably the simulations of Liebau's ring that have the most complicated boundary in the form of the cyclic boundary condition. For the embryonic heart the boundary condition at the arterial end includes two additional differential equations to the computation, but they are both very simple and should hardly be the cause for any problems.

The difference in the tracing of the tubes in the embryonic heart and the Liebau model is in the radial dimensions of the tube; the rubber tubes in Liebau's ring has uniform radius or axial lengths, while the tubular heart tapers towards the arterial end of the tube and for higher HH-stages it even has several bulges. The axial lengths of the embryonic heart tubes are demonstrated by the staircase functions in figure 7.7. In principle a tube with changing cross-sectional dimensions should not be a problem for the model, not even for the shear elasticity that is designed for changing axial dimensions. However when the flow and pressure generated by contraction in a wide part of the tube reaches tube sections that are substantially thinner, numerical problems may cause the Runge-Kutta algorithm to take smaller time steps. This could be one reason for the problems. Yet when a simulation with an untapering tube defined with mean values of the dimensions in figure 7.7 is attempted, the problem persists, the same is the case for an uncurving tube.

Finally the pumping mechanism is fundamentally different between the two model setups; for Liebau's ring the pumping mechanism is a typical Liebau pump that only affects a short length of the tube, while the embryonic heart has a pumping mechanism that contracts a large part of the tube and potentially acts as a peristaltic pump. In the simulation of the Liebau model the pumping mechanism is implemented by letting the equations of the pump overwrite the differential equations of the outer radius in the affected tube sections, it was seen that this causes mismatch problems in those sections so for the embryonic heart the pumping function is implemented differently. Instead of overwriting the equations for the outer radius of the tube, the derivative of the pumping equation, defined in by the functions in figure 7.7, is added to the differential equation of the outer radius and iterated in the Runge-Kutta algorithm.

This should create a more smooth working pumping mechanism compared to the simulations of Liebau's ring, though perhaps the part of the pumping function in figure 7.7 where the heart actively dilates following the contraction should have been omitted from the function. The elasticity of the layered tube should be able

to produce a relaxation to back to the initial position through passive release of potential energy, an active dilation function may cause artificial effects where the heart dilates more than it should.

Furthermore the contraction of the outer layer of the tube may cause situations in the tube where the inner lumen comes close to occlusion, especially in the sections where the cardiac jelly takes up more space of the cross-sectional area. Total occlusion is not possible in the model, except though numerical error in the Runge-Kutta algorithm. Thus when the length of the minor elliptical axis comes closer to zero the computational routine will reduce time steps and activate its built-in algorithm to check for convergence of the solutions.

A combination of the tapering embedded tube and the application of the pumping mechanism may be the cause of the problems for the 'ode45' solver in MatLab. The effects will cause the program to reduce the time steps to very small numbers while convergence is checked by special routines in the solver. In the end this will create immense amounts of data that MatLab handles by creating swap disks on the computer, storing and loading data from those is extremely time consuming.

It was assumed a priori in chapter 1 that the model could produce peristaltic flow without problems, yet in the analysis of the problems of the simulations it seems that this is exactly what causes the problems: A peristaltic contraction function that nearly closes the lumen, traveling on a tapering tube.

9.3 Simulations of Liebau's ring

Contrary to the simulations of the embryonic heart the simulations of Liebau's ring work without problems. A computation of Liebau's ring with $N = 60$ section and 100 periods takes about 30 minutes when loaded up to the server used for the computations in this thesis. This proves that the models themselves are functional and with the right setup MatLab has no problems with running the simulations.

In section 5.5 it was attempted to validate the simulations of the cylindric Liebau's ring in relation to reported data by Ottesen [2003] and Snitker et al. [2000], this comparison was only partly successful. It was made clear that the simulation results compared fairly to the reported data by Ottesen, at least for small values of the compression ratio, but none of the simulations were able to reproduce the experimental results by Snitker et al. [2000]. Interestingly when Liebau's ring was setup with the elliptic model the eccentric pumping mechanism given by equation 8.2 and 8.3 easily reproduced the experimental data for an elliptic tube with eccentricity 0.1 (almost circular).

The difference is the pumping mechanism; none of the pumping functions employed in the simulations in chapter 5 could produce flow to match the experimental results, apparently the eccentric deformation used in chapter 8 can.

This illustrates the overall conclusion that the pumping mechanism is absolutely important for the observed Liebau effect.

Many things have influence on the mean flow induced by the Liebau effect, among those are: the differences in impedance in relation to the position of the pumping site as seen on figure 5.6, the frequency of the compression as explained in section 5.3 and visible in figure 5.5, but far the most influential factor is the pumping mechanism. For instance while one pumping function produce flow in a clockwise direction another pump may produce flow in a counter-clockwise direction, which is visible in figure 8.2.

No way of determining the efficiency of a given pumping mechanism has been found, but it will certainly be interesting to investigate what the defining factors in the pumping mechanism could be. The volume of displaced liquid was used as a method of comparison in section 5.5 but it was made clear that this was not a defining number for the efficiency of the pump. Similarly the energy cost of a compression was used in chapter 8, this is also not defining for the pumping function as number was used to compare energy efficiency for different pumping functions.

The simulations of Liebau's ring were used to validate the model: in chapter 5 through a comparison with reported data from other experiments and through an investigation of the different elements in the model, in chapter 8 it was used to validate the elliptic models in the light that the embryonic simulations have failed. From those three validation attempts it is clear that the model works and produces results that are comparable to physical experiments, though only in the case that the pumping mechanisms are comparable.

The investigation of model elements in chapter 5 produced a clear result that especially the impedance in the model has a major influence in the observed mean flow. As such the removal of impedance in the tube walls in section 5.6.2 produced a clear non-damped flow, and the removal of impedance from the curvature of the tube in section 5.6.3 produced extreme mean flows compared to the normal simulations. It is perhaps a little surprising that curvature should have so much influence on the mean flow.

On the other hand the investigation of the Womersley number in section 5.6.1 and the removal of shear elasticity in section 5.6.2 proved how elasticity in the tube and inertial effects are responsible for the frequency spectrum of the Liebau effect. Section 5.3 explains how the resonance frequencies are decided by the Moens- Korteweg equation. The investigation of the Womersley number and the shear elasticity proves that the Womersley number has its rightful place in the Moens-Korteweg equation, and furthermore that the representation of wall elasticity by Young's modulus in the equation is in fact a simplification of the complicated effects in the tube.

Finally the investigations of the total number of sections in the model, N, revealed that there are some differences in the simulation results. This was especially seen in the calculation of the mean flow, which differed a great deal. The explanation is given by the pumping mechanism used in the simulations, because of the different number of sections the pumping mechanism also had to be implemented differently. Furthermore from preliminary investigations of model stability it is found that the results are stable when N is high enough so that the length of one section is comparable to the diameter of the tube.

The results from the simulations of Liebau's ring proved that comparability of the simulations is only possible when pumping mechanisms are comparable, and that the pumping mechanism by far is the most important factor for the observed Liebau effect. In turn the simulations validate the model both in respect to different effects in the tube and in relation to results by other authors.

9.4 Elliptic vs. circular cross-section

The second of the three questions posed in chapter 1 is answered by use of the simulations of the elliptic Liebau's ring: In relation to the possible pumping mechanisms of the embryonic heart are elliptic contractions of the heart tube optimal compared to concentric contractions?

According to Männer et al. [2010] it has already been suggested by results from other researchers that peristaltic pumping has favorable conditions with an elliptic cross-section of the tube, which has previously been used as an argument for the peristaltic pumping of the embryonic heart. Though a similar investigation has not been done for the Liebau effect.

Thus to answer this question a comparison between the Liebau generated flow in elliptic and circular tubes is needed, as well as a comparison between the Liebau generated flow induced by concentric and eccentric pumping mechanism. Such a comparison is made with the simulations of Liebau's ring.

Starting with the question if tubes with elliptic cross-section give better conditions for the Liebau effect compared to circular cross-section. The Liebau effect is defined by the pumping mechanism employed, for a cylindric tube with concentric deformation the mean flow was -1.78 cm^3/s, while for a elliptic tube with concentric deformation the flow was -1.59 cm^3/s. Furthermore the mean flow in the elliptic tube decreases with the increase of eccentricity of the ellipse as demonstrated by figure 8.3. Thus in the simple situation the elliptic cross-section does not appear to be an advantage for the Liebau effect.

When considering a layered tube with an inner elliptic lumen and outer circular mantle comparable to the cross-section of the embryonic heart, it is seen that the mean flow is generally lower than what can be produced in a cylindric tube

with cross-section comparable to the lumen of the layered tube and with concentric contraction. However the mean flow produced in the layered tube depends on the eccentricity of the elliptic inner lumen, an as figure 8.5 demonstrates an eccentricity around 0.4 is optimal for the flow. Thus for the embryonic heart it seems there is an advantage for the Liebau effect if the elliptic lumen of the heart has a specific eccentricity.

The second question if eccentric contraction is optimal compared to concentric contraction. Figure 8.2 shows a comparison between simulations for an elliptic tube with concentric contraction and a similar elliptic tube with eccentric deformation. It is seen that the eccentric contraction is far superior to the concentric for all simulated frequencies. Furthermore figure 8.3 shows a comparison between the concentric and eccentric contraction for different configuration of the eccentricity of the elliptic cross-section of the tube. It is seen that even for eccentricities going towards the circular limit the eccentric contraction is superior. For high eccentricities an artificial effect of the eccentric deformation makes the results unreliable. Thus the eccentric deformation gives a clear advantage compared to concentric contraction in this case.

As stated before the Liebau effect is highly dependent on the pumping function and as such another eccentric contraction of the tube may be less effective compared to the one demonstrated in this thesis. For instance an obvious choice of deformation could be that only one elliptical axis is contracted while the other is kept constant. Thus a conclusive answer can not be given to this question.

9.5 Peristaltic pumping vs. the Liebau effect

The third of the three questions posed in chapter 1 is difficult to answer considering that the simulations of the embryonic heart models did not succeed: Given the morphology and cross-sectional shape of the tubular heart will a peristaltic or Liebau pumping principle be desirable for the propagation of blood?

It has been suggested by Liebau [1955] and several others that the Liebau effect is the mechanism responsible for the flow of blood in the embryonic heart instead of peristaltic pumping, or that the effect could contribute to the flow. In fact researchers have discovered embryonic hearts in fish that apparently work solely from a Liebau principle [Männer et al., 2010].

The two hypotheses of the pumping mechanism in the heart have different observations speaking for and against them. For the peristaltic pumping the problems are typically that the flow produced by peristaltic waves is continuous, not pulsatile, and that the flow in the embryonic heart supersedes the speed and frequency of the peristaltic contraction waves. For the Liebau effect the problems are typically that the Liebau effect is caused by periodic contractions at a single

point and that the flow generated is dependent on a multitude of things, among those the frequency, which makes the mechanism seem unstable.

The research community is divided on this question, different researchers favor different hypotheses as this question is still undecided. Instead of discussing which of these is the correct pumping mechanism for the embryonic heart it is perhaps more relevant to discus if they mutually exclude each other, is it possible that both effects are present in the embryonic heart?

The Liebau effect is not a pumping mechanism, it is an effect of the pulsating pressure waves in the tube. Pressure waves will be present in the tubular heart even if they are deliberately induced or not, thus even for a peristaltic compression there may be basis for a Liebau effect. The deciding factor in the Liebau effect is not the induced pumping but the reflection of the waves by the changes of tube impedance, to produce a clear Liebau effect there has to be a clear change in impedance, such as change in elasticity, thickness or cross-sectional area of the tube or such as a branching of the tube. In the embryonic heart the tube branches in both the venous and the arterial end.

Furthermore for the effectiveness of the Liebau effect the pressure waves should be able to propagate even if the lumen is occluded by contraction of the tube, as such the cardiac jelly may have an additional function in the embryonic heart, as a medium for the propagation of pressure waves.

In relation to the simulations of the embryonic heart it was the idea to setup simulations with a variance of frequency, contraction rates and possibly the eccentricity of the inner lumen, just as for the simulations of Liebau's ring, such that the pumping mechanism could be investigated in more detail. Especially the variance in frequency is interesting for the Liebau effect, as it is potentially one of the defining characteristics of the Liebau effect in the heart tube that it will portray a frequency spectrum just as in figure 5.5 for Liebau's ring, whereas a peristaltic pumping effect is linear with the frequency.

In this way it could potentially be proved that the Liebau effect is present in the embryonic heart, though probably not that the effect governs the flow of the heart. On the other hand, if the simulations of the embryonic heart had worked, the whole point in discussing whether it is governed by Liebau or peristaltic pumping becomes pointless. In that instance there was proof that the pumping mechanism of the heart could be modeled and simulated, so who cares if it is peristaltic of Liebau driven.

9.6 Conclusion

In this thesis the energy bond technique is applied in the construction of models of the liquid flow in elastic tubes. The purpose is to answer three questions posed about the tubular embryonic chick heart.

The first of the three questions pertains to the modeling of the embryonic heart: Will the complicated flow and pressure conditions exhibited by the embryonic heart be adequately modeled by the energy bond models constructed in this thesis?

The aim is to construct a model that compares the tubular heart to a complicated rubber tube, in the respect that the effects of the elasticity of the tube and the pulsatile flow of the liquid can be equated to the complicated pulsatile flow and pressure phenomena of the embryonic heart.

The model is constructed in several steps in a discretization of the fluid mechanical equations using the energy bond technique to continuously expand previous models with additional effects. The final model depicts the embryonic heart as a multilayered elastic tube with an elliptic inner lumen embedded in a an outer mantle with circular cross-section. The model includes complicated elastic effects of all the layers, a Womersley modified inertia, a Poiseuille resistance and a resistance due to curvature of the tube.

It is the conclusion that this model includes all the major effects of the tubular embryonic heart apart from the boundary conditions of the model and contraction of the beating heart. The model gives a set of differential equations for the axial dimensions of the tube and the momentum of the flow, corresponding to a discretization of the equation of continuity and the Euler equation of fluid motion.

Through the use of experimental reports of the chick embryonic heart the model was setup with parameters corresponding to the stage 10, 12, 14 and 16 of the developmental stages by Hamburger and Hamilton [1951]. The setup includes the dimensions of the tubular heart, physical parameter values, boundaries of the embryonic heart modeled through a Windkessel principle, and a contraction function of the beating heart. Model simulations are programmed in MatLab v. 7.5 (copyright The MathWorks Inc.) and use MatLab's inherent Runge-Kutta solver to find solutions to the differential equations.

A model of this size and detail for the early stages of the embryonic heart has not been attempted before. Unfortunately the simulations of the model are inconclusive, and as such the first question is only answered from a modeling perspective.

The second question pertains to the elliptic cross-sectional lumen of the tubular embryonic heart: In relation to the possible pumping mechanisms of the embryonic heart are elliptic contractions of the heart tube optimal compared to concentric contractions?

With the constructed model the aim is to investigate the difference between flow in tubes with circular and elliptic cross-sections as well as flow induced by concentric and eccentric contractions of the tubes. This should be investigated for the possible pumping mechanisms of the embryonic heart; peristaltic pumping and the Liebau effect, though as reports have already been published suggesting that elliptic tubes may be optimal for peristaltic pumping, focus is put on the Liebau effect.

By use of a constructed case of two elastic tubes with different elastic modulus joined together end-to-end to form a ring and filled with water the Liebau effect is investigated for different configurations of pumping mechanisms and cross-sectional shape.

It is concluded from the simulations of this case that a tube with elliptic cross-section gives worse conditions for the Liebau effect than a tube with circular cross-section, and the calculated mean flow of the Liebau effect decreases as eccentricity of the ellipse increases. On the other hand when elastic tubes corresponding to the multilayered model of the embryonic heart are setup in this configuration the simulations demonstrate a peak in the mean flow for an elliptic lumen with eccentricity 0.4. This suggests that for the layered tubular heart the elliptic lumen may provide advantageous conditions for the Liebau effect.

Through comparison of concentric and eccentric pumping functions for a system with elliptic tubes it is clear that eccentric contractions produce a mean flow of far higher magnitude. This result persists even for tubes approaching a circular cross-section. In general it is evident that the contraction function is very influential on the observed Liebau effect, in some respects even more influential than pumping frequency and position of the pump. This suggests that eccentric contractions may be optimal for the Liebau effect in the embryonic heart.

The third question pertains to the pumping principle of the tubular embryonic heart: Given the morphology and cross-sectional shape of the tubular heart will a peristaltic or Liebau pumping principle be desirable for the propagation of blood?

With the constructed model and the setup according to the embryonic heart it is the aim to investigate the possible mechanics in the propagation of blood. This would be done through simulations with varying frequency of the heart's pumping mechanism as the effect of peristaltic pumping is linear with frequency while the Liebau effect is clearly non-linear and demonstrate resonance effects, thus through investigation of the frequency spectrum it could be decided, which pumping mechanism is dominant in the models.

As the simulations of the embryonic heart are unsuccessful this approach is not viable and this question is given only minor attention. It is suggested that the two pumping principles are in fact not mutually exclusive and thus both potentially could contribute to the propulsion of blood. Nothing in the theory suggests

that the pumping effects exclude each other, and potentially a function of the layers in the embryonic heart could be to allow for both effects.

The results of this thesis contribute an understanding of the multilayered tubular nature of the embryonic heart that has not been reported earlier. The results indicate that the elliptic lumen and the elliptic contraction of the embryonic heart could potentially optimize conditions for a Liebau pumping phenomena, while at the same time suggesting that peristaltic pumping and the Liebau effect can co-exist as blood propagation mechanisms in the tubular heart.

The modeling and simulation of the tubular heart of various stages in the early embryonic development has never been attempted before in the size and detail as in this thesis, it is concluded that the model includes all major effects pertaining to the flow and elasticity of the heart tube. As such the modeling has value in itself. Unfortunately the simulations are inconclusive, which is something that has to be remedied in the future.

Bibliography

P. W. Alford and L. A. Taber. Regional epicardial strain in the embryonic chick heart during the early looping stages. *Journal of Biomechanics*, 36:1135–1141, 2003.

Aristotle. *Historia Animalum by D'Arcy Wentworth Thompson*. Translated by J.A. Smith and W.D. Ross. Clarendon Press, Oxford, 1910.

K. Azer and C. S. Peskin. A One-dimensional Model of Blood Flow in Arteries with Friction and Convection Based on the Womersley Velocity Profile. *Cardiovascular Engineering*, 7:51–73, 2007.

R. W. Barnard, K. Pearce, and L. Schovanec. Inequalities for the Perimeter of an Ellipse. *Journal of Mathematical Analysis and Applications*, 260:295–306, 2001.

A. Barry. The Functional Significance of the Cardiac Jelly in the Tubular Heart of the Chick Embryo. *The Anatomical Record*, 102(3):289–298, 1948.

S. Berger, L. Talbot, and L. Yao. Flow in Curved Pipes. *Annual Review of Fluid Mechanics*, 15:461–512, 1983.

M. Butlin. *Structural and functional effects on large artery stiffness: an in-vivo experimental investigation*. The university of New South Wales, Sydney, 2007.

K. A. Campbell, N. Hu, E. B. Clark, and B. B. Keller. Analysis of Dynamic Atrial Dimension and Function during Early Cardiac Development in the Chick Embryo. *Pediatric Research*, 32(3):333–337, 1992.

A. Castenholz and T. Flórez-Cossio. Mikrokymographische Untersuchungen zur Herz- und Kreislaufdynamik in der frühen Embryonalentwicklung des Hühnchens. In: *Altern und Entwicklung, Bd 4*. Stuttgart, New York: Akad Wiss Literat Mainz, pages 41–61, 1972.

P. V. Christiansen. *Imfufa tekst 22: Semiotik og Systemegenskaber (1) - 1-port lineært response og støj i fysikken*. Imfufa, Roskilde University, 1979.

P. V. Christiansen. *Imfufa tekst 238: Semiotik og Systemegenskaber (2) - vektorbånd og tensorer*. Imfufa, Roskilde University, 1993.

P. V. Christiansen. *Imfufa tekst 419: Energy bond graphs - a semiotic formalization of modern physics*. Imfufa, Roskilde University, 2003.

Crane Co. *Technical Paper No. 410M: Flow of Fluids - through valves, fittings, and pipe (Metric edition - SI units)*. Crane Company, 300 Park Avenue, New York, 1982.

B. J. Damon, M. C. Rémond, M. R. Bigelow, T. C. Trusk, W. Xie, R. Perucchio, D. Sedmera, S. Denslow, and R. P. Thompson. Patterns of Muscular Strain in the Embryonic Heart Wall. *Developmental Dynamics*, 238:1535–1546, 2009.

A. Davis, J. Izatt, and F. Rothenberg. Quantitative Measurement of Blood Flow Dynamics in Embryonic Vasculature Using Spectral Doppler Velocimetry. *The Anatomical Record*, 292(3):311–319, 2009.

R. P. Feynman, R. B. Leighton, and M. Sands. *The Feynman Lectures on Physics - The Difinitive Edition*, volume II. Addison-Wesley Publishing Company, Reading, Massachusetts, 1964. ISBN 0-8053-9047-2.

W. C. Gibson. Celebrating the "compleat observer": William Harvey's 400th birthday. *Canadian Medical Association Journal*, 119(7):793–801, 1978.

R. A. Granger. *Fluid Mechanics*. Dover Publications, New York, 1995.

J. Hale, D. McDonald, and J. Womersley. Velocity Profiles of Oscillating Arterial Flow with some Calculations of Viscous Drag and the Reynolds Number. *Journal of Physiology*, 128:629–640, 1955.

V. Hamburger and H. L. Hamilton. A Series of Normal Stages in the Development of the Chick Embryo. *Journal of Morphology*, 88(1):49–92, 1951.

R. Hoeben. *Experimental investigations into the role of impedence defined flow during CPR,* (MSc thesis). Eindhoven University of Technology, Department of Biomedical Engineering, 2009.

N. Hu and E. B. Clark. Hemodynamics of the stage 12 to stage 29 chick embryo. *Circulation Research*, 65:1665–1670, 1989.

N. Hu, D. M. Connuck, B. B. Keller, and E. B. Clark. Diastolic Filling Charateristics in the Stage 12 to 27 Chick Embryo Ventricle. *Pediatric Research*, 29(4): 334–337, 1991.

B. Keller, N. Hu, P. Serrino, and E. Clark. Ventricular pressure-area loop characteristics in the stage 16 to 24 chick embryo. *Circulation Research*, 68:226–231, 1991.

B. B. Keller, N. Hu, and E. B. Clark. Correlation of ventricular area, perimeter, and conotruncal diameter with ventricular mass and function in the chick embryo from stages 12 to 24. *Circulation Research*, 66:109–114, 1990.

G. R. Keller. *Hydraulic System Analysis*. Editors of Hydraulics & Pneumatics Magazine, Cleveland, 1978.

J. K. Larsen, V. Andreasen, H. Larsen, M. S. Olufsen, and J. T. Ottesen. *Cardiovascular modelling at IMFUFA* from *The Way Through Science and Philosophy: Essays in Honour of Stig Andur Pedersen*. College Publications, London, 2006. ISBN 1-904987-33-8.

K. S. Latacha, M. C. Rémond, A. Ramasubramanian, A. Y. Chen, E. L. Elson, and L. A. Taber. Role of Actin Polymerization in Bending of the Early Heart Tube. *Developmental Dynamics*, 233:1272–1286, 2005.

B. Lautrup. *Physics of Continuous Matter - Exotic and Everyday Phenomena in the Macroscopic World*. Institute of Physics Publishing, 2005. ISBN 0-7503-0752-8.

G. Liebau. Über ein ventilloses Pumpprinzip. *Naturwissenschaften*, 41(14):327, January 1954.

G. Liebau. Herzpulsation und Blutbewegung. *Zeitschrift für die gesamte experimentelle Medizin*, 125:482–498, 1955.

I.-E. Lin and L. A. Taber. Mechanical Effects of Looping in the Embryonic Chick Heart. *Journal of Biomechanics*, 27(3):311–321, 1994.

A. Liu, R. Wang, K. L. Thornburg, and S. Rugonyi. Efficient postacquisition synchronization of 4-D nongated cardiac images obtained from optical coherence tomography: application to 4-D reconstruction of the chick embryonic heart. *Journal of Biomedical Optics*, 14(4):044020, 2009.

C. G. Manopoulos, D. S. Mathioulakis, and S. G. Tsangaris. One-dimensional model of valveless pumping in a closed loop and a numerical solution. *Physics of Fluids*, 18(1):017106–16, 2006.

B. J. Martinsen. Reference Guide to the Stages of Chick Heart Embryology. *Developmental Dynamics*, 233:1217–1237, 2005.

D. A. McDonald. The Occurence of Turbulent Flow in the Rabbit Aorta. *Journal of Physiology*, 118:340–347, 1952.

D. A. McDonald. The Relation of Pulsatile Pressure to Flow in Arteries. *Journal of Physiology*, 127:533–552, 1955.

D. A. McDonald. Hemodynamics. *Annual Review of Physiology*, 30:525–556, 1968.

G. Meier. Viscous Flow in the Embryonic Heart Geometry. *Embryologische Hefte*, 1:1–19, 1987.

C. Miller, M. Vanni, L. Taber, and B. Keller. Passive Stress-Strain Measurements in the Stage-16 and Stage-18 Embryonic Chick Heart. *Journal of Biomechanical Engineering*, 119:445–451, 1997a.

C. E. Miller, M. A. Vanni, and B. B. Keller. Characterization of Passive Embryonic Myocardium by Quasi-Linear Viscoelastic Theory. *Journal of Biomechanics*, 30(9):985–988, 1997b.

J. Männer. Cardiac Looping in the Chick Embryo: A Morphological Review With Special Reference to Terminological and Biomechanical Aspects of the Looping Process. *The Anatomical Record*, 259:248–262, 2000.

J. Männer. On Rotation, Torsion, Lateralization and Hnededness of the Embryonic Heart Loop: New Insights From a Simulation Model for the Heart Loop of Chick Embryos. *The Anatomical Record Part A*, 278A:481–´492, 2004.

J. Männer. Ontogenetic development of the helical heart: concepts and facts. *European Journal of Cardio-thoracic Surgery*, 295:S69–S74, 2006.

J. Männer. The Anatomy of Cardiac Looping: A Step Towards the Understanding of the Morphogenesis of Several Forms of Congenital Cardiac Malformations. *Clinical Anatomy*, 21, 2008.

J. Männer, L. Thrane, K. Norozi, and T. M. Yelbuz. High-Resolution In Vivo Imaging of the Cross-Sectional Deformations of Contracting Embryonic Heart Loops Using Optical Coherence Tomography. *Developmental Dynamics*, 237: 953–961, 2008.

J. Männer, L. Thrane, K. Norozi, and T. M. Yelbuz. In Vivo Imaging of the Cyclic Changes in Cross-sectional Shape of the Ventricular Segment of Pulsating Embryonic Chick Hearts at Stages 14 to 17: A Contribution to the Understanding of the Ontogenesis of Cardiac Pumping Function. *Developmental Dynamics*, 238:3273–3284, 2009.

J. Männer, A. Wessel, and T. M. Yelbuz. How Does the Tubular Embryonic Heart Work? Looking for the Physical Mechanism Generating Unidirectional Blood Flow in the Valveless Embryonic Heart Tube. *Developmental Dynamics*, 239: 1035–1046, 2010.

W. W. Nichols and M. F. O'Rourke. *McDonald's Blood Flow in Arteries - Theoretical, experimental and clinical principles*. Arnold, a member of the Hodder Headline Group, London, 4th edition, 1998. ISBN 0-340-64614-4.

W. W. Nichols and M. F. O'Rourke. The life and times of Donald A. McDonald. *Artery Research*, 2:1–8, 2008.

G. J. Noordergraaf, J. T. Ottesen, W. J. Kortsmit, W. H. Schilders, G. J. Scheffer, and A. Noordergraaf. The Donders Model of the Circulation in Normo- and Pathophysiology. *Cardiovascular Engineering*, 6:53–72, 2006.

T. Nørgaard, J. Ellegaard, J. Jalving, J. B. Pedersen, P. Gregersen, S. I. Meyer, and H. Wittus. *Aorta-modellering*. 4th semester, Naturvidenskabelig Basis, Roskilde University, 1993.

M. S. Olufsen. *Imfufa tekst 419: Modeling the Arterial System with Reference to an Anestesia Simulator*. Imfufa, Roskilde University, 1998.

J. T. Ottesen. Valveless pumping in a fluid-filled closed elastic tube-system: one-dimensional theory with experimental validation. *Journal of Mathematical Biology*, 46:309–332, 2003.

B. M. Patten, T. C. Kramer, and A. Barry. Valvular Action in the Embryonic Chick Heart by Localized Apposition of Endocardial Masses. *The Anatomical Record*, 102(3):299–311, 1948.

A. Pressley. *Elementary Differential Geometry*. Springer-Verlag, London, 2001. ISBN 1-85233-152-6.

V. C. Rideout. *Mathematical and Computer Modeling of Physiological Systems*. Prentice Hall, 1991. ISBN 0-13-563354-0.

A. Snitker, A.-G. Knudsen, H. Skourup, J. Lauridsen, J. Hansen, and K. Olesen. *Bestemmelse af flowretning i et lukket elastisk kredsløb*. 2nd semester, Naturvidenskabelig Basis, Roskilde University, 2000.

L. A. Taber. Mechanical aspects of cardiac development. *Progress in Biophysics and Molecular Biology*, 69:237–255, 1998.

L. A. Taber. Biophysical mechanisms of cardiac looping. *International Journal of Developmental Biology*, 50:323–332, 2006a.

L. A. Taber. Computational Model for Early Cardiac Looping. *Annals of Biomedical Engineering*, 34(8):1655–1669, 2006b.

L. A. Taber, B. B. Keller, and E. B. Clark. Cardiac Mechanics in the Stage-16 Chick Embryo. *Journal of Biomechanical Engineering*, 114:427–434, 1992.

L. A. Taber, I. E. Lin, and E. B. Clark. Mechanics of Cardiac Looping. *Developmental Dynamics*, 203:42–50, 1995.

J. Womersley. Oscillatory Motion of a Viscous Liquid in a Thin-Walled Elastic Tube - 1: The Linear Approximation for Long Waves. *Philosophical Magazine*, 46:199–221, 1955a.

J. Womersley. Method for the Calculation of Velocity, Rate of Flow and Viscous Drag in Arteries when the Pressure Gradient is Known. *Journal of Physiology*, 127:553–563, 1955b.

T.-S. Yang and C.-C. Wang. Effects of Actuator Impact on the Nonlinear Dynamics of a Valveless Pumping System. *Journal of Mechanics in Medicine and Biology*, 0(1):1–33, 2010.

T. M. Yelbuz, M. A. Choma, L. Thrane, M. L. Kirby, and J. A. Izatt. Optical Coherence Tomography: A New High-Resolution Imaging Technology to Study Cardiac Development in Chick Embryos. *Circulation*, 106:2771–2774, 2002.

M. Yoshigi and B. B. Keller. Linearity of Pulsatile Pressure-Flow Relations in the Embryonic Chick Vacular System. *Circulation Research*, 79:864–870, 1996.

M. Yoshigi and B. B. Keller. Characterization of embryonic aortic impedance with lumped parameter models. *American Journal of Physiology*, 273(1 pt 2): H19–27, 1997.

M. Yoshigi, G. D. Knott, and B. B. Keller. Lumped parameter estimation for the embryonic chick vascular system: a time-domain approach using MLAB. *Computer Methods and Programs in Biomedicine*, 63:29–41, 2000.

K. Zahka, N. Hu, K. Brin, F. Yin, and E. Clark. Aortic impedance and hydraulic power in the chick embryo from stages 18 to 29. *Circulation Research*, 64: 1091–1095, 1989.

E. A. Zamir and L. A. Taber. Material Properties and Residual Stress in the Stage 12 Chick Heart During Cardiac Looping. *Journal of Biomechanical Engineering*, 126:823–830, 2004.

E. A. Zamir, V. Srinivasan, R. Perucchio, and L. A. Taber. Mechanical Asymmetry in the Embryonic Chick Heart During Looping. *Annals of Biomedical Engineering*, 31:1327–1336, 2003.

Appendix A

Simulation Code for Liebau's Ring

For the simulations of Liebau's ring the cylindric model presented in chapter 4 is implemented into MatLab v. 7.5 (copyright The MathWorks Inc.).

The implementation into MatLab requires two separate programs that are referred to as the iterative program and the master program. The master program defines the material parameters of the tubes and the desired conditions chosen for the simulation. Specifically the master program initiates the vectors for the dynamic radius and momentum of the tube, `r` and `p`, each containing `N` elements corresponding to the number of sections in the model. It then calculates the elements of the model such as capacitance, inductance and resistance and with those values it calls the iterative routine.

MatLab contains an inherent fourth-order Runge-Kutta solver 'ode45.m' that will handle the time-iteration of the differential equations specified by the model. The 'ode45' solver is initiated by the master program and it then subsequently calls the iterative program.

The iterative program works in the way that given the values of the vectors `r` and `p` it will calculate their derivatives for each section, `dr` and `dp`, and return them to the Runge-Kutta solver, which will then evaluate these derivatives and give the iterative program a new set of vectors `r` and `p`. This continues for a time duration set by the master program.

When the time-iteration in the Runge-Kutta solver is completed 'ode45' returns the vector functions `r` and `p` to the master program. These functions are now transformed to `t` by `N` matrices, where `t` is the number of time-steps done by the iteration. From those two matrices the master program will calculate the corresponding functions of pressure and flow, `P` and `Q`, with the same dimension as the `r` and `p`.

The rutine is the same in all the programs used in this thesis, and therefore this will not be explained again in B and C. The programs are presented below.

The iterative program

```
% rkliebau.m
% Runge-Kutta iteration of the cylindric model.
% Modification of the model to fit Liebau's Ring.

function output = rkliebau(t,z)
global N f x R eta f_B C L C_s Z_s;
global psection plength delay Comp;

% Defining radii and momentum from the input vector
r = z(1:N-plength)';
p = z(N+1-plength:end)';

% The piston pump
r(psection+plength:N) = r(psection:N-plength);
r_min = sqrt(R(psection:psection+plength-1).^2
      - (R(psection:psection+plength-1).^2
      - (R(psection:psection+plength-1).* sqrt(1-Comp)).^2)
      .* (sin((pi/(plength+1)).*[1:plength])));
for j=1:plength
    r(psection+j-1) = R(psection+j-1);
    r(psection+j-1) = sqrt(R(psection+j-1)^2
                    - (R(psection+j-1)^2-r_min(j)^2)
                    * sin(pi*f/0.1 * (t-delay*(j-1)))
                    * (0<=mod(t-delay*(j-1),1/f))
                    * ((0.1/f)>=mod(t-delay*(j-1),1/f)));
end

% Equations for the rate of change of the radii
dr(1) = 1/(2*pi*x*r(1))
      * ((p(N)/L(N))*sqrt(r(N)*r(1)/(R(N)*R(1)))
      - (p(1)/L(1))*sqrt(r(1)*r(2)/(R(1)*R(2))));
dr(2:N-1) = 1./(2.*pi.*x.*r(2:N-1)).*((p(1:N-2)./L(1:N-2))
          .* sqrt(r(1:N-2).*r(2:N-1)./(R(1:N-2).*R(2:N-1)))
          - (p(2:N-1)./L(2:N-1))
          .*sqrt(r(2:N-1).*r(3:N)./(R(2:N-1).*R(3:N))));
dr(N) = 1/(2*pi*x*r(N)) * ((p(N-1)/L(N-1))
      * sqrt(r(N-1)*r(N)/(R(N-1)*R(N)))
      - (p(N)/L(N))*sqrt(r(N)*r(1)/(R(N)*R(1))));
```

```
% Equations for the pressure
P(1) = 1/(2*pi*x*r(1)) * ( (r(1)-R(1))/C(1)
     + ((r(1)-R(1))-(r(N)-R(N)))/C_s(N)+Z_s(N)*(dr(1)-dr(N))
     - ((r(2)-R(2))-(r(1)-R(1)))/C_s(1)-Z_s(1)*(dr(2)-dr(1))
     + (p(N)^2)/(2*r(1)*L(N)) + (p(1)^2)/(2*r(1)*L(1)) );
P(2:N-1) = 1./(2.*pi.*x.*r(2:N-1))
         .* ( (r(2:N-1)-R(2:N-1))./C(2:N-1)
         + ((r(2:N-1)-R(2:N-1))
         - (r(1:N-2)-R(1:N-2)))./C_s(1:N-2)
         + Z_s(1:N-2).*(dr(2:N-1)-dr(1:N-2))
         - ((r(3:N)-R(3:N))-(r(2:N-1)-R(2:N-1)))./C_s(2:N-1)
         - Z_s(2:N-1).*(dr(3:N)-dr(2:N-1))
         + (p(1:N-2).^2)./(2.*r(2:N-1).*L(1:N-2))
         + (p(2:N-1).^2)./(2.*r(2:N-1).*L(2:N-1)) );
P(N) = 1/(2*pi*x*r(N)) * ( (r(N)-R(N))/C(N)
     + ((r(N)-R(N))-(r(N-1)-R(N-1)))/C_s(N-1)
     + Z_s(N-1)*(dr(N)-dr(N-1))
     - ((r(1)-R(1))-(r(N)-R(N)))/C_s(N)
     - Z_s(N)*(dr(1)-dr(N))
     + (p(N-1)^2)/(2*r(N)*L(N-1))
     + (p(N)^2)/(2*r(N)*L(N)) );

% Equations for the rate of change of the momentum
dp(1) = sqrt(r(1)*r(2)/(R(1)*R(2)))
      * ( P(1) - P(2) - ( (8*eta*x)/(pi*r(1)^2*r(2)^2)
      + (f_B(1)*sqrt(R(1)*R(2))
      * sign(p(1))*p(1))/(4*pi*r(1)^2*r(2)^2) )
      * p(1)/L(1) * sqrt(r(1)*r(2)/(R(1)*R(2))) )
      + (p(1)/(2*r(1)))*dr(1) + (p(1)/(2*r(2)))*dr(2);
dp(2:N-1) = sqrt(r(2:N-1).*r(3:N)./(R(2:N-1).*R(3:N)))
          .* ( P(2:N-1) - P(3:N)
          - ( (8.*eta.*x)./(pi.*r(2:N-1).^2.*r(3:N).^2)
          + (f_B(2:N-1).*sqrt(R(2:N-1).*R(3:N))
          .* sign(p(2:N-1)).*p(2:N-1))
          ./ (4.*pi.*r(2:N-1).^2.*r(3:N).^2) )
          .* p(2:N-1)./L(2:N-1)
          .* sqrt(r(2:N-1).*r(3:N)./(R(2:N-1).*R(3:N))) )
          + (p(2:N-1)./(2.*r(2:N-1))).*dr(2:N-1)
          + (p(2:N-1)./(2.*r(3:N))).*dr(3:N);
```

```
dp(N) = sqrt(r(N)*r(1)/(R(N)*R(1)))
        * ( P(N) - P(1) - ( (8*eta*x)/(pi*r(N)^2*r(1)^2)
        + (f_B(N)*sqrt(R(N)*R(1))
        * sign(p(N))*p(N))/(4*pi*r(N)^2*r(1)^2) )
        * p(N)/L(N) * sqrt(r(N)*r(1)/(R(N)*R(1))) )
        + (p(N)/(2*r(N)))*dr(N) + (p(N)/(2*r(1)))*dr(1);

dr = [dr(1:psection-1) dr(psection+plength:N)];

% The output to the main program
output = [dr';dp'];
```

The master program

```
% liebau.m
% A model for pulsating flow in elastic tubes.
% The model is used to simulate Liebau's Ring.

function liebau

% Initializing variables
global N f x R eta f_B C L C_s Z_s;
global psection plength delay Comp;
r = 0; p = 0; P = 0; Q = 0; R = 0;

% The numbers we can change
N = 60; % The number of sections in the model
psection = 5; % The first section of the pump
plength = 3; % The number of sections of the pump
delay = 0; % The delay time in sequential pumping
Comp = 0.25; % The cross-sectional compression ratio
f = 2.06; %Hz % The frequency of the pump
periods = 50; % The number of periods in the simulation
time = periods * 1/f; %s % The time of the simulation

% The parameters of the tube at rest
l = 1.0; %m % The length of the tube
x = l/N; %m % Length per section
R(1:N/2) = 0.01; %m The radius of the soft tube at rest
R(N/2+1:N) = 0.008; %m The radius of the rigid tube at rest
r(1:N) = R(:); %m % The dynamic radii of the tube
p(1:N) = 0; %kg*m/s % The initial momentum of the flow
```

```
% The curvature of the tube
R_B(1:N) = l/(2*pi); % The bend radius for each section
theta(1:N) = (x.*360)./(2.*pi.*R_B); %deg. % The bend angle

% The physical properties of the tube and the liquid
rho = 1000; %kg/m3 % The density of the liquid (water)
eta = 0.001; %Pa.s % The viscosity of the liquid (water)
P_0 = 1e5; %Pa % The pressure outside the tube
E1 = 4.1e5; %Pa % Young's modulus for the soft tube
E2 = 4.3e5; %Pa % Young's modulus for the rigid tube
h1 = 0.001; %m % Wall thickness of the soft tube
h2 = 0.003; %m % Wall thickness of the rigid tube

% Womersley theory
alpha(1:N-1) = sqrt(R(1:N-1).*R(2:N))*sqrt(2*pi*f*rho/eta);
alpha(N) = sqrt(R(N).*R(1)).*sqrt(2*pi*f*rho/eta);
psi = real(1 ./ (1 - 2./(alpha.*sqrt(-i))
    .* besselj(1,alpha.*sqrt(-i))
    ./ besselj(0,alpha.*sqrt(-i))) - 8./(i.*alpha.^2));

% Equations for the curvature of the tube
xi = 0.042 .* theta.^0.69;
K_B(1:N-1) = 9.0704.*(log(R_B(1:N-1)
           ./ (2.*sqrt(R(1:N-1).*R(2:N))))).^2
           - 16.9345.*(log(R_B(1:N-1)
           ./ (2.*sqrt(R(1:N-1).*R(2:N))))) + 19.6437;
K_B(N) = 9.0704.*(log(R_B(N)./(2.*sqrt(R(N).*R(1))))).^2
       - 16.9345.*(log(R_B(N)./(2.*sqrt(R(N).*R(1)))))
       + 19.6437;
f_T(1:N-1) = 0.0478.*(2.*sqrt(R(1:N-1).*R(2:N))).^(-0.2245);
f_T(N) = 0.0478.*(2.*sqrt(R(N).*R(1))).^(-0.2245);

% The calculation of the elements of the model
C(1:N/2) = 1/(2*pi*x*E1*h1) * R(1:N/2); %cm/dyn
C(N/2+1:N) = 1/(2*pi*x*E2*h2) * R(N/2+1:N); %cm/dyn
L(1:N-1) = psi(1:N-1).*rho.*x./(pi*(R(1:N-1).*R(2:N)));
L(N) = psi(N)*rho*x/(pi*R(N)*R(1)); %g/cm4
C_s(1:N/2) = x./(2*pi*(1/3)*E1*h1
           * sqrt(R(1:N/2).*R(2:N/2+1))); %cm/dyn
C_s(N/2+1:N-1) = x./(2*pi*(1/3)*E2*h2
               * sqrt(R(N/2+1:N-1).*R(N/2+2:N))); %cm/dyn
C_s(N/2) = x./(2*pi*(1/3)*sqrt(E1*h1*E2*h2)
         * sqrt(R(N/2)*R(N/2+1))); %cm/dyn
```

```
C_s(N) = x./(2*pi*(1/3)*sqrt(E1*h1*E2*h2)
       * sqrt(R(N)*R(1))); %cm/dyn
Z_s(1:N) = 0.01./C_s; %dyn/cm
f_B = xi.*K_B.*f_T./psi; % The friction factor

% Call MatLab's solver for ordinary differential equations
r = [r(1:psection-1) r(psection+plength:N)];
[t,z] = ode45('rkliebau',[0 time],[r p]);
r = z(:,1:N-plength); p = z(:,N+1-plength:end);

% The compression pump
r(1:length(t),psection+plength:N) =
      r(1:length(t),psection:N-plength);
r_min = sqrt(R(psection:psection+plength-1).^2
      - (R(psection:psection+plength-1).^2
      - (R(psection:psection+plength-1).*sqrt(1-Comp)).^2)
      .* (sin((pi/(plength+1)).*[1:plength])));
for j=1:plength
    r(1:length(t),psection+j-1) = R(psection+j-1);
    r(1:length(t),psection+j-1) = sqrt(R(psection+j-1).^2
                      - (R(psection+j-1).^2-r_min(j).^2)
                      .* sin(pi*f/0.1 .* (t-delay*(j-1)))
                      .* (0<=mod(t-delay*(j-1),1/f))
                      .* ((0.1/f)>=mod(t-delay*(j-1),1/f)));
end

% Calculation of driving pressure and volume flow
T = length(t);
P(1,1:N) = P_0; %Pa % The outside pressure
Q(1,1:N) = 0; %cm3/s % Initial volume flow is set to zero

P(2:T,1) = 1./(2.*pi.*x.*r(2:T,1)) .* ((r(2:T,1)-R(1))./C(1)
         + ((r(2:T,1)-R(1))-(r(2:T,N)-R(N)))./C_s(N)
         + Z_s(N).*((r(2:T,1)-r(1:T-1,1))./(t(2:T)-t(1:T-1))
         - (r(2:T,N)-r(1:T-1,N))./(t(2:T)-t(1:T-1)))
         - ((r(2:T,2)-R(2))-(r(2:T,1)-R(1)))./C_s(1)
         - Z_s(1).*((r(2:T,2)-r(1:T-1,2))./(t(2:T)-t(1:T-1))
         - (r(2:T,1)-r(1:T-1,1))./(t(2:T)-t(1:T-1)))
         + (p(2:T,N).^2)./(2.*r(2:T,1).*L(N))
         + (p(2:T,1).^2)./(2.*r(2:T,1).*L(1))) + P_0;
```

```
P(2:T,2:N-1) = 1./(2.*pi.*x.*r(2:T,2:N-1)) .* ((r(2:T,2:N-1)
             - ones(T-1,1)*R(2:N-1))./(ones(T-1,1)*C(2:N-1))
             + ((r(2:T,2:N-1)-ones(T-1,1)*R(2:N-1))
             - (r(2:T,1:N-2)-ones(T-1,1)*R(1:N-2)))
             ./ (ones(T-1,1)*C_s(1:N-2))
             + (ones(T-1,1)*Z_s(1:N-2)).*((r(2:T,2:N-1)
             - r(1:T-1,2:N-1))./((t(2:T)-t(1:T-1))
             * ones(1,N-2))-(r(2:T,1:N-2)-r(1:T-1,1:N-2))
             ./ ((t(2:T)-t(1:T-1))*ones(1,N-2)))
             - ((r(2:T,3:N)-ones(T-1,1)*R(3:N))
             - (r(2:T,2:N-1)-ones(T-1,1)*R(2:N-1)))
             ./ (ones(T-1,1)*C_s(2:N-1))
             - (ones(T-1,1)*Z_s(2:N-1)).*((r(2:T,3:N)
             - r(1:T-1,3:N))./((t(2:T)-t(1:T-1))
             * ones(1,N-2))-(r(2:T,2:N-1)-r(1:T-1,2:N-1))
             ./ ((t(2:T)-t(1:T-1))*ones(1,N-2)))
             + (p(2:T,1:N-2).^2)./(2.*r(2:T,2:N-1)
             .* (ones(T-1,1)*L(1:N-2)))
             + (p(2:T,2:N-1).^2)./(2.*r(2:T,2:N-1)
             .* (ones(T-1,1)*L(2:N-1)))) + P_0;
P(2:T,N) = 1./(2.*pi.*x.*r(2:T,N)) .* ((r(2:T,N)-R(N))./C(N)
         + ((r(2:T,N)-R(N))-(r(2:T,N-1)-R(N-1)))./C_s(N-1)
         + Z_s(N-1).*((r(2:T,N)-r(1:T-1,N))
         ./ (t(2:T)-t(1:T-1))-(r(2:T,N-1)-r(1:T-1,N-1))
         ./ (t(2:T)-t(1:T-1)))-((r(2:T,1)-R(1))
         - (r(2:T,N)-R(N)))./C_s(N)- Z_s(N).*((r(2:T,1)
         - r(1:T-1,1))./(t(2:T)-t(1:T-1))-(r(2:T,N)
         - r(1:T-1,N))./(t(2:T)-t(1:T-1)))
         + (p(2:T,N-1).^2)./(2.*r(2:T,N).*L(N-1))
         + (p(2:T,N).^2)./(2.*r(2:T,N).*L(N))) + P_0;
Q(2:T,1:N-1) = p(2:T,1:N-1)./(ones(T-1,1)*L(1:N-1))
             .* sqrt(r(2:T,1:N-1).*r(2:T,2:N)
             ./ (ones(T-1,1)*(R(1:N-1).*R(2:N))) );
Q(2:T,N) = p(2:T,N)./L(N) .* sqrt( r(2:T,N).*r(2:T,1)
         ./ (R(N).*R(1)) );

save 'liebau.mat' r p P Q t f
```

Appendix B

Simulation Code for the Tubular Heart

The simulations of embryonic heart is made similar to the simulations of Liebau's ring following the same procedure as described in appendix A. Each HH-stage of the embryo modeled has its own master program detailing the specific conditions at that stage, but the iterative program applied in the simulations is the same.

The iterative program

```
% rkembryo.m
% Runge-Kutta iteration of the embedded tubular flow
% model as used in the modeling of chick embryonic hearts.

function output = rkembryo(t,z)
%% Initialization of the cycle

global N x A B; % The dimensions of the tubular heart
global C_sn C_vn C_r C_j L C_sa Z_sa L_c R_c R_p C_p;
global P_0 eta f_B f IFT_con Vent_con OFT_con;
global Pumpsections Pumptimes delay;

% Defining the radii and momentum from the input vector
a = (z(1:N))'; b = (z(N+1:2*N))'; p = (z(2*N+1:end-2))';
V = z(end-1); M = z(end);
```

```
%% Defining variables for the cycle

% Calculation of the elliptic integrals
ecc = sqrt(1 - (min(a,b)./max(a,b)).^2); % eccentricity
first = (pi/2) .* ( 1 + (1/2)^2*ecc.^2 + (3/8)^2*ecc.^4
      + (15/48)^2*ecc.^6 + (105/384)^2*ecc.^8 );
second = (pi/2) .* (1-(1/2)^2*ecc.^2-(1/3)*(3/8)^2*ecc.^4
       - (1/5)*(15/48)^2*ecc.^6+(1/7)*(105/384)^2*ecc.^8 );

% Calculation of the surface derivatives
dsda = (a>b).*(x.*(4./((a~=b).*a.^2-b.^2))
     .* (a.^2.*second-b.^2.*first)) + (a==b).*x.*pi
     + (a<b).*((4.*b.*a./((a<b).*b.^2-a.^2))
     .* (first-second));
dsdb = (a>b).*(x.*(4.*a.*b./((a~=b).*a.^2-b.^2))
     .* (first-second)) + (a==b).*x.*pi
     + (a<b).*(x.*(4./((a<b).*b.^2-a.^2))
     .* (b.^2.*second-a.^2.*first));

% Calculation of the chi factor
chi = ( ((b./a).*dsdb.^2-dsda.*dsdb)./C_sn
    + 2.*((2.*a.*b)./(a.^2+b.^2)).^2.*(1./(a.*b)).*(1./C_vn)
    + (pi*x)^2.*2.*a.^2./C_j )
    ./ ( (dsda.^2-(b./a).*dsda.*dsdb)./C_sn
    + 2.*((2.*a.*b)./(a.^2+b.^2)).^2.*(1./a.^2).*(1./C_vn)
    + (pi*x)^2.*2.*a.*(2.*a-b)./C_j + 1./C_r );

%% The pumping mechanism

% Pumping is made by contracting the outer radius
% by means of derivative of the contraction function
% dr = -pi abc R_0 exp(-ct) cos(pi b(1-exp(-ct))
time(1:N) = (t-delay*((1:N)-Pumpsections(1))); dr(1:N) = 0;
dr(Pumpsections(1):Pumpsections(2)) =
  - pi*IFT_con(1)*IFT_con(2)*IFT_con(3)
  .* A(Pumpsections(1):Pumpsections(2))
  .* exp(-IFT_con(3).*time(Pumpsections(1):Pumpsections(2)))
  .* cos(pi.*IFT_con(2).*(1-exp(-IFT_con(3)
  .* time(Pumpsections(1):Pumpsections(2)))))
  .* (0<=mod(time(Pumpsections(1):Pumpsections(2)),1/f))
  .* (Pumptimes(1)>=mod(time(Pumpsections(1)
  : Pumpsections(2)),1/f));
```

```
dr(Pumpsections(2):Pumpsections(3)) =
  - pi*Vent_con(1)*Vent_con(2)*Vent_con(3)
  .* A(Pumpsections(2):Pumpsections(3)).*exp(-Vent_con(3)
  .* time(Pumpsections(2):Pumpsections(3)))
  .* cos(pi.*Vent_con(2).*(1-exp(-Vent_con(3)
  .* time(Pumpsections(2):Pumpsections(3)))))
  .* (0<=mod(time(Pumpsections(2):Pumpsections(3)),1/f))
  .* (Pumptimes(2)>=mod(time(Pumpsections(2)
  : Pumpsections(3)),1/f));
dr(Pumpsections(3):Pumpsections(4)) =
  - pi*OFT_con(1)*OFT_con(2)*OFT_con(3)
  .* A(Pumpsections(3):Pumpsections(4))
  .* exp(-OFT_con(3).*time(Pumpsections(3):Pumpsections(4)))
  .* cos(pi.*OFT_con(2).*(1-exp(-OFT_con(3)
  .* time(Pumpsections(3):Pumpsections(4)))))
  .* (0<=mod(time(Pumpsections(3):Pumpsections(4)),1/f))
  .* (Pumptimes(3)>=mod(time(Pumpsections(3)
  : Pumpsections(4)),1/f));

%% Calculation of model variables

% Calculation of the flow
Q(1) = (p(1)/L(1)) * sqrt( (sqrt(a(1)*A(1))*sqrt(b(1)*B(1)))
     / (A(1)*B(1)) );
Q(2:N) = (p(2:N)./L(2:N))
       .* sqrt( (sqrt(a(1:N-1).*a(2:N))
       .* sqrt(b(1:N-1).*b(2:N))./(sqrt(A(1:N-1).*A(2:N))
       .* sqrt(B(1:N-1).*B(2:N))) );
Q(N+1) = M/L_c;

% Equations for the rate of change of the axes
da = (Q(1:N)-Q(2:N+1))/(pi*x) .* (chi./(a+chi.*b)) + dr;
db = (Q(1:N)-Q(2:N+1))/(pi*x) .* (1./(a+chi.*b));

% Equations for the dynamic pressure
P(1) = (1/(pi*x*b(1))) * ( (a(1)-A(1))/C_r(1)
     + dsda(1)*(dsda(1)*(a(1)-A(1))/C_sn(1)
     + dsdb(1)*(b(1)-B(1))/C_sn(1))
     + ((2*a(1)*b(1))/(a(1)^2+b(1)^2))*(1/a(1))
     * tan(((2*a(1)*b(1))/(a(1)^2+b(1)^2))
     * ((1/a(1))*(a(1)-A(1))/C_vn(1)-(1/b(1))
     * (b(1)-B(1))/C_vn(1)))-(x*pi)^2*(2*a(1)-b(1))
     * ((2*a(1)-b(1))*(a(1)-A(1))/C_j(1)
```

```
     - a(1)*(b(1)-B(1))/C_j(1))
     + (a(1)-A(1))/C_sa(1) + Z_sa(1)*da(1)
     - ((a(2)-A(2))-(a(1)-A(1)))/C_sa(2)
     - Z_sa(2)*(da(2)-da(1))
     + (p(1)^2)/(4*a(1)*L(1)) + (p(2)^2)/(4*a(1)*L(2)) );
P(2:N-1) = (1./(pi.*x.*b(2:N-1)))
         .* ( (a(2:N-1)-A(2:N-1))./C_r(2:N-1)
         + dsda(2:N-1).*(dsda(2:N-1).*(a(2:N-1)
         - A(2:N-1))./C_sn(2:N-1) + dsdb(2:N-1).*(b(2:N-1)
         - B(2:N-1))./C_sn(2:N-1))
         + ((2.*a(2:N-1).*b(2:N-1))./(a(2:N-1).^2
         + b(2:N-1).^2)).*(1./a(2:N-1))
         .* tan(((2.*a(2:N-1).*b(2:N-1))./(a(2:N-1).^2
         + b(2:N-1).^2)).*((1./a(2:N-1))
         .*(a(2:N-1)-A(2:N-1))./C_vn(2:N-1)
         - (1./b(2:N-1)).*(b(2:N-1)-B(2:N-1))./C_vn(2:N-1)))
         - (x*pi).^2.*(2.*a(2:N-1)-b(2:N-1))
         .* ((2.*a(2:N-1)-b(2:N-1)).*(a(2:N-1)-A(2:N-1))
         ./ C_j(2:N-1)-a(2:N-1).*(b(2:N-1)-B(2:N-1))
         ./ C_j(2:N-1))+((a(2:N-1)-A(2:N-1))
         - (a(1:N-2)-A(1:N-2)))./C_sa(2:N-1)
         + Z_sa(2:N-1).*(da(2:N-1)-da(1:N-2))
         - ((a(3:N)-A(3:N))-(a(2:N-1)-A(2:N-1)))./C_sa(3:N)
         - Z_sa(3:N).*(da(3:N)-da(2:N-1))
         + (p(2:N-1).^2)./(4.*a(2:N-1).*L(2:N-1))
         + (p(3:N).^2)./(4.*a(2:N-1).*L(3:N)) );
P(N) = (1/(pi*x*b(N))) * ( (a(N)-A(N))/C_r(N)
     + dsda(N)*(dsda(N)*(a(N)-A(N))/C_sn(N)
     + dsdb(N)*(b(N)-B(N))/C_sn(N))
     + ((2*a(N)*b(N))/(a(N)^2+b(N)^2))*(1/a(N))
     * tan(((2*a(N)*b(N))/(a(N)^2+b(N)^2))
     * ((1/a(N))*(a(N)-A(N))/C_vn(N)-(1/b(N))*(b(N)-B(N))
     / C_vn(N)))-(x*pi)^2*(2*a(N)-b(N))*((2*a(N)-b(N))
     * (a(N)-A(N))/C_j(N) - a(N)*(b(N)-B(N))/C_j(N))
     + ((a(N)-A(N))-(a(N-1)-A(N-1)))/C_sa(N)
     + Z_sa(N)*(da(N)-da(N-1))
     + (a(N)-A(N))/C_sa(N+1)
     + Z_sa(N+1)*da(N) + (p(N)^2)/(4*a(N)*L(N)) );
P(N+1) = V/C_p - P_0;

% Equations for the rate of change of the momentum
dp(1) = sqrt(sqrt(A(1)*a(1))*sqrt(B(1)*b(1))/(A(1)*B(1)))
      * ( P_0 - P(1) - ( (4*eta*x*(A(1)*a(1)+B(1)*b(1)))
```

```
      / (sqrt(A(1)*a(1))^3*sqrt(B(1)*b(1))^3)
      + (f_B(1)*(1/(4*pi))*sqrt(A(1)*B(1)/(sqrt(A(1)*a(1))^5
      * sqrt(B(1)*b(1))^5))*sqrt((A(1)*a(1)+B(1)*b(1))/2)
      * sign(p(1))*p(1)) ) * Q(1) ) + (p(1)/(4*a(1)))*da(1)
      + (p(1)/(4*b(1)))*db(1);
dp(2:N) = sqrt(sqrt(a(1:N-1).*a(2:N)).*sqrt(b(1:N-1).*b(2:N))
        ./ (sqrt(A(1:N-1).*A(2:N)).*sqrt(B(1:N-1).*B(2:N))))
        .* ( P(1:N-1) - P(2:N) - ( (4.*eta.*x.*(a(1:N-1)
        .* a(2:N)+b(1:N-1).*b(2:N)))
        ./ (sqrt(a(1:N-1).*a(2:N)).^3
        .* sqrt(b(1:N-1).*b(2:N)).^3)
        + (f_B(2:N).*(1./(4.*pi))
        .* sqrt(sqrt(A(2:N).*A(1:N-1).*B(2:N).*B(1:N-1))
        ./ (sqrt(a(2:N).*a(1:N-1)).^5
        .* sqrt(b(2:N).*b(1:N-1)).^5))
        .* sqrt((a(2:N).*a(1:N-1)+b(2:N).*b(1:N-1))./2)
        .* sign(p(2:N)).*p(2:N)) ) .* Q(2:N) )
        + (p(2:N)./(4.*a(1:N-1))).*da(1:N-1)
        + (p(2:N)./(4.*a(2:N))).*da(2:N)
        + (p(2:N)./(4.*b(1:N-1))).*db(1:N-1)
        + (p(2:N)./(4.*b(2:N))).*db(2:N);

% Equations for the windkessel termination
dV = Q(N+1) - P(N+1)/R_p; dM = P(N) - P(N+1) - Q(N+1)*R_c;

% The output to the main program
output = [da';db';dp';dV;dM];
```

The hh10 master program

```
% hh10.m
% A model of blood flow of a HH-stage 10 embryonic heart.
% The flow model is based on the embedded tube model.

function hh10

%% Initialization of the model
global N x A B; % The dimensions of the tubular heart
global C_sn C_vn C_r C_j L C_sa Z_sa L_c R_c R_p C_p;
global P_0 eta f_B f IFT_con Vent_con OFT_con;
global Pumpsections Pumptimes delay;
a = 0; b = 0; p = 0; P = 0; Q = 0;

N = 30; % The number of sections in the model
% Acceptable numbers = [1 2 3 5 6 8 10 11 15 22 30 33 55 66]

f = 1.0; %Hz % The frequency of the pump
% Frequencies measured = [0.8 1.0 1.2];

periods = 3; % The number of periods in the simulation
time = periods * 1/f; %seconds % The time of the simulation

%% Tracing of the heart loop

% Lengths
L_Sinus_venosis = 50e-6; %m
L_Left_ventricle = 130e-6; %m
L_Right_ventricle = 250e-6; %m
L_Proximal_outflow_tract = 230e-6; %m

% Diameters
D_Sinus_venosis = 330e-6; %m
D_Venous_pole = 300e-6; %m
D_Central_left_ventricle = 270e-6; %m
D_Left_lateral_furrow = 250e-6; %m
D_Central_right_ventricle = 250e-6; %m
D_Conoventricular_sulcus = 200e-6; %m
D_Proximal_outflow_tract = 170e-6; %m
D_Arterial_outlet = 120e-6; %m
```

```
% Layers
h_my = 18e-6; %m % The thickness of the myocardial layer
h_cj = 52e-6; %m % The thickness of the cardiac jelly
h_en = h_my/2; %m % The thickness of the endocardial layer

% Dimension setup
tubelength = L_Sinus_venosis + L_Left_ventricle
           + L_Right_ventricle + L_Proximal_outflow_tract;

lengths = [0 L_Sinus_venosis
        L_Sinus_venosis+L_Left_ventricle/2
        L_Sinus_venosis+L_Left_ventricle
        L_Sinus_venosis+L_Left_ventricle+L_Right_ventricle/2
        L_Sinus_venosis+L_Left_ventricle+L_Right_ventricle
        L_Sinus_venosis+L_Left_ventricle
        +L_Right_ventricle+L_Proximal_outflow_tract/2
        tubelength];
diameters = [D_Sinus_venosis D_Venous_pole
          D_Central_left_ventricle D_Left_lateral_furrow
          D_Central_right_ventricle D_Conoventricular_sulcus
          D_Proximal_outflow_tract D_Arterial_outlet];
relative_cardiac_jelly = [0.8 0.9 0.9 1.1 1 1.4 1.3 1.1]
                     * (h_cj/(D_Central_right_ventricle/2));
x = tubelength/N; %m % The length of a section of the tube

% The major and minor axis of the model
l_array = 0:10^(-6):tubelength;
for d=1:length(diameters)-1
    coef = polyfit(lengths(d:d+1),diameters(d:d+1)/2,1);
    a_array((10^6*lengths(d)+1):(10^6*lengths(d+1)+1)) =
       polyval(coef,l_array((10^6*lengths(d)+1)
       :(10^6*lengths(d+1)+1)));
    coef = polyfit(lengths(d:d+1),(diameters(d:d+1)/2)
         .* (1-relative_cardiac_jelly(d:d+1)),1);
    b_array((10^6*lengths(d)+1):(10^6*lengths(d+1)+1)) =
       polyval(coef,l_array((10^6*lengths(d)+1)
       :(10^6*lengths(d+1)+1)));
end
for n=1:N
    index = uint16(((n-1)*x+x/2)*10^6);
    A(n) = a_array(index); %m % The major axis of at rest
    B(n) = b_array(index); %m % The minor axis of at rest
end
```

```
a(1:N) = A(1:N); %m % The dynamic major axis of the tube
b(1:N) = B(1:N); %m % The dynamic minor axis of the tube

% Curvature
R_B(1:N) = 550e-6; %m % The radius of curvature
startindex = find(x*(1:N)>L_Sinus_venosis,1,'first');
endindex = find(x*(1:N)>L_Sinus_venosis
         + L_Left_ventricle+L_Right_ventricle
         + (1/4)*L_Proximal_outflow_tract,1,'first');
theta(1:N) = 0; %deg. % The bending angle for each section
theta(startindex:endindex) = (x./(2.*pi
                        .* R_B(startindex:endindex))).*360;

% Boundary conditions

P_0 = 26.7; %Pa % The mean pressure at the venous end
L_c = 14.87e8; %kg/m4 % Inertance of the vascular system
R_c = 5.41e11; %Pa.s/m3 % Characteristic resistance
R_p = 10.74e11; %Pa.s/m3 % Peripheral resistance
C_p = 0.31e-12; %m3/Pa % Capacitance of the vascular system

V_0 = P_0*C_p; %m3 % Equilibrium vascular system volume
V = V_0; %m3 % The dynamical volume of the vascular system
M = 0; %Pa.s % The momentum through the vascular system

%% Parameter estimation

% The physical parameters of the heart tube and the blood
rho = 1.0e3; %kg/m3 % The density of embryonic blood
eta = 3.8e-3; %Pa.s % The viscosity of embryonic blood
E_my = 60; %Pa % Young's modulus for the myocardial layer
E_cj = 12; %Pa % Young's modulus for the cardiac jelly
E_en = E_my; %Pa % Young's modulus for the endocardial layer

%% The pumping mechanism

p(1:N) = 0; %kg*m/s % The initial momentum of the flow
T_prox_contraction = 170.0e-3; %s % Proximal contraction
T_dist_contraction = 228.0e-3; %s % Distal contraction
T_prox_relaxation = 275.6e-3; %s % Proximal relaxation
T_dist_relaxation = 286.0e-3; %s % Distal relaxation
Wave_velocity = 3.3e-3; %m/s % Contraction wave velocity
Diametric_contraction = 0.15; % Diametric contraction ratio
```

```
% Tracing of the contraction functions
% Given by: X(t) = 1 - a*sin(pi*b*(1-exp(-c*time)))
IFT_con = [0.4287 1.3480 0.001015];
Vent_con = [0.3329 1.0635 0.001418];
OFT_con = [0.3072 6.6597 0.00006598];

IFT_con(1) = (Diametric_contraction/Vent_con(1))
           * IFT_con(1);
OFT_con(1) = (Diametric_contraction/Vent_con(1))
           * OFT_con(1);
Vent_con(1) = (Diametric_contraction/Vent_con(1))
            * Vent_con(1);

IFT_con(3) = -log((Vent_con(2)-1)/Vent_con(2))
           / (T_prox_contraction+T_prox_relaxation)
           * (IFT_con(3)/Vent_con(3));
Vent_con(3) = -log((Vent_con(2)-1)/Vent_con(2))
            / (T_prox_contraction+T_prox_relaxation);
OFT_con(3) = -log((OFT_con(2)-1)/OFT_con(2))
           / (T_dist_contraction+T_dist_relaxation);

% Defining the contraction durations
IFT_time = (-1/IFT_con(3))*log((IFT_con(2)-1)/IFT_con(2));
Vent_time = (-1/Vent_con(3))
          * log((Vent_con(2)-1)/Vent_con(2));
OFT_time = (-1/OFT_con(3))*log((OFT_con(2)-1)/OFT_con(2));
Pumptimes = [IFT_time Vent_time OFT_time];

% Defining the contraction zones
IFT_section = find(x*(1:N)>L_Sinus_venosis,1,'first');
Vent_section = find(x*(1:N)>L_Sinus_venosis,1,'first');
OFT_section = find(x*(1:N)>L_Sinus_venosis+L_Left_ventricle
            + L_Right_ventricle,1,'first');
End_section = find(x*(1:N)>L_Sinus_venosis+L_Left_ventricle
            + L_Right_ventricle+(1/2)
            * L_Proximal_outflow_tract,1,'first');
Pumpsections = [IFT_section Vent_section
                OFT_section End_section];

% Defining the phase shift between sections
delay = x/Wave_velocity;
```

```
%% The model engine

% Calculated characteristics of the elliptic tube
S(1:N) = x*pi*(A+B).*(1+3*((A-B)./(A+B)).^2.
       / (10+sqrt(4-3*((A-B)./(A+B)).^2))); %m2
Omega(1) = pi.*(A(1)+B(1)).*(1
         + 3*((A(1)-B(1))./(A(1)+B(1))).^2./(10
         + sqrt(4-3.*((A(1)-B(1))./(A(1)+B(1))).^2))); %m
Omega(2:N) = pi.*(sqrt(A(1:N-1).*A(2:N))+sqrt(B(1:N-1)
           .* B(2:N))).*(1+3*((sqrt(A(1:N-1).*A(2:N))
           - sqrt(B(1:N-1).*B(2:N))./(sqrt(A(1:N-1)
           .* A(2:N))+sqrt(B(1:N-1).*B(2:N)))).^2./(10
           + sqrt(4-3.*((sqrt(A(1:N-1).*A(2:N))
           - sqrt(B(1:N-1).*B(2:N))./(sqrt(A(1:N-1)
           .* A(2:N))+sqrt(B(1:N-1).*B(2:N)))).^2)) ); %m
Omega(N+1) = pi.*(A(N)+B(N)).*(1
           + 3*((A(N)-B(N))./(A(N)+B(N))).^2./(10
           + sqrt(4-3.*((A(N)-B(N))./(A(N)+B(N))).^2))); %m

% Womersley theory
alpha(1) = sqrt((2*A(1)^2*B(1)^2)/(A(1)^2+B(1)^2))
         * sqrt(2*pi*f*rho/eta);
alpha(2:N) = sqrt((2.*A(1:N-1).*A(2:N).*B(1:N-1).*B(2:N))
           ./ (A(1:N-1).*A(2:N)+B(1:N-1).*B(2:N)))
           .* sqrt(2*pi*f*rho/eta);
psi = real(1 ./ (1 - 2./(alpha.*sqrt(-i))
    .* besselj(1,alpha.*sqrt(-i))
    ./ besselj(0,alpha.*sqrt(-i))) - 8./(i.*alpha.^2));

% Equations for the curvature of the tube
xi = 0.042 .* theta.^0.69;
l_c(1) = sqrt(2*A(1)^2*B(1)^2 / (A(1)^2+B(1)^2)); %m
l_c(2:N) = sqrt(2.*A(1:N-1).*A(2:N).*B(1:N-1).*B(2:N)
         ./ (A(1:N-1).*A(2:N)+B(1:N-1).*B(2:N))); %m
K_B(1:N) = 9.0704.*(log(R_B(1:N)./(2.*l_c(1:N)))).^2
         - 16.9345.*(log(R_B(1:N)./(2.*l_c(1:N))))+19.6437;
f_T(1:N) = 0.0478.*(2.*l_c(1:N)).^(-0.2245);
f_B = xi.*K_B.*f_T./psi;

% The calculation of the primary elements of the model
C_sn(1:N) = S./(E_en.*h_en); %m/Pa=m3/N
C_vn(1:N) = 1./(S.*(1/3).*E_en.*h_en); %(Pa.m3)^-1=(N.m)^-1
C_r(1:N) = 1./(pi*x*E_my*h_my) .* (A(1:N)); %(Pa.m)^-1=m/N
```

```
C_j(1:N) = (pi.*x.*(A(1:N).^2-A(1:N).*B(1:N)))./E_cj; %m3/Pa
L(1) = psi(1)*rho*x./(pi*A(1).*B(1)); %kg/m4
L(2:N) = psi(2:N).*rho.*x./(pi.
       * sqrt(A(1:N-1).*A(2:N).*B(1:N-1).*B(2:N))); %kg/m4

% The calculation of the shear elements of the network model
C_sa(1) = 2.*x ./ ( (1/3).*E_en.*h_en.*Omega(1)
        + 4.*pi.*(1/3).*E_my.*h_my.*A(1) ); %(Pa.m)^-1=m/N
C_sa(2:N) = 2.*x ./ ( (1/3).*E_en.*h_en.*Omega(2:N) + 4.*pi
          .* (1/3).*E_my.*h_my.*sqrt(A(1:N-1).*A(2:N)) );
C_sa(N+1) = 2.*x ./ ( (1/3).*E_en.*h_en.*Omega(N+1)
          + 4.*pi.*(1/3).*E_my.*h_my.*A(N) ); %(Pa.m)^-1=m/N
C_sb(1:N+1) = 2.*x ./ ( (1/3).*E_en.*h_en.*Omega(1:N+1) );
Z_sa(1:N+1) = 0.01./C_sa; %Pa.m=N/m
Z_sb(1:N+1) = 0.01./C_sb; %Pa.m=N/m

%% The Runge-Kutta algorithm

% Call MatLab's solver for ordinary differential equations
options = odeset('RelTol',1e-3,'AbsTol',1e-6,'Stats','on');
[t,z] = ode45('rkembryo',[0 time],[a b p V M],options);
a = z(:,1:N); b = z(:,N+1:2*N); p = z(:,2*N+1:end-2);
V = z(:,end-1); M = z(:,end);

%% Calculation of flow and pressure

T = length(t);

% Calculation of the elliptic integrals
ecc = sqrt(1-(min(a,b)./max(a,b)).^2); % Eccentricity
first = (pi/2).*(1+(1/2)^2*ecc.^2+(3/8)^2*ecc.^4
      + (15/48)^2*ecc.^6+(105/384)^2*ecc.^8);
second = (pi/2).*(1-(1/2)^2*ecc.^2-(1/3)*(3/8)^2*ecc.^4
       - (1/5)*(15/48)^2*ecc.^6+(1/7)*(105/384)^2*ecc.^8);

% Calculation of the surface derivatives
dsda = (a>b).*(x.*(4./((a>b).*a.^2-b.^2))
     .* (a.^2.*second-b.^2.*first))+(a==b).*x.*pi+(a<b)
     .* ((4.*b.*a./((a<b).*b.^2-a.^2)).*(first-second));
dsdb = (a>b).*(x.*(4.*a.*b./((a<b).*a.^2-b.^2))
     .* (first-second))+(a==b).*x.*pi+(a<b).*(x.*(4./((a<b)
     .* b.^2-a.^2)).*(b.^2.*second-a.^2.*first));
```

```
% Calculation of the dynamic pressure
P(1,1:N+1) = 0; %Pa % Initial pressure is set to zero
P(2:T,1) = 1./(pi.*x.*b(2:T,1)) .* ((a(2:T,1)-A(1))./C_r(1)
         + dsda(2:T,1).*(dsda(2:T,1).*(a(2:T,1)-A(1))
         ./ C_sn(1)+dsdb(2:T,1).*(b(2:T,1)-B(1))./C_sn(1))
         + ((2.*a(2:T,1).*b(2:T,1))./(a(2:T,1).^2
         + b(2:T,1).^2)).*(1./a(2:T,1)).*tan(((2.*a(2:T,1)
         .* b(2:T,1))./(a(2:T,1).^2+b(2:T,1).^2))
         .* ((1./a(2:T,1)).*(a(2:T,1)-A(1))./C_vn(1)
         - (1./b(2:T,1)).*(b(2:T,1)-B(1))./C_vn(1)))
         + (x.*pi).^2.*(2.*a(2:T,1)-b(2:T,1))
         .* ((2.*a(2:T,1)-b(2:T,1))
         .* (a(2:T,1)-A(1))./C_j(1)-a(2:T,1).*(b(2:T,1)
         - B(1))./C_j(1)) + (a(2:T,1)-A(1))./C_sa(1)
         + Z_sa(1).*(a(2:T,1)-a(1:T-1,1))./(t(2:T)
         - t(1:T-1))-((a(2:T,2)-A(2))-(a(2:T,1)-A(1)))
         ./ C_sa(2)-Z_sa(2).*((a(2:T,2)-a(1:T-1,2))
         ./ (t(2:T)-t(1:T-1))-(a(2:T,1)-a(1:T-1,1))
         ./ (t(2:T)-t(1:T-1)))+(p(2:T,1).^2)./(4.*a(2:T,1)
         .* L(1))+(p(2:T,2).^2)./(4.*a(2:T,1).*L(2)));
P(2:T,2:N-1) = 1./(pi.*x.*b(2:T,2:N-1)) .* ((a(2:T,2:N-1)
         - ones(T-1,1)*A(2:N-1))./(ones(T-1,1)*C_r(2:N-1))
         + dsda(2:T,2:N-1).*(dsda(2:T,2:N-1).*(a(2:T,2:N-1)
         - ones(T-1,1)*A(2:N-1))./(ones(T-1,1)*C_sn(2:N-1))
         + dsdb(2:T,2:N-1).*(b(2:T,2:N-1)-ones(T-1,1)
         * B(2:N-1))./(ones(T-1,1)*C_sn(2:N-1)))+((2
         .* a(2:T,2:N-1).*b(2:T,2:N-1))./(a(2:T,2:N-1).^2
         + b(2:T,2:N-1).^2)).*(1./a(2:T,2:N-1))
         .* tan(((2.*a(2:T,2:N-1).*b(2:T,2:N-1))
         ./ (a(2:T,2:N-1).^2+b(2:T,2:N-1).^2))
         .* ((1./a(2:T,2:N-1)).*(a(2:T,2:N-1)-ones(T-1,1)
         * A(2:N-1))./(ones(T-1,1)*C_vn(2:N-1))
         - (1./b(2:T,2:N-1)).*(b(2:T,2:N-1)-ones(T-1,1)
         * B(2:N-1))./(ones(T-1,1)*C_vn(2:N-1))))
         + (x.*pi).^2.*(2.*a(2:T,2:N-1)-b(2:T,2:N-1))
         .* ((2.*a(2:T,2:N-1)-b(2:T,2:N-1)).*(a(2:T,2:N-1)
         - ones(T-1,1)*A(2:N-1))./(ones(T-1,1)*C_j(2:N-1))
         - a(2:T,2:N-1).*(b(2:T,2:N-1)-ones(T-1,1)
         * B(2:N-1))./(ones(T-1,1)*C_j(2:N-1)))
         + ((a(2:T,2:N-1)-ones(T-1,1)*A(2:N-1))
         - (a(2:T,1:N-2)-ones(T-1,1)*A(1:N-2)))
         ./ (ones(T-1,1)*C_sa(2:N-1))+(ones(T-1,1)
         * Z_sa(2:N-1)).*((a(2:T,2:N-1)-a(1:T-1,2:N-1))
```

```
          ./ ((t(2:T)-t(1:T-1))*ones(1,N-2))-(a(2:T,1:N-2)
          - a(1:T-1,1:N-2))./((t(2:T)-t(1:T-1))*ones(1,N-2)))
          - ((a(2:T,3:N)-ones(T-1,1)*A(3:N))-(a(2:T,2:N-1)
          -ones(T-1,1)*A(2:N-1))).*(ones(T-1,1)*C_sa(3:N))
          + (ones(T-1,1)*Z_sa(3:N)).*((a(2:T,3:N)
          - a(1:T-1,3:N)).*((t(2:T)-t(1:T-1))*ones(1,N-2))
          - (a(2:T,2:N-1)-a(1:T-1,2:N-1)).*((t(2:T)-t(1:T-1))
          * ones(1,N-2)))+(p(2:T,2:N-1).^2).*(4*a(2:T,2:N-1)
          .* (ones(T-1,1)*L(2:N-1))) + (p(2:T,3:N).^2)
          .* (4*a(2:T,2:N-1).*(ones(T-1,1)*L(3:N))));
P(2:T,N) = 1./(pi.*x.*b(2:T,N)) .* ((a(2:T,N)-A(N))./C_r(N)
          + dsda(2:T,N).*(dsda(2:T,N).*(a(2:T,N)-A(N))
          ./ C_sn(N)+dsdb(2:T,N).*(b(2:T,N)-B(N))./C_sn(N))
          + ((2.*a(2:T,N).*b(2:T,N))./(a(2:T,N).^2
          + b(2:T,N).^2)).*(1./a(2:T,N)).*tan(((2.*a(2:T,N)
          .* b(2:T,N))./(a(2:T,N).^2+b(2:T,N).^2))
          .* ((1./a(2:T,N)).*(a(2:T,N)-A(N))./C_vn(N)
          - (1./b(2:T,N)).*(b(2:T,N)-B(N))./C_vn(N)))
          + (x.*pi).^2.*(2.*a(2:T,N)-b(2:T,N))
          .* ((2.*a(2:T,N)-b(2:T,N)).*(a(2:T,N)-A(N))
          ./ C_j(N)-a(2:T,N).*(b(2:T,N)-B(N))./C_j(N))
          + ((a(2:T,N)-A(N))-(a(2:T,N-1)-A(N-1)))./C_sa(N)
          + Z_sa(N).*((a(2:T,N)-a(1:T-1,N))./(t(2:T)
          - t(1:T-1))-(a(2:T,N-1)-a(1:T-1,N-1))./(t(2:T)
          - t(1:T-1)))+(a(2:T,N)-A(N))./C_sa(N+1)
          + Z_sa(N+1).*(a(2:T,N)-a(1:T-1,N))./(t(2:T)
          - t(1:T-1)) + (p(2:T,N).^2)./(4.*a(2:T,N).*L(N)));
P(2:T,N+1) = V(2:T)./C_p-P_0;

% Calculation of the flow
Q(1,1:N+1) = 0; %m3/s % Initial volume flow is set to zero
Q(2:T,1) = p(2:T,1)./L(1) .* sqrt( (sqrt(a(2:T,1).*A(1))
          .* sqrt(b(2:T,1).*B(1))) ./ (A(1)*B(1)) );
Q(2:T,2:N) = p(2:T,2:N)./(ones(T-1,1)*L(2:N))
            .* sqrt( (sqrt(a(2:T,1:N-1).*a(2:T,2:N))
            .* sqrt(b(2:T,1:N-1).*b(2:T,2:N)))
            ./ (ones(T-1,1)*(sqrt(A(1:N-1).*A(2:N))
            .*sqrt(B(1:N-1).*B(2:N)))) );
Q(2:T,N+1) = M(2:T)./L_c;

% Model output
save 'hh10.mat' t a b p P Q V M f
```

The hh12 master program

```
% hh12.m
% A model for blood flow of a HH-stage 12 embryonic heart.
% The flow model is based on the embedded tube model.

function hh12

%% Initialization of the model
global N x A B; % The dimensions of the tubular heart
global C_sn C_vn C_r C_j L C_sa Z_sa L_c R_c R_p C_p;
global P_0 eta f_B f IFT_con Vent_con OFT_con;
global Pumpsections Pumptimes delay;
a = 0; b = 0; p = 0; P = 0; Q = 0;

N = 29; % The number of sections in the model
% Acceptable numbers = [1 2 4 5 10 20 29 58 97 116]

f = 1.5; %Hz % The frequency of the pump
% Frequencies measured = [1.25 1.32 1.72 1.90];

periods = 3; % The number of periods in the simulation
time = periods * 1/f; %seconds % The time of the simulation

%% Tracing of the heart loop

% Lengths
L_Sinus_venosis = 70e-6; %m
L_Primitive_atrium = 200e-6; %m
L_Left_ventricle = 270e-6; %m
L_Right_ventricle = 370e-6; %m
L_Proximal_outflow_tract = 250e-6; %m

% Diameters
D_Sinus_venosis = 350e-6; %m
D_Venous_pole = 330e-6; %m
D_Central_atrium = 320e-6; %m
D_Upper_atrium = 280e-6; %m
D_lower_left_ventricle = 250e-6; %m
D_Central_left_ventricle = 250e-6; %m
D_Left_lateral_furrow = 250e-6; %m
D_Central_right_ventricle = 230e-6; %m
```

```
D_Upper_right_ventricle = 170e-6; %m
D_Conoventricular_sulcus = 150e-6; %m
D_Proximal_outflow_tract = 150e-6; %m
D_Distal_outflow_tract = 150e-6; %m
D_Arterial_outlet = 130e-6; %m

% Layers
h_my = 15e-6; %m % The thickness of the myocardial layer
h_cj = 70e-6; %m % The thickness of the cardiac jelly
h_en = h_my/2; %m % The thickness of the endocardial layer

% Dimension setup
tubelength = L_Sinus_venosis+L_Primitive_atrium
           + L_Left_ventricle+L_Right_ventricle
           + L_Proximal_outflow_tract;
lengths = [0 L_Sinus_venosis L_Sinus_venosis
           +3*L_Primitive_atrium/8 L_Sinus_venosis
           +6*L_Primitive_atrium/8 L_Sinus_venosis
           +L_Primitive_atrium+L_Left_ventricle/3
           L_Sinus_venosis+L_Primitive_atrium
           +2*L_Left_ventricle/3 L_Sinus_venosis
           +L_Primitive_atrium+L_Left_ventricle
           L_Sinus_venosis+L_Primitive_atrium
           +L_Left_ventricle+4*L_Right_ventricle/10
           L_Sinus_venosis+L_Primitive_atrium
           +L_Left_ventricle+7*L_Right_ventricle/10
           L_Sinus_venosis+L_Primitive_atrium
           +L_Left_ventricle+L_Right_ventricle
           L_Sinus_venosis+L_Primitive_atrium
           +L_Left_ventricle+L_Right_ventricle
           +2*L_Proximal_outflow_tract/5
           L_Sinus_venosis+L_Primitive_atrium
           +L_Left_ventricle+L_Right_ventricle
           +9*L_Proximal_outflow_tract/15 tubelength];
diameters = [D_Sinus_venosis D_Venous_pole D_Central_atrium
             D_Upper_atrium D_lower_left_ventricle
             D_Central_left_ventricle D_Left_lateral_furrow
             D_Central_right_ventricle
             D_Upper_right_ventricle
             D_Conoventricular_sulcus
             D_Proximal_outflow_tract
             D_Distal_outflow_tract D_Arterial_outlet];
```

```
relative_cardiac_jelly = [0.7 0.9 0.8 0.7 0.9 0.9 1 1 1
                          1.35 1.3 1.1 1.1] * (h_cj
                          /(D_Central_right_ventricle/2));
x = tubelength/N; %m % The length of a section of the tube

% The major and minor axis of the model
l_array = 0:10^(-6):tubelength;
for d=1:length(diameters)-1
    coef = polyfit(lengths(d:d+1),diameters(d:d+1)/2,1);
    a_array((10^6*lengths(d)+1):(10^6*lengths(d+1)+1)) =
       polyval(coef,l_array((10^6*lengths(d)+1)
       :(10^6*lengths(d+1)+1)));
    coef = polyfit(lengths(d:d+1),(diameters(d:d+1)/2)
         .*(1-relative_cardiac_jelly(d:d+1)),1);
    b_array((10^6*lengths(d)+1):(10^6*lengths(d+1)+1)) =
       polyval(coef,l_array((10^6*lengths(d)+1)
       :(10^6*lengths(d+1)+1)));
end

for n=1:N
    index = uint16(((n-1)*x+x/2)*10^6);
    A(n) = a_array(index); %m % The major axis at rest
    B(n) = b_array(index); %m % The minor axis at rest
end
a(1:N) = A(1:N); %m % The dynamic major axis of the tube
b(1:N) = B(1:N); %m % The dynamic minor axis of the tube

% Curvature
R_B(1:N) = 500e-6; %m % The radius of curvature
startindex = find(x*(1:N)>L_Sinus_venosis,1,'first');
endindex = find(x*(1:N)>L_Sinus_venosis+L_Primitive_atrium
         + L_Left_ventricle+L_Right_ventricle+(1/4)
         * L_Proximal_outflow_tract,1,'first');
theta(1:N) = 0; %deg. % The bending angle for each section
theta(startindex:endindex) = (x./(2.*pi
                        .* R_B(startindex:endindex))).*360;

%% Boundary conditions
P_0 = 26.7; %Pa % The mean pressure at the venous end
L_c = 6.52e8; %kg/m4 % Inertance of the vascular system
R_c = 3.55e11; %Pa.s/m3 % Characteristic resistance
R_p = 9.62e11; %Pa.s/m3 % Peripheral resistance
C_p = 0.36e-12; %m3/Pa % Capacitance of the vascular system
```

```
V_0 = P_0*C_p; %m3 % Equilibrium vascular system volume
V = V_0; %m3 % The dynamical volume of the vascular system
M = 0; %Pa.s % The momentum through the vascular system

%% Parameter estimation

% The physical parameters of the heart tube and the blood
rho = 1.0e3; %kg/m3 % The density of embryonic blood
eta = 3.8e-3; %Pa.s % The viscosity of embryonic blood
E_my = 66.6; %Pa % Young's modulus for the myocardial layer
E_cj = 18; %Pa % Young's modulus for the cardiac jelly
E_en = E_my; %Pa % Young's modulus for the endocardial layer

%% The pumping mechanism

p(1:N) = 0; %kg*m/s % The initial momentum of the flow

T_prox_contraction = 123.7e-3; %s % Proximal contraction
T_dist_contraction = 168.6e-3; %s % Distal contraction
T_prox_relaxation = 193.0e-3; %s % Proximal relaxation
T_dist_relaxation = 245.5e-3; %s % Distal relaxation
Wave_velocity = 4.2e-3; %m/s % Contraction wave velocity
Diametric_contraction = 0.25; % Diametric contraction ratio

% Tracing of the contraction functions
% Given by: X(t) = 1 - a*sin(pi*b*(1-exp(-c*time)))
IFT_con = [0.4287 1.3480 0.001015];
Vent_con = [0.3329 1.0635 0.001418];
OFT_con = [0.3072 6.6597 0.00006598];

IFT_con(1) = (Diametric_contraction/Vent_con(1))
           * IFT_con(1);
OFT_con(1) = (Diametric_contraction/Vent_con(1))
           * OFT_con(1);
Vent_con(1) = (Diametric_contraction/Vent_con(1))
            * Vent_con(1);
IFT_con(3) = -log((Vent_con(2)-1)/Vent_con(2))
           / (T_prox_contraction+T_prox_relaxation)
           * (IFT_con(3)/Vent_con(3));
Vent_con(3) = -log((Vent_con(2)-1)/Vent_con(2))
            / (T_prox_contraction+T_prox_relaxation);
OFT_con(3) = -log((OFT_con(2)-1)/OFT_con(2))
           / (T_dist_contraction+T_dist_relaxation);
```

```
% Defining the contraction durations
IFT_time = (-1/IFT_con(3))*log((IFT_con(2)-1)/IFT_con(2));
Vent_time = (-1/Vent_con(3))
          * log((Vent_con(2)-1)/Vent_con(2));
OFT_time = (-1/OFT_con(3))*log((OFT_con(2)-1)/OFT_con(2));
Pumptimes = [IFT_time Vent_time OFT_time];

% Defining the contraction zones
IFT_section = find(x*(1:N)>L_Sinus_venosis,1,'first');
Vent_section = find(x*(1:N)>L_Sinus_venosis
             + L_Primitive_atrium,1,'first');
OFT_section = find(x*(1:N)>L_Sinus_venosis
            + L_Primitive_atrium+L_Left_ventricle
            + L_Right_ventricle,1,'first');
End_section = find(x*(1:N)>L_Sinus_venosis
            + L_Primitive_atrium+L_Left_ventricle
            + L_Right_ventricle
            + (2/3)*L_Proximal_outflow_tract,1,'first');
Pumpsections = [IFT_section Vent_section
                OFT_section End_section];

% Defining the phase shift between sections
delay = x/Wave_velocity;
```

The rest of the hh12 master program is similar to the master program for the stage 10 embryo and thus it will not be repeated here.

The hh14 master program

```
% hh14.m
% A model for blood flow of a HH-stage 14 embryonic heart.
% The flow model is based on the embedded tube model.

function hh14
%% Initialization of the model
global N x A B; % The dimensions of the tubular heart
global C_sn C_vn C_r C_j L C_sa Z_sa L_c R_c R_p C_p;
global P_0 eta f_B f IFT_con Vent_con OFT_con;
global Pumpsections Pumptimes delay;
a = 0; b = 0; p = 0; P = 0; Q = 0;

N = 45; % The number of sections in the model
% Acceptable numbers = [1 3 5 9 15 19 45 57 95 171]

f = 1.8; %Hz % The frequency of the pump
% Frequencies measured = [1.70 1.90 1.93 1.97];

periods = 3; % The number of periods in the simulation
time = periods * 1/f; %seconds % The time of the simulation

%% Tracing of the heart loop

% Lengths
L_Sinus_venosis = 170e-6; %m
L_Primitive_atrium = 230e-6; %m
L_Left_ventricle = 480e-6; %m
L_Right_ventricle = 500e-6; %m
L_Proximal_outflow_tract = 230e-6; %m
L_Distal_outflow_tract = 100e-6; %m

% Diameters
D_Sinus_venosis = 450e-6; %m
D_Venous_pole = 250e-6; %m
D_Central_atrium = 270e-6; %m
D_Upper_atrium = 270e-6; %m
D_Atrioventricular_canal = 250e-6; %m
D_lower_left_ventricle = 280e-6; %m
D_Central_left_ventricle = 350e-6; %m
D_Upper_left_ventricle = 330e-6; %m
D_Left_lateral_furrow = 320e-6; %m
```

```
D_Lower_right_ventricle = 330e-6; %m
D_Central_right_ventricle = 320e-6; %m
D_Upper_right_ventricle = 250e-6; %m
D_Conoventricular_sulcus = 200e-6; %m
D_Proximal_outflow_tract = 200e-6; %m
D_Distal_outflow_tract = 180e-6; %m
D_Arterial_outlet = 130e-6; %m

% Layers
h_my = 18e-6; %m % The thickness of the myocardial layer
h_cj = 85e-6; %m % The thickness of the cardiac jelly
h_en = h_my/2; %m % The thickness of the endocardial layer

% Dimension setup
tubelength = L_Sinus_venosis+L_Primitive_atrium
           + L_Left_ventricle+L_Right_ventricle
           + L_Proximal_outflow_tract
           + L_Distal_outflow_tract;
lengths = [0 L_Sinus_venosis/2 L_Sinus_venosis
           L_Sinus_venosis+4*L_Primitive_atrium/10
           L_Sinus_venosis+7*L_Primitive_atrium/10
           L_Sinus_venosis+L_Primitive_atrium
           L_Sinus_venosis+L_Primitive_atrium
           +L_Left_ventricle/4 L_Sinus_venosis
           +L_Primitive_atrium+L_Left_ventricle/2
           L_Sinus_venosis+L_Primitive_atrium
           +3*L_Left_ventricle/4 L_Sinus_venosis
           +L_Primitive_atrium+L_Left_ventricle
           L_Sinus_venosis+L_Primitive_atrium
           +L_Left_ventricle+L_Right_ventricle/4
           L_Sinus_venosis+L_Primitive_atrium
           +L_Left_ventricle+L_Right_ventricle/2
           L_Sinus_venosis+L_Primitive_atrium
           +L_Left_ventricle+3*L_Right_ventricle/4
           L_Sinus_venosis+L_Primitive_atrium
           +L_Left_ventricle+L_Right_ventricle
           L_Sinus_venosis+L_Primitive_atrium
           +L_Left_ventricle+L_Right_ventricle
           +L_Proximal_outflow_tract/2 L_Sinus_venosis
           +L_Primitive_atrium+L_Left_ventricle
           +L_Right_ventricle+L_Proximal_outflow_tract
           +L_Distal_outflow_tract/2 tubelength];
```

```
diameters = [D_Sinus_venosis D_Sinus_venosis D_Venous_pole
             D_Central_atrium D_Upper_atrium
             D_Atrioventricular_canal
             D_lower_left_ventricle
             D_Central_left_ventricle D_Upper_left_ventricle
             D_Left_lateral_furrow D_Lower_right_ventricle
             D_Central_right_ventricle
             D_Upper_right_ventricle
             D_Conoventricular_sulcus
             D_Proximal_outflow_tract
             D_Distal_outflow_tract D_Arterial_outlet];
relative_cardiac_jelly = [0.7 0.9 1 0.9 0.9 0.97 1 1 1
                          1 1 1 1.2 1.2 1.1 1 0.8] * (h_cj
                          /(D_Central_right_ventricle/2));
x = tubelength/N; %m % The length of a section of the tube

% The major and minor axis of the model
l_array = 0:10^(-6):tubelength;
for d=1:length(diameters)-1
    coef = polyfit(lengths(d:d+1),diameters(d:d+1)/2,1);
    a_array((10^6*lengths(d)+1):(10^6*lengths(d+1)+1)) =
       polyval(coef,l_array((10^6*lengths(d)+1)
       :(10^6*lengths(d+1)+1)));
    coef = polyfit(lengths(d:d+1),(diameters(d:d+1)/2)
         .*(1-relative_cardiac_jelly(d:d+1)),1);
    b_array((10^6*lengths(d)+1):(10^6*lengths(d+1)+1)) =
       polyval(coef,l_array((10^6*lengths(d)+1)
       :(10^6*lengths(d+1)+1)));
end
for n=1:N
    index = uint16(((n-1)*x+x/2)*10^6);
    A(n) = a_array(index); %m % The major axis at rest
    B(n) = b_array(index); %m % The minor axis at rest
end
a(1:N) = A(1:N); %m % The dynamic major axis of the tube
b(1:N) = B(1:N); %m % The dynamic minor axis of the tube

% Curvature
R_B(1:N) = 550e-6; %m % The radius of curvature
startindex = find(x*(1:N)>L_Sinus_venosis,1,'first');
endindex = find(x*(1:N)>L_Sinus_venosis+L_Primitive_atrium
         + L_Left_ventricle+L_Right_ventricle
         + L_Proximal_outflow_tract,1,'first');
```

```
theta(1:N) = 0; %deg. % The bending angle for each section
theta(startindex:endindex) = (x./(2.*pi
                        .* R_B(startindex:endindex))).*360;

%% Boundary conditions

P_0 = 26.7; %Pa % The mean pressure at the venous end
L_c = 1.38e8; %kg/m4 % Inertance of the vascular system
R_c = 0.86e11; %Pa.s/m3 % Characteristic resistance
R_p = 3.51e11; %Pa.s/m3 % Peripheral resistance
C_p = 1.39e-12; %m3/Pa % Capacitance of the vascular system

V_0 = P_0*C_p; %m3 % Equilibrium vascular system volume
V = V_0; %m3 % The dynamical volume of the vascular system
M = 0; %Pa.s % The momentum through the vascular system

%% Parameter estimation

% The physical parameters of the heart tube and the blood
rho = 1.0e3; %kg/m3 % The density of embryonic blood
eta = 3.8e-3; %Pa.s % The viscosity of embryonic blood
E_my = 93.3; %Pa % Young's modulus for the myocardial layer
E_cj = 39; %Pa % Young's modulus for the cardiac jelly
E_en = E_my; %Pa % Young's modulus for the endocardial layer

%% The pumping mechanism

p(1:N) = 0; %kg*m/s % The initial momentum of the flow

T_prox_contraction = 88.8e-3; %s % Proximal contraction
T_dist_contraction = 150.1e-3; %s % Distal contraction
T_prox_relaxation = 144.5e-3; %s % Proximal relaxation
T_dist_relaxation = 145.5e-3; %s % Distal relaxation
Wave_velocity = 9.4e-3; %m/s % Contraction wave velocity
Diametric_contraction = 0.263; % Diametric contraction ratio

% Tracing of the contraction functions
% Given by: X(t) = 1 - a*sin(pi*b*(1-exp(-c*time)))
IFT_con = [0.4287 1.3480 0.001015];
Vent_con = [0.3329 1.0635 0.001418];
OFT_con = [0.3072 6.6597 0.00006598];
```

```
IFT_con(1) = (Diametric_contraction/Vent_con(1))
           * IFT_con(1);
OFT_con(1) = (Diametric_contraction/Vent_con(1))
           * OFT_con(1);
Vent_con(1) = (Diametric_contraction/Vent_con(1))
            * Vent_con(1);

IFT_con(3) = -log((Vent_con(2)-1)/Vent_con(2))
           / (T_prox_contraction+T_prox_relaxation)
           * (IFT_con(3)/Vent_con(3));
Vent_con(3) = -log((Vent_con(2)-1)/Vent_con(2))
            / (T_prox_contraction+T_prox_relaxation);
OFT_con(3) = -log((OFT_con(2)-1)/OFT_con(2))
           / (T_dist_contraction+T_dist_relaxation);

% Defining the contraction durations
IFT_time = (-1/IFT_con(3))*log((IFT_con(2)-1)/IFT_con(2));
Vent_time = (-1/Vent_con(3))
          * log((Vent_con(2)-1)/Vent_con(2));
OFT_time = (-1/OFT_con(3))*log((OFT_con(2)-1)/OFT_con(2));
Pumptimes = [IFT_time Vent_time OFT_time];

% Defining the contraction zones
IFT_section = find(x*(1:N)>L_Sinus_venosis,1,'first');
Vent_section = find(x*(1:N)>L_Sinus_venosis
             + L_Primitive_atrium,1,'first');
OFT_section = find(x*(1:N)>L_Sinus_venosis
            + L_Primitive_atrium+L_Left_ventricle
            + L_Right_ventricle,1,'first');
End_section = find(x*(1:N)>L_Sinus_venosis
            + L_Primitive_atrium+L_Left_ventricle
            + L_Right_ventricle+L_Proximal_outflow_tract
            +(1/2)*L_Distal_outflow_tract,1,'first');
Pumpsections = [IFT_section Vent_section
                OFT_section End_section];

% Defining the phase shift between sections
delay = x/Wave_velocity;
```

The rest of the hh14 master program is similar to the master program for the stage 10 embryo and thus it will not be repeated here.

The hh16 master program

```
% hh16.m
% A model for blood flow of a HH-stage 16 embryonic heart.
% The flow model is based on the embedded tube model.

function hh16

%% Initialization of the model
global N x A B; % The dimensions of the tubular heart
global C_sn C_vn C_r C_j L C_sa Z_sa L_c R_c R_p C_p;
global P_0 eta f_B f IFT_con Vent_con OFT_con;
global Pumpsections Pumptimes delay;
a = 0; b = 0; p = 0; P = 0; Q = 0;

N = 30; % The number of sections in the model
% Acceptable numbers = [1 2 3 5 6 9 10 13 15 18 26 30 39
                        45 65 78 90 117 130]

f = 2.0; %Hz % The frequency of the pump
% Frequencies measured = [1.76 2.00 2.03];

periods = 3; % The number of periods in the simulation
time = periods * 1/f; %seconds % The time of the simulation

%% Tracing of the heart loop
% Lengths
L_Sinus_venosis = 230e-6; %m
L_Primitive_atrium = 470e-6; %m
L_Left_ventricle = 700e-6; %m
L_Right_ventricle = 500e-6; %m
L_Proximal_outflow_tract = 270e-6; %m
L_Distal_outflow_tract = 170e-6; %m

% Diameters
D_Sinus_venosis = 470e-6; %m
D_Venous_pole = 370e-6; %m
D_Central_atrium = 370e-6; %m
D_Upper_atrium = 350e-6; %m
D_Atrioventricular_canal = 330e-6; %m
D_lower_left_ventricle = 380e-6; %m
D_Central_left_ventricle = 470e-6; %m
D_Upper_left_ventricle = 400e-6; %m
```

```
D_Left_lateral_furrow = 350e-6; %m
D_Lower_right_ventricle = 350e-6; %m
D_Central_right_ventricle = 350e-6; %m
D_Upper_right_ventricle = 300e-6; %m
D_Conoventricular_sulcus = 270e-6; %m
D_Proximal_outflow_tract = 250e-6; %m
D_Distal_outflow_tract = 200e-6; %m
D_Arterial_outlet = 170e-6; %m

% Layers
h_my = 20e-6; %m % The thickness of the myocardial layer
h_cj = 85e-6; %m % The thickness of the cardiac jelly
h_en = h_my/2; %m % The thickness of the endocardial layer

% Dimension setup
tubelength = L_Sinus_venosis+L_Primitive_atrium
           + L_Left_ventricle+L_Right_ventricle
           + L_Proximal_outflow_tract
           + L_Distal_outflow_tract;
lengths = [0 L_Sinus_venosis/2 L_Sinus_venosis
           L_Sinus_venosis+4*L_Primitive_atrium/10
           L_Sinus_venosis+7*L_Primitive_atrium/10
           L_Sinus_venosis+L_Primitive_atrium
           L_Sinus_venosis+L_Primitive_atrium
           +L_Left_ventricle/4 L_Sinus_venosis
           +L_Primitive_atrium+L_Left_ventricle/2
           L_Sinus_venosis+L_Primitive_atrium
           +3*L_Left_ventricle/4 L_Sinus_venosis
           +L_Primitive_atrium+L_Left_ventricle
           L_Sinus_venosis+L_Primitive_atrium
           +L_Left_ventricle+L_Right_ventricle/4
           L_Sinus_venosis+L_Primitive_atrium
           +L_Left_ventricle+L_Right_ventricle/2
           L_Sinus_venosis+L_Primitive_atrium
           +L_Left_ventricle+3*L_Right_ventricle/4
           L_Sinus_venosis+L_Primitive_atrium
           +L_Left_ventricle+L_Right_ventricle
           L_Sinus_venosis+L_Primitive_atrium
           +L_Left_ventricle+L_Right_ventricle
           +L_Proximal_outflow_tract/2 L_Sinus_venosis
           +L_Primitive_atrium+L_Left_ventricle
           +L_Right_ventricle+L_Proximal_outflow_tract
           +L_Distal_outflow_tract/2 tubelength];
```

```
diameters = [D_Sinus_venosis D_Sinus_venosis D_Venous_pole
             D_Central_atrium D_Upper_atrium
             D_Atrioventricular_canal
             D_lower_left_ventricle
             D_Central_left_ventricle
             D_Upper_left_ventricle
             D_Left_lateral_furrow D_Lower_right_ventricle
             D_Central_right_ventricle
             D_Upper_right_ventricle
             D_Conoventricular_sulcus
             D_Proximal_outflow_tract
             D_Distal_outflow_tract D_Arterial_outlet];
relative_cardiac_jelly = [0.7 0.9 1 0.9 0.9 1 0.8 0.75 0.8
                          1 0.95 1 1.1 1.4 1.3 1.1 1]*(h_cj
                          /(D_Central_right_ventricle/2));
x = tubelength/N; %m % The length of a section of the tube

% The major and minor axis of the model
l_array = 0:10^(-6):tubelength;
for d=1:length(diameters)-1
    coef = polyfit(lengths(d:d+1),diameters(d:d+1)/2,1);
    a_array((10^6*lengths(d)+1):(10^6*lengths(d+1)+1)) =
       polyval(coef,l_array((10^6*lengths(d)+1)
       :(10^6*lengths(d+1)+1)));
    coef = polyfit(lengths(d:d+1),(diameters(d:d+1)/2)
         .*(1-relative_cardiac_jelly(d:d+1)),1);
    b_array((10^6*lengths(d)+1):(10^6*lengths(d+1)+1)) =
       polyval(coef,l_array((10^6*lengths(d)+1)
       :(10^6*lengths(d+1)+1)));
end
for n=1:N
    index = uint16(((n-1)*x+x/2)*10^6);
    A(n) = a_array(index); %m % The major axis at rest
    B(n) = b_array(index); %m % The minor axis at rest
end
a(1:N) = A(1:N); %m % The dynamic major axis of the tube
b(1:N) = B(1:N); %m % The dynamic minor axis of the tube

% Curvature
R_B(1:N) = 600e-6; %m % The radius of curvature
startindex = find(x*(1:N)>L_Sinus_venosis,1,'first');
endindex = find(x*(1:N)>L_Sinus_venosis+L_Primitive_atrium
         + L_Left_ventricle+L_Right_ventricle
```

```
          + L_Proximal_outflow_tract
          + (1/4)*L_Distal_outflow_tract,1,'first');
theta(1:N) = 0; %deg. % The bending angle for each section
theta(startindex:endindex) = (x./(2.*pi
                        .* R_B(startindex:endindex))).*360;

%% Boundary conditions

P_0 = 26.7; %Pa % The mean pressure at the venous end
L_c = 0.75e8; %kg/m4 % Inertance of the vascular system
R_c = 0.51e11; %Pa.s/m3 % Characteristic resistance
R_p = 1.87e11; %Pa.s/m3 % Peripheral resistance
C_p = 2.21e-12; %m3/Pa % Capacitance of the vascular system
V_0 = P_0*C_p; %m3 % Equilibrium vascular system volume
V = V_0; %m3 % The dynamical volume of the vascular system
M = 0; %Pa.s % The momentum through the vascular system

%% Parameter estimation

% The physical parameters of the heart tube and the blood
rho = 1.0e3; %kg/m3 % The density of embryonic blood
eta = 3.8e-3; %Pa.s % The viscosity of embryonic blood
E_my = 120; %Pa % Young's modulus for the myocardial layer
E_cj = 60; %Pa % Young's modulus for the cardiac jelly
E_en = E_my; %Pa % Young's modulus for the endocardial layer

%% The pumping mechanism

p(1:N) = 0; %kg*m/s % The initial momentum of the flow
T_prox_contraction = 109.6e-3; %s % Proximal contraction
T_dist_contraction = 154.1e-3; %s % Distal contraction
T_prox_relaxation = 169.2e-3; %s % Proximal relaxation
T_dist_relaxation = 156.0e-3; %s % Distal relaxation
T_atrium_contraction = 140.0e-3; %s %Atrial contraction
Wave_velocity = 9.4e-3; %m/s % Contraction wave velocity
Diametric_contraction = 0.244; % Diametric contraction ratio
Diametric_contraction_atrium = 0.338; % Atrial contraction

% Tracing of the contraction functions
% Given by: X(t) = 1 - a*sin(pi*b*(1-exp(-c*time)))
IFT_con = [0.4287 1.3480 0.001015];
Vent_con = [0.3329 1.0635 0.001418];
OFT_con = [0.3072 6.6597 0.00006598];
```

```
IFT_con(1) = (Diametric_contraction/Vent_con(1))
           * IFT_con(1);
OFT_con(1) = (Diametric_contraction/Vent_con(1))
           * OFT_con(1);
Vent_con(1) = (Diametric_contraction/Vent_con(1))
            * Vent_con(1);

IFT_con(3) = -log((Vent_con(2)-1)/Vent_con(2))
           / (T_prox_contraction+T_prox_relaxation)
           * (IFT_con(3)/Vent_con(3));
Vent_con(3) = -log((Vent_con(2)-1)/Vent_con(2))
            / (T_prox_contraction+T_prox_relaxation);
OFT_con(3) = -log((OFT_con(2)-1)/OFT_con(2))
           / (T_dist_contraction+T_dist_relaxation);

% Defining the contraction durations
IFT_time = (-1/IFT_con(3))*log((IFT_con(2)-1)/IFT_con(2));
Vent_time = (-1/Vent_con(3))
          * log((Vent_con(2)-1)/Vent_con(2));
OFT_time = (-1/OFT_con(3))*log((OFT_con(2)-1)/OFT_con(2));
Pumptimes = [IFT_time Vent_time OFT_time];

% Defining the contraction zones
IFT_section = find(x*(1:N)>L_Sinus_venosis,1,'first');
Vent_section = find(x*(1:N)>L_Sinus_venosis
             + L_Primitive_atrium,1,'first');
OFT_section = find(x*(1:N)>L_Sinus_venosis
            + L_Primitive_atrium+L_Left_ventricle
            + L_Right_ventricle,1,'first');
End_section = find(x*(1:N)>L_Sinus_venosis
            + L_Primitive_atrium+L_Left_ventricle
            + L_Right_ventricle+L_Proximal_outflow_tract
            +(2/3)*L_Distal_outflow_tract,1,'first');
Pumpsections = [IFT_section Vent_section
                OFT_section End_section];

% Defining the phase shift between sections
delay = x/Wave_velocity;
```

The rest of the hh16 master program is similar to the master program for the stage 10 embryo and thus it will not be repeated here.

Appendix C

Simulation Code for the Elliptic Liebau's Ring

For the simulations of Liebau's ring with the elliptic and the embedded models two separate program rutines are used. Both follow the principles explained in appendix A. The iterative and master program of the tube with elliptic cross-section is presented first, followed by the iterative and master program of the layered tube model.

The iterative elliptic program

```
% rkeliebau.m
% Runge-Kutta iteration of the elliptic flow model.

function output = rkeliebau(t,z)

global N f x A B S eta f_B C_sn C_vn L C_s Z_s;
global psection plength delay Comp;

% Defining radii and momentum from the input vector
a = (z(1:N-plength))';
b = (z(N-plength+1:2*(N-plength)))';
p = (z(2*(N-plength)+1:end))';

% The piston pump
a(psection+plength:N) = a(psection:N-plength);
b(psection+plength:N) = b(psection:N-plength);
```

```
a_max = A(psection:psection+plength-1) .* (1
      + sqrt(Comp.*(sin((pi/(plength+1)).*[1:plength]))));
b_min = B(psection:psection+plength-1) .* (1
      - sqrt(Comp.*(sin((pi/(plength+1)).*[1:plength]))));
for pump=1:plength
    a(psection+pump-1) = A(psection+pump-1);
    b(psection+pump-1) = B(psection+pump-1);
    a(psection+pump-1) = A(psection+pump-1)
                       + (a_max(pump)-A(psection+pump-1))
                       .* sin(pi*f/0.1 .* (t-delay*(pump-1)))
                       .* (0<=mod(t-delay*(pump-1),1/f))
                       .* ((0.1/f)>=mod(t-delay*(pump-1),1/f))
                       .* sin((pi/(plength+1)).*pump);
    b(psection+pump-1) = B(psection+pump-1)
                       - (B(psection+pump-1)-b_min(pump))
                       .* sin(pi*f/0.1 .* (t-delay*(pump-1)))
                       .* (0<=mod(t-delay*(pump-1),1/f))
                       .* ((0.1/f)>=mod(t-delay*(pump-1),1/f))
                       .* sin((pi/(plength+1)).*pump);
end

% Calculation of the elliptic integrals
ecc = sqrt(1 - (min(a,b)./max(a,b)).^2); % Eccentricity
first = (pi/2) .* ( 1 + (1/2)^2*ecc.^2 + (3/8)^2*ecc.^4
      + (15/48)^2*ecc.^6 + (105/384)^2*ecc.^8 );
second = (pi/2) .* ( 1 - (1/2)^2*ecc.^2
       - (1/3)*(3/8)^2*ecc.^4 - (1/5)*(15/48)^2*ecc.^6
       + (1/7)*(105/384)^2*ecc.^8 );

% Calculation of the surface derivatives
dsda = (a>b).*(x.*(4./((a~=b).*a.^2-b.^2))
     .* (a.^2.*second-b.^2.*first)) + (a==b).*x.*pi + (a<b)
     .* ((4.*b.*a./((a<b).*b.^2-a.^2)).*(first-second));
dsdb = (a>b).*(x.*(4.*a.*b./((a~=b).*a.^2-b.^2))
     .* (first-second)) + (a==b).*x.*pi
     + (a<b).*(x.* (4./((a<b).*b.^2-a.^2))
     .* (b.^2.*second-a.^2.*first));

% Calculation of the chi factor
chi = ((1./b).*dsda.*dsdb-(1./a).*dsdb.^2-(2./3).*(S.^2)
    .* (((2.*a.*b)./(a.^2+b.^2)).^2).*(1./(a.*b.^2)))
    ./ ((1./a).*dsda.*dsdb-(1./b).*dsda.^2-(2./3).*(S.^2)
    .* (((2.*a.*b)./(a.^2+b.^2)).^2).*(1./(a.^2.*b)));
```

```
% Calculation of the flow
Q(1:N-1) = (p(1:N-1)./L(1:N-1))
         .* sqrt((sqrt(a(1:N-1).*a(2:N))
         .* sqrt(b(1:N-1).*b(2:N)))
         ./ (sqrt(A(1:N-1).*A(2:N))
         .* sqrt(B(1:N-1).*B(2:N))));
Q(N) = (p(N)/L(N)) * sqrt((sqrt(a(N)*a(1))*sqrt(b(N)*b(1)))
     / (sqrt(A(N)*A(1))*sqrt(B(N)*B(1))));

% Equations for the rate of change of the axes
da(1) = (Q(N)-Q(1))/(pi*x).*(chi(1)./(a(1)+chi(1).*b(1)));
db(1) = (Q(N)-Q(1))/(pi*x).*(1./(a(1)+chi(1).*b(1)));
da(2:N) = (Q(1:N-1)-Q(2:N))/(pi*x)
        .* (chi(2:N)./(a(2:N)+chi(2:N).*b(2:N)));
db(2:N) = (Q(1:N-1)-Q(2:N))/(pi*x)
        .* (1./(a(2:N)+chi(2:N).*b(2:N)));

% Equations for the dynamic pressure
P(1) = (1/(pi*x*b(1))) * ( dsda(1)*(dsda(1)*(a(1)-A(1))
     / C_sn(1) + dsdb(1)*(b(1)-B(1))/C_sn(1))
     + ((2*a(1)*b(1))/(a(1)^2+b(1)^2))*(1/a(1))
     * tan(((2*a(1)*b(1))/(a(1)^2+b(1)^2))*((1/a(1))
     * (a(1)-A(1))/C_vn(1)-(1/b(1))*(b(1)-B(1))/C_vn(1)))
     + ((a(1)-A(1))-(a(N)-A(N)))/C_s(N) + Z_s(N)
     * (da(1)-da(N)) - ((a(2)-A(2))-(a(1)-A(1)))/C_s(1)
     - Z_s(1)*(da(2)-da(1)) + (p(N)^2)/(4*a(1)*L(N))
     + (p(1)^2)/(4*a(1)*L(1)) );
P(2:N-1) = (1./(pi.*x.*b(2:N-1))) .* ( dsda(2:N-1)
         .* (dsda(2:N-1).*(a(2:N-1)-A(2:N-1))./C_sn(2:N-1)
         + dsdb(2:N-1).*(b(2:N-1)-B(2:N-1))./C_sn(2:N-1))
         + ((2.*a(2:N-1).*b(2:N-1))./(a(2:N-1).^2
         + b(2:N-1).^2)).*(1./a(2:N-1)).*tan(((2.*a(2:N-1)
         .* b(2:N-1))./(a(2:N-1).^2+b(2:N-1).^2))
         .* ((1./a(2:N-1)).*(a(2:N-1)-A(2:N-1))
         ./ C_vn(2:N-1)-(1./b(2:N-1)).*(b(2:N-1)-B(2:N-1))
         ./ C_vn(2:N-1))) + ((a(2:N-1)-A(2:N-1))-(a(1:N-2)
         - A(1:N-2)))./C_s(1:N-2) + Z_s(1:N-2).*(da(2:N-1)
         - da(1:N-2)) - ((a(3:N)-A(3:N))-(a(2:N-1)
         - A(2:N-1)))./C_s(2:N-1) - Z_s(2:N-1).*(da(3:N)
         - da(2:N-1)) + (p(1:N-2).^2)./(4.*a(2:N-1)
         .* L(1:N-2)) + (p(2:N-1).^2)./(4.*a(2:N-1)
         .* L(2:N-1)) );
```

```
P(N) = (1/(pi*x*b(N))) * ( dsda(N)*(dsda(N)*(a(N)-A(N))
     / C_sn(N) + dsdb(N)*(b(N)-B(N))/C_sn(N)) + ((2*a(N)
     * b(N))/(a(N)^2+b(N)^2))*(1/a(N))*tan(((2*a(N)*b(N))
     / (a(N)^2+b(N)^2))*((1/a(N))*(a(N)-A(N))/C_vn(N)
     - (1/b(N))*(b(N)-B(N))/C_vn(N))) + ((a(N)-A(N))
     - (a(N-1)-A(N-1)))/C_s(N-1) + Z_s(N-1)*(da(N)-da(N-1))
     - ((a(1)-A(1))-(a(N)-A(N)))/C_s(N) - Z_s(N)*(da(1)
     - da(N)) + (p(N-1)^2)/(4*a(N)*L(N-1)) + (p(N)^2)
     / (4*a(N)*L(N)) );

% Equations for the rate of change of the momentum
dp(1) = sqrt(sqrt(a(1)*a(2))*sqrt(b(1)*b(2))/(sqrt(A(1)
      * A(2))*sqrt(B(1)*B(2)))) * ( P(1) - P(2)
      - ( (4*eta*x*(a(1)*a(2)+ b(1)*b(2)))/(sqrt(a(1)
      * a(2))^3*sqrt(b(1)*b(2))^3) + (f_B(1)*(1/(4*pi))
      * sqrt(sqrt(A(1)*A(2)*B(1)*B(2))/(sqrt(a(1)*a(2))^5
      * sqrt(b(1)*b(2))^5))*sqrt((a(1)*a(2)+b(1)*b(2))/2)
      * sign(p(1))*p(1)) ) * Q(1) ) + (p(1)/(4*a(1)))*da(1)
      + (p(1)/(4*a(2)))*da(2) + (p(1)/(4*b(1)))*db(1)
      + (p(1)/(4*b(2)))*db(2);
dp(2:N-1) = sqrt(sqrt(a(2:N-1).*a(3:N)).*sqrt(b(2:N-1)
          .* b(3:N))./(sqrt(A(2:N-1).*A(3:N))
          .* sqrt(B(2:N-1).*B(3:N)))).*( P(2:N-1) - P(3:N)
          - ( (4.*eta.*x.*(a(2:N-1).*a(3:N)+b(2:N-1)
          .* b(3:N))).*(sqrt(a(2:N-1).*a(3:N)).^3
          .* sqrt(b(2:N-1).*b(3:N)).^3) + (f_B(2:N-1).*(1
          ./ (4.*pi)).*sqrt(sqrt(A(2:N-1).*A(3:N).*B(2:N-1)
          .* B(3:N))./(sqrt(a(2:N-1).*a(3:N)).^5
          .* sqrt(b(2:N-1).*b(3:N)).^5)).*sqrt((a(2:N-1)
          .* a(3:N)+b(2:N-1).*b(3:N))./2).*sign(p(2:N-1))
          .* p(2:N-1)) ) .* Q(2:N-1) ) + (p(2:N-1)./(4
          .* a(2:N-1))).*da(2:N-1) + (p(2:N-1)./(4
          .* a(3:N))).*da(3:N) + (p(2:N-1)./(4.*b(2:N-1)))
          .* db(2:N-1) + (p(2:N-1)./(4.*b(3:N))).*db(3:N);
dp(N) = sqrt(sqrt(a(N)*a(1))*sqrt(b(N)*b(1))/(sqrt(A(N)
      * A(1))*sqrt(B(N)*B(1)))) * ( P(N) - P(1) - ( (4*eta
      * x*(a(N)*a(1)+b(N)*b(1)))/(sqrt(a(N)*a(1))^3
      * sqrt(b(N)*b(1))^3) + (f_B(N)*(1/(4*pi))
      * sqrt(sqrt(A(N)*A(1)*B(N)*B(1))/(sqrt(a(N)*a(1))^5
      * sqrt(b(N)*b(1))^5))*sqrt((a(N)*a(1)+b(N)*b(1))/2)
      * sign(p(N))*p(N)) ) * Q(N) ) + (p(N)/(4*a(N)))*da(N)
      + (p(N)/(4*a(1)))*da(1) + (p(N)/(4*b(N)))*db(N)
      + (p(N)/(4*b(1)))*db(1);
```

```
da = [da(1:psection-1) da(psection+plength:N)];
db = [db(1:psection-1) db(psection+plength:N)];

% The output to the main program
output = [da';db';dp'];
```

The master elliptic program

```
% eliebau.m
% A model for flow in tubes with elliptic cross-section.
% The model is used to simulate an elliptic Liebau's Ring.

function eliebau

% Initializing variables
global N f x A B S eta f_B C_sn C_vn L C_s Z_s;
global psection plength delay Comp;
a = 0; b = 0; p = 0; P = 0; Q = 0;

% The numbers we can change
N = 60; % The number of sections in the model
psection = 5; % The first section of the pump
plength = 3; % The number of sections of the pump
delay = 0; % The delay time for sequential pumping
Comp = 0.25; % The cross-sectional compression ratio
f = 2.06; %Hz % The frequency of the pump
periods = 50; % The number of periods in the simulation
time = periods * 1/f; %seconds % The time of the simulation

% The parameters of the tube at rest
l = 1.0; %m % The length of the tube
x = l/N; %m % Length per section
Eccentricity = 0.3; % Desired eccentricity of the ellipse
R1 = 0.01; %m The equivalent radius of the soft tube
R2 = 0.008; %m The equivalent radius of the rigid tube

A(1:N/2) = sqrt(R1^2 * (1/sqrt(1-Eccentricity^2))); %m
A(N/2+1:N) = sqrt(R2^2 * (1/sqrt(1-Eccentricity^2))); %m
B(1:N/2) = sqrt(R1^2 * sqrt(1-Eccentricity^2)); %m
B(N/2+1:N) = sqrt(R2^2 * sqrt(1-Eccentricity^2)); %m
a(1:N) = A(:); %m % The dynamic major axis of the tube
b(1:N) = B(:); %m % The dynamic minor axis of the tube
```

```
p(1:N) = 0; %kg*m/s % The initial momentum of the flow
R_B(1:N) = l/(2*pi); % The bend radius for each section
theta(1:N) = (x.*360)./(2.*pi.*R_B); %deg. % The bend angle
S(1:N) = x*pi*(A+B).*(1+3*((A-B)./(A+B)).^2
       ./ (10+sqrt(4-3*((A-B)./(A+B)).^2))); %m2

% The physical properties of the tube and the liquid
rho = 1000; %kg/m3 % The density of the liquid (water)
eta = 0.001; %Pa.s % The viscosity of the liquid (water)
P_0 = 1e5; %Pa % The pressure outside the tube
E1 = 4.1e5; %Pa % Young's modulus for the soft tube
E2 = 4.3e5; %Pa % Young's modulus for the stiff tube
h1 = 0.001; %m % The wall thickness of the soft tube
h2 = 0.003; %m % The wall thickness of the rigid tube

% Womersley theory
alpha(1:N-1) = sqrt((2.*A(1:N-1).*A(2:N).*B(1:N-1).*B(2:N))
             ./ (A(1:N-1).*A(2:N)+B(1:N-1).*B(2:N)))
             .* sqrt(2*pi*f*rho/eta);
alpha(N) = sqrt((2.*A(N).*A(1).*B(N).*B(1))./(A(N).*A(1)
         + B(N).*B(1))).*sqrt(2*pi*f*rho/eta);
psi = real(1 ./ (1 - 2./(alpha.*sqrt(-i))
    .* besselj(1,alpha.*sqrt(-i))
    ./ besselj(0,alpha.*sqrt(-i))) - 8./(i.*alpha.^2));

% Equations for the curvature of the tube
xi = 0.042 .* theta.^0.69; % Angle correction factor
l_c(1:N-1) = sqrt(2.*A(1:N-1).*A(2:N).*B(1:N-1).*B(2:N)
           ./ (A(1:N-1).*A(2:N)+B(1:N-1).*B(2:N)));
l_c(N) = sqrt(2.*A(N).*A(1).*B(N).*B(1)
       ./ (A(N).*A(1)+B(N).*B(1)));
K_B(1:N) = 9.0704.*(log(R_B(1:N)./(2.*l_c(1:N)))).^2
         - 16.9345.*(log(R_B(1:N)./(2.*l_c(1:N))))+19.6437;
f_T(1:N) = 0.0478.*(2.*l_c(1:N)).^(-0.2245);

% The calculation of the elements of the model
C_sn(1:N/2) = S(1:N/2)./(E1*h1); %m/Pa
C_sn(N/2+1:N) = S(N/2+1:N)./(E2*h2); %m/Pa
C_vn(1:N/2) = 1./(S(1:N/2).*(1/3).*(E1*h1)); %(Pa.m3)^-1
C_vn(N/2+1:N) = 1./(S(N/2+1:N).*(1/3).*(E2*h2));
L(1:N-1) = psi(1:N-1).*rho.*x./(pi.*sqrt(A(1:N-1)
         .* A(2:N).*B(1:N-1).*B(2:N))); %kg/m4
L(N) = psi(N)*rho*x./(pi.*sqrt(A(N).*A(1).*B(N).*B(1)));
```

```
C_s(1:N/2-1) = (x./((1/3)*(E1*h1))) .* 2./(pi
             .* (sqrt(A(1:N/2-1).*A(2:N/2))+sqrt(B(1:N/2-1)
             .* B(2:N/2))).*(1+3*((sqrt(A(1:N/2-1)
             .* A(2:N/2))-sqrt(B(1:N/2-1).*B(2:N/2)))
             ./ (sqrt(A(1:N/2-1).*A(2:N/2))+sqrt(B(1:N/2-1)
             .* B(2:N/2)))).^2./(10+sqrt(4
             - 3.*((sqrt(A(1:N/2-1).*A(2:N/2))
             - sqrt(B(1:N/2-1).*B(2:N/2)))
             ./ (sqrt(A(1:N/2-1).*A(2:N/2))+sqrt(B(1:N/2-1)
             .* B(2:N/2)))).^2)))); %(Pa.m)^-1
C_s(N/2) = ((x./((1/3)*sqrt(E1*h1*E2*h2))).*2./( pi
         .* (sqrt(A(N/2).*A(N/2+1))+sqrt(B(N/2).*B(N/2+1)))
         .* (1+3*((sqrt(A(N/2).*A(N/2+1))-sqrt(B(N/2)
         .* B(N/2+1))).^2./(10+sqrt(4-3.*((sqrt(A(N/2)
         .* A(N/2+1))-sqrt(B(N/2).*B(N/2+1))).^2)) ))
         + (x./((1/3)*(E2*h2))).* 2./( pi.*(sqrt(A(N/2)
         .* A(N/2+1))+sqrt(B(N/2).*B(N/2+1))).*(1
         + 3*((sqrt(A(N/2).*A(N/2+1))-sqrt(B(N/2)
         .* B(N/2+1))).^2./(10+sqrt(4-3.*((sqrt(A(N/2)
         .* A(N/2+1))-sqrt(B(N/2).*B(N/2+1))).^2)) )))/2;
C_s(N/2+1:N-1) = (x./((1/3)*(E2*h2))) .* 2./( pi
               .* (sqrt(A(N/2+1:N-1).*A(N/2+2:N))
               + sqrt(B(N/2+1:N-1).*B(N/2+2:N))).*(1
               + 3*((sqrt(A(N/2+1:N-1).*A(N/2+2:N))
               - sqrt(B(N/2+1:N-1).*B(N/2+2:N)))
               ./ (sqrt(A(N/2+1:N-1).*A(N/2+2:N))
               + sqrt(B(N/2+1:N-1).*B(N/2+2:N)))).^2./(10
               + sqrt(4-3.*((sqrt(A(N/2+1:N-1).*A(N/2+2:N))
               - sqrt(B(N/2+1:N-1).*B(N/2+2:N)))
               ./ (sqrt(A(N/2+1:N-1).*A(N/2+2:N))
               + sqrt(B(N/2+1:N-1).*B(N/2+2:N)))).^2)) ));
C_s(N) = ((x./((1/3)*sqrt(E1*h1*E2*h2))) .* 2./( pi
       .* (sqrt(A(N).*A(1))+sqrt(B(N).*B(1))).*(1
       + 3*((sqrt(A(N).*A(1))-sqrt(B(N).*B(1))).^2./(10+sqrt(4
       - 3.*((sqrt(A(N).*A(1))-sqrt(B(N).*B(1))).^2))))+(x./((1/3)*(E2
       * h2))) .* 2./( pi.*(sqrt(A(N).*A(1))
       + sqrt(B(N).*B(1))).*(1+3*((sqrt(A(N).*A(1))
```

```
       - sqrt(B(N).*B(1))./(sqrt(A(N).*A(1))+sqrt(B(N)
       .* B(1)))).^2./(10+sqrt(4-3.*((sqrt(A(N).*A(1))
       - sqrt(B(N).*B(1))./(sqrt(A(N).*A(1))
       + sqrt(B(N).*B(1)))).^2)) )))/2; %(Pa.m)^-1
Z_s(1:N) = 0.01./C_s; %Pa.m
f_B = xi.*K_B.*f_T./psi; % The friction factor

% Call MatLab's solver for ordinary differential equations
a = [a(1:psection-1) a(psection+plength:N)];
b = [b(1:psection-1) b(psection+plength:N)];
[t,z] = ode45('rkeliebau',[0 time],[a b p]);
a = z(:,1:N-plength); b = z(:,N-plength+1:2*(N-plength));
p = z(:,2*(N-plength)+1:end);

% The pressure actuator
a(1:length(t),psection+plength:N) =
      a(1:length(t),psection:N-plength);
b(1:length(t),psection+plength:N) =
      b(1:length(t),psection:N-plength);
a_max = A(psection:psection+plength-1) .* (1 + sqrt(Comp
      .* (sin((pi/(plength+1)).*[1:plength]))));
b_min = B(psection:psection+plength-1) .* (1 - sqrt(Comp
      .* (sin((pi/(plength+1)).*[1:plength]))));
for pump=1:plength
    a(1:length(t),psection+pump-1) = A(psection+pump-1);
    b(1:length(t),psection+pump-1) = B(psection+pump-1);
    a(1:length(t),psection+pump-1) = A(psection+pump-1)
                    + (a_max(pump)-A(psection+pump-1))
                    .* sin(pi*f/0.1 .* (t-delay*(pump-1)))
                    .* (0<=mod(t-delay*(pump-1),1/f))
                    .* ((0.1/f)>=mod(t-delay*(pump-1),1/f))
                    .* sin((pi/(plength+1)).*pump);
    b(1:length(t),psection+pump-1) = B(psection+pump-1)
                    - (B(psection+pump-1)-b_min(pump))
                    .* sin(pi*f/0.1 .* (t-delay*(pump-1)))
                    .* (0<=mod(t-delay*(pump-1),1/f))
                    .* ((0.1/f)>=mod(t-delay*(pump-1),1/f))
                    .* sin((pi/(plength+1)).*pump);
end
```

```
% Calculation of the elliptic integrals
ecc = sqrt(1 - (min(a,b)./max(a,b)).^2);
first = (pi/2) .* ( 1 + (1/2)^2*ecc.^2 + (3/8)^2*ecc.^4
      + (15/48)^2*ecc.^6 + (105/384)^2*ecc.^8 );
second = (pi/2) .* ( 1 - (1/2)^2*ecc.^2
       - (1/3)*(3/8)^2*ecc.^4 - (1/5)*(15/48)^2*ecc.^6
       + (1/7)*(105/384)^2*ecc.^8 );

% Calculation of the surface derivatives
dsda = (a>b).*(x.*(4./((a>b).*a.^2-b.^2)).*(a.^2.*second
     - b.^2.*first)) + (a==b).*x.*pi + (a<b)
     .* ((4.*b.*a./((a<b).*b.^2-a.^2)).*(first-second));
dsdb = (a>b).*(x.*(4.*a.*b./((a<b).*a.^2-b.^2))
     .* (first-second)) + (a==b).*x.*pi + (a<b).*(x.*(4
     ./ ((a<b).*b.^2-a.^2)).*(b.^2.*second-a.^2.*first));

% Calculation of driving pressure and volume flow
T = length(t);
P(1,1:N) = P_0; %Pa % The outside pressure
Q(1,1:N) = 0; %cm3/s % Initial volume flow is set to zero
P(2:T,1) = 1./(pi.*x.*b(2:T,1)).*(dsda(2:T,1).*(dsda(2:T,1)
         .* (a(2:T,1)-A(1))./C_sn(1)+dsdb(2:T,1)
         .* (b(2:T,1)-B(1))./C_sn(1)) + ((2.*a(2:T,1)
         .* b(2:T,1))./(a(2:T,1).^2+b(2:T,1).^2)).*(1
         ./ a(2:T,1)).*tan(((2.*a(2:T,1).*b(2:T,1))
         ./ (a(2:T,1).^2+b(2:T,1).^2)).*((1./a(2:T,1))
         .* (a(2:T,1)-A(1))./C_vn(1)-(1./b(2:T,1))
         .* (b(2:T,1)-B(1))./C_vn(1)))
         + ((a(2:T,1)-A(1))-(a(2:T,N)-A(N)))./C_s(N)
         + Z_s(N).*((a(2:T,1)-a(1:T-1,1))./(t(2:T)
         - t(1:T-1))-(a(2:T,N)-a(1:T-1,N))./(t(2:T)
         - t(1:T-1))) - ((a(2:T,2)-A(2))-(a(2:T,1)-A(1)))
         ./ C_s(1) - Z_s(1).*((a(2:T,2)-a(1:T-1,2))
         ./ (t(2:T)-t(1:T-1))-(a(2:T,1)-a(1:T-1,1))
         ./ (t(2:T)-t(1:T-1))) + (p(2:T,N).^2)./(4
         .* a(2:T,1).*L(N)) + (p(2:T,1).^2)./(4.*a(2:T,1)
         .* L(1))) + P_0;
P(2:T,2:N-1) = 1./(pi.*x.*b(2:T,2:N-1)) .* (dsda(2:T,2:N-1)
             .* (dsda(2:T,2:N-1).*(a(2:T,2:N-1)-ones(T-1,1)
             * A(2:N-1))./(ones(T-1,1)*C_sn(2:N-1))
             + dsdb(2:T,2:N-1).*(b(2:T,2:N-1)-ones(T-1,1)
             * B(2:N-1))./(ones(T-1,1)*C_sn(2:N-1))) + ((2
             .* a(2:T,2:N-1).*b(2:T,2:N-1))
```

```
                ./ (a(2:T,2:N-1).^2+b(2:T,2:N-1).^2)).*(1
                ./ a(2:T,2:N-1)).*tan(((2.*a(2:T,2:N-1)
                .* b(2:T,2:N-1))./(a(2:T,2:N-1).^2
                + b(2:T,2:N-1).^2)).*((1./a(2:T,2:N-1))
                .* (a(2:T,2:N-1)-ones(T-1,1)*A(2:N-1))
                ./ (ones(T-1,1)*C_vn(2:N-1))-(1./b(2:T,2:N-1))
                .* (b(2:T,2:N-1)-ones(T-1,1)*B(2:N-1))
                ./ (ones(T-1,1)*C_vn(2:N-1))))+((a(2:T,2:N-1)
                - ones(T-1,1)*A(2:N-1))-(a(2:T,1:N-2)
                - ones(T-1,1)*A(1:N-2))./(ones(T-1,1)
                * C_s(1:N-2))+(ones(T-1,1)*Z_s(1:N-2))
                .* ((a(2:T,2:N-1)-a(1:T-1,2:N-1))./((t(2:T)
                - t(1:T-1))*ones(1,N-2))-(a(2:T,1:N-2)
                - a(1:T-1,1:N-2))./((t(2:T)-t(1:T-1))
                * ones(1,N-2)))-((a(2:T,3:N)-ones(T-1,1)
                * A(3:N))-(a(2:T,2:N-1)-ones(T-1,1)*A(2:N-1)))
                ./ (ones(T-1,1)*C_s(2:N-1))+(ones(T-1,1)
                * Z_s(2:N-1)).*((a(2:T,3:N)-a(1:T-1,3:N))
                ./ ((t(2:T)-t(1:T-1))*ones(1,N-2))
                - (a(2:T,2:N-1)-a(1:T-1,2:N-1))./((t(2:T)
                - t(1:T-1))*ones(1,N-2)))+(p(2:T,1:N-2).^2)
                ./ (4.*a(2:T,2:N-1).*(ones(T-1,1)*L(1:N-2)))
                + (p(2:T,2:N-1).^2)./(4.*a(2:T,2:N-1)
                .* (ones(T-1,1)*L(2:N-1))) ) + P_0;
P(2:T,N) = 1./(pi.*x.*b(2:T,N)) .* ( dsda(2:T,N)
          .*(dsda(2:T,N).*(a(2:T,N)-A(N))./C_sn(N)
          + dsdb(2:T,N).*(b(2:T,N)-B(N))./C_sn(N))
          + ((2.*a(2:T,N).*b(2:T,N))./(a(2:T,N).^2
          + b(2:T,N).^2)).*(1./a(2:T,N)).*tan(((2.*a(2:T,N)
          .* b(2:T,N))./(a(2:T,N).^2+b(2:T,N).^2)).*((1
          ./ a(2:T,N)).*(a(2:T,N)-A(N))./C_vn(N)-(1
          ./ b(2:T,N)).*(b(2:T,N)-B(N))./C_vn(N)))
          + ((a(2:T,N)-A(N))-(a(2:T,N-1)-A(N-1)))./C_s(N-1)
          + Z_s(N-1).*((a(2:T,N)-a(1:T-1,N))./(t(2:T)
          - t(1:T-1))-(a(2:T,N-1)-a(1:T-1,N-1))./(t(2:T)
          - t(1:T-1)))-((a(2:T,1)-A(1))-(a(2:T,N)-A(N)))
          ./ C_s(N)-Z_s(N).*((a(2:T,1)-a(1:T-1,1))./(t(2:T)
          - t(1:T-1))-(a(2:T,N)-a(1:T-1,N))./(t(2:T)
          - t(1:T-1))) + (p(2:T,N-1).^2)./(4.*a(2:T,N)
          .* L(N-1)) + (p(2:T,N).^2)./(4.*a(2:T,N).*L(N)) )
          + P_0;
```

```
Q(2:T,1:N-1) = p(2:T,1:N-1)./(ones(T-1,1)*L(1:N-1))
             .* sqrt( (sqrt(a(2:T,1:N-1).*a(2:T,2:N))
             .* sqrt(b(2:T,1:N-1).*b(2:T,2:N)))
             ./ (ones(T-1,1)*(sqrt(A(1:N-1).*A(2:N))
             .* sqrt(B(1:N-1).*B(2:N))) );
Q(2:T,N) = p(2:T,N)./L(N) .* sqrt((sqrt(a(2:T,N).*a(2:T,1))
         .* sqrt(b(2:T,N).*b(2:T,1))) ./ (sqrt(A(N)*A(1))
         * sqrt(B(N)*B(1))));

save 'eliebau.mat' t a b p P Q f
```

The iterative embedded program

```
% rkembliebau.m
% Runge-Kutta iteration of the embedded Liebau's ring

function output = rkembliebau(t,z)
global N f x A B S eta f_B C_rn C_sn C_vn C_jn L C_s Z_s;
global psection plength delay Comp;

% Defining the radii and momentum from the input vector
a = (z(1:N-plength))'; b = (z(N-plength+1:2*N-plength))';
p = (z(2*N-plength+1:end))';

% The piston pump
a(psection+plength:N) = a(psection:N-plength);
a_min = sqrt(A(psection:psection+plength-1).^2
      - (A(psection:psection+plength-1).^2
      - (A(psection:psection+plength-1).* sqrt(1-Comp)).^2)
      .* (sin((pi/(plength+1)).*[1:plength])));
for pump=1:plength
    a(psection+pump-1) = A(psection+pump-1);
    a(psection+pump-1) = sqrt(A(psection+pump-1)^2
                  - (A(psection+pump-1)^2-a_min(pump)^2)
                  * sin(pi*f/0.1 * (t-delay*(pump-1)))
                  * (0<=mod(t-delay*(pump-1),1/f))
                  * ((0.1/f)>=mod(t-delay*(pump-1),1/f)));
end
```

```
% Calculation of the elliptic integrals
ecc = sqrt(1 - (min(a,b)./max(a,b)).^2);
first = (pi/2) .* ( 1 + (1/2)^2*ecc.^2 + (3/8)^2*ecc.^4
      + (15/48)^2*ecc.^6 + (105/384)^2*ecc.^8 );
second = (pi/2) .* ( 1 - (1/2)^2*ecc.^2
       - (1/3)*(3/8)^2*ecc.^4 - (1/5)*(15/48)^2*ecc.^6
       + (1/7)*(105/384)^2*ecc.^8 );

% Calculation of the surface derivatives
dsda = (a>b).*(x.*(4./((a~=b).*a.^2-b.^2)).*(a.^2.*second
     - b.^2.*first)) + (a==b).*x.*pi + (a<b).*((4.*b.*a
     ./ ((a<b).*b.^2-a.^2)).*(first-second));
dsdb = (a>b).*(x.*(4.*a.*b./((a~=b).*a.^2-b.^2)).*(first
     - second)) + (a==b).*x.*pi + (a<b).*(x.*(4./((a<b)
     .* b.^2-a.^2)).*(b.^2.*second-a.^2.*first));

% Calculation of the chi factor
chi = ((1./b).*dsda.*dsdb - (1./a).*dsdb.^2-(2./3).*(S.^2)
    .* (((2.*a.*b)./(a.^2+b.^2)).^2).*(1./(a.*b.^2)))
    ./ ((1./a).*dsda.*dsdb - (1./b).*dsda.^2-(2./3).*(S.^2)
    .* (((2.*a.*b)./(a.^2+b.^2)).^2).*(1./(a.^2.*b)));

% Calculation of the flow
Q(1:N-1) = (p(1:N-1)./L(1:N-1)).*sqrt((sqrt(a(1:N-1)
         .* a(2:N)).*sqrt(b(1:N-1).*b(2:N)))
         ./ (sqrt(A(1:N-1).*A(2:N))
         .* sqrt(B(1:N-1).*B(2:N))));
Q(N) = (p(N)/L(N)) * sqrt((sqrt(a(N)*a(1))*sqrt(b(N)*b(1)))
     / (sqrt(A(N)*A(1))*sqrt(B(N)*B(1))));

% Equations for the rate of change of the axes
da(1) = (Q(N)-Q(1))/(pi*x).*(chi(1)./(a(1)+chi(1).*b(1)));
db(1) = (Q(N)-Q(1))/(pi*x).*(1./(a(1)+chi(1).*b(1)));
da(2:N) = (Q(1:N-1)-Q(2:N))/(pi*x)
        .* (chi(2:N)./(a(2:N)+chi(2:N).*b(2:N)));
db(2:N) = (Q(1:N-1)-Q(2:N))/(pi*x)
        .* (1./(a(2:N)+chi(2:N).*b(2:N)));
```

```
% Equations for the dynamic pressure
P(1) = (1/(pi*x*b(1))) * ( (a(1)-A(1))/C_rn(1) + dsda(1)
     * (dsda(1)*(a(1)-A(1))/C_sn(1)+dsdb(1)*(b(1)-B(1))
     / C_sn(1)) + ((2*a(1)*b(1))/(a(1)^2+b(1)^2))*(1/a(1))
     * tan(((2*a(1)*b(1))/(a(1)^2+b(1)^2))*((1/a(1))*(a(1)
     - A(1))/C_vn(1)-(1/b(1))*(b(1)-B(1))/C_vn(1)))
     - (x*pi)^2*(2*a(1)-b(1))*((2*a(1)-b(1))*(a(1)-A(1))
     / C_jn(1)-a(1)*(b(1)-B(1))/C_jn(1)) + ((a(1)-A(1))
     - (a(N)-A(N)))/C_s(N) + Z_s(N)*(da(1)-da(N)) - ((a(2)
     - A(2))-(a(1)-A(1)))/C_s(1) - Z_s(1)*(da(2)-da(1))
     + (p(N)^2)/(4*a(1)*L(N)) + (p(1)^2)/(4*a(1)*L(1)) );
P(2:N-1) = (1./(pi.*x.*b(2:N-1))) .* ( (a(2:N-1)-A(2:N-1))
         ./ C_rn(2:N-1) + dsda(2:N-1).*(dsda(2:N-1)
         .* (a(2:N-1)-A(2:N-1))./C_sn(2:N-1)+dsdb(2:N-1)
         .* (b(2:N-1)-B(2:N-1))./C_sn(2:N-1))+((2.*a(2:N-1)
         .* b(2:N-1))./(a(2:N-1).^2+b(2:N-1).^2)).*(1
         ./ a(2:N-1)).*tan(((2.*a(2:N-1).*b(2:N-1))
         ./ (a(2:N-1).^2+b(2:N-1).^2)).*((1./a(2:N-1))
         .* (a(2:N-1)-A(2:N-1))./C_vn(2:N-1)-(1./b(2:N-1))
         .* (b(2:N-1)-B(2:N-1))./C_vn(2:N-1))) - (x*pi).^2
         .* (2.*a(2:N-1)-b(2:N-1)).*((2.*a(2:N-1)-b(2:N-1))
         .* (a(2:N-1)-A(2:N-1))./C_jn(2:N-1)-a(2:N-1)
         .* (b(2:N-1)-B(2:N-1))./C_jn(2:N-1)) + ((a(2:N-1)
         - A(2:N-1))-(a(1:N-2)-A(1:N-2)))./C_s(1:N-2)
         + Z_s(1:N-2).*(da(2:N-1)-da(1:N-2)) - ((a(3:N)
         - A(3:N))-(a(2:N-1)-A(2:N-1)))./C_s(2:N-1)
         - Z_s(2:N-1).*(da(3:N)-da(2:N-1))
         + (p(1:N-2).^2)./(4.*a(2:N-1).*L(1:N-2))
         + (p(2:N-1).^2)./(4.*a(2:N-1).*L(2:N-1)) );
P(N) = (1/(pi*x*b(N))) * ( (a(N)-A(N))/C_rn(N) + dsda(N)
     * (dsda(N)*(a(N)-A(N))/C_sn(N)+dsdb(N)*(b(N)-B(N))
     / C_sn(N)) + ((2*a(N)*b(N))/(a(N)^2+b(N)^2))*(1/a(N))
     * tan(((2*a(N)*b(N))/(a(N)^2+b(N)^2))*((1/a(N))*(a(N)
     - A(N))/C_vn(N)-(1/b(N))*(b(N)-B(N))/C_vn(N)))
     - (x*pi)^2*(2*a(N)-b(N))*((2*a(N)-b(N))*(a(N)-A(N))
     / C_jn(N)-a(N)*(b(N)-B(N))/C_jn(N)) + ((a(N)-A(N))
     - (a(N-1)-A(N-1)))/C_s(N-1) + Z_s(N-1)*(da(N)-da(N-1))
     - ((a(1)-A(1))-(a(N)-A(N)))/C_s(N) - Z_s(N)*(da(1)
     - da(N)) + (p(N-1)^2)/(4*a(N)*L(N-1))
     + (p(N)^2)/(4*a(N)*L(N)) );
```

```
% Equations for the rate of change of the momentum
dp(1) = sqrt(sqrt(a(1)*a(2))*sqrt(b(1)*b(2))/(sqrt(A(1)
      * A(2))*sqrt(B(1)*B(2)))) * ( P(1) - P(2) - ( (4*eta
      * x*(a(1)*a(2)+b(1)*b(2)))/(sqrt(a(1)*a(2))^3
      * sqrt(b(1)*b(2))^3) + (f_B(1)*(1/(4*pi))
      * sqrt(sqrt(A(1)*A(2)*B(1)*B(2))/(sqrt(a(1)*a(2))^5
      * sqrt(b(1)*b(2))^5))*sqrt((a(1)*a(2)+b(1)*b(2))/2)
      * sign(p(1))*p(1)) ) * Q(1) ) + (p(1)/(4*a(1)))*da(1)
      + (p(1)/(4*a(2)))*da(2) + (p(1)/(4*b(1)))*db(1)
      + (p(1)/(4*b(2)))*db(2);
dp(2:N-1) = sqrt(sqrt(a(2:N-1).*a(3:N)).*sqrt(b(2:N-1)
          .* b(3:N))./(sqrt(A(2:N-1).*A(3:N))
          .* sqrt(B(2:N-1).*B(3:N)))).*( P(2:N-1) - P(3:N)
          - ( (4.*eta.*x.*(a(2:N-1).*a(3:N)+b(2:N-1)
          .* b(3:N)))./(sqrt(a(2:N-1).*a(3:N)).^3
          .* sqrt(b(2:N-1).*b(3:N)).^3) + (f_B(2:N-1).*(1
          ./ (4.*pi)).*sqrt(sqrt(A(2:N-1).*A(3:N).*B(2:N-1)
          .* B(3:N))./(sqrt(a(2:N-1).*a(3:N)).^5
          .* sqrt(b(2:N-1).*b(3:N)).^5)).*sqrt((a(2:N-1)
          .* a(3:N)+b(2:N-1).*b(3:N))./2).*sign(p(2:N-1))
          .* p(2:N-1)) ) .* Q(2:N-1) ) + (p(2:N-1)./(4
          .* a(2:N-1))).*da(2:N-1) + (p(2:N-1)./(4
          .* a(3:N))).*da(3:N) + (p(2:N-1)./(4.*b(2:N-1)))
          .* db(2:N-1) + (p(2:N-1)./(4.*b(3:N))).*db(3:N);
dp(N) = sqrt(sqrt(a(N)*a(1))*sqrt(b(N)*b(1))/(sqrt(A(N)
      * A(1))*sqrt(B(N)*B(1)))) * ( P(N) - P(1) - ( (4*eta
      * x*(a(N)*a(1)+b(N)*b(1)))/(sqrt(a(N)*a(1))^3
      * sqrt(b(N)*b(1))^3) + (f_B(N)*(1/(4*pi))
      * sqrt(sqrt(A(N)*A(1)*B(N)*B(1))/(sqrt(a(N)*a(1))^5
      * sqrt(b(N)*b(1))^5))*sqrt((a(N)*a(1)+b(N)*b(1))/2)
      * sign(p(N))*p(N)) ) * Q(N) ) + (p(N)/(4*a(N)))*da(N)
      + (p(N)/(4*a(1)))*da(1) + (p(N)/(4*b(N)))*db(N)
      + (p(N)/(4*b(1)))*db(1);

da = [da(1:psection-1) da(psection+plength:N)];

% The output to the main program
output = [da';db';dp'];
```

The master embedded program

```
% embliebau.m
% A model for pulsating flow in a layered tube.
% The model is used to simulate Liebau's Ring.

function embliebau

% Initializing variables
global N f x A B S eta f_B C_rn C_sn C_vn C_jn L C_s Z_s;
global psection plength delay Comp;
a = 0; b = 0; p = 0; P = 0; Q = 0;

% The numbers we can change
N = 60; % The number of sections in the model
psection = 5; % The first section of the pump
plength = 3; % The number of sections of the pump
delay = 0; % The delay time for sequential pumping
Comp = 0.1; % The cross-sectional compression ratio
f = 2.06; %Hz % The frequency of the pump
periods = 50; % The number of periods in the simulation
time = periods * 1/f; %seconds % The time of the simulation

% The parameters of the tube at rest
l = 1.0; %m % The length of the tube
x = l/N; %m % Length per section
Eccentricity = 0.3; % Desired eccentricity of the ellipse
R1 = 0.01; %m The equivalent radius of the soft tube
R2 = 0.008; %m The equivalent radius of the rigid tube
A(1:N/2) = sqrt((R1^2)*(1/sqrt(1-Eccentricity))); %m
A(N/2+1:N) = sqrt((R2^2)*(1/sqrt(1-Eccentricity))); %m
B(1:N/2) = sqrt((R1^2)*sqrt(1-Eccentricity)); %m
B(N/2+1:N) = sqrt((R2^2)*sqrt(1-Eccentricity)); %m
a(1:N) = A(:); %m % The dynamic major axis of the tube
b(1:N) = B(:); %m % The dynamic minor axis of the tube
p(1:N) = 0; %kg*m/s % The initial momentum of the flow
R_B(1:N) = l/(2*pi); % The bend radius for each section
theta(1:N) = (x.*360)./(2.*pi.*R_B); %deg. % The bend angle
S(1:N) = x*pi*(A+B).*(1+3*((A-B)./(A+B)).^2
       ./(10+sqrt(4-3*((A-B)./(A+B)).^2))); %m2
```

```
% The physical properties of the tube and the liquid
rho = 1000; %kg/m3 % The density of the liquid (water)
eta = 0.001; %Pa.s % The viscosity of the liquid (water)
P_0 = 1e5; %Pa % The pressure outside the tube
E1 = 4.1e5; %Pa % Young's modulus for the soft tube
E2 = 4.3e5; %Pa % Young's modulus for the rigid tube
h1 = 0.001; %m % The wall thickness of the soft tube
h2 = 0.003; %m % The wall thickness of the rigid tube
K1 = E1/10; %Pa % Volume modulus of the soft tube
K2 = E2/10; %Pa % Volume modulus of the rigid tube

% Womersley theory
alpha(1:N-1) = sqrt((2.*A(1:N-1).*A(2:N).*B(1:N-1).*B(2:N))
             ./(A(1:N-1).*A(2:N)+B(1:N-1).*B(2:N)))
             .* sqrt(2*pi*f*rho/eta);
alpha(N) = sqrt((2.*A(N).*A(1).*B(N).*B(1))
         ./ (A(N).*A(1)+B(N).*B(1))).*sqrt(2*pi*f*rho/eta);
psi = real(1 ./ (1 - 2./(alpha.*sqrt(-i))
    .* besselj(1,alpha.*sqrt(-i))
    ./ besselj(0,alpha.*sqrt(-i))) - 8./(i.*alpha.^2));

% Equations for the curvature of the tube
xi = 0.042 .* theta.^0.69; l_c(1:N-1) =
sqrt(2.*A(1:N-1).*A(2:N).*B(1:N-1).*B(2:N)
           ./ (A(1:N-1).*A(2:N)+B(1:N-1).*B(2:N)));
l_c(N) = sqrt(2.*A(N).*A(1).*B(N).*B(1)
       ./ (A(N).*A(1)+B(N).*B(1)));
K_B(1:N) = 9.0704.*(log(R_B(1:N)./(2.*l_c(1:N)))).^2
         - 16.9345.*(log(R_B(1:N)./(2.*l_c(1:N))))+19.6437;
f_T(1:N) = 0.0478.*(2.*l_c(1:N)).^(-0.2245);

% The calculation of the elements of the network model
C_rn(1:N/2) = 1./(2*pi*x*E1*h1).*(A(1:N/2)); %(Pa.m)^-1
C_rn(N/2+1:N) = 1./(2*pi*x*E2*h2).*(A(N/2+1:N)); %(Pa.m)^-1
C_sn(1:N/2) = S(1:N/2)./(E1*h1/2); %m/Pa
C_sn(N/2+1:N) = S(N/2+1:N)./(E2*h2/2); %m/Pa
C_vn(1:N/2) = 1./(S(1:N/2).*(1/3).*(E1*h1/2)); %(Pa.m3)^-1
C_vn(N/2+1:N) = 1./(S(N/2+1:N).*(1/3).*(E2*h2/2));
C_jn(1:N/2) = (pi.*x.*(A(1:N/2).^2
            - A(1:N/2).*B(1:N/2))) ./ K1; %m^3/Pa
C_jn(N/2+1:N) = (pi.*x.*(A(N/2+1:N).^2
              - A(N/2+1:N).*B(N/2+1:N))) ./ K2; %m^3/Pa
```

```
L(1:N-1) = psi(1:N-1).*rho.*x./(pi.*sqrt(A(1:N-1).*A(2:N)
         .* B(1:N-1).*B(2:N))); %kg/m4
L(N) = psi(N)*rho*x./(pi.*sqrt(A(N).*A(1).*B(N).*B(1)));
C_s(1:N/2-1) = (x./((1/3)*(E1*h1))) .* 2./( pi
             .* (sqrt(A(1:N/2-1).*A(2:N/2))+sqrt(B(1:N/2-1)
             .* B(2:N/2))).*(1+3*((sqrt(A(1:N/2-1)
             .* A(2:N/2))-sqrt(B(1:N/2-1).*B(2:N/2)))
             ./ (sqrt(A(1:N/2-1).*A(2:N/2))+sqrt(B(1:N/2-1)
             .* B(2:N/2)))).^2./(10+sqrt(4
             - 3.*((sqrt(A(1:N/2-1).*A(2:N/2))
             - sqrt(B(1:N/2-1).*B(2:N/2)))
             ./ (sqrt(A(1:N/2-1).*A(2:N/2))
             + sqrt(B(1:N/2-1).*B(2:N/2)))).^2)) ));
C_s(N/2) = ((x./((1/3)*sqrt(E1*h1*E2*h2))) .* 2./( pi
         .* (sqrt(A(N/2).*A(N/2+1))+sqrt(B(N/2).*B(N/2+1)))
         .* (1+3*((sqrt(A(N/2).*A(N/2+1))-sqrt(B(N/2)
         .* B(N/2+1))))./(sqrt(A(N/2).*A(N/2+1))+sqrt(B(N/2)
         .* B(N/2+1)))).^2./(10+sqrt(4-3.*((sqrt(A(N/2)
         .* A(N/2+1))-sqrt(B(N/2).*B(N/2+1))))./(sqrt(A(N/2)
         .* A(N/2+1))+sqrt(B(N/2).*B(N/2+1)))).^2)) )) + (x
         ./ ((1/3)*(E2*h2))).*2./( pi.*(sqrt(A(N/2)
         .* A(N/2+1))+sqrt(B(N/2).*B(N/2+1))).*(1+3
         * ((sqrt(A(N/2).*A(N/2+1))-sqrt(B(N/2).*B(N/2+1)))
         ./ (sqrt(A(N/2).*A(N/2+1))+sqrt(B(N/2)
         .* B(N/2+1)))).^2./(10+sqrt(4-3.*((sqrt(A(N/2)
         .* A(N/2+1))-sqrt(B(N/2).*B(N/2+1))))./(sqrt(A(N/2)
         .* A(N/2+1))+sqrt(B(N/2).*B(N/2+1)))).^2)) )))/2;
C_s(N/2+1:N-1) = (x./((1/3)*(E2*h2))) .* 2./( pi
               .* (sqrt(A(N/2+1:N-1).*A(N/2+2:N))
               + sqrt(B(N/2+1:N-1).*B(N/2+2:N))).*(1
               + 3*((sqrt(A(N/2+1:N-1).*A(N/2+2:N))
               - sqrt(B(N/2+1:N-1).*B(N/2+2:N)))
               ./ (sqrt(A(N/2+1:N-1).*A(N/2+2:N))
               + sqrt(B(N/2+1:N-1).*B(N/2+2:N)))).^2./(10
               + sqrt(4-3.*((sqrt(A(N/2+1:N-1).*A(N/2+2:N))
               - sqrt(B(N/2+1:N-1).*B(N/2+2:N)))
               ./ (sqrt(A(N/2+1:N-1).*A(N/2+2:N))
               + sqrt(B(N/2+1:N-1).*B(N/2+2:N)))).^2)) ));
```

```
C_s(N) = ((x./((1/3)*sqrt(E1*h1*E2*h2))) .* 2./( pi
       .* (sqrt(A(N).*A(1))+sqrt(B(N).*B(1))).*(1
       + 3*((sqrt(A(N).*A(1))-sqrt(B(N).*B(1))).^2./(10+sqrt(4-3
       .* ((sqrt(A(N).*A(1))-sqrt(B(N).*B(1))).^2)) )) + (x./((1/3)*(E2
       * h2))).*2./(pi.*(sqrt(A(N).*A(1))+sqrt(B(N).*B(1)))
       .* (1+3*((sqrt(A(N).*A(1))-sqrt(B(N).*B(1)))
       ./ (sqrt(A(N).*A(1))+sqrt(B(N).*B(1)))).^2./(10
       + sqrt(4-3.*((sqrt(A(N).*A(1))-sqrt(B(N).*B(1)))
       ./ (sqrt(A(N).*A(1))+sqrt(B(N).*B(1)))).^2)) )))/2;
Z_s(1:N) = 0.01./C_s; %Pa.m
f_B = xi.*K_B.*f_T./psi; % The friction factor

% Call MatLab's solver for ordinary differential equations
a = [a(1:psection-1) a(psection+plength:N)];
[t,z] = ode45('rkembliebau',[0 time],[a b p]);
a = z(:,1:N-plength);
b = z(:,N-plength+1:2*N-plength);
p = z(:,2*N-plength+1:end);

% The compression pump
a(1:length(t),psection+plength:N) =
      a(1:length(t),psection:N-plength);
a_min = sqrt(A(psection:psection+plength-1).^2
      - (A(psection:psection+plength-1).^2
      - (A(psection:psection+plength-1).* sqrt(1-Comp)).^2)
      .* (sin((pi/(plength+1)).*[1:plength])));

for pump=1:plength
 a(1:length(t),psection+pump-1) = A(psection+pump-1);
 a(1:length(t),psection+pump-1) = sqrt(A(psection+pump-1).^2
                  - (A(psection+pump-1).^2-a_min(pump).^2)
                  .* sin(pi*f/0.1 .* (t-delay*(pump-1)))
                  .* (0<=mod(t-delay*(pump-1),1/f))
                  .* ((0.1/f)>=mod(t-delay*(pump-1),1/f)));
end
```

```
% Calculation of the elliptic integrals
ecc = sqrt(1 - (min(a,b)./max(a,b)).^2);
first = (pi/2) .* ( 1 + (1/2)^2*ecc.^2 + (3/8)^2*ecc.^4
      + (15/48)^2*ecc.^6 + (105/384)^2*ecc.^8 );
second = (pi/2) .* ( 1 - (1/2)^2*ecc.^2
       - (1/3)*(3/8)^2*ecc.^4 - (1/5)*(15/48)^2*ecc.^6
       + (1/7)*(105/384)^2*ecc.^8 );

% Calculation of the surface derivatives
dsda = (a>b).*(x.*(4./((a>b).*a.^2-b.^2)).*(a.^2.*second
     - b.^2.*first)) + (a==b).*x.*pi + (a<b).*((4.*b.*a
     ./ ((a<b).*b.^2-a.^2)).*(first-second));
dsdb = (a)>b).*(x.*(4.*a.*b./((a<b).*a.^2-b.^2)).*(first
     - second)) + (a==b).*x.*pi + (a<b).*(x.*(4./((a<b)
     .* b.^2-a.^2)).*(b.^2.*second-a.^2.*first));

% Calculation of driving pressure and volume flow
T = length(t);
P(1,1:N) = P_0; %Pa % The outside pressure
Q(1,1:N) = 0; %cm3/s % Initial volume flow is set to zero

P(2:T,1) = 1./(pi.*x.*b(2:T,1)).*((a(2:T,1)-A(1))./C_rn(1)
         + dsda(2:T,1).*(dsda(2:T,1).*(a(2:T,1)-A(1))
         ./ C_sn(1)+dsdb(2:T,1).*(b(2:T,1)-B(1))./C_sn(1))
         + ((2.*a(2:T,1).* b(2:T,1))./(a(2:T,1).^2
         + b(2:T,1).^2)).*(1./a(2:T,1)).*tan(((2.*a(2:T,1)
         .* b(2:T,1))./(a(2:T,1).^2+b(2:T,1).^2)).*((1
         ./ a(2:T,1)).*(a(2:T,1)-A(1))./C_vn(1)-(1
         ./ b(2:T,1)).*(b(2:T,1)-B(1))./C_vn(1)))
         - (x*pi).^2.*(2.*a(2:T,1)-b(2:T,1)).*((2.*a(2:T,1)
         - b(2:T,1)).*(a(2:T,1)-A(1))./C_jn(1)-a(2:T,1)
         .* (b(2:T,1)-B(1))./C_jn(1)) + ((a(2:T,1)-A(1))
         - (a(2:T,N)-A(N)))./C_s(N) + Z_s(N).*((a(2:T,1)
         - a(1:T-1,1))./(t(2:T)-t(1:T-1))-(a(2:T,N)
         - a(1:T-1,N))./(t(2:T)-t(1:T-1)))-((a(2:T,2)-A(2))
         - (a(2:T,1)-A(1)))./C_s(1) - Z_s(1).*((a(2:T,2)
         - a(1:T-1,2))./(t(2:T)-t(1:T-1))-(a(2:T,1)
         - a(1:T-1,1))./(t(2:T)-t(1:T-1))) + (p(2:T,N).^2)
         ./ (4.*a(2:T,1).*L(N)) + (p(2:T,1).^2)./(4
         .* a(2:T,1).*L(1))) + P_0;
```

```
P(2:T,2:N-1) = 1./(pi.*x.*b(2:T,2:N-1)) .* ( (a(2:T,2:N-1)
             - ones(T-1,1)*A(2:N-1))./(ones(T-1,1)
             * C_rn(2:N-1)) + dsda(2:T,2:N-1)
             .* (dsda(2:T,2:N-1).*(a(2:T,2:N-1)-ones(T-1,1)
             * A(2:N-1))./(ones(T-1,1)*C_sn(2:N-1))
             + dsdb(2:T,2:N-1).*(b(2:T,2:N-1)-ones(T-1,1)
             * B(2:N-1))./(ones(T-1,1)*C_sn(2:N-1)))
             + ((2.*a(2:T,2:N-1).*b(2:T,2:N-1))
             ./ (a(2:T,2:N-1).^2+b(2:T,2:N-1).^2))
             .* (1./a(2:T,2:N-1)).*tan(((2.*a(2:T,2:N-1)
             .* b(2:T,2:N-1))./(a(2:T,2:N-1).^2
             + b(2:T,2:N-1).^2)).*((1./a(2:T,2:N-1))
             .* (a(2:T,2:N-1)-ones(T-1,1)*A(2:N-1))
             ./ (ones(T-1,1)*C_vn(2:N-1))-(1./b(2:T,2:N-1))
             .* (b(2:T,2:N-1)-ones(T-1,1)*B(2:N-1))
             ./(ones(T-1,1)*C_vn(2:N-1)))) - (x*pi).^2.*(2
             .* a(2:T,2:N-1)-b(2:T,2:N-1))
             .* ((2.*a(2:T,2:N-1)-b(2:T,2:N-1))
             .* (a(2:T,2:N-1)-ones(T-1,1)*A(2:N-1))
             ./ (ones(T-1,1)*C_jn(2:N-1))-a(2:T,2:N-1)
             .* (b(2:T,2:N-1)-ones(T-1,1)*B(2:N-1))
             ./ (ones(T-1,1)*C_jn(2:N-1)))+((a(2:T,2:N-1)
             - ones(T-1,1)*A(2:N-1))-(a(2:T,1:N-2)
             - ones(T-1,1)*A(1:N-2))./(ones(T-1,1)
             * C_s(1:N-2))+(ones(T-1,1)*Z_s(1:N-2))
             .* ((a(2:T,2:N-1)-a(1:T-1,2:N-1))./((t(2:T)
             - t(1:T-1))*ones(1,N-2))-(a(2:T,1:N-2)
             - a(1:T-1,1:N-2))./((t(2:T)-t(1:T-1))
             * ones(1,N-2))) - ((a(2:T,3:N)-ones(T-1,1)
             * A(3:N))-(a(2:T,2:N-1)-ones(T-1,1)*A(2:N-1)))
             ./ (ones(T-1,1)*C_s(2:N-1)) + (ones(T-1,1)
             * Z_s(2:N-1)).*((a(2:T,3:N)-a(1:T-1,3:N))
             ./ ((t(2:T)-t(1:T-1))*ones(1,N-2))
             - (a(2:T,2:N-1)-a(1:T-1,2:N-1))./((t(2:T)
             - t(1:T-1))*ones(1,N-2))) + (p(2:T,1:N-2).^2)
             ./ (4.*a(2:T,2:N-1).*(ones(T-1,1)*L(1:N-2)))
             + (p(2:T,2:N-1).^2)./(4.*a(2:T,2:N-1)
             .*(ones(T-1,1)*L(2:N-1))) ) + P_0;
```

```
P(2:T,N) = 1./(pi.*x.*b(2:T,N)).*((a(2:T,N)-A(N))./C_rn(N)
         + dsda(2:T,N).*(dsda(2:T,N).*(a(2:T,N)-A(N))
         ./ C_sn(N)+dsdb(2:T,N).*(b(2:T,N)-B(N))./C_sn(N))
         + ((2.*a(2:T,N).*b(2:T,N))./(a(2:T,N).^2
         + b(2:T,N).^2)).*(1./a(2:T,N)).*tan(((2.*a(2:T,N)
         .* b(2:T,N))./(a(2:T,N).^2+b(2:T,N).^2))
         .* ((1./a(2:T,N)).*(a(2:T,N)-A(N))./C_vn(N)
         - (1./b(2:T,N)).*(b(2:T,N)-B(N))./C_vn(N)))
         - (x*pi).^2.*(2.*a(2:T,N)-b(2:T,N)).*((2.*a(2:T,N)
         - b(2:T,N)).*(a(2:T,N)-A(N))./C_jn(N)-a(2:T,N)
         .* (b(2:T,N)-B(N))./C_jn(N)) + ((a(2:T,N)-A(N))
         - (a(2:T,N-1)-A(N-1)))./C_s(N-1) + Z_s(N-1)
         .* ((a(2:T,N)-a(1:T-1,N))./(t(2:T)-t(1:T-1))
         - (a(2:T,N-1)-a(1:T-1,N-1))./(t(2:T)-t(1:T-1)))
         - ((a(2:T,1)-A(1))-(a(2:T,N)-A(N)))./C_s(N)
         - Z_s(N).*((a(2:T,1)-a(1:T-1,1))./(t(2:T)
         - t(1:T-1))-(a(2:T,N)-a(1:T-1,N))./(t(2:T)
         - t(1:T-1))) + (p(2:T,N-1).^2)./(4.*a(2:T,N)
         .* L(N-1)) + (p(2:T,N).^2)./(4.*a(2:T,N).*L(N)) )
         + P_0;

Q(2:T,1:N-1) = p(2:T,1:N-1)./(ones(T-1,1)*L(1:N-1))
             .* sqrt( (sqrt(a(2:T,1:N-1).*a(2:T,2:N))
             .* sqrt(b(2:T,1:N-1).*b(2:T,2:N)))
             ./ (ones(T-1,1)*(sqrt(A(1:N-1).*A(2:N))
             .* sqrt(B(1:N-1).*B(2:N)))) );
Q(2:T,N) = p(2:T,N)./L(N) .* sqrt((sqrt(a(2:T,N).*a(2:T,1))
         .* sqrt(b(2:T,N).*b(2:T,1)))
         ./ (sqrt(A(N)*A(1))*sqrt(B(N)*B(1))));

save 'embliebau.mat' t a b p P Q f
```